RUPRECHT-KARLS-UNIVERSITÄT HEIDELBERG

Silicon microstrip detectors and the measurement of lifetimes of charmed hadrons

Silvia Masciocchi

1996

MAX-PLANCK-INSTITUT FÜR KERNPHYSIK
HEIDELBERG

INAUGURAL-DISSERTATION

zur

Erlangung der Doktorwürde

der

Naturwissenschaftlichen-Mathematischen

Gesamtfakultät

der

Ruprecht-Karls-Universität

Heidelberg

vorgelegt von

Silvia Masciocchi

aus Mailand

Tag der mündlichen Prüfung 16.10.1996

Silicon microstrip detectors

and the measurement of lifetimes

of charmed hadrons

Gutachter : Prof. Dr. Bogdan Povh
Prof. Dr. Franz Eisele

Sempre caro mi fu quest'ermo colle,
e questa siepe, che da tanta parte
dell'ultimo orizzonte il guardo esclude.
Ma sedendo e mirando, interminati
spazi di là da quella, e sovrumani
silenzi, e profondissima quiete
io nel pensier mi fingo; ove per poco
il cor non si spaura. E come il vento
odo stormir tra queste piante, io quello
infinito silenzio a questa voce
vo comparando: e mi sovvien l'eterno,
e le morte stagioni, e la presente
e viva, e il suon di lei. Così tra questa
immensità s'annega il pensier mio;
e il naufragar m'è dolce in questo mare.

"L'infinito", *Giacomo Leopardi*

Contents

Introduction

In the framework of the Standard Model, the heavy flavor sector still requires further experimental investigation. The weak decays of heavy quarks give the possibility to study the interplay of weak and strong interactions and to investigate the structure of hadrons. In particular, better experimental information on charmed baryons is needed.

Of the four weakly decaying charmed baryons, the Λ_c^+ is relatively well measured, while the three baryons with charm *and* strange content (Ξ_c^+, Ξ_c^0 and Ω_c^0) are still poorly known. Models exist with which matrix elements of baryon decays are calculated and the corresponding inclusive decay amplitudes are estimated. This information is used to predict the lifetime hierarchy of the four charmed baryons. Important indications on the validity of the models and on the relative weight of the processes involved can be therefore obtained with the experimental determination of these lifetimes and their ratios. An overview of the weak decays of heavy flavors and the existing predictions for the lifetime hierarchy of charmed baryons are given in chapter 1.

In fixed target experiments, a large acceptance forward spectrometer with high precision track reconstruction and momentum measurement, and good particle identification is required in order to reconstruct and select charmed hadron candidates from a very large background due to lighter quarks.

In particular, the range of lifetimes to measure (10^{-13} - 10^{-12} sec) imposes severe requirements on the tracking detectors to achieve the high resolution necessary to reconstruct well identified and separate production and decay points of the charmed hadrons. This is an essential condition to measure the particle decay time event by event, and estimate the mean lifetime. Silicon microstrip counters are the only detectors which offer the resolution, compactness, speed and stability of operation to fulfill the above requirements.

Single sided microstrip detectors with 25 μm pitch were tested, equipped with VLSI readout electronics performing zero suppression, and installed in the vertex area of the hyperon beam fixed target experiment WA89 at CERN. The single sided detectors, the readout electronics, and the system performance during the 1993 and 1994 data taking periods are described in chapter 2, and the WA89 experimental apparatus is reviewed in chapter 4.

The excellent quality, detection efficiency, and high resolution of the microstrip detectors provide the information necessary to reconstruct primary and secondary vertices of charmed hadrons with very high precision, and consequently they allow the measurement of lifetimes of mesons and baryons with charm content. In particular, the analysis presented in this thesis is focused on the search for the $\overline{D}^0$ and D^- mesons and the charmed

strange baryon Ξ_c^+ in the decay channels $\Lambda^0 K^- \pi^+ \pi^+$ and $\Xi^- \pi^+ \pi^+$.
The data processing and the methods used for the analysis are illustrated in chapter 5: In particular, the program based on a candidate driven approach used for the selection of charmed hadron candidates and the method used for lifetime fitting are discussed. The results of the analysis and the measured lifetimes are presented in chapter 6 and discussed in chapter 7.

A significant improvement in tracking and particularly in pattern recognition can be achieved with double sided detectors, even though their implementation in fixed target experiments requires major developments. Double sided counters have been tested, assembled, studied with beams of high energy particles, and installed in the "next generation" hyperon beam experiment SELEX at Fermilab, downstream of the vertex area. This is the first time that double sided detectors read out in sparse mode were implemented in a fixed target experiment. The success of the project supports the attractive possibility of including double sided detectors close to the vertex area to limit the amount of scattering material and improve pattern recognition.
The double sided counters installed in SELEX, the development of a reliable readout in sparse mode and preliminary test beam results are presented in chapter 3.

Chapter 1

The physics of charmed baryons

1.1 Introduction

Since the discovery of the charm quark in 1974, heavy quarks and their fundamental interactions became a major field of research in high energy physics. The bottom quark discovered in 1977 and the top quark, of which evidence was lately obtained, complete the three quark weak doublets:

$$\begin{pmatrix} u \\ d' \end{pmatrix} \quad \begin{pmatrix} c \\ s' \end{pmatrix} \quad \begin{pmatrix} t \\ b' \end{pmatrix} \tag{1.1}$$

These, together with the corresponding lepton doublets formed by electron, muon and tau, and the three neutrinos, are considered the basic constituents of matter in the standard theory of electroweak and strong interactions.
The unified theory of electromagnetic and weak interactions is described by the *Standard Model*, a gauge theory based on the group SU(2)⊗U(1). This model has been largely tested and is supported by considerable experimental evidence. Still, some of its parameters are not yet well established and the heavy quark sector particularly requires further experimental exploration. The weak decays of heavy quarks are the most suitable processes to study their weak interaction.
However quarks are confined in bound hadronic states by the effect of strong interactions. These are described by the Quantum ChromoDynamics (QCD) gauge theory, based on the group SU(3). Each quark flavor exists in three colors; leptons and bound quark states (hadrons) are color neutral objects.
In order to study the parameters of the weak interactions from observed properties of hadron decays, the impact of strong interactions must be understood and correctly taken into account. And conversely, further information on strong interactions can be obtained by the study of heavy flavor decays.

Due to the short-range nature of the weak force, weak decays allow the study of the dynamical behaviour of quarks at very small space-time distances. In this range hard gluon interactions modify the structure and effective strength of the weak couplings. But the calculable short-distance effects of strong interactions are alone not enough to describe properly heavy hadron decays. From the study of experimental results from

charmed hadron decays published in the late 1970s, it was realized that the soft gluons and the light quarks present in hadronic bound states induce significant effects on the decays. Consequently, both short and long distance effects must be taken into account in order to give a complete description of the weak decays. And only the collection of large samples of experimental data will improve the understanding of the relative weight of the different processes.
Charmed hadron decays provide an excellent environment to study weak decays of heavy flavors and better understand the involved dynamics.

1.2 Charmed baryons

Even though, in experiments, the statistics of charmed baryons is far smaller than that of charmed mesons, it is important and interesting to study charmed baryons. The presence of three quarks instead of only a quark and an antiquark allows a larger variety of possible processes. For baryons there are decay mechanisms that do not exist in charmed mesons. There are also decay mechanisms that are suppressed but not forbidden in charmed meson decays, and they can be fully studied in charmed baryon decays. These can be used to make higher order corrections to meson decays. Moreover, further experimental information on the structure of baryons can be obtained.

In the (u d)(s c) 4-quark model, charmed baryons are classified as members of the SU(4) multiplets with spin=1/2 and spin=3/2, respectively. The two multiplets contain 20 particles each, as schematically represented in figure 1.1. No doubly charmed baryons have been observed so far and only first evidence has been lately obtained of the Ξ_c^* states among the spin=3/2 baryons [1].

Baryons with spin=1/2 containing one charm quark (C=1) can be described combining the SU(3) flavor symmetry group of the three lighter quarks u, d, and s. Considering the flavor symmetry of the diquark in the baryon formed by the pair of light quarks, the baryon multiplet can be represented as the combination of an antisymmetric triplet and a symmetric sextet:

$$\mathbf{3} \otimes \mathbf{3} = \overline{\mathbf{3}} \oplus \mathbf{6} \tag{1.2}$$

The nine components of the baryon multiplet and the respective quark content are listed below. The brackets denote antisymmetric and symmetric diquark states:

Antisymmetric triplet	Λ_c^+	$c[ud]$
	Ξ_c^+	$c[su]$
	Ξ_c^0	$c[sd]$
Symmetric sextet	Σ_c^0	cdd
	Σ_c^+	$c\{ud\}$
	Σ_c^{++}	cuu
	$\Xi_c^{+,}$	$c\{us\}$
	$\Xi_c^{0,}$	$c\{ds\}$
	Ω_c^0	css

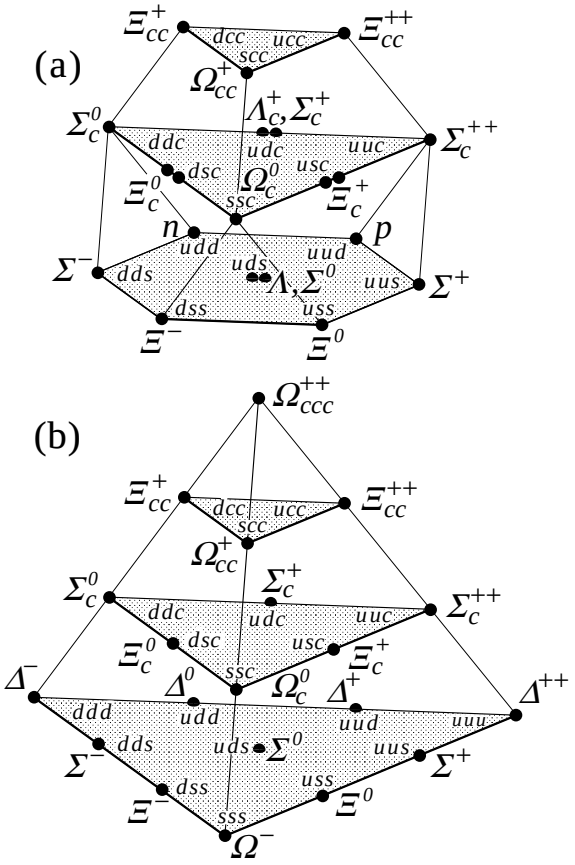

Figure 1.1: The SU(4) baryon multiplets, with spin=1/2 (a) and spin=3/2 (b).

Among the nine baryons listed above, the Ξ_c' states have not been observed yet; The Λ_c^+ is relatively well measured, and all others need considerably more statistics and more precise measurements.

Only four of the singly charmed baryons with spin=1/2 decay weakly: the Λ_c^+, Ξ_c^+, Ξ_c^0, and the Ω_c^0, and their lifetime is measurable. The other states either decay strongly (Σ_c) or radiatively ($\Xi_c^{'}$) into one of the other four particles.

The characteristics of the four weakly decaying charmed baryons which have been experimentally observed, reported by the Particle Data Group, are listed in table 1.1.

Charmed hadron	Quark content	Mass [MeV/c^2]	Lifetime [psec]
Λ_c^+	(udc)	2285.1 ± 0.6	$0.200^{+0.011}_{-0.010}$
Ξ_c^+	(usc)	2465.1 ± 1.6	$0.35^{+0.07}_{-0.04}$
Ξ_c^0	(dsc)	2470.3 ± 1.8	$0.098^{+0.023}_{-0.015}$
Ω_c^0	(ssc)	2710 ± 5	$0.065^{+0.019\dagger}_{-0.020}$

Table 1.1: Mass and lifetime world average values of the weakly decaying charmed baryons [2]. † The lifetime of the Ω_c^0 has been calculated as average of the two measurements published in 1995 [3, 4]

1.3 Weak decays of heavy quarks

1.3.1 The *c* quark free decay

Flavor changing weak decays proceed via charged current interactions, that is to say via exchange or radiation of a $W^{\pm}$ boson, since flavor changing neutral currents are forbidden. The relevant term of the fundamental Lagrangian is:

$$L_c = \frac{-e}{\sqrt{2}\sin\theta_W}(W_\mu^+ (h^\mu + l^\mu) + h.c.) \tag{1.3}$$

with the hadronic charged current

$$h_\mu = (\overline{u}\,\overline{c}\,\overline{t})\,\gamma_\mu(1-\gamma_5)V_{CKM}\begin{pmatrix} d \\ s \\ b \end{pmatrix} \tag{1.4}$$

and the leptonic current

$$l_\mu = (\overline{\nu_e}\,\overline{\nu_\mu}\,\overline{\nu_\tau})\,\gamma_\mu(1-\gamma_5)\begin{pmatrix} e^- \\ \mu^- \\ \tau^- \end{pmatrix} \tag{1.5}$$

V_{CKM} is the Cabibbo-Kobayashi-Maskawa matrix which describes the mixing between the weak eigenstates d', s', and b' indicated in (1.1) and the mass eigenstates d, s, and b. For the "reduced" 4-quark model, the d-s mixing is expressed with only one parameter, the Cabibbo angle θ_C:

$$\begin{aligned} d' &= \cos\theta_C\, d + \sin\theta_C\, s \\ s' &= \cos\theta_C\, d - \sin\theta_C\, s \end{aligned} \tag{1.6}$$

where $\sin\theta_C \approx 0.23$. As a consequence of this mixing, $c \to s$ and $u \to d$ transitions are "Cabibbo favored" (modulated by the factor $\cos^2\theta_C$), while the $c \to d$ and $s \to u$ transitions are "Cabibbo suppressed" (modulated by the factor $\sin^2\theta_C$). The latter will be ignored in the following.

Since all quarks established are much lighter than the W boson, the momentum transfer involved in weak decays is considerably smaller than the W mass and it is appropriate to take the limit $m_W \to \infty$. With this assumption we can write the effective Hamiltonian for the hadronic component as:

$$H_{eff}^{had}(0) = \frac{G_F}{\sqrt{2}}(h^\mu h_\mu^\dagger + h.c.) \qquad \text{where} \quad g_W^2 = 4\sqrt{2}G_F m_W^2 \tag{1.7}$$

The T-matrix element for a weak transition $i \to f$, in second order of the weak coupling, is given by:

$$T_{fi} = \langle f | \int \mathrm{d}^4 x_f\, \mathrm{d}^4 x_i\, T[H(x_f)H^\dagger(x_i)|i\rangle \tag{1.8}$$

where T denotes the time ordering operator. Consequently, for the optical theorem, summing over all possible final states, the total decay amplitude is given by:

$$\Gamma = \frac{1}{2m}\,\mathrm{Im}\langle i|T|i\rangle = \frac{1}{m}\,\mathrm{Im}\langle i|\mathrm{i}\int \mathrm{d}x^4\mathrm{T}[H_{eff}(x)H_{eff}^{\dagger}(0)]|i\rangle \tag{1.9}$$

The effective Hamiltonian bears a clear similarity to the one describing the muon decay. This can be used to deduce the expression of the total amplitude of the free decay of the c quark:

$$\begin{aligned}\Gamma(c \to s\overline{d}u) &= 5\left(\frac{m_c}{m_\mu}\right)^5 |V_{cs}|^2\Gamma(\mu \to \nu_\mu\overline{\nu_e}e)\\ &= 5\frac{G_F^2 m_c^5}{192\pi^3}|V_{cs}|^2\end{aligned} \tag{1.10}$$

The factor 5 comes from counting the number of open decay channels: The W boson can decay with two leptonic channels $e^+\nu_e$, $\mu^+\nu_\mu$ and three $u\overline{d}$ quark channels, accounting for three colors.
Assuming $m_c \simeq 1.5\ \mathrm{GeV}/c^2$, one obtains for the lifetime of the free charm quark a value of about 0.7 psec. This value gives the right order of magnitude for the lifetimes of charmed mesons. We would expect equal lifetimes if we assume similar mechanisms in charmed mesons and charmed baryon decays. The fact that charmed baryon lifetimes are shorter needs explanation: effects induced by strong interactions must be taken into account.

1.3.2 Short distance QCD corrections

Because of confinement, weak decays of hadrons necessarily involve strong interactions. According to the characteristic momentum scales involved, one can divide the strong interaction effects into long and short distance phenomena. Normally it is assumed that, in spite of the complexity of their interplay, one can separate long and short distance interactions. Long distance effects are then absorbed in the initial and final hadronic wavefunctions.
Short distance effects originate in hard gluon interactions and the respective corrections can be included in the effective Hamiltonian [5]. This is done in perturbation theory because of the asymptotic freedom property of QCD.
Four graphs which modify at first order the hadronic decay amplitude of the charm quark decay are illustrated in figure 1.2.
In processes happening at energies at the scale $\mu \sim m_c \ll m_W$, m_W can be taken as an ultraviolet cut-off in the evaluation of the four indicated graphs and they turn out to be finite. Therefore, their contributions in the first order of $\ln\frac{m_W^2}{\mu^2}$ can be added to the effective Hamiltonian (the reader can refer to [5] for the complete calculation).
The new effective Hamiltonian can be written as:

$$H_{eff} = \frac{G_F}{\sqrt{2}}V_{ud}^* V_{cs}(C_- O_- + C_+ O_+) \tag{1.11}$$

where V_{ud}^* and V_{cs} are the elements of the Cabibbo-Kobayashi-Maskawa matrix involved in the process; O_+ and O_- are the 4-quark operators for the antitriplet and the sextet

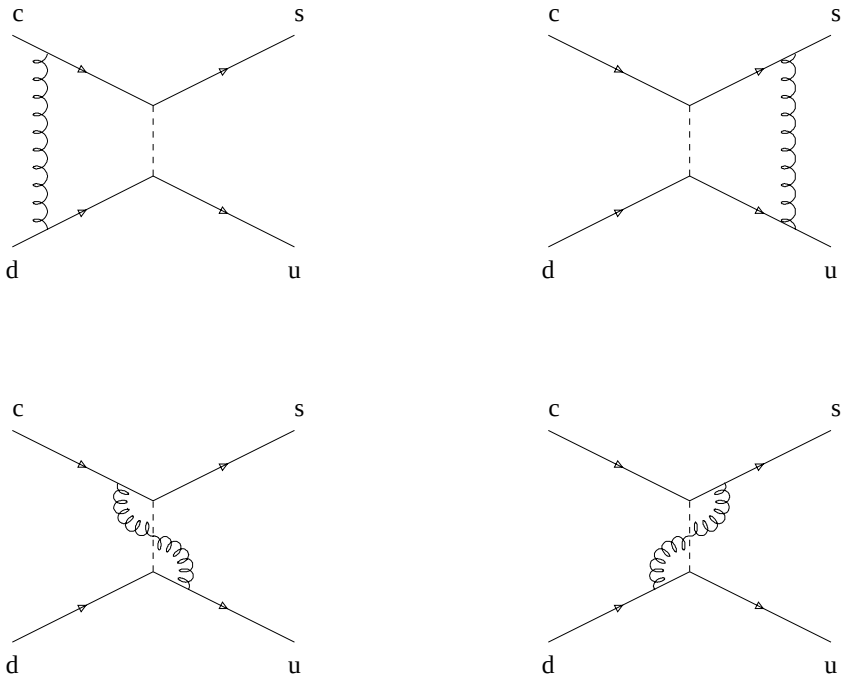

Figure 1.2: First order QCD corrections to the charm decay amplitude.

channels in the SU(3) color representation; the Wilson coefficients C_+ and C_- are expressed by:

$$\begin{aligned} C_+ &= \frac{1}{\sqrt{C_-}} = \left(\frac{\alpha_s(\mu^2)}{\alpha_s(m_W^2)}\right)^{-\frac{2}{b}} \\ &= \left(1 + \alpha_s(\mu^2)\frac{b}{4\pi}\ln\frac{m_W^2}{\mu^2}\right)^{-\frac{2}{b}} \end{aligned} \tag{1.12}$$

where $b = 11 - \frac{2}{3}N_f$ and N_f is the number of relevant quark flavors.
The corrections at the next orders turn out to be significant and can not be neglected. In the *leading log approximation* the sum on all orders in α_s is estimated.
Several values of the $C_\pm$ coefficients are given depending on the different methods applied. Calculations done by Guberina et al. [6], considering Λ_{QCD} ≈250 MeV, and the number of flavors equal four, give the following values:

$$C_- = 1.80 \qquad \text{and} \qquad C_+ = 0.74 \tag{1.13}$$

1.3.3 Long distance effects

With the effective Hamiltonian, the decay amplitude of a baryon B can be calculated as:

$$\Gamma_{had}(B) = \frac{1}{M_B}\,\mathrm{Im}\langle B|\mathrm{i}\int \mathrm{d}x^4 \mathrm{T}[H_{eff}(x)H_{eff}^{\dagger}(0)]|B\rangle \tag{1.14}$$

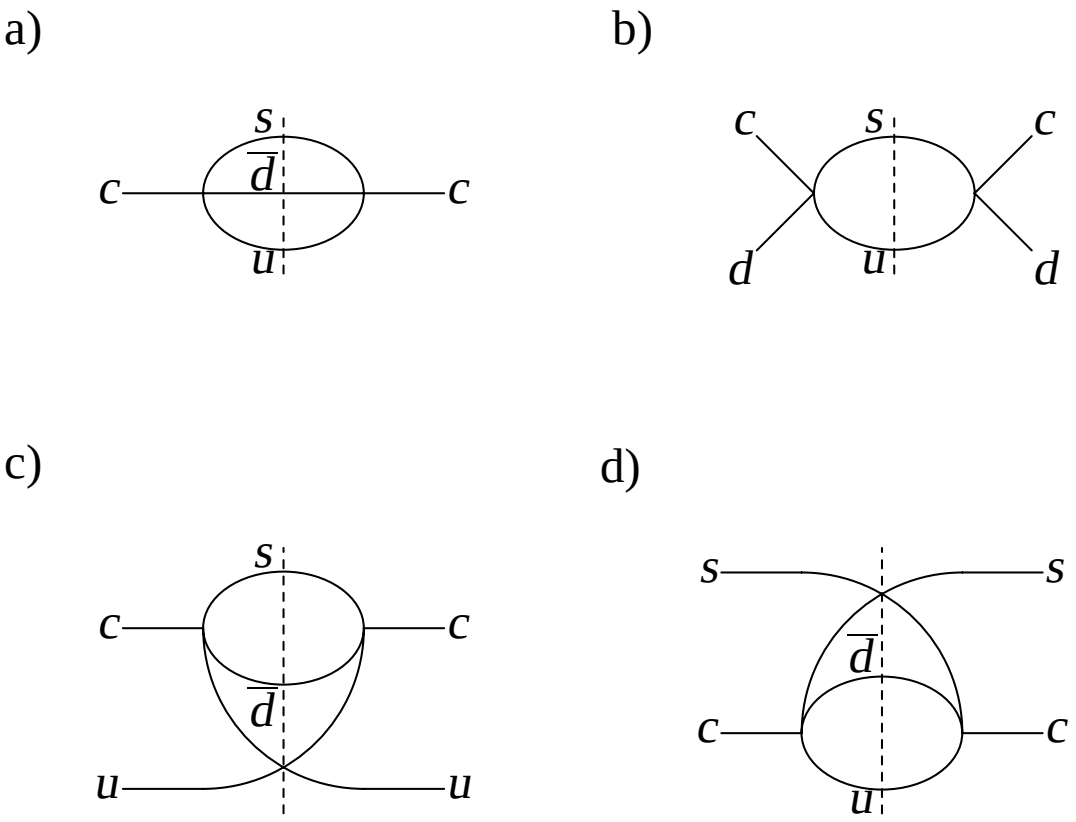

Figure 1.3: Contributions to the hadronic decay amplitude of charmed hadrons derived from the matrix element $\langle B|H_{eff}H_{eff}^{\dagger}|B\rangle$. a) Free decay of the charm quark; b) W-exchange with a d quark; c) Interference with a u quark of the initial state; d) Interference with an s quark of the initial state.

The graphs given by the matrix element above are illustrated in figure 1.3. The physical meaning of the four graphs is indicated below:

a) The first is the free quark decay diagram. It is also called factorization diagram since the W^+ decay vertex can be treated independently from the processes on the baryon side. This diagram is important for all charmed hadrons.

b) The second graph represents the W-exchange, which can only occur in the presence of a d quark in the initial baryon (or an $\overline{s}$ quark or an $\overline{u}$ quark in D_s and D^0 mesons, in which case it is called annihilation diagram). This process is relevant only for the decays of Λ_c^+ (udc) and Ξ_c^0 (dsc) and should lead to a larger total decay amplitude for them compared to the other two baryons.

c) The third graph is the first example of interference which happens when the baryon contains a quark flavor (the u in this diagram) which is also present in the decay of a free c quark. In this case an intermediate quark from the c decay can mix with the spectator quark. The u interference is connected to the color sextet operator and consequently turns out to be destructive (reduces the decay width). This process is present for the Λ_c^+ (udc) and Ξ_c^+ (usc) baryons.

d) The second type of interference, involving an s quark, is illustrated by the fourth graph. This type of interference is connected to the antitriplet color operator and

thus it is constructive. It concerns all charmed strange baryons: Ξ_c^+ (usc), Ξ_c^0 (dsc) and Ω_c^0 (ssc).

These four contributions to the hadronic decay rate can be expressed as follows:

$$\begin{aligned}
\Gamma^{spe}(B) &= \frac{G_F^2 m_c^5}{192\pi^3}\xi(2C_+^2 + C_-^2)\frac{1}{2M_B}\langle B|\overline{c}(1-\gamma_5)c|B\rangle \\
\Gamma^{exc}(B) &= \frac{G_F^2 m_c^2}{2\pi}\xi C_-^2\frac{1}{2M_B}\langle B|(\overline{c}\gamma^\mu(1-\gamma_5)c)(\overline{d}\gamma_\mu(1-\gamma_5)d)|B\rangle \\
\Gamma_-^{int}(B) &= \frac{G_F^2 m_c^2}{4\pi}\xi C_+^2(C_+ - 2C_-)\frac{1}{2M_B}\langle B|(\overline{c}\gamma^\mu(1-\gamma_5)c)(\overline{u}\gamma_\mu(1-\gamma_5)u)|B\rangle \\
\Gamma_+^{int}(B) &= \frac{G_F^2 m_c^2}{4\pi}\xi C_+^2(2C_- + C_+)\frac{1}{2M_B}\langle B|(\overline{c}\gamma^\mu(1-\gamma_5)c)(\overline{s}\gamma_\mu(1-\gamma_5)s) \\
&\quad + \frac{2}{3}(\overline{c}\gamma^\mu\gamma_5 c)(\overline{s}\gamma_\mu(1-\gamma_5)s)|B\rangle
\end{aligned}$$

where $\xi = |V_{ud}|^2|V_{cs}|^2$. The matrix elements must be evaluated within the framework of some quark model. The phenomenologic nature of these models induce large uncertainties in the predictions. Because the rates scale like m_c^5 for the spectator decay and m_c^2 for the non-spectator terms, numerical calculations are very sensitive to the precise choice of m_c. The ratios of interference to exchange contributions and constructive to destructive interference are, however, free from uncertainties in m_c. The signs of each of the four contributions listed are unambiguously fixed since $C_- > C_+ > 0$ for all values of m_c.
The important point consists in determining the relative weight of the four processes to estimate the total decay amplitude of charmed baryons and, consequently, their lifetimes. Several models exist: their predictions will be summarized in the next section.

1.3.4 Lifetime hierarchy of charmed baryons

The total non-leptonic decay rates for $\Lambda_c^+(udc)$, $\Xi_c^+(usc)$, $\Xi_c^0(dsc)$ and $\Omega_c^0(ssc)$ can be written as:

$$\begin{aligned}
\Gamma_{NL}(\Lambda_c^+) &= \Gamma^{spe}(\Lambda_c^+) + \Gamma^{exc}(\Lambda_c^+)_d + \Gamma_-^{int}(\Lambda_c^+)_u \\
\Gamma_{NL}(\Xi_c^+) &= \Gamma^{spe}(\Xi_c^+) + \Gamma_-^{int}(\Xi_c^+)_u + \Gamma_+^{int}(\Xi_c^+)_s \\
\Gamma_{NL}(\Xi_c^0) &= \Gamma^{spe}(\Xi_c^0) + \Gamma^{exc}(\Xi_c^0)_d + \Gamma_+^{int}(\Xi_c^0)_s \\
\Gamma_{NL}(\Omega_c^0) &= \Gamma^{spe}(\Omega_c^0) + \Gamma_+^{int}(\Omega_c^0)_s
\end{aligned}$$

The interference contribution for the Ω_c^0 needs special consideration because of the presence of two spectator s quarks in the final state, which interfere with the s from the c quark decay.
Qualitative lifetime differences can be obtained by applying specific quark models. Guberina, Rückl and Trampetić [6] use the values of the Wilson coefficients given above ($C_+ = 0.74$ and $C_- = 1.8$), and apply in one case a non-relativistic model. They obtain:

$$\Gamma^{exc} : \Gamma_+^{int}(\Xi_c^{0,+}) : \Gamma_-^{int}(\Xi_c^{0,+}) \simeq 1 : 0.5 : -0.3 \qquad \text{and} \qquad \Gamma_+^{int}(\Omega_c^0) = \frac{10}{3}\Gamma_+^{int}(\Xi_c^{0,+}) \tag{1.15}$$

from which the lifetime hierarchy follows:

$$\tau(\Omega_c^0) \;:\; \tau(\Xi_c^0) \;:\; \tau(\Lambda_c^+) \;:\; \tau(\Xi_c^+) \;\approx\; 0.60 \;:\; 0.64 \;:\; 1 \;:\; 1.6 \tag{1.16}$$

Voloshin and Shifman [7] use a non-relativistic approach similar to that used by Guberina et al. but incorporating soft gluon modifications to the effective weak Hamiltonian by employing a logarithmic renomalization technique. The predicted lifetime hierarchy is:

$$\tau(\Omega_c^0) \;:\; \tau(\Xi_c^0) \;:\; \tau(\Lambda_c^+) \;:\; \tau(\Xi_c^+) \;\approx\; 0.58 \;:\; 0.74 \;:\; 1 \;:\; 1 \tag{1.17}$$

A more recent work by Blok and Shifman [8] takes into account in the matrix elements higher order operators. The resulting hierarchy is:

$$\tau(\Omega_c^0) : \tau(\Xi_c^0) : \tau(\Lambda_c^+) : \tau(\Xi_c^+) \approx\; 0.32 : 0.46 : 1 : 1.3 \tag{1.18}$$

The predictions listed above are strongly model dependent and are affected by large uncertainties. Only good experimental measurements of charmed baryon lifetimes will allow a better understanding of the weak decay dynamics and the influence of baryonic structure.

Bibliography

[1] CLEO Collaboration, “Observation of an excited charmed baryon decaying into $\Xi_c^0\pi^+$”, CLNS-96-1394, February 1996

[2] The Particle Data Group, “Review of particle properties”, Phys. Rev. D3 (1994)

[3] E687 Collaboration, “First measurement of the lifetime of the Ω_c^0”, Phys. Lett. B357 (1995) 678-684

[4] WA89 Collaboration, “Measurement of the Ω_c^0 lifetime”, Phys. Lett. B358 (1995) 151-161

[5] R. Rückl, “Weak decays of heavy flavours”, Habilitationsschrift, Universität München, 1993

[6] B. Guberina, R. Rückl and J. Trampetić, “Charmed baryon lifetime differences”, Z. Phys. C 33 (1986) 297-305

[7] M.B. Voloshin and M.A. Shifman, “Lifetime hierarchy of charmed and beautiful hadrons”, Sov. Phys. JETP 64 (1986) 698-705

[8] B. Blok and M. Shifman, “Lifetimes of charmed hadrons revisited. Facts and fancy”, hep-ph 9311331, TPI-MINN-93/55-T (1993)

Chapter 2

Single sided microstrip detectors in WA89

2.1 Silicon microstrip detectors

Since the beginning of the 1980s, silicon microstrip detectors have played a key role in high energy physics experiments. The small feature size possible on strip devices makes compact detectors with excellent spatial, and consequently angular, resolution possible for tracking applications.
Semiconductor materials have been extensively used and developed as radiation detectors since the 1960s in nuclear physics for energy measurements (first signals were seen in 1951, from α particles crossing a reverse biased germanium junction [1]). During the 1970s they appeared in high energy physics experiments: surface barrier diodes were initially used mainly to measure the energy loss, for example, of recoil nuclei in segmented targets to localize interactions, or of secondary particles to measure their multiplicity, and only later for tracking. One side of the junction can be segmented with the signals recorded on the individual segments used to determine particle positions. The first important results obtained with a silicon surface barrier microstrip detector are given in reference [2].
The reason for the wide use of such detectors is related to some basic properties of semiconductors. Germanium and silicon are solid and compact and work well in vacuum and in magnetic fields making them suitable for operation in many difficult environments. They have a high intrinsic energy resolution. In silicon, for example, 3.6 eV are enough to create an electron-hole pair, a very low value compared to 30 eV necessary to ionize a molecule in a gas detector or about 300 eV to extract an electron from a photocathode coupled to a scintillator.
The high energy loss for minimum ionizing particles in silicon (3.88 MeV/cm) allows the use of very thin detectors (100 - 500 μm), an advantage in all applications where it is important to limit the multiple scattering effects which degrade the track quality, Bremsstrahlung, and the probability of secondary interactions.
The high mobility of charge carriers in the crystal allows a very fast charge collection (in typical times of the order of 10-20 nsec) and consequently very fast signals.
Some relevant parameters of silicon are summarized in table 2.1.
An important impetus to the spreading of microstrip devices came in the 1980s from the

Atomic number Z	14
Atomic weight A	28.09
Density	2.33 g/cm^3
Dielectric constant ϵ	11.7
Band gap	1.115 eV
Intrinsic carrier concentration n_i	1.45x10^{10} cm^{-3}
Electron mobility $\mu = v / E$	1350 cm^2/Vsec
Hole mobility $\mu = v / E$	480 cm^2/Vsec
Energy per electron/hole pair	3.66 eV
Electron diffusion constant	34.6 cm^2/sec
Hole diffusion constant	12.3 cm^2/sec
Radiation length	9.36 cm
Interaction length	24 cm
Breakdown field	30 V/μm

Table 2.1: Physical properties of silicon at room temperature (300^{o}K).

application of the planar technology to silicon detector production (J. Kemmer [3, 4]). The planar process was initially developed in the electronics industry and later applied to detector fabrication. It presents fundamental advantages with respect to the previous production of silicon surface barrier detectors. Though these had very low generation currents because there were no high temperature treatments during production, they showed rather high surface leakage currents, and had a very time consuming fabrication cycle because every single detector had to be fabricated and tested individually. In contrast, the planar process allows faster production at a lower price of a high number of detectors with very small tolerances in their geometrical and electrical properties, with high precision elements (thanks to ion implantation and photoengraving techniques) and good control of leakage currents (due to oxide passivation procedures).
Since then microstrip detectors have had a very fast development and came into regular use in high energy experiments where high resolution tracking is required. A complete and detailed guide to the development of these detectors can be found in reference [5].

2.1.1 Microstrip detectors

Semiconductor detectors are basically a p-n junction operated with a reverse bias. This creates a sensitive region depleted of free charge carriers and sets up an electric field across the detector. Particles traversing the depleted region liberate charge by ionization, and this moves to the electrodes under the influence of the electric field. Basics on intrinsic and doped semiconductors, the p-n junction, its fundamental characteristics and its use as a radiation detector will not be given here and can be found in references [5, 6, 7, 8].
In order to achieve high spatial resolution, the p-n junction can be segmented in many independent, very narrow, parallel strips each connected to a readout circuit. This is called *microstrip detector* and is realized in the following way.

The basic material is an n-type silicon crystal with low level doping and consequently high resistivity (1-10 kΩ·cm). For this application it is now possible to grow ingots of a diameter up to 4". These are sliced to wafers about 500 μm thick and then polished to obtain a very smooth and clean surface with the desired thickness of 100-300 μm. The crystal usually has a <111> structure, which gives the highest energy loss.
One face of the crystal is n^+ doped (where '+' means high doping concentration) and aluminized. This is indicated as **n-side** or **ohmic side** of the detector. On the other face narrow p^+ strips are produced by means of ion implantation or diffusion, using the photomasking technique. The fine strips create asymmetric, nearly abrupt p-n junctions. The strips are usually 3-10 μm wide, with a 10-200 μm pitch and up to few centimeters long. They are then provided with aluminum contacts to allow ultrasonic bonding to the electronics. This is called **p-side** or **junction side**.
The p^+ elements serve to reverse polarize the junction and the n^+ to prevent the depletion zone from reaching the backplane and to ensure a good ohmic contact. For n^+ doping mostly arsenic and phosphorus are used, while p^+ doping is usually done with boron. A passivation oxide serves to protect the silicon surface.
The cross section of a strip detector is shown in figure 2.1.

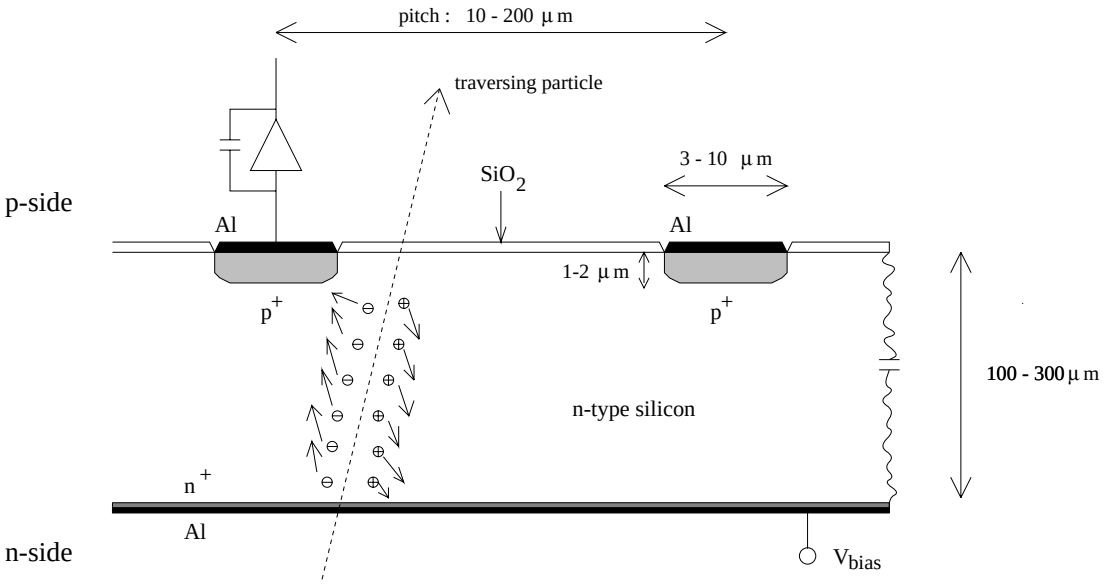

Figure 2.1: Cross section of a microstrip detector.

Usually an additional p^+ line with the shape of a ring is implanted all around the sensitive area of the detector on the junction side; it is called *guard ring* and has the main function of rectifying the field lines at the edges of the detector and collecting the surface leakage current contributions. These functions are of extreme importance especially after the detector is cut from the wafer, an operation which always introduces irregularities in the crystal at the edges.

Initially microstrip detectors equipped with hybrid or component readout electronics were used in fixed target experiments. Tracking devices included up to roughly 10000 readout

channels. In order to increase the number of channels and to extend the use of microstrips in collider experiments, the use of LSI[1] electronics with multiplexing became mandatory because of the lack of space close to the interaction region. This motivated important developments in the technology of microstrip detectors.

DC-coupled and AC-coupled detectors

In *DC-coupled* detectors the aluminum readout strip covers directly the p^+ implantation and is then connected to the amplifier, as shown in figure 2.2 on the left. This connection has the disadvantage that the leakage current of the junction is fed directly into the amplifier, inducing considerable base line differences between channels of one chip and requiring an otherwise unnecessarily large dynamic range of the ADCs. In hybrid electronics this problem was solved by putting a discrete coupling capacitor of a few tens of picofarads at the input of the amplifier. This solution cannot be adopted for LSI electronics due to a lack of space for the capacitor.
One solution consists of integrating the coupling capacitors on the detectors themselves separating the p^+ strip from the metal readout line by a thin layer of silicon dioxide [9, 10], as shown in figure 2.2 on the right. The area of metal defines the coupling capacitor. The capacitor value can be tailored by varying the oxide thickness (typically between 100 and 200 nm to give respectively a coupling capacitance of about 20 and 10 pF/cm related to the strip length).

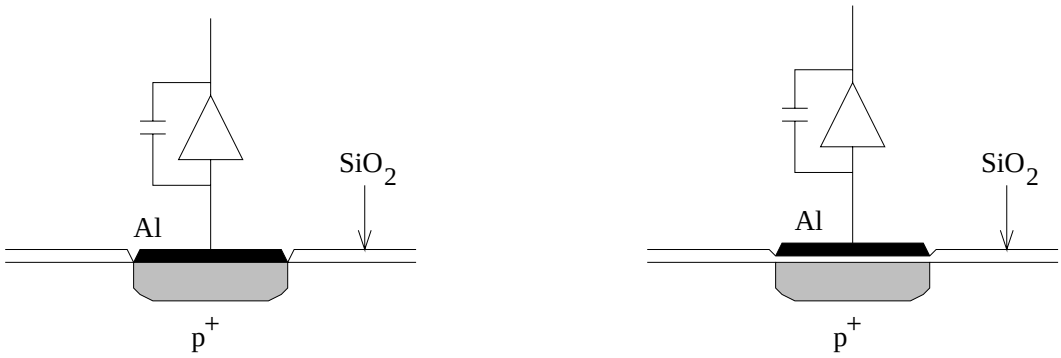

Figure 2.2: DC- and AC-coupled strip.

The total value of the capacitance must be high enough to guarantee the good operation of the detector. It has to be large compared to the capacitance to the backplane and to the *interstrip capacitance* (the capacitance between one strip and its neighbours) in order to avoid signal losses by capacitive induction. It has also to be larger than the feedback capacitance of the charge sensitive amplifier in order not to deteriorate the signal-to-noise ratio at the output of the amplifier.
The quality of the thin coupling oxide must be excellent because defects result in short-circuits (called *pinholes*) in the capacitors. Such a high quality oxide is able to withstand a voltage difference of 50 to more than 100 V. In order to decrease the risk of pinholes, a layer of silicon nitride (Si_3N_4) is sometimes added on top of the silicon dioxide. The

[1] Large Scale Integrated

probability that a pinhole in the nitride falls exactly in front of a pinhole in the oxide is extremely small.

With this system the leakage current is decoupled from the amplifier input and is called an *AC-coupled* detector.

An alternative is to use DC-coupled detectors together with external capacitors placed on a separate chip. This solution will be illustrated in the next chapter.

For DC-coupled detectors the bias voltage is brought to the single strips by the same connection to the amplifiers, so that the counter can be uniformly depleted. A different way of biasing is required for AC-coupled detectors. This is done with a common bias line (generally a metal line which surrounds the active area of the counter) connected to the single strips by individual resistors integrated on the detector. The resistors can be made of polysilicon, a polycrystalline state of silicon having very high resistivity. Using ion implantation, it is possible to make thin lines, from the bias line to the strip, of length (number of squares) adjusted to obtain the total desired resistance. Usually one wants to have a few MΩ so that most of the charge created in silicon is collected by the amplifiers (100-200 nsec integration time) before being discharged through the resistors towards the bias line. The value should not be too high though, since in the case of localized high leakage currents this could create a potential difference between strips. It is also very important that the value of the resistance is uniform through the whole detector in order to guarantee uniformity of the bias voltage at the strips.

A top view and a section of strips connected to a bias line in the described way is shown in figure 2.3. The indicated contact hole allows a direct contact to the p^+ strips and resistors in order to perform measurements.

Other biasing methods are possible, such as FOXFETs, punch-throughs and electronic channels. The last two will be described in detail in the next chapter.

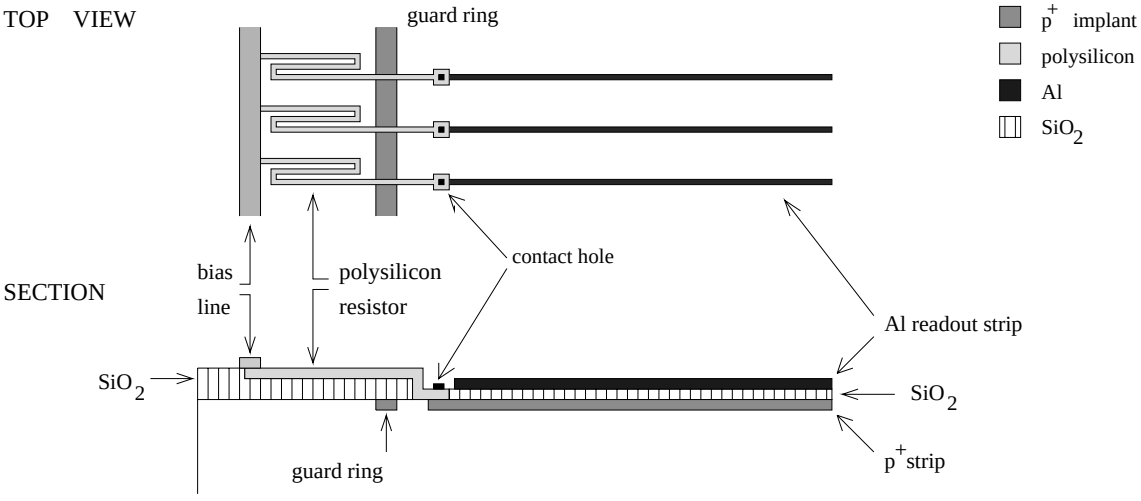

Figure 2.3: Top view and section of AC-coupled strips connected to a common bias line through a polysilicon resistor.

2.1.2 Energy deposition and charge collection

A particle traversing the depleted p-n junction interacts through various mechanisms and deposits part of its energy. Electromagnetic interaction induces both excitation and ionization. A fraction of all deposited energy is spent to create electron-hole pairs. The energy deposited and consequently the number of pairs created are approximately described by a Landau distribution (see figure 2.19a) but the distribution is wider because of the effect of the binding energy of electrons in silicon atoms (the Landau theory assumes a free electron cross section). For a MIP (Minimum Ionizing Particle) crossing a 300 μm thick layer of silicon, the most probable energy loss is approximately 26 keV/100 μm and the mean loss is 39 keV/100 μm. Consequently the most probable and average number of created pairs is 25000 (≈ 4fC) and 32000 respectively.
The ionization charges are created in a narrow tube around the particle path. Under the influence of the electric field, they migrate in the depleted region, the electrons drifting towards the n-side and the holes towards the diode strips. During the migration time, the narrow tube of charge carriers widens because of transverse diffusion and electrostatic repulsion. Finally the holes are collected by the strips. The charge collection time is of the order of about 8 nsec for electrons and 25 nsec for holes.
An attempt was already made in early works [11], to calculate the shape of the collected charge distribution. Assume that the detector is uniformly irradiated with high energy particles and for every event the values of the pulse height (PH) of the individual strips are recorded. A sample of events with particles traversing the counter between the adjacent strips L and R is selected. For those we calculate the following quantity:

$$\eta = \frac{PH(R)}{PH(L) + PH(R)} \tag{2.1}$$

An example of the distribution $dN / d\eta$ is shown in figure 2.4, on the left side on top.
If p is the strip pitch, the average impact point x_0 for a given η can be obtained by:

$$x_0 = \frac{p}{N_0} \int_0^{\eta} \frac{dN}{d\eta'} d\eta' - X_0 \tag{2.2}$$

For the derivation it was assumed that N_0 particles, uniformly distributed in x_0, have traversed the counter in the pitch distance between strips L and R. X_0 is the constant which relates the origin of the η scale to the origin of the x_0 scale. In absence of magnetic fields the deposited charge spreads symmetrically around the particle trajectory and X_0=p/2. The distribution of x_0 is shown in figure 2.4, on the left side on bottom.
The distribution $dN / d\eta$ can then be used to determine $f(\xi)$, the Gaussian distribution of charge carriers at the readout plane. For a particle traversing the counter at x_0, the measured pulse heights are related to $f(\xi)$ by: $PH(L) \propto \int_{-\infty}^{x_0} f(\xi) d\xi$ and $PH(R) \propto \int_{x_0}^{\infty} f(\xi) d\xi$.
Using the definition of η we obtain $d\eta / dx_0 = f(x_0)$ and from this follows that:

$$\frac{dN}{d\eta} = \frac{dN}{dx_0}\frac{dx_0}{d\eta} = \frac{N_0}{p}\frac{1}{f(x_0)}. \tag{2.3}$$

Equation 2.2 allows the determination of x_0 for every η bin. Using equation 2.3 the corresponding value of $f(x_0)$ can be calculated.

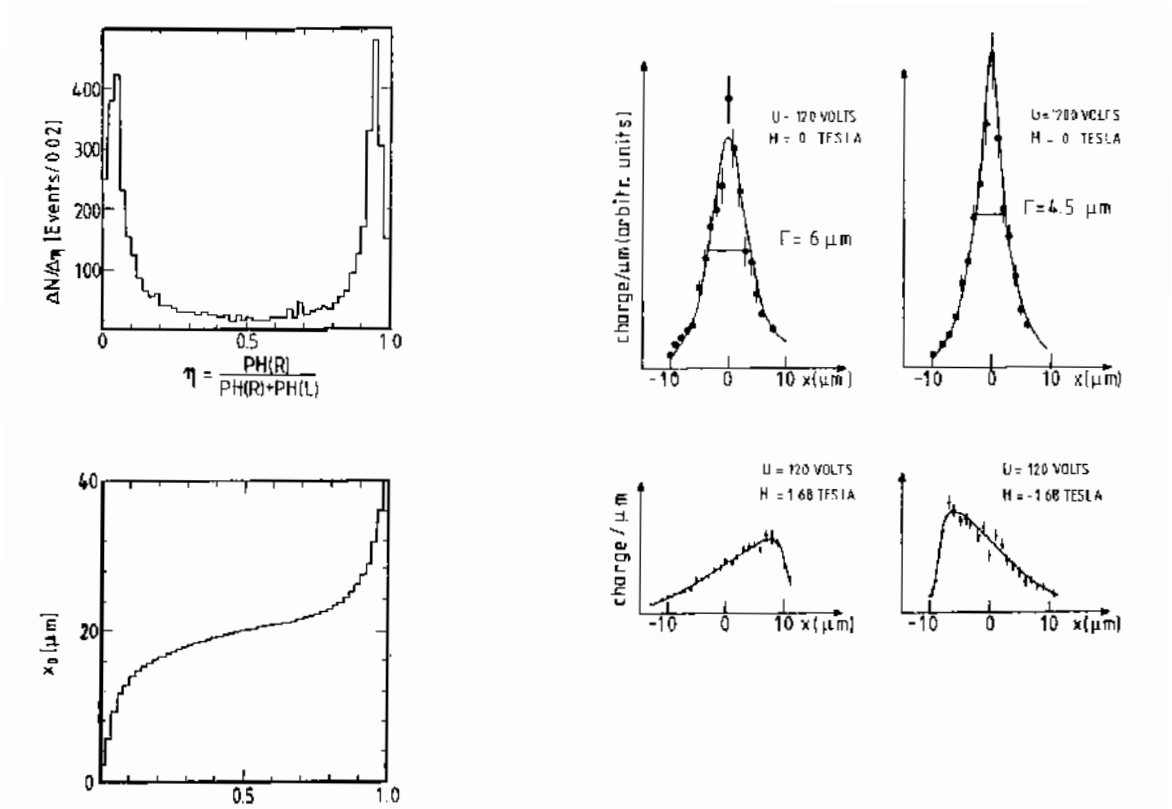

Figure 2.4: On the top left: $dN / d\eta$ distribution. On the bottom left: x_0 dependence on η. On the right: charge distribution at the readout plane in absence (top) and in presence (bottom) of a magnetic field, for different bias voltages. All pictures are taken from reference [11].

The ACCMOR collaboration also measured this charge distribution, using a detector with 25 μm readout pitch [11]. The calculated curves and the measured points are shown in figure 2.4 on the right part, for different bias voltages and magnetic fields. Without a magnetic field the charge distribution is symmetric with a full width of 10 μm at depletion voltage (50 V, not shown), decreasing to 6 and 4.5 μm at higher voltages. In presence of a magnetic field the charge distribution is asymmetric. For example, a field of 1.68 T parallel to the direction of the strips introduces a systematic shift of the measured coordinate of the order of 10 μm and an increase in the width of the collected charge distribution from 5 to approximately 12 μm.

The charge localization is actually spoiled by the emission of high energy electrons (δ electrons) along the ionization path. The probability of such emission is rather low but the electron range can be quite big and this causes a displacement of the track position of a few microns. Such events can be recognized because the signal recorded is higher. In these cases the track position is measured with a more significant error. In fact the intrinsic spatial resolution of microstrip detectors is ultimately limited to approximately 1 μm exactly by this effect.

2.1.3 Digital, analog and capacitive charge division readout

The information provided by a microstrip counter is used to localize the position where a particle crossed the detector. The accuracy with which this can be done depends on the following factors, among others:

- the strip pitch and the readout pitch;
- the diffusion of charge carriers during their drift to the electrodes;
- the possibility to readout only the digital or also the analog information concerning the signals.

When the detector is operated in over-depletion (when the bias voltage is significantly higher than the depletion voltage) the resistance between adjacent strips becomes extremely high. In addition the charge collection time is decreased. The latter effect is also caused by a not optimal fabrication process which significantly reduces the minority carriers lifetime. Because of these effects the charge diffusion is reduced and consequently the signal is spread over a narrower area. If tracks are mostly perpendicular to the detector, the charge produced by the particle will be collected by one single strip. This provides a digital information. In this case the spatial resolution or accuracy with which to determine the position of the track is given by the strip pitch itself. Assuming a rectangular hit distribution over one strip, the resolution is σ = pitch/$\sqrt{12}$. Reducing the strip pitch is not always the solution for improving the resolution: the number of channels increases dramatically and some noise parameters of the detector tend to become dominant.

The ionization charge can also be distributed over several strips. This happens in particular when the detector is operated at a voltage not much higher than the depletion voltage (so that more transverse diffusion can take place) and in the case of inclined tracks.
If, in addition, one can have the analog information regarding the charge collected by the single strips, it is possible to improve the resolution. One can simply calculate the charge center of gravity and linearly extrapolate the track position. Even better results are obtained with a non-linear method [11], using the η distribution introduced in the previous paragraph. This, in fact, takes into account the real Gaussian distribution of the charge and the non-linear correlation of the predicted and measured positions (see figure 2.4). With such a method resolutions as good as a few microns are possible. With very low noise readout electronics a precision as small as 1.25 μm has been reached [12], down from 5 μm reported already in 1983 [13].
The influence of the applied bias voltage on the resolution is shown in figure 2.5 from reference [14]. The measurement was performed by the ACCMOR group, with a 25 μm readout pitch detector, depleted at 50 V. The best resolution is obtained exactly at the depletion voltage. For lower voltages it gets worse because part of the charge is created in the non-depleted region and lost, and the noise is relatively higher. For higher voltages drift time and diffusion are reduced, there are more events with only one hit strip and the resolution is again slightly worse.

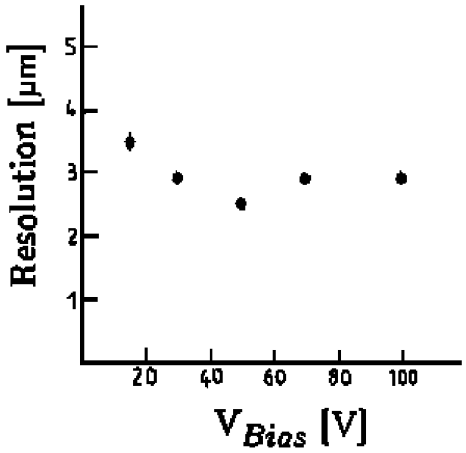

Figure 2.5: Dependence of the spatial resolution on the bias voltage, from reference [14].

So far it was always assumed that every individual strip is connected. An alternative way of readout is based on charge division by capacitive coupling [15, 16]. This is done by connecting to the electronics only every Nth strip, where N can be 2, 3, or even more. The other "floating" strips are nevertheless brought to the same potential of the ones read out (either by the effect of surface leakage currents or by individual biasing resistors) in order to preserve the field uniformity in the counter. When a particle traverses one of the unconnected strips, the charge liberated is collected on that strip in 10-20 nsec and decays away slowly. Thus image charges are induced on the closest readout strips by capacitive coupling. Their amplitude is inversely proportional to the distance between the hit strip and the readout strip. The charge division is determined purely by the geometry, provided that the detector is correctly depleted.
This method reduces the number of readout channels but nevertheless allows good spatial resolution. In fact this turns out to be better compared to the case of a detector with the same readout pitch but without the intermediate strips (interesting examples can be found in references [11] and [14]).
For capacitive charge division to work as desired, several conditions have to be met:

- for uniform charge collection, it is important that the intermediate strips reach the same potential of the ones read out, as already mentioned;
- to avoid crosstalk, the impedance between readout strips has to be significantly larger than the input impedance of the electronics (this is generally not difficult to achieve since the interstrip capacitance is only a few picofarads);
- in order to obtain optimum spatial resolution and uniformity of pulse height response, it is desirable to avoid signal losses to the backplane of the detector. To fulfill this condition, the interstrip capacitance must be larger than the capacitance of the strips to the backplane. Figure 2.6 shows the main elements of the capacitive network in a strip detector and some optimal values for the capacitance involved. In this example only every second strip is read out.

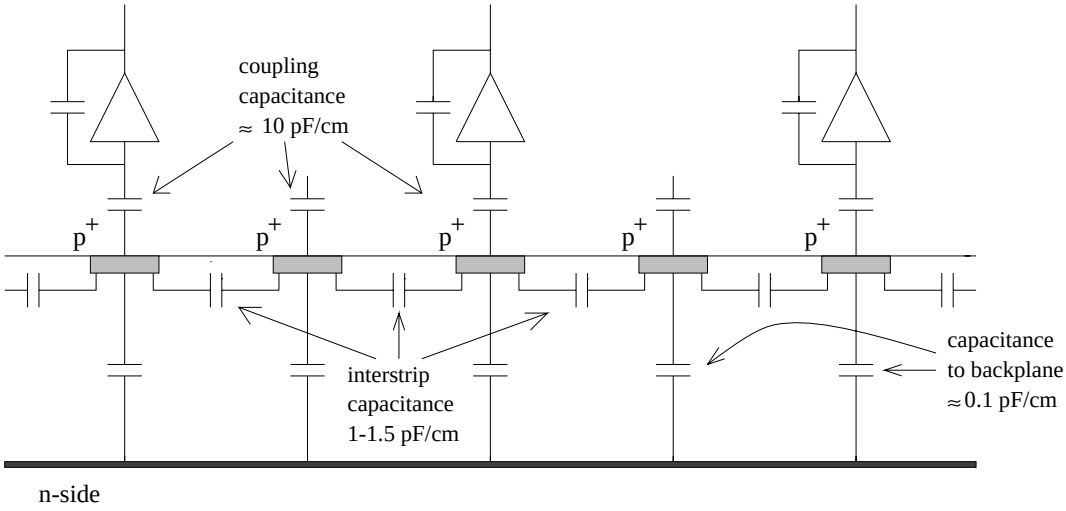

Figure 2.6: Capacitive network in a microstrip detector.

The advantage of the capacitive charge division method is the significant reduction in number of electronics channels. Problems arise when more tracks traverse the detector close to each other and their clusters overlap. In that case this method yields worse two-track separation with respect to reading out every channel.

2.1.4 Noise

In the case of silicon detectors, the noise problem is important. In a p-n junction there is no multiplication of charge and the ≈25000 charges created by a traversing MIP can be even spread over more strips. In order to preserve the accuracy in position measurements, it is essential to limit the noise per strip and have a relatively high signal-to-noise ratio in the readout channels.

The signal-to-noise ratio is determined both by the electronics and by the detector itself. The electronics noise has a constant part (depending on the specific design of the readout chip) and a part which is a function of detector parameters. In this second part there are three main contributions: one coming from the load capacitance to the preamplifier, one from the detector leakage current, and a third from the bias resistors [5].

The most relevant term is the one depending on the load capacitance. This is mostly given by the capacitance of one strip to its neighbours (called interstrip capacitance). This value strongly depends on the geometry of the detector (the smaller the pitch and the longer the strip, the higher the capacitance). It is important to keep it as low as possible. For conventional charge sensitive amplifiers the electronics noise is calculated as an equivalent

noise charge (ENC) from the formula:

$$ENC_{C_{load}} = A + B \cdot C \tag{2.4}$$

where A and B are constants and C is the detector capacitance. The constants A and B vary depending on the preamplifier and the electronics design. An example of this dependence is given in figure 2.16 for the specific case of the SVX readout chip.

Particular efforts have been made to improve these parameters of the electronics. A novel readout chip developed at CERN (called VA2 [17]) has the constants A and B equal to 60 (80) electrons and 11 (15) electrons/pF respectively for 1 μsec (2 μsec) shaping time. Usually this contribution to the noise can vary between 300 and even more than 1000 electrons.

Another term takes into account the contribution of the detector leakage current. The equivalent noise for a simple CR-RC filter is given by:

$$ENC_{I_{leakage}} = e \cdot \sqrt{\frac{IT_p}{4q}} \tag{2.5}$$

where e is the natural logarithm base, q is the electron charge, I is the diode leakage current and T_p is the peaking time, equal to the integration time of the shaper. For a peaking time of 1 μsec and a typical leakage current of 1 nA per strip, this term contributes about 130 electrons.

The contribution of the bias resistors can be expressed in the following way:

$$ENC_{R_{bias}} = \frac{e}{q} \cdot \sqrt{\frac{T_p kT}{2R}} \tag{2.6}$$

where k is the Boltzmann constant, T the temperature and R the value of the bias resistors. For a case similar to the previous example and a bias resistor of 5 MΩ, this contribution is about 420 electrons.

The various contributions must be summed in squares to give the total ENC and with it the signal-to-noise ratio is calculated. This value determines directly the spatial resolution. Figure 2.7 from reference [18] shows the obtained resolution as a function of the signal-to-noise ratio for a detector with 25 μm pitch and the readout pitch of 25 and 50 μm.

As we can see, the reduction of the noise is very important. This can be achieved with the optimal choice of the readout electronics (taking into account the requirements of the experiment) and with the proper detector design aiming for low interstrip capacitance, high coupling capacitance, low leakage currents and high bias resistance.

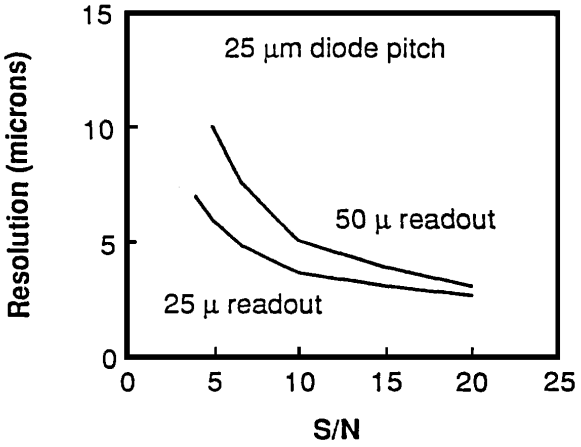

Figure 2.7: Spatial resolution as a function of the signal-to-noise ratio, from reference [18].

2.2 The single sided detectors in WA89

The microstrip counters used by our group for the WA89 vertex region are single sided, AC-coupled detectors produced by Hamamatsu Photonics, Japan. They are fabricated on 300 μm thick, 4" diameter, very high resistivity wafers.

The detectors have a very large active area of 63.5x63.5 mm^2. Including all parts around the active region (the bias resistors, the bonding pads, the bias line and the guard ring which surrounds all the previous elements) the total detector size is 70.0x66.0 mm^2. On 4" wafers this is the maximum size possible to realize. It was chosen in order to achieve good transversal acceptance and improve the reconstruction efficiency in the vertex region of the experiment.

The active area includes 2540 p^+ strips with 25 μm pitch. Each strip is connected to a common bias line by an individual polysilicon resistor which provides the depletion voltage. Odd and even strips have resistors respectively on opposite ends of the strip itself and the bias line is surrounding the whole active area.

The implant strips are aluminized, in order to reduce the series resistance and to make the connection to the readout electronics possible. All metal lines have four bonding pads. Usually only the first one is used for connection to the electronics. The spare ones are available in case of unsuccessful first pad bonding.

In case of 25 μm readout pitch, odd and even strips are read out on opposite edges of the detector in order to match the standard 50 μm pitch of readout electronics channels. For 50 μm readout pitch only every second strip is connected to the readout electronics (which is then placed only on one edge of the detector) and intermediate strips are left floating.

Some parameters of the Hamamatsu detectors are summarized in the top part of table 2.2.

When ordering detectors from a company as in the case of Hamamatsu, some limits and reference quantities (called specifications) are fixed in order to define when the quality of a detector meets the customers' requirements. Only pieces satisfying the specifications are delivered.

The specifications agreed upon with Hamamatsu Photonics are listed in the bottom part of table 2.2. A strip is defined 'not good' when it has a shorted capacitor (or pinhole) for a voltage lower than 30 V applied across the coupling capacitance oxide.

n-type silicon resistivity	≥ 5 kΩ·cm
detector thickness	300 μm
active area	63.5x63.5 mm^2
total detector size	70.0x66.0 mm^2
number of strips	2540
strip pitch	25 μm
p^+ doping concentration	$5x10^{19}/cm^3$
strip bonding pad size	150x50 μm^2
bias and guard ring bonding pad size	150x150 μm^2
quality of strips	50% of detectors with at least 99% good strips 50% of detectors with at least 98% good strips
leakage current	≤ 1 μA at 100 V
depletion voltage	≤ 80 V
coupling capacitance	≥ 5 pF/cm
bias resistors (first batch)	1-3 MΩ
bias resistors (second and third batch)	3-8 MΩ

Table 2.2: Parameters and specifications of the Hamamatsu detectors.

We received detectors with this design from three different productions: 12 pieces were delivered at the end of 1992, other 23 in spring 1994 (from batch SSX311579 and SSX40702) and other 10 in autumn 1994 (from batch SSX40702 and SSX40797). They were 45 counters in total, later used for various applications.

Before the delivery, some tests were performed by the company itself. They measured the total leakage current, the number of defective lines (by probing all strips individually) and the value of the polysilicon resistors and of the coupling capacitors on side test structures, by random sampling tests. Only detectors within specifications were delivered, consequently we do not know the overall yield of the Hamamatsu production.

When the detectors arrived, we performed full and detailed electric measurements on all counters. Even after the preliminary tests performed by the producer, it is essential to check the status of the detectors after transport and delivery and to repeat in a more systematic way the evaluation of detector components (resistors, capacitors), determine the operating conditions of the counters and study their stability in time.

The measurements and the results are presented in the next section. After the tests, the counters were mounted on ceramic boards and connected to the electronics. The readout chip is described in paragraph 2.4.

The photograph on the next page shows the enlarged view of one corner of one single sided detector.

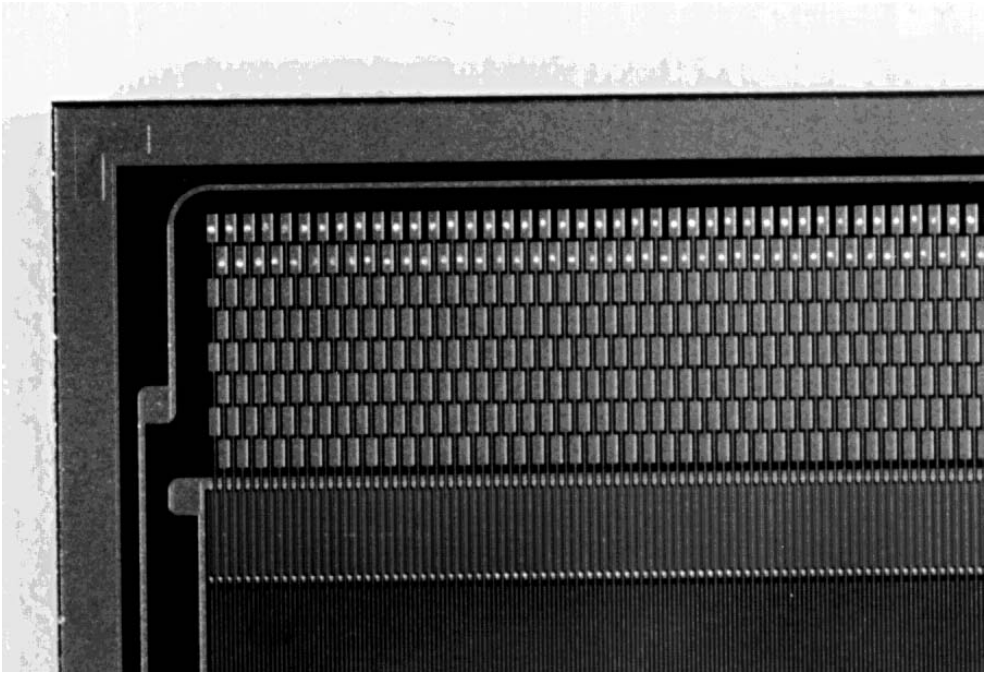

Figure 2.8: Photograph of one corner of a single sided detector. The thin outer metal line indicates the guard ring, with a large square pad for bonding. The inner square pad belongs to the bias line: This runs horizontally below the strip bonding pads, and is connected to the polysilicon bias resistors, which appear as slightly green vertical lines. The ending part of the microstrips is visible on the bottom: Each metal strip has four bonding pads.

2.3 Measurement of the detector quality

Tracking devices made with microstrip detectors are required to have a uniform and stable behaviour, good detection efficiency, and high spatial resolution. In order to satisfy these requirements it is mandatory to use high quality silicon counters and to operate them in optimal conditions. In particular the various regions of a detector must have very uniform parameters, the percentage of defective elements has to be minimal and the behaviour must be stable in time.

In order to select the counters with highest quality and to know the optimal conditions for their operation, systematic and detailed tests are performed in the laboratory before the mounting procedure and the connection to the readout electronics. The tests consisted of static electric measurements dedicated to study the parameters of each detector and all its elements.

The evaluation of the depletion voltage allows the determination of the bias needed during operation and a check of the resistivity of the silicon wafer.

The leakage current flowing in the junction, the bias resistors, and the load capacitance value were measured. These are the more important parameters determining the electronics noise, as seen in paragraph 2.1.4. We also checked the stability of the leakage current in time and the uniformity of resistor and capacitor values over the whole area of the counter.

The interstrip resistance and the capacitive network were measured in order to insure

the correct sharing of charge among neighbouring strips and guarantee high resolution in position determination.

All measurements were performed in a *probe station* inside a light tight box. The detector was placed on a special chuck covered with teflon or conductive rubber (to avoid mechanical damages) and held by a vacuum system. Contacts were made with probes having micrometric tips in order to be able to reach the small elements of the detectors. The probes were equipped with special mechanisms to move the tips with high precision. The connections were made with the use of a microscope mounted on the probe station. The single probes were then connected to the measuring instruments placed outside the box via BNC cables.
Silicon detectors should be handled in a clean room, with great care taken not to damage them mechanically or contaminate their surfaces with grease or dust.

Because of the typical range of currents, resistances and capacitances to be measured, very sophisticated high precision instruments must be used.
Currents, resistances, and voltage levels were measured with a Hewlett Packard 4155A Semiconductor Parameter Analyzer [19]. It has four built-in source/monitor units, two voltage source units and two voltage monitor units. These have 10 fA/2 μV resolution, 3 pA/700 μV accuracy, 10 fA-1A and 2 μV-200 V measurement ranges. The instrument offers very high flexibility in performing and programming measurements and the possibility to store setups and collected data on diskettes.
A Keithley 590 CV Analyzer [20] was used to measure capacitance values. It uses a 15 mV signal both at 100 kHz and 1 MHz frequency. It has a resolution of 1 fF (100 fF) in the 2 pF (2 nF) measuring range, and an accuracy of about 1%. Apart from a built-in bias source (able to provide from -20 V to 20 V), the instrument can also handle an external voltage source and can provide an analog output which allows the CV meter to be connected to the Semiconductor Analyzer and perform measurements with the two instruments together. The CV meter is able to distinguish the capacitive and the resistive components of a net, in series or in parallel, by selecting the proper measuring modality.
Very well stabilized power supplies must be used.
During the tests described in this paragraph the single sided detectors were usually biased by applying a positive voltage to the backplane (n-side) while the bias line and the guard ring on the p-side were kept at ground potential.
The single measurements and the obtained results will be shown in the next sections.

2.3.1 The leakage current

The measurement of the current flowing across a reverse biased junction is one of the fundamental elements to estimate the quality of a detector. In fact, it strongly influences the noise level per readout channel, as shown in section 2.1.4.
The main contribution to the leakage current comes from minority charge carriers thermally generated in the silicon bulk. The depleted region is free of majority carriers (electrons in the n-type material and holes in the p-type material) but under equilibrium conditions electron-hole pairs are generated continually in the crystal volume. In absence of an electric field the created pairs recombine. If, however, an electric field is present, the pairs

are separated and have little chance to recombine. Electrons and holes drift under the influence of the electric field giving rise to a current. This is called *generation current* and can be expressed as [7]

$$I_{gen} = \frac{n_i}{2\tau_0}\, e\, S\, d \tag{2.7}$$

where n_i is the intrinsic charge carrier density (of the order of $1.5{\cdot}10^{10}$ cm^{-3}); S is the active surface and d the thickness of the depleted area; e is the electric charge ($1.6{\cdot}10^{-19}$ C) and τ_0 is the effective lifetime of the minority carriers. Its value can vary from about 100 nsec to more than 1 msec, depending on the care taken in the silicon processing. It is given by:

$$\tau_0 = \frac{1}{\sigma_0\, v\, N_t} \tag{2.8}$$

where v is the thermal velocity of the charge carriers; N_t is the density of generation-recombination centers and σ_0 is their capture cross section. In fact, most generation of electron-hole pairs does not occur directly but by means of intermediate generation-recombination centers (due to impurities and lattice defects) creating new energy levels near the band-gap center. Thus an electron-hole pair may be thermally created in a process where the hole is free in the valence band and the electron is captured by the trapping center, to be subsequently emitted into the conduction band. These bulk trapping states strongly decrease the minority carrier lifetime and increase the generation of current across the junction. Their density depends on the purity of the crystal and, as already mentioned, on the fabrication process. Consequently high quality silicon must be used and particular care taken in the wafer treatment [4].

According to equation 2.7 the generation current is increasing linearly with the surface of the junction and with the thickness of the depleted region. In particular the thickness d can be expressed as [7]

$$d = \sqrt{2\epsilon\mu\rho V} \tag{2.9}$$

where ϵ is the silicon dielectric constant; μ is the majority carrier mobility; ρ is the silicon resistivity and V the applied voltage. Once all other parameters are fixed for a given detector, the generation leakage current component is expected to increase linearly with $\sqrt{V}$ until the junction is fully depleted.

The temperature dependence of the generation current does not appear explicitly in the above equations but is contained in the n_i term ($n_i = CT^{3/2}e^{-\frac{E_g}{2kT}}$ where C is a constant, T is the absolute temperature, E_g is the band gap and k the Boltzmann constant). As n_i doubles with an increase of only 8^{o}C around room temperature, it is extremely important to keep the temperature constant to guarantee a stable behaviour of the detector.

A second component is represented by surface and edge currents also due to generation-recombination centers, caused by imperfections at the edges and on the surface of the crystal. The amount of this contribution largely depends on the fabrication process and on possible humidity or other contaminants present on the detector surface. Normally edge currents are efficiently collected by the guard ring.

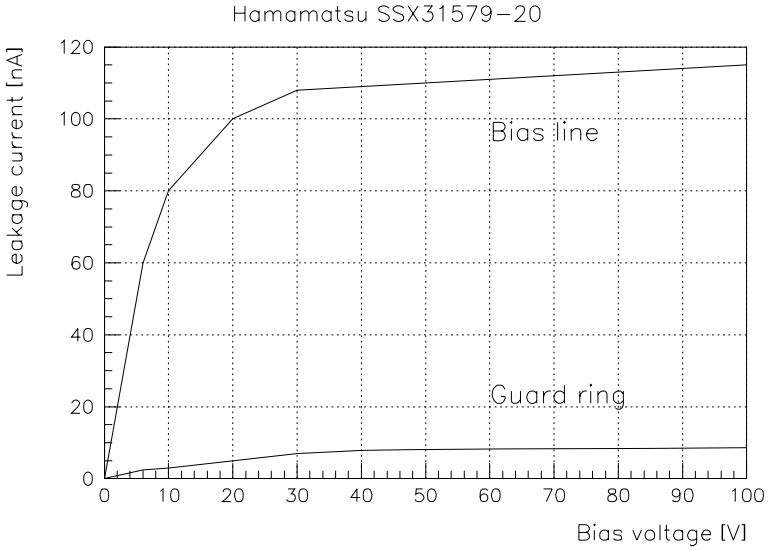

Figure 2.9: IV curve: dependence of the current collected by the bias line and by the guard ring on the applied bias voltage.

The first measurement performed concerns the dependence of the total leakage current on the reverse voltage, which determines the *IV curve*. Because all strips are connected to the bias line through the polysilicon resistors, it is possible to collect the current generated in the whole active area by simply connecting to the bias line. A variable bias voltage is applied to the n-side of the detector and the current is measured separately from the guard ring and from the bias line.

A typical IV curve is shown in figure 2.9. The bulk generation current collected by the bias line shows approximately the expected $\sqrt{V}$ dependence together with some surface contributions. Note that the total level of current is also very low.

This measurement was performed for each detector. It always showed the expected behaviour proving that the counters were working correctly and were not damaged during transport.

In order to collect and compare all results, the value of the bias line and the guard ring leakage current at 100 V reverse voltage was recorded. The distribution of the value of the active area current for the 45 detectors tested is shown in figure 2.10.

The average leakage current per detector was 156 nA, corresponding to 3.9 nA/cm^2 (a useful expression to make comparisons with detectors of different geometry) or 62 pA/strip (the value to be considered while calculating the noise per channel), a very good value for large area AC-coupled detectors.

For several detectors the leakage current behaviour at a given bias voltage as a function of time was also studied. The measurements were taken over 1 to 3 days, with the temperature continuously monitored. No detector showed significant instabilities: the current level stayed constant within a few percent, an important condition for stable operation in the experiment.

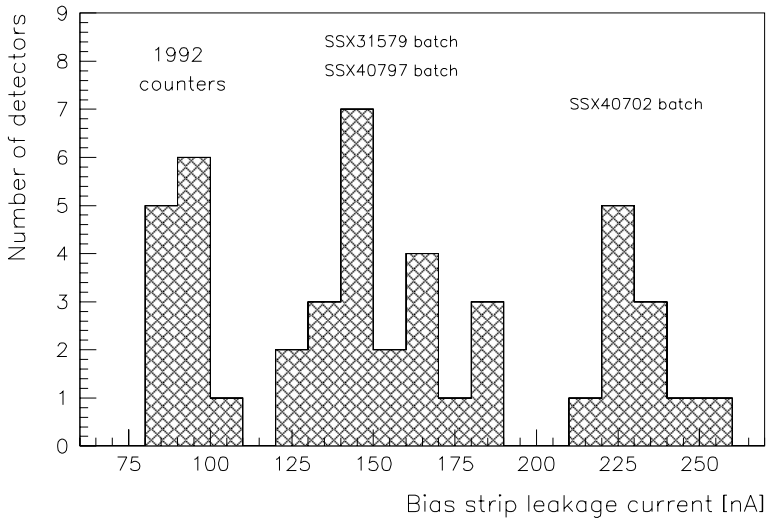

Figure 2.10: Distribution of the leakage current from the active area measured at 100 V for the 45 detectors tested.

2.3.2 Depletion voltage

In a simplified model, a p-n junction can be considered as a capacitor where an insulator layer (the depleted region) is placed between two conducting plates (one represented by the n^+ layer and the other given by the sum of all the p^+ strips).
The capacitance across the junction is given by:

$$C = \frac{\epsilon S}{d} = \sqrt{\frac{\epsilon}{2\mu\rho V}}\, S = \sqrt{\frac{\epsilon e N_d}{2V}}\, S \qquad (2.10)$$

where N_d is the donor density and V the applied voltage.
As we can see from the formula, the value of the capacitance C decreases for increasing bias voltage as $1/\sqrt{V}$ (all other terms in the formula are constant in a detector). It reaches a minimum constant level when the detector is fully depleted. In fact, if we consider the linear dependence of $1 / C^2$ on V, the proportionality factor is $2 / (\epsilon e S^2 N_d)$. At fixed detector geometry, the factor depends only on N_d, the donor density in the n-type silicon. The factor becomes practically zero when the depleted region reaches the n^+ layer, where N_d is very high, and $1 / C^2$ becomes constant.

By measuring the dependence of the junction capacitance on the reverse bias (the *CV curve*), we can determine the *depletion voltage* corresponding to the point where the capacitance reaches the constant value.
This measurement is done by connecting the bias line and the guard ring together and evaluating the total capacitance between them and the n-side of the detector. One example of a CV curve is shown in figure 2.11: on the left the dependence of C is shown, on the right the one of $1 / C^2$. In this case, the depletion voltage is approximately 40 V. The total capacitance is about 1.45 nF, corresponding to approximately 0.57 pF/strip and 0.09 pF/cm

referred to the strip length. The measurement is performed with the Keithley CV Analyzer with a frequency of 100 kHz.

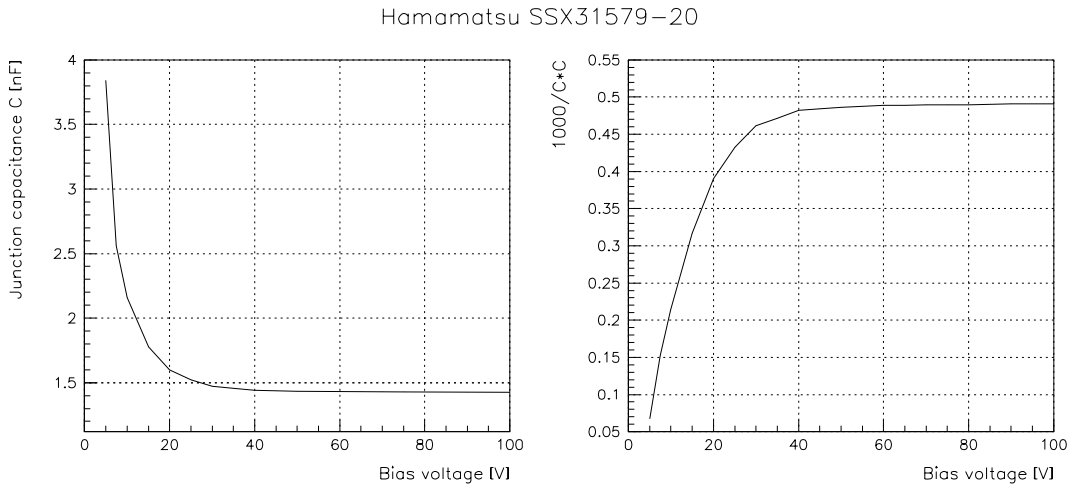

Figure 2.11: CV curve: dependence of the junction capacitance C (on the left) and of $1/C^2$ (on the right) on the applied bias voltage (the value of $1/C^2$ has been multiplied by 1000 for convenience).

The CV curve has been recorded for every detector in order to check the proper operation of the junction and determine the operational voltage of each counter. The measured depletion voltage value was always between 20 and 40 Volts. The operational voltage is usually chosen to be slightly higher than the depletion value to ensure full depletion of the counter.

2.3.3 Silicon resistivity

Using the information given from the previous measurement we can also determine the resistivity of the silicon substrate. From equation 2.9 we can obtain the following relation:

$$V_{depl} = \frac{d_{tot}^2}{2\,\epsilon\,\mu\,\rho} \tag{2.11}$$

Knowing the total thickness of the detector (d_{tot}=300 μm in our case), the dielectric constant (ϵ=11.7 $\cdot\epsilon_0 \approx$ 1 pF/cm) and the majority charge carrier mobility (μ=1350 $\frac{cm^2}{Vsec}$), we can write the dependence of the depletion voltage on the silicon resistivity ρ as follows:

$$V \simeq \frac{300\,Volt}{\rho[k\Omega \cdot cm]} \tag{2.12}$$

Having determined the depletion voltage, we can deduce the resistivity. For all the measured detectors its value was very high, between 6 and 15 kΩ·cm, another indication of the excellent quality of the crystals used.
The high resistivity of silicon allows operation of the detectors at relatively low bias voltage, and thus smaller drift velocity. Consequently, the charge has a longer time to diffuse and spreads over a larger area giving improved spatial resolution, using proper algorithms, as indicated above.

2.3.4 Polysilicon bias resistors

As explained in the introductory part, individual polysilicon resistors connect the p^+ strips to a common bias line. It is extremely important that the values of the resistors are uniform throughout the whole detector: this guarantees that all strips are held at the same potential level and that the field lines in the bulk are uniform.
Furthermore the resistance has to be high enough (> 1 MΩ) to allow most of the charge accumulated on single strips to be collected by the amplifiers before being discharged through the resistors. Besides, as shown by equation 2.6, a higher value of the bias resistance reduces the electronics noise.

As indicated in figure 2.3, a contact can be made at the point where the polysilicon is connected to the p^+ implant which allows the measurement of the value of the individual resistors. We applied a small voltage difference (variable between ± 250 mV) between the contact point and the bias line (where the other end of the resistor is connected). The resistance value can be estimated by measuring the induced current. This test should be done while the detector is fully depleted.
The result of one measurement of this kind, performed with the Semiconductor Parameter Analyzer, is shown in figure 2.12. Fitting the current dependence on the applied voltage difference we can calculate the resistance (in this case equal to 4.6 MΩ).
In case of a significant leakage current, its contribution per strip can give an offset at zero voltage difference.

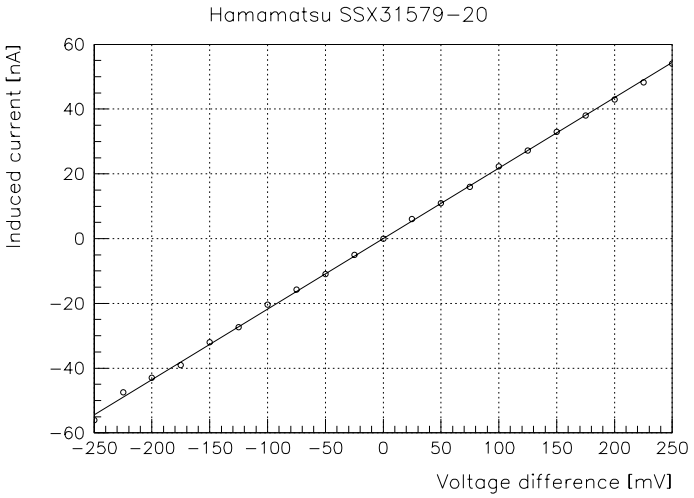

Figure 2.12: Measurement of the value of a polysilicon bias resistor: the dependence of the induced current on the applied voltage gives a resistance of 4.6 MΩ in the case shown.

It is important not to apply voltage differences higher than 250-500 mV. Too high potential differences between the measured strip and its neighbours cause the induced current to be non-linear and hence the resistance measurement can be distorted.
For each detector several resistors located in different areas of the counter were measured in order to check their uniformity. The result was always very good indicating an almost constant value of the resistance inside one detector.

The average value changed from the first batch of detectors (in which it was approximately 1.3 MΩ) to the later ones due to our explicit requirement that the value be 4-8 MΩ.

2.3.5 Interstrip resistance

Another important parameter of the detectors is the resistance between neighbouring strips, the *interstrip resistance*. It influences the charge sharing among adjacent strips. Its value must be high enough to prevent a too large distribution of the charge cloud over many strips, which would limit the position resolution. A safe lower limit is given by the requirement $R_{interstrip} > 10 \cdot R_{polysilicon}$.
The measurement is performed by applying a voltage difference (varying from -250 mV to +250 mV) between the contact points of two adjacent strips, while the detector is depleted. From the induced current the resistor value can be estimated.
This measurement is particularly delicate for two main reasons. Due to the very high resistance (of the order of 0.1-10 GΩ) the induced current is extremely small. Consequently a very high sensitivity instrument is needed and the measurement has to be performed in a very accurate way. In particular, one has to remove possible distortions created by the constant leakage current flowing in the single strips.
The interstrip resistance is part of a complex resistive network formed by all polysilicon resistors and by the resistance between all the other strips of the detector. Disentangling the exact value of the interstrip resistance is very complex and is beyond the aim of our measurement. In this test it is important to obtain an approximate value and verify that it is higher than the lower limit imposed.

The interstrip resistance has been measured between several pairs of adjacent strips located in different regions of a detector. Also in this case it is extremely important to verify its uniformity through the whole counter. The average value measured for several detectors was between 2 and 10 GΩ. The measurement was usually not too difficult to perform thanks to the low leakage current of the detectors and to the high sensitivity of the Semiconductor Analyzer.

2.3.6 Coupling capacitance

In our detectors, capacitive coupling to the readout electronics is made by a thin layer of SiO_2 placed between the p^+ implantation and the metal readout line. As explained in section 2.1.1, the capacitance value must be high enough to avoid signal losses to the backplane and to the neighbouring strips.
The measurement of this value is relatively simple. It is possible to make a connection to individual p^+ strips (one “plate” of the capacitor) through the contact holes and to the metal lines (the other “plate” of the capacitor) at the bonding pads. The test can be performed without depleting the detector and in the presence of light. The Keithley CV Analyzer was used and operated at 100 kHz. It is important to calibrate the instrument correctly in order to subtract the stray capacitance due to cables and probes (of the order of a few pF).
The coupling capacitance was measured for several strips on a few detectors and found to be nearly identical for each counter. Its average total value was approximately 55 pF, corresponding to about 8.7 pF/cm.

It is also possible to make the measurement faster by connecting to the bias line instead of the single contact holes. The measuring instrument offers the possibility to automatically disentangle the bias resistance in series with the capacitor measured. This solution is very convenient for testing large numbers of strips.

Using a simplified expression for the coupling capacitance of

$$C_{coupling} = \frac{\epsilon \cdot S}{d_{SiO_2}} = \frac{\epsilon \cdot l \cdot w}{d_{SiO_2}} \tag{2.13}$$

we can roughly estimate the oxide thickness. In the formula ϵ is the oxide dielectric constant (=3.9·ϵ_0=0.34 pF/cm); S is the capacitor plate area. This can be approximated by the product of l and w, the average length and width of the implanted strip and the metal line, respectively. The oxide thickness is indicated as d_{SiO_2}.
In our case l=6.35 cm, w=8 μm and $C_{coupling}$=55 pF. The corresponding oxide thickness can be estimated to be approximately 315 nm.

As already mentioned, the defects of the coupling oxide can produce pinholes, i.e., short circuits of the capacitors. Usually the corresponding readout channels show a very high noise as the leakage current is directly fed into the preamplifier. Sometimes it is even necessary to remove the connection to the defective channels. It is therefore essential to limit the number of pinholes per detector.
This condition was included in the specifications of our detectors. Hamamatsu performed the test of all individual strips, checking if the coupling oxide would withstand a 30 V voltage difference. In order to satisfy the specifications half of the detectors had to have at most 1% defective lines and the other half at most 2% defective lines. Figure 2.13 shows the distribution of pinholes in the delivered detectors, according to the results provided by the producer.

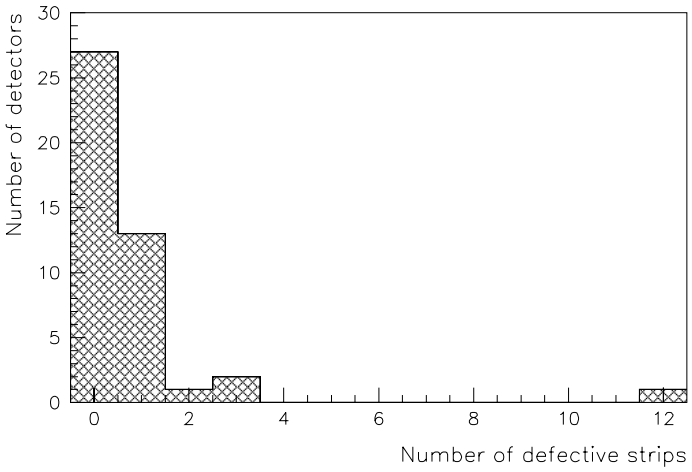

Figure 2.13: Distribution of pinholes for the 45 delivered detectors, according to the tests performed by Hamamatsu Photonics (one detector with 22 defective lines is not shown).

2.3.7 Interstrip capacitance

One of the main contributions to the electronics noise is the load capacitance. In a microstrip detector this is given by the capacitance between one strip and all its neighbours (called *interstrip capacitance*) and the capacitance between the strip and the backplane of the detector.

The first contribution is the more relevant one and it is an important parameter to measure for a certain detector design. Its value is mostly determined by the geometry of the counter (the strip width and pitch, the coupling oxide thickness) and by the materials used in the fabrication. It generally does not vary from counter to counter.

This test is extremely delicate. A detailed discussion of similar measurements can be found in reference [21]. The capacitance value is small (between 1 and 20 pF per strip). In order to achieve sufficient precision a very careful calibration of the system must be done before the measurement and has to be repeated after any change of the connections. Cables and probes contribute significantly (a few pF) to the total capacitance measured. Their contribution must be therefore carefully evaluated and corrected for.

The other challenging point is to reproduce the real working conditions of the detectors where all readout lines are kept at a common potential level by means of the connection to the electronics. In our measurement it is essential to have a similar situation. Evaluating the capacitance between two adjacent strips would not give a sensible information. Therefore for one counter 300(150) strips had been connected to each other by means of ultrasonic bonding, 150(75) on each side of the strip to be measured at 25(50) μm pitch. In this way the capacitance between the single strip and the group of all others could be measured with a relatively simple connection.

As shown in reference [5], the main contribution to the interstrip capacitance comes from the closest neighbours (up to approximately 10-15 adjacent lines), while strips further apart contribute less and less. Consequently, one can assume that in the condition described above the measured capacitance approximates well the load capacitance seen by the preamplifier.

The measurement was performed with the CV Analyzer, with the detector fully depleted. Equal results were obtained for 100 kHz and 1 MHz frequencies. All measurements were made over a long time interval to be sure that stable conditions were reached.

The obtained capacitance values are 7.1 pF/strip for 50 μm readout pitch (with intermediate floating strips) and 9.3 pF/strip for 25 μm readout pitch. They correspond to a capacitance per unitary length of 1.13 pF/cm and 1.48 pF/cm respectively.

Figure 2.14 shows the dependence of the interstrip capacitance on the applied bias voltage. Its value reaches a plateau above about 15 V, since full sideways depletion is already reached at low bias voltage.

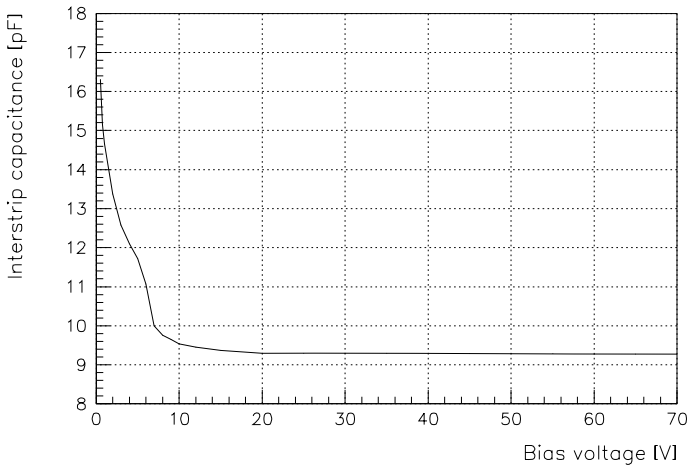

Figure 2.14: Dependence of the interstrip capacitance on the applied bias voltage.

Summary

All detectors received were accurately tested and showed an excellent and very uniform behaviour. All parameters measured confirmed the expected quality level and satisfy the stringent requirements for an efficient and precise tracking device. The test also proved the high quality and purity of the used silicon crystals and the very good control of the fabrication process by the producer.

2.4 The SVX readout chip

The readout of our microstrip detectors is performed by the SVX (Silicon VerteX) chip, a fully customized VLSI[2] circuit, fabricated using a 3 μm CMOS[3] technology. The chip contains 128 parallel channels; their bonding pads are staggered in two rows, at 50 μm pitch. Each channel includes a charge integrator, an amplifier, a comparator, an analog multiplexer, nearest neighbour logic and priority search logic. The information supplied consists of both the digital address of the strip and the corresponding analog signal.

This chip has been chosen because of the possibility to perform zero suppression (or sparsification) on the chip itself. This means that it is possible to identify the channels which effectively collected a signal and read out those only, neglecting the empty channels. This is done by storing the analog information on a capacitor, comparing it to a programmable threshold and setting a latch in presence of a signal. In the proper operation mode, only latched channels are read out. Sparsification allows efficient management of low occupancy events.

In a system like ours the number of channels is high, about 47000, but the fraction of hit channels in any given event is usually small (less than a few hundred). Other standard chips read out all channels and the strips containing hit information are later selected by software. This procedure seriously limits the readout speed and requires a system able to handle an enormous amount of data.

The long readout time required is a serious problem for fixed target experiments. Random triggers and high incoming particle fluxes (1-10 MHz) demand that hit information can be collected quickly and that fast resets clear the electronics in case of rejected triggers. The readout time and the time spent to clear the system must be minimized in order to limit the deadtime (the time during which the experiment is not in the condition to accept triggers, losing sensitivity also to useful events). Performing the zero suppression on the readout chip allows a considerable saving of time and reduction of the amount of information to be transferred.

The SVX chip was developed at the Lawrence Berkeley Laboratory starting in 1987 [22, 23, 24, 25]. It was designed for use at the Collider Detector Facility (CDF) at Fermilab [26, 27, 28], so it is particularly tuned for the well-known time structure of data acquisition in colliding beam experiments. As the beams are bunched, interactions can occur only in short intervals, separated by a much longer time. In this situation one has a well defined time at which the system must be ready to accept a possible event, and a relatively long time to cancel switching noise, leakage current effects and to clear the system.

This is not the case in fixed target experiments, where the time interval between successive events is random. Nevertheless, the possibility of performing very fast resets in the SVX chip makes its operation also possible there.

Different versions of the SVX chip were developed, with the goal of optimizing the noise performance and radiation hardness. In WA89 we have used the D version and the

[2] Very Large Scale Integrated

[3] Complementary Metal Oxide Semiconductor

radiation hardened H version (produced by Hewlett Packard and the United Technologies Microelectronics Center respectively).

In the following sections I will discuss some parts and functions of the SVX chip which are interesting for our application. A more detailed and technical description can also be found in the references mentioned before.

2.4.1 The analog part

The analog part of each channel includes a low noise, low power charge integrator, an amplifier, a sample and hold circuit, a multi-stage comparator and a signal multiplexing circuit. Each stage is capacitively coupled (to preserve voltage differences between amplifiers) and includes a simple two transistor amplifier with a reset switch. Figure 2.15 shows the layout of a single channel.

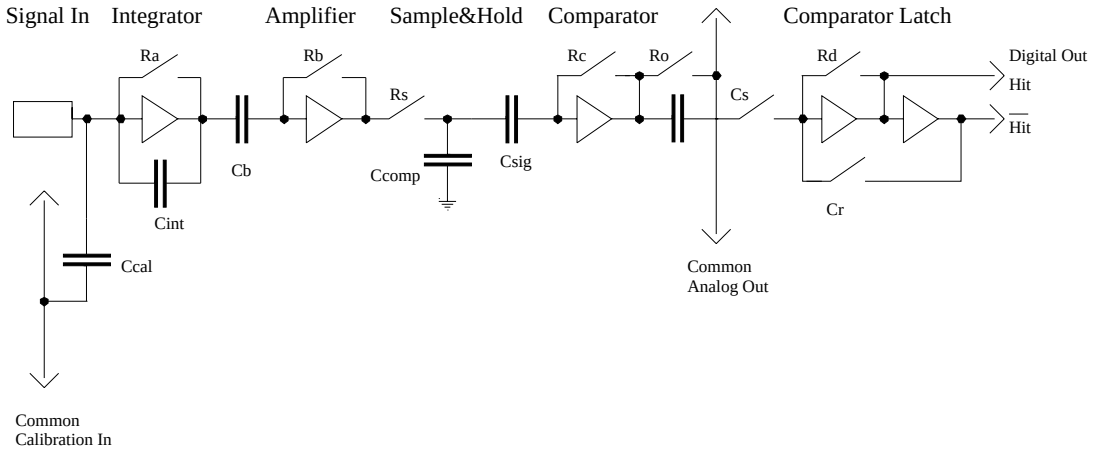

Figure 2.15: Scheme of one channel of the SVX chip.

During initialization of the analog section all stages are reset (by closing their switches) to their quiescent states, where their input and output voltage levels are equal. During reset the system cannot accept triggers. Immediately after the chip is prepared for readout. When a trigger occurs, the signal from the strip enters through the bonding pad. The first two stages of the electronics, controlled by the switches R_a and R_b, integrate and amplify the signal (15 mV/fC). The output is then stored on the capacitor C_{sig}. Zero suppression is performed comparing this signal to an adjustable threshold. A calibration pulse is fed into the common calibration line and stored on the capacitor C_{comp}. Transferring the particle signal to the output effectively subtracts the calibration signal from the data. The comparator then detects if the remaining pulse is a hit and indicates its decision to the readout logic by setting a latch. The readout logic then toggles through all channels, searching for the latched ones, which will be read out. The analog signal is placed on an analog bus while the corresponding digital address appears on a 7 bit digital bus.
As the speed of the integrator and amplifier is of the order of 100 nsec, no event-specific triggering can be achieved. Instead we operate the chip in a mode of continuous sensitivity with interleaved resets, optimized to minimize deadtime.

The SVX chip can be operated both in the quad sampling mode and in the double sampling mode (also called the two or one integration window mode). The first case is designed to remove detector leakage current effects. Usually one integration window is used first for the particle signal and then for the calibration signal. In quad mode, after every signal (or before in case of collider experiments), the integration window is repeated with reversed polarity in absence of the signal itself. The second part thus contains the integration of the detector leakage current and is subtracted from the first one.
When leakage currents are not relevant, the chips can also be operated in a more standard double correlated sampling mode with a resulting lower noise (see figure 2.16).
During WA89 data taking two integration windows were always used. Measurements with one window readout have been performed in a later test beam (see chapter 3).

2.4.2 The digital part

The SVX is operated by 11 Input/Output lines. When configured as input, they are used to control the analog section of the chip, to program chip identification numbers and to set special functions. When configured as output, they transmit the chip and channel address of the recorded hits.
The SVX includes chip and channel priority search logic. Each channel assumes a certain readout priority determined by its physical position. The logic can quickly locate the first hit channel (having the highest priority) and read it out (encoding the number of the channel, while the relative analog signal is gated into an internal bus). Once the readout of that channel begins, it releases priority, allowing the next hit channel to be found. Many chips can be daisy-chained and participate together in the priority search. Combining 7 bit chip and 7 bit channel numbers permit unique identification of over 16000 channels per bus system during sparse readout. The readout of the pure digital information can operate up to 2-10 MHz rates, while the time necessary to read out both the digital and the analog information is about 1.5 μsec per channel (0.67 MHz).
In our case, for an average multiplicity of 40 hits per plane per event, we achieve a total readout time of 150 μsec (including also the data transfer to an event builder). It is also possible to enable the readout of all channels, regardless of the comparator outputs. We call this mode latch-all and use it to determine the pedestal and noise level of each channel. The pedestal level can be later subtracted to obtain the pure signal amplitudes. The noise level can be used to monitor the operation of the system.
The SVX chip also includes the nearest neighbour logic that, in addition to reading out hit channels, will also read out adjacent channels whose signals were too low to trigger their comparators. This feature can be very helpful to improve the accuracy of track position determination as explained in a previous paragraph.

Some technical data regarding the SVX chip are summarized in table 2.3.

Number of channels/chip	128
Channel pitch	50 μm
Power consumption	150 mW/D-chip, 250 mW/H-chip
Nominal gain of analog channel	15 mV/fC
Integrator feedback capacitance	0. 3 pF
Calibration line input capacitance	0. 06 pF
Linear bipolar range	40 fC (≈ 20 MIPs)
Supply voltages	analog 6 V, digital 5 V
Maximum readout speed	analog: 1 MHz digital only: 10 MHz

Table 2.3: Parameters of the SVX chips.

The noise of the SVX chip (D version) has been measured as a function of the input load capacitance in both double and quad sampling modes [25]. The results are shown in figure 2.16. For higher values of capacitance, the ratio of quad sampling noise to double sampling noise is very close to $\sqrt{2}$.

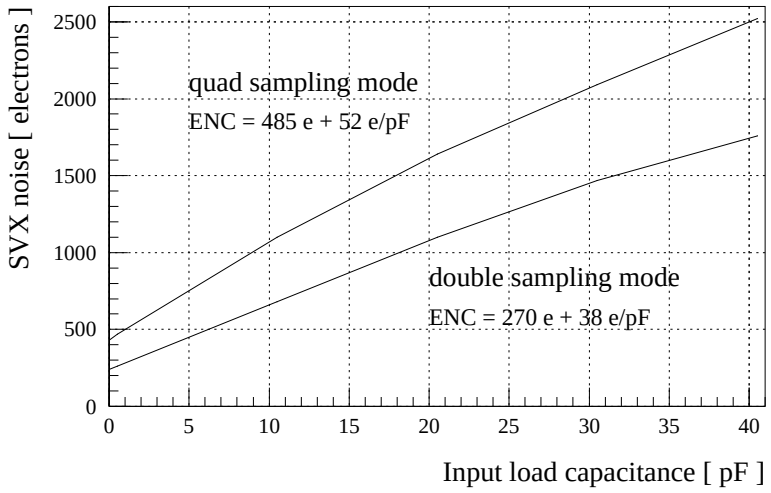

Figure 2.16: SVX-D noise as a function of the input load capacitance.

2.4.3 The SVX chip control and data transfer

The chip control is performed by a CAMAC module called SRS (SVX Readout Sequencer), originally developed at LBL [29, 30] and redesigned for our application. The sequencer contains a 10 MHz CPU and a 6 kByte RAM. From the local computer system, a binary pattern can be stored in the RAM and the CPU sends it sequentially to the SVXs via a control bus. The pattern consists of a sequence of instructions which are used to open and close the switches in the chip, enable special conditions and synchronize data acquisition. For the input of external communication signals (trigger, ready's, etc.) the SRS has an externally accessible condition register, which can be checked and requested

within the pattern sequence. A TTL output register is used for the threshold control of the chips.
The SRS controls the communication with all systems involved: trigger logic, data acquisition and the detectors themselves. In particular the SRS can accept trigger and clear decisions, inhibit the trigger logic during reset, strobe the FADC and the FIFO memory to store all digital data from one event, send a 'ready for readout' signal to the data acquisition system to indicate a filled event buffer. A more detailed description of all functions can be found in references [30, 31, 32].
In our case, the more important requirements come from running the SVXs in a fixed target experiment, where a randomly timed input must be accepted:

- periodic resets must be done to remove unwanted interactions and charge from leakage currents; these resets should be as short as possible in order to minimize deadtime. This point becomes even more important if we take into account that the probability for our incoming beam to interact in the target is about 5% and only 6% of the interactions are then accepted as interesting. It is essential to have good data rejection capability, so fast clear features;
- the operation of the system must be stable for random intervals between inputs;
- the readout time itself must be as short as possible, also to reduce deadtime.

The pattern used during the WA89 data taking period takes into account these considerations. Its structure will be illustrated in the next section.

2.5 The detectors in WA89

2.5.1 The setup

The silicon detectors equipped with SVX readout were introduced in WA89 in two steps. In 1993 the first 12 planes, with 25 μm readout pitch, were installed in the vertex region, close to the target. They were grouped in 3 structures called *stars*, each with four detectors, measuring four projections (vertical, horizontal and at $\pm 45^o$). The vertex detector setup is shown in figure 2.17. A detailed description of the mechanical and electronical layout of the system can be found in references [31, 32].
In 1994 other 13 planes were added, all with 50 μm readout pitch. Six of them were placed in front of the target as beam detectors, the other 7 downstream of the vertex area. The new setup can be seen in figure 4.5. For the 1994 run we also installed an under-pressure water cooling and a slow control system.

All silicon detectors are mounted on 11.5x11.5 cm^2, 600 μm thick Al_2O_3 boards. They have a central opening for the detector and a printed circuit with five conductive layers which provides all communication signals to the SVX chips. These are mounted on the board with conductive epoxy glue. All connections between the board and the pads of the readout chips, and between the SVX channels and the single strips are realized by ultrasonic bonding, with 17.5 μm diameter Al wires (with 1% Si content).

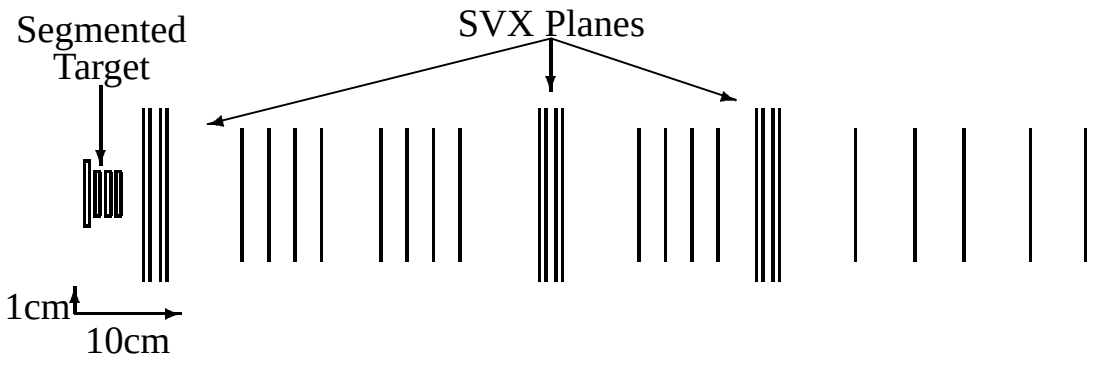

Figure 2.17: Vertex detector setup downstream of the target in 1993.

The fully equipped boards are then mounted either directly on massive brass frames (for the 1993 and the beam stars) or on a wider and lighter honeycomb structure (for the two 1994 downstream stars). The mounting accuracy achieved with respect to the frame is about 4 μm perpendicular to the strips and 25 μm in the direction of the strips. The stars are sealed with silicone rubber and covered with 20 μm thick aluminum foil.
The detector boards are connected via 30 μm thick capton cables to the main electronic boards, placed around the mounting frames. The analog and digital parts of the control and readout system are separated to minimize crosstalk. The digital boards multiplex the binary control pattern from the SRS into the SVX control bus and the digital data from the SVX chips into local FIFO memories and then to FASTBUS memories. On the analog boards 8 bit FADCs digitize the analog signals, DACs adjust the threshold levels for the SVX chips and set an offset for the FADCs. In addition there are voltage regulators for biasing the SVX chips (more details can be found in reference [31]).

In our setup there are a total of 370 SVX chips. Part of them were delivered already tested. A second part, for the 1994 detectors, was not tested. We developed a procedure to check their parameters and select the good chips.We used a special card with 33 needles in the probe station, where we placed full wafers (each containing 312 chips). Approximately 50% of the chips were accepted.

2.5.2 The readout cycle

The structure of the pattern used in WA89 for the readout of the silicon detectors can be summarized as follows:

- The chip initialization is performed, giving to each chip of a detector a unique identification number;
- A loop of integrations, short and long resets follows, waiting for a trigger signal. We use an integration window of variable length (between 1.5 μsec and 4 μsec) allowing an interruption of the integration once a trigger is received. Having a complete

reset after every not interacting beam particle would cause too high deadtime. Consequently only a 300 nsec reset (clear of the capacitor and amplifier) is performed every time while a 1.5 μsec long reset of the integrator is performed after 50 short reset cycles. The deadtime due to such readout cycle is about 18%. The drawback of this longer integration time is that 1.8 additional tracks (from the beam and its halo) and 2.4% additional interactions per detector per event are recorded together with the valid data. Some external means must be provided to sort them out. In WA89 we use the information provided by other silicon detectors present in the vertex region, equipped with high speed amplifiers (COROM, see in chapter 4);

- If a *clear* signal comes from the trigger logic, the SVXs are reset and wait for the next trigger. Otherwise, after an accepted trigger, the calibration signal is sent in the common calibration line, a second integration is performed and the readout mode (sparse or latch-all) is requested;

- The analog signals are converted by an FADC and stored, together with the relative chip and channel number, in a local event buffer (from there they will be transferred to large FIFO FASTBUS memories for event building). This continues until a *priority out* signal indicates the end of data;

- The SRS sends a *ready* signal to the data acquisition system and the SVXs are switched back into the trigger wait loop;

- During off-spill the SVXs are switched into a low power consumption state.

2.5.3 The monitoring of the system

During the data taking periods, the stability of the system was checked in various ways.
Pedestal levels of all channels were continuously measured and stored, for subtraction from the recorded analog signal. On the time scale of few days they were very stable. Long term variations were taken care of by the daily pedestal measurements. At the same time the noise level of single channels, defined as the width of the pedestal variation, was evaluated and recorded.
The left part of figure 2.18 shows the pedestal level of 2560 channels of one of the 1993 detectors. It is possible to identify the structure of the 20 SVX-H chips present. The linear decrease of the pedestal value with the channel address within one chip is a feature of the SVX-H version and due to a defect of the power distribution line. Even though this is also reflected in a linear variation of the optimized threshold level over a single chip and only a single threshold per chip can be applied, no effect on efficiencies was observed.
The right part of figure 2.18 shows the noise profile for the same detector. With the exception of few noisy channels (mostly due to local defects in the silicon or to bonding failures) the noise is nearly constant through the whole counter.
In our system 1 ADC count corresponds to about 0.5 mV. Using the relation 15 mV/fC valid for the SVX chips, an average noise level of 3 ADC counts corresponds to approximately 0.1 fC (about 1/16 of a MIP).

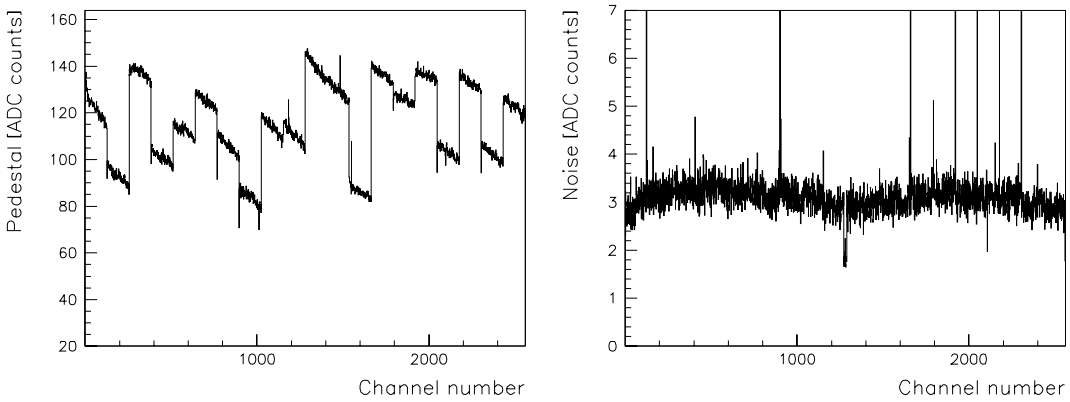

Figure 2.18: Pedestal level (on the left) and noise profile (on the right) for one of the 1993 detectors.

Calibration of the SVX chips is a very important aspect as it strongly determines the quality of data and the performance of the system. This operation consists of selecting for every chip the best threshold in order to perform zero suppression with high efficiency and low noise at the same time. Optimized thresholds were set to a level allowing about 1 to 2 noise hits per event per plane. They were checked and adjusted (if needed) every few days.

For the slow control system, PT100 temperature sensors were installed on all detectors. A CAMAC-controlled system formed by a high precision multimeter and a switching card measured the temperature, bias voltage, and leakage current of each detector every 2 minutes. An alarm system gave a warning in case of dangerous variations of the parameters. An accurate description of the setup and the presentation of results can be found in reference [33]. A precise correlation between the leakage current of the detectors and their operational temperature was seen. Due to the cooling system, this temperature was reduced from about 45-50^o of the previous year to 24-30^o. The average leakage currents were about 1-3 μA per detector.

The leakage currents increased slightly from the beginning to the end of the run after accounting for the temperature effects. This could be due to some moderate radiation damage of the detectors (the deposited dose is never more than 20-30 krad per run period).

No radiation damage of the SVX chips is expected because they are not hit directly by the beam and the deposited dose is negligible. Nevertheless some measurements have been performed on the SVX-C version (fabricated without a radiation hardening process). Working chips were exposed to Cobalt 60 gamma radiation. The results indicate a doubling of the electronic noise for a dose of 20 krad for a detector capacitance of 30 pF. More details about the measurements and the results can be found in reference [34]. The H version, fabricated with a radiation hardening process, should show better resistance to radiation damage.

The inner volume of the stars was always flushed with nitrogen to avoid humidity.

2.5.4 The performance

The results presented here concern the detector operation during both 1993 and 1994 data taking periods.
The efficiency of the SVX detectors was continuously monitored, using tracks reconstructed from the full WA89 vertex detector. With these tracks the impact position on the detector under study is predicted. The probability of finding the corresponding hit determines the efficiency of the counter. The average value was estimated to be more than 98% for all individual detectors.

Figure 2.19a (referring to the 25 μm readout pitch detectors) shows the analog signal distribution, which correctly follows a Landau shape. In figure 2.19b we can see the different contributions from hits with cluster size 1, 2 and 3 respectively. In general the quality of the analog information is degraded when sparse readout mode is used because the comparison with the calibration threshold tends to suppress the tails of the signal and slightly distort the analog distribution. In sparse mode the signal to noise ratio, defined as the ratio of the Landau maximum to the 1 σ pedestal variation, was measured to be 12:1 and 15:1 for H and D chips respectively.

From the distribution of the difference between the predicted impact point and the found hits we derive the spatial resolution. The measured positions can be estimated differently depending on the cluster size. As shown in figure 2.19c, clusters with at most 2 strips account for 97% of all hits.
In case of a single strip hit the resolution is given by the standard deviation of a rectangular hit distribution over the strip, which is equal to pitch/$\sqrt{12}$. This corresponds to 7.2 and 14.4 μm for 25 and 50 μm readout pitch respectively.
For two or more strip clusters, the spatial resolution can be improved. For two strips, in the case of the 25 μm readout pitch detectors, using only the binary digital hit information we have a resolution better than 6.5 μm. Using the analog information we can also calculate a correction function as explained in paragraph 2.1.2. Using a linear correction function we obtained a resolution better than 5.3 μm. These results are shown in figure 2.19d.
In the case of the 50 μm readout pitch detectors, the resolution we can obtain with optimized digital information and analog information is, respectively, 12.5 μm and 10.0 μm.

The analog information can be used also to reject noise hits and to identify double tracks or interactions in the detector. If a secondary interaction happens in the counter, the silicon nucleus usually breaks apart and a large amount of energy is released locally (within 10-100 μm). These events can be recognized by means of their very high analog signal. It is important to be able to tag and reject secondary interactions as they may resemble hadron decays.
More information about the detector performance and the obtained results can be found in references [31] and [33].

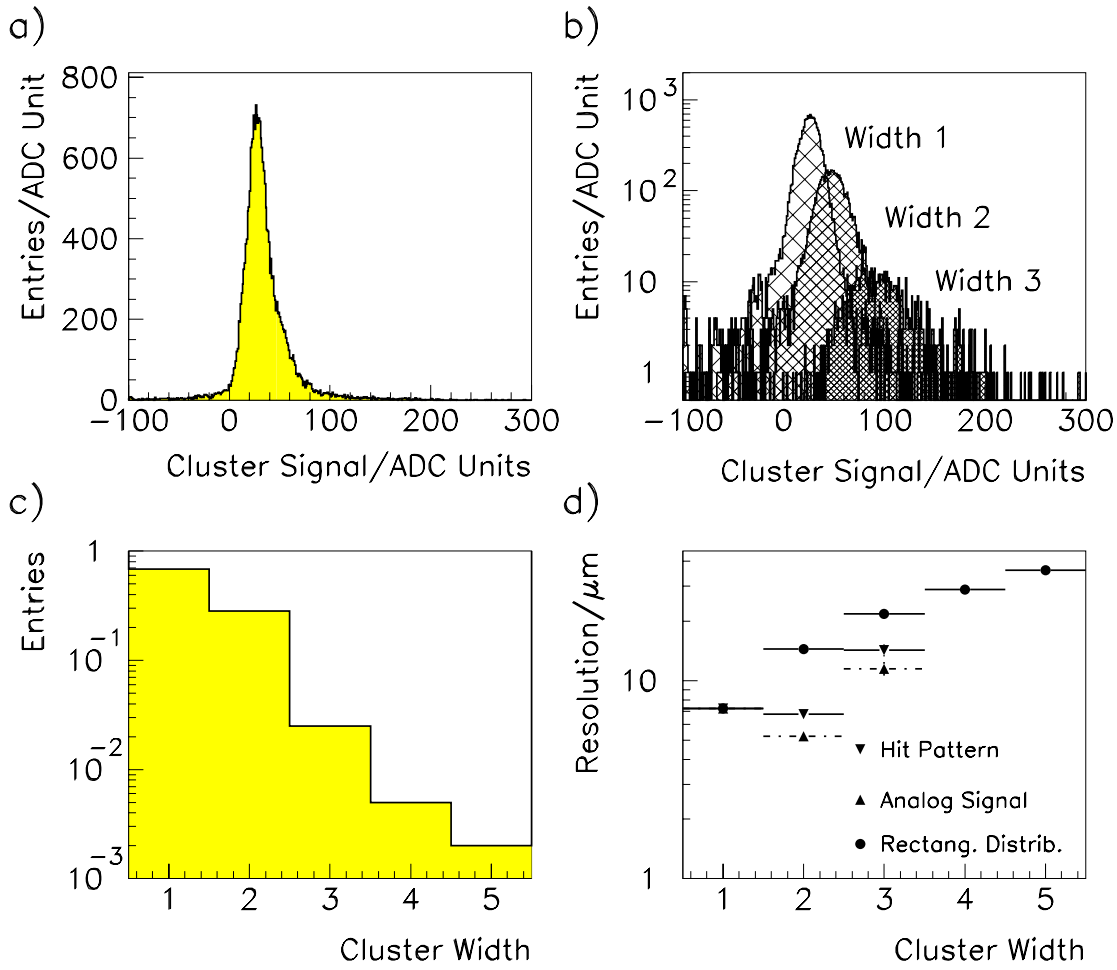

Figure 2.19: Use of the analog information to improve spatial resolution in case of 25 µm readout pitch detectors: a) pulse height distribution; b) pulse height distribution for different cluster widths; c) cluster width distribution; d) detector spatial resolution.

Bibliography

[1] K.G. McKay, “Electron-hole production in germanium by alpha-particles”, Phys. Rev., Vol. 84, No. 4 (1951) 829-832

[2] E.H.M. Heijne et al., “A silicon surface barrier microstrip detector designed for high energy physics”, Nucl. Instr. and Meth. 178 (1980) 331-343

[3] J. Kemmer, “Fabrication of low noise silicon radiation detectors by the planar process”, Nucl. Instr. and Meth. 169 (1980) 499-502
J. Kemmer et al., “Performance and application of passivated ion-implanted silicon detectors”, Nuclear Science Symposium, San Francisco, 21-23 October 1981

[4] J. Kemmer, “Improvement of detector fabrication by the planar process”, Nucl. Instr. and Meth. 226 (1984) 89-93

[5] A. Peisert, “Silicon microstrip detectors”, in “Instrumentation in high energy physics”, edited by F. Sauli, World Scientific Editing Company, Singapore, 1992

[6] G.F. Knoll, “Radiation detection and measurement”, J. Wiley & Sons, 1989

[7] A.S. Grove, “Physics and technology of semiconductor devices”, J. Wiley & Sons, 1967

[8] C.J.S. Damerell, “Vertex detectors”, RAL 86-077, July 1986

[9] M. Caccia et al., “A silicon strip detector with integrated coupling capacitors”, Nucl. Instr. and Meth. A260 (1987) 124-131

[10] L. Evensen et al., “Recent development of detectors with integrated capacitors and polysilicon resistors”, IEEE Trans. on Nucl. Sci., Vol. 35, No. 1, February 1988, 428-431

[11] E. Belau et al., “Charge collection in silicon strip detectors”, Nucl. Instr. and Meth. 214 (1983) 253-260

[12] J. Straver et al., “One micron spatial resolution with silicon strip detectors”, CERN-PPE/94-26

[13] B. Hyams et al., “A silicon counter telescope to study short-lived particles in high-energy hadronic interactions”, Nucl. Instr. and Meth. 205 (1983) 99-105

[14] P. Weilhammer, “Experience with Si detectors in NA32”, CERN-EP/86-54

[15] J.B.A. England et al., “Capacitive charge division read-out with a silicon strip detector”, Nucl. Instr. and Meth. 185 (1981) 43-47

[16] U. Kötz et al., “Silicon strip detectors with capacitive charge division”, Nucl. Instr. and Meth. A235 (1985) 481-487

[17] IDEAS, Integrated Detector & Electronic AS, Oslo, Norway, Catalogue 1995-1996

[18] V.Chabaud et al., “Beam test results from a prototype fro the DELPHI microvertex detector”, Nucl. Instr. and Meth. A292 (1990) 75-80

[19] HP4155A Semiconductor Parameter Analyzer, Instruction Manual

[20] Keithley Model 590 CV Analyzer, Instruction Manual

[21] S. Masciocchi et al., “Capacitance measurements on silicon microstrip detectors”, IEEE Trans. on Nucl. Sci., Vol. 40, No. 4, August 1993, 328-334

[22] R.J. Yarema, “A beginners guide to the LBL silicon strip readout chip”, LBL Internal Memorandum, March 1987

[23] S.A. Kleinfelder et al., “A flexible 128 channel silicon strip detector instrumentation integrated circuit with sparse data readout”, IEEE Trans. on Nucl. Sci., Vol. 35, No. 1, February 1988, 171-175

[24] J. Russ et al., “Studies of the LBL CMOS integrated amplifier/discriminator for randomly timed inputs from fixed target experiments”, IEEE Trans. on Nucl. Sci., Vol. 36, No. 1, February 1989, 477-481

[25] T. Zimmerman and R. Yarema, “Preliminary SVX-D test results”, CDF/DOC/SEC-VTX/CDFR/990, May 1989

[26] F. Badeschi et al., “CDF silicon detector prototype test beam results”, IEEE Trans. on Nucl. Sci., Vol. 36, No. 1, February 1989, 35-39

[27] C. Haber et al., “Design and prototyping of the front end readout system for the CDF silicon vertex detector”, IEEE Trans. on Nucl. Sci., Vol. 37, No. 3, June 1990, 1120-1126

[28] W.C. Carithers et al., “The CDF SVX: a silicon vertex detector for a hadron collider”, Nucl. Instr. and Meth. A289 (1990) 388-399

[29] F.A. Kirsten and C. Haber, “A versatile, programmable control and data acquisition system for complex integrated circuits”, IEEE Trans. on Nucl. Sci., Vol. 37, No. 2, April 1990, 288-292

[30] C. Haber, “Users guide to SRS/SDA control software”, LBL Internal Memorandum, December 1989

[31] W. Brückner et al., “Silicon microstrip detectors with SVX chip readout”, Nucl. Instr. and Meth. A357 (1995) 274-282

[32] R. Werding, PhD thesis, University of Heidelberg, 1994

[33] M. Zizlsperger, Diploma thesis, University of Heidelberg, 1995

[34] R.J. Yarema et al., “Radiation effects on the SVX silicon strip readout chip”, IEEE Trans. on Nucl. Sci., Vol. 37, No. 2, April 1990, 434-438

Chapter 3

Double sided detectors

3.1 Introduction

The properties of single sided microstrip counters as fast and high resolution tracking devices have been further improved and extended by the development of *double sided detectors*. For these detectors the strip pattern is made on both faces of the silicon plane. The strips on the two sides can be oriented orthogonally with respect to each other, as indicated in figure 3.1, in order to read out two orthogonal coordinates.

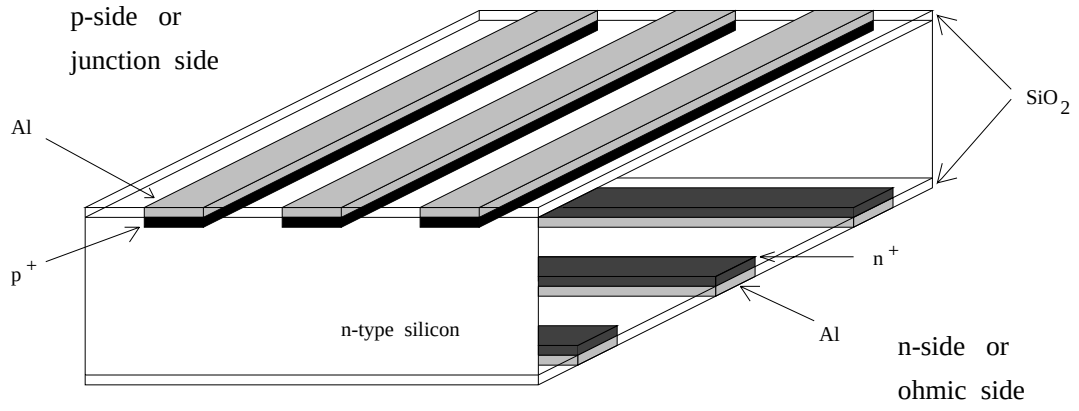

Figure 3.1: Schematic drawing of a double sided silicon strip detector (no isolation structures are shown on the n-side).

Compared to the conventional single sided ones, these detectors have the obvious advantage of measuring two coordinates from one plane and therefore provide a three-dimensional information on the trajectory of traversing particles (at least in the case of single particle hits), without any additional scattering material. Consequently, they are particularly advantageous for use in systems where compactness and minimization of scattering material are important.

In addition, the simultaneous measurement in the same plane of both coordinates allows the reduction of ambiguities in associating hits identified in the silicon planes to tracks

reconstructed by other detectors. In fact, when a particle crosses the detector the amount of charge collected by the strips of one side should be the same as collected by the strips on the opposite side, and this amount varies from particle to particle following a Landau distribution.
If two particles cross the same detector, the height of their pulses differs due to the Landau fluctuations and this difference helps to correlate the signals from the two sides. This idea is schematically shown in figure 3.2. Particles P1 and P2 cross a detector in points 1 and 2 respectively and release charges Q_1 and Q_2 which are seen on the junction side as Q_1^p and Q_2^p and on the ohmic side as Q_1^n and Q_2^n. There are two possibilities: the particles can either have passed points 1 and 2 or points 3 and 4. This ambiguity can be solved by a proper matching with tracks reconstructed by further tracking devices. But double sided detectors offer also the other possibility: associating the largest (smallest) charge on the n-side to the largest (smallest) one on the p-side and determining the correct combination. Consequently real space points can be measured instead of their uncorrelated projections as obtained with single sided counters, solving ambiguities and improving the tracking quality.

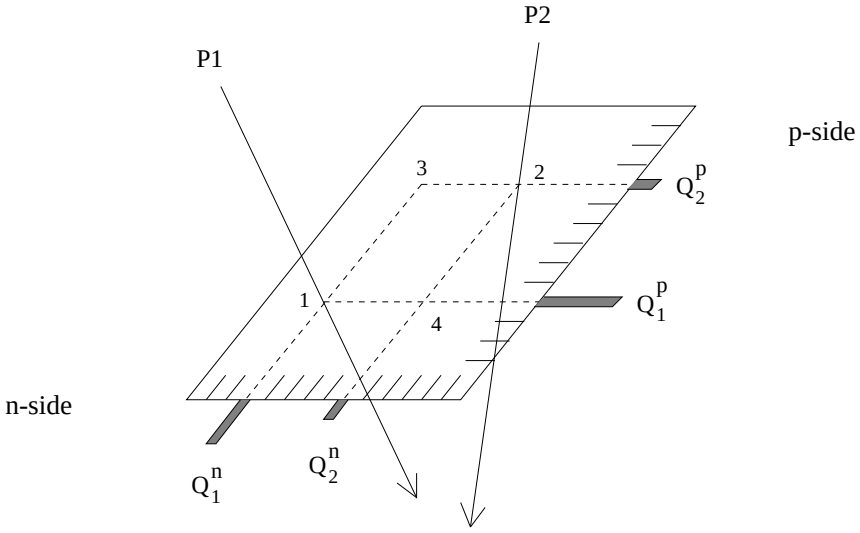

Figure 3.2: Illustration of the ambiguity arising when two particles hit the same detector.

3.2 The problem of separation on the ohmic side

The fabrication of a double sided detector as illustrated in figure 3.1 is not straightforward. If an n-type silicon wafer is used as substrate, on the junction side strips are made by means of p^+ implantation. But the simple attempt to subdivide the ohmic side of the diode (namely to realize n^+ strips on the n-type silicon) would be unsuccessful.
The difficulty is related to the manufacturing procedure used in the conventional planar technique. At the interface between the silicon and the oxide layer formed during the passivation of the crystal, before the n^+ ion implantation, the oxide becomes a site of fixed positive charges. The presence of this positive charge induces an electron accumulation

layer in the n-type silicon substrate, short-circuiting adjacent n^+ strips as shown in figure 3.3. An explanation of the mechanism can be found in reference [1].
The sheet resistivity of the accumulation layer depends heavily on the fabrication process (values ranging from 20 to 50 kΩ/□ have been measured). These electrons cannot be removed by any reasonable bias voltage applied across the wafer.

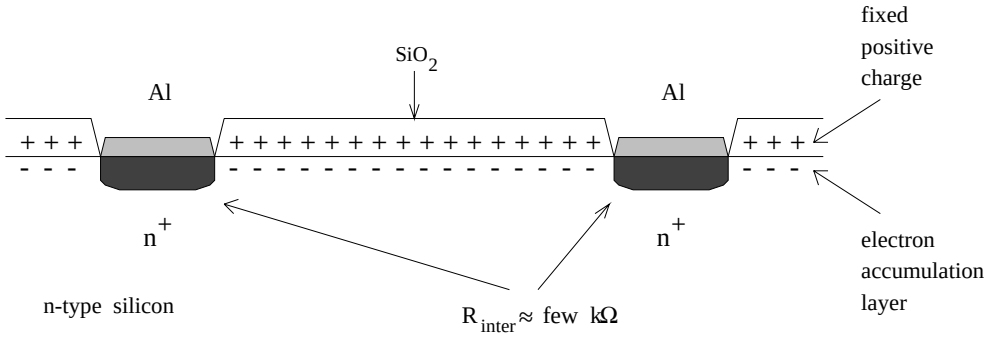

Figure 3.3: The problem of separation on the ohmic side.

This conduction channel decreases the resistance between two adjacent n^+ strips to a few kΩ. In this situation, the charge produced by traversing particles spreads over many strips and this makes any precise position measurement practically impossible.

One possible solution makes use of field plates over the oxide to create a field which repels electrons [2]. This is done using a MOS (Metal-Oxide-Silicon) structure.
If two phosphorus-doped areas in an n-type substrate are separated by an oxide with metal gate, one can control the current flowing between the two contacts with the gate voltage. A negative potential applied to the gate with respect to the substrate creates an electric field in the oxide which leads to a decrease in the conduction electron density. At a sufficiently high negative gate voltage a field induced depletion region is created between the strips and strip separation is achieved.

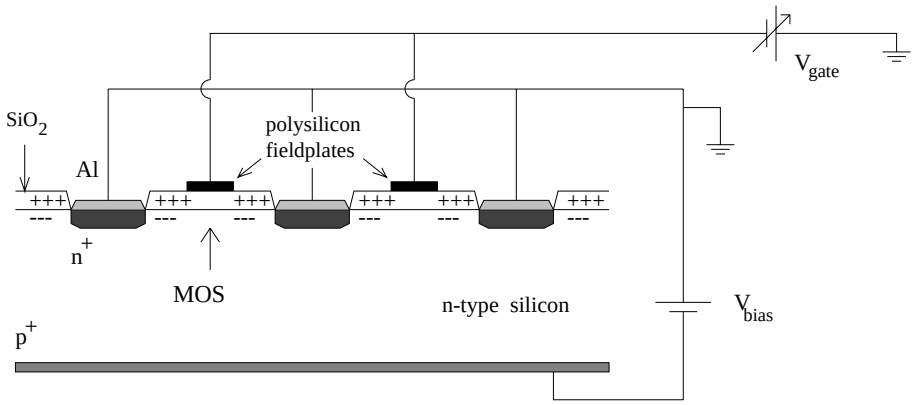

Figure 3.4: Separation on the ohmic side by means of a MOS structure.

The basic model is illustrated in figure 3.4. Separate lines (here made of polysilicon) are processed on the thick oxide between two adjacent n^+ strips and act as fieldplates. They

can be biased independently so that the induced field breaks the conducting accumulation layer.
The same idea can be realized in an even simpler way in the case of detectors with integrated coupling capacitors using the coupling oxide and the aluminium lines which can be biased independently. This solution is shown in figure 3.5.

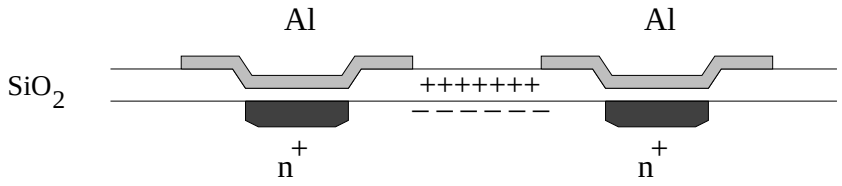

Figure 3.5: Separation on the ohmic side by means of fieldplates in case of an AC coupled detector.

By extending the metal readout lines sideways beyond the n^+ strips, the MOS gate structure is created. Under proper operating conditions, two field-induced junctions are created and they isolate the n^+ implants. Normally the positive bias voltage is applied to the n^+ strips, while ground is kept at the p-side and on the metal readout lines of the ohmic side.
This design has the advantage of requiring no extra masks or processing steps with comparison to the p-side. On the contrary one more implantation step is necessary to produce the polysilicon lines and a separate bias line is needed to provide them with the gate voltage.

A second solution to this problem consists in inserting a p^+ blocking strip between every two n^+ strips [3], as shown in figure 3.6. All p^+ lines (often indicated as “p-stops”) are left floating. When the depletion zone, originating from the junction side, reaches the ohmic side, the p^+ strips charge up to a potential that inhibits the flow of electrons between the n^+ strips. These are then insulated from each other and the interstrip resistance increases up to a value of several MΩ.

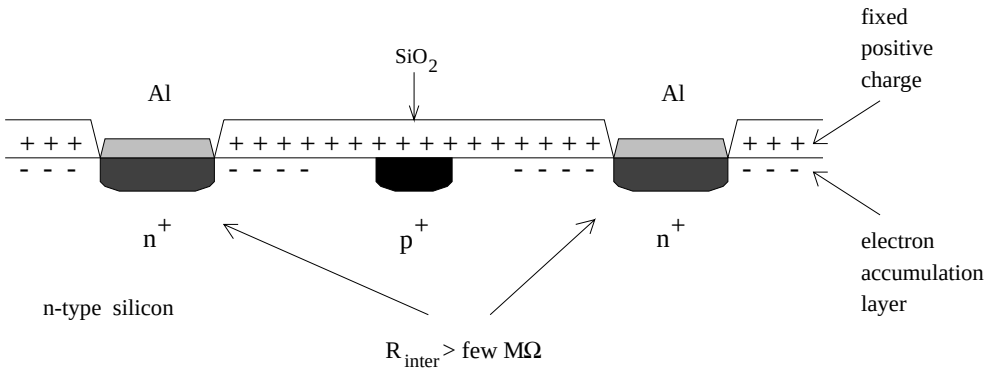

Figure 3.6: Separation on the ohmic side by means of p^+ blocking strips.

3.3 Our CSEM double sided detectors

We decided to make use of double sided counters for part of the Large Angle Silicon Detector (LASD) for the SELEX experiment at Fermilab (this project will be described in detail in the last section of this chapter).
For this application we needed double sided detectors with the largest possible sensitive area and stable operation. Similar counters had already been used in the ALEPH minivertex at LEP, CERN, since 1990. They had been developed by INFN[1] Pisa (Italy) in collaboration with CSEM[2], Neuchatel (Switzerland). A complete description of these detectors and their performance in ALEPH can be found in the references listed from [3] to [12].
Based on the proven and successful technique, the group developed new counters to be installed in ALEPH for the 1995 upgrade. We could have a batch of these latest design detectors. They were manufactured at CSEM, on very high resistivity (≥5 kΩ·cm), n-type silicon wafers.
The detectors have an active area of 52.6x65.4 mm^2. On the junction side p^+ strips are 65.4 mm long and placed at 25 μm distance. On the ohmic side the n^+ strips have 50 μm pitch and are interleaved, at 25 μm pitch, with p^+ blocking strips, used as separation method. All strips have a nominal width of 12 μm. Bonding pads are provided with 50 μm pitch on both sides.
The detectors are DC coupled (the aluminum readout line is in direct contact with the implanted strip). The AC coupling to the electronics is provided by external capacitor chips described in a later section.
Our batch of 24 wafers was processed at CSEM and delivered in February 1995.

3.3.1 The fabrication process

The detectors are based on a well proven and extensively tested design and technology. The fabrication process was developed by INFN Pisa and CSEM.
The starting material consists of 300 μm thick, 4" diameter, n-doped silicon wafers, manufactured by Wacker Chemitronic. They are polished on both sides to allow for double sided processing. The crystal has the <111> orientation.
The process for the junction side is the standard one, while on the ohmic side it is more complex because of the implantation of both p^+ and n^+ structures. A total of eight masks are used, plus an additional passivation step to protect the wafers from contamination and mechanical damage.
Registration marks are etched on the two sides of a wafer (there is only one side-to-side alignment operation at the beginning of the process). Then a thermal oxide layer is grown on the silicon wafer at 900^{o}C. After silicon nitride deposition, the wafers pass several lithography and implantation steps. Doping is performed through the thermal oxide using photoresist patterns as masks. First p^+ implantation is done with boron (at 50 keV with $3x10^{14}$ cm^{-2} flux), then n^+ structures are realized with phosphorus (at 100 keV with $3x10^{15}$ cm^{-2} flux). Annealing of implant damage and dopant activation is performed at 850^{o}C.

[1] Istituto Nazionale di Fisica Nucleare
[2] Centre Suisse d'Électronique et de Microtechnique

A 0.7 μm thick LTO (Low Temperature Oxide) layer is deposited and contacts to the silicon are defined. Then a 1 μm Al layer is deposited and patterned on both sides.

More details concerning the process can be found in references [3], [7], [8] and [9].

The large double sided counter is placed in the central region of the wafer. The remaining surface is occupied by other small strip detectors and test structures. The first purpose of such structures is to help keeping the fabrication process under control and to understand the detailed behaviour of the detector.

CMOS capacitors allow the measurement of the surface doping profiles and fixed charge densities. With 0.1 cm^2 diodes with guard ring the wafer depletion voltage and the bulk generation current can be estimated and studied depending on variable parameters of the process (like annealing temperature and doping concentrations). Interdigitated gate-controlled diodes are used to analyse the surface generation at the depleted Si-SiO_2 interface. Other structures are specific to double sided detectors, to study the separation method used on the ohmic side.

The photograph shows the n-side of one full wafer, with the large double sided microstrip detector surrounded by several test structures.

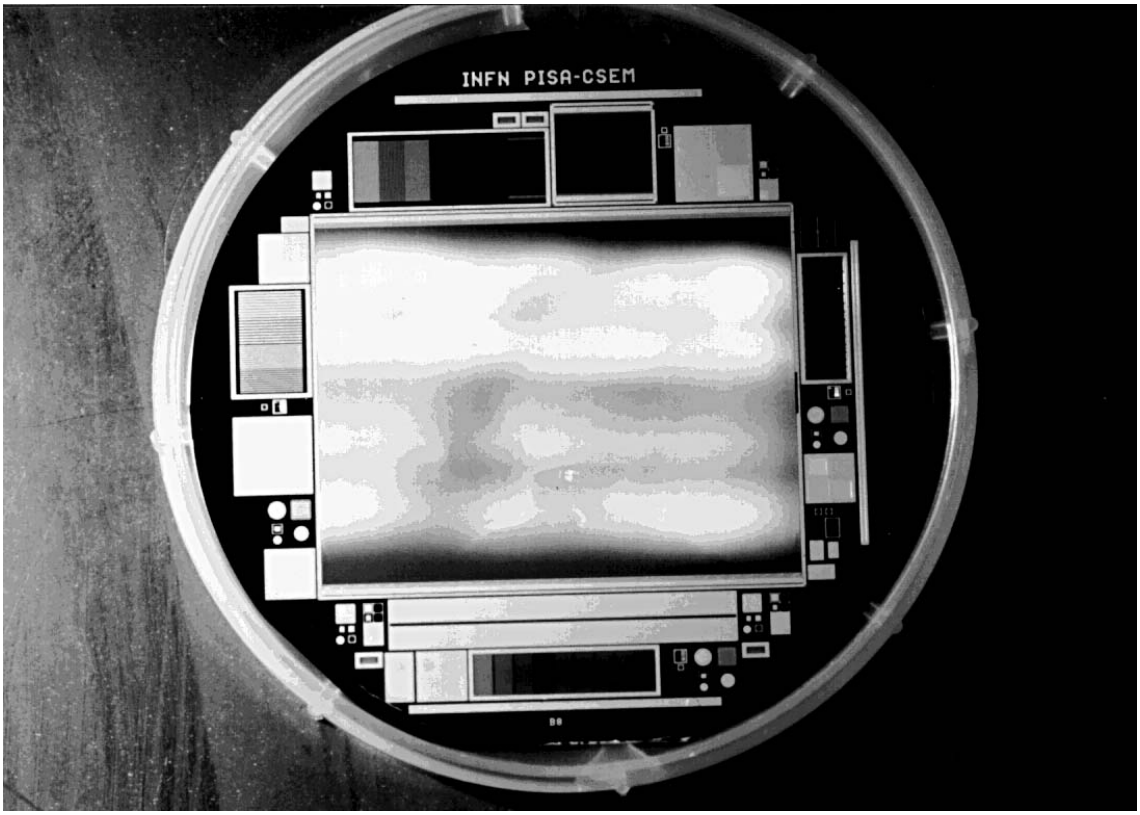

Figure 3.7: Photograph of the n-side of one full CSEM wafer: The double sided microstrip detector is surrounded by several test structures.

3.3.2 Design and bias scheme of the junction side

The junction side of the detectors is schematically shown in picture 3.8. The left part shows a cross section while the right part is a top view of the ending portion of the strips, close to the detector edge.

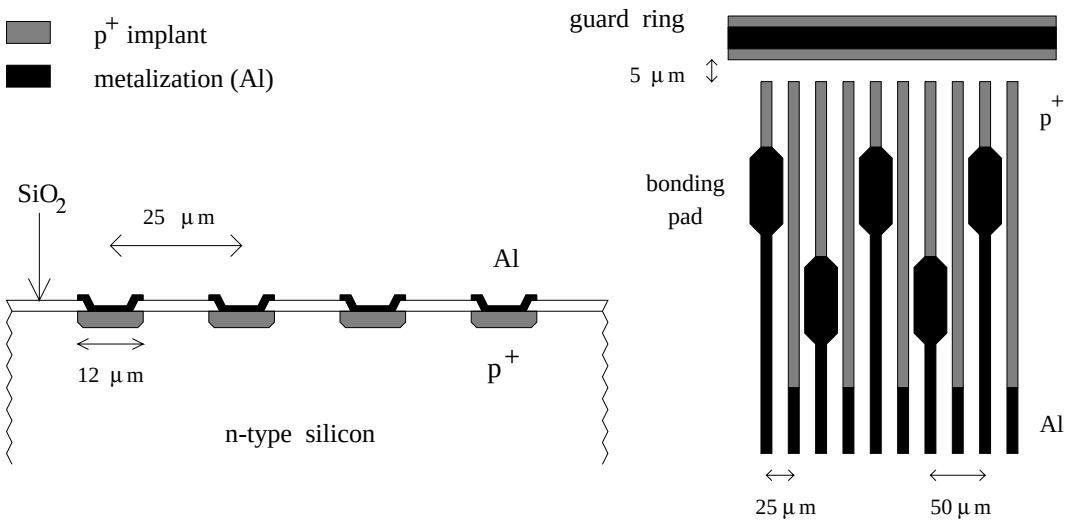

Figure 3.8: Cross section (left) and top view (right) of the junction side of the CSEM double sided detectors.

The strips consist of a p^+ implantation to form a rectifying junction with the n substrate, plus an aluminum contact metallization. They are 65.4 mm long, 12 µm wide and are placed at 25 µm distance. There are in total 2048 p^+ strips.

A bonding pad is provided to every second strip, a 50 µm pitch. Consequently the readout pitch can be any multiple of 50 µm. Hit positions are interpolated by exploiting the capacitive charge division between intermediate floating strips and the nearest readout lines (as explained in the previous chapter).

Since the aluminum is in contact with the implantation, it is possible to perform direct measurements of the electrical properties of each individual diode (such as the leakage current of single strips and the potential level).

All p^+ strips end 5 µm from the inner one of two p^+ guard rings which surround the whole active area. These guard rings have the double function of stopping the component of leakage current coming from edge effects and providing the bias voltage to the diode strips.

The biasing mechanism is based on a punch-through effect between two close p^+ implants [6]. Only the inner guard ring, acting as bias line, is connected to a power supply, while the single strips are left floating and are biased via the common line. The mechanism is illustrated in figure 3.9, where the n-side is kept at ground potential.

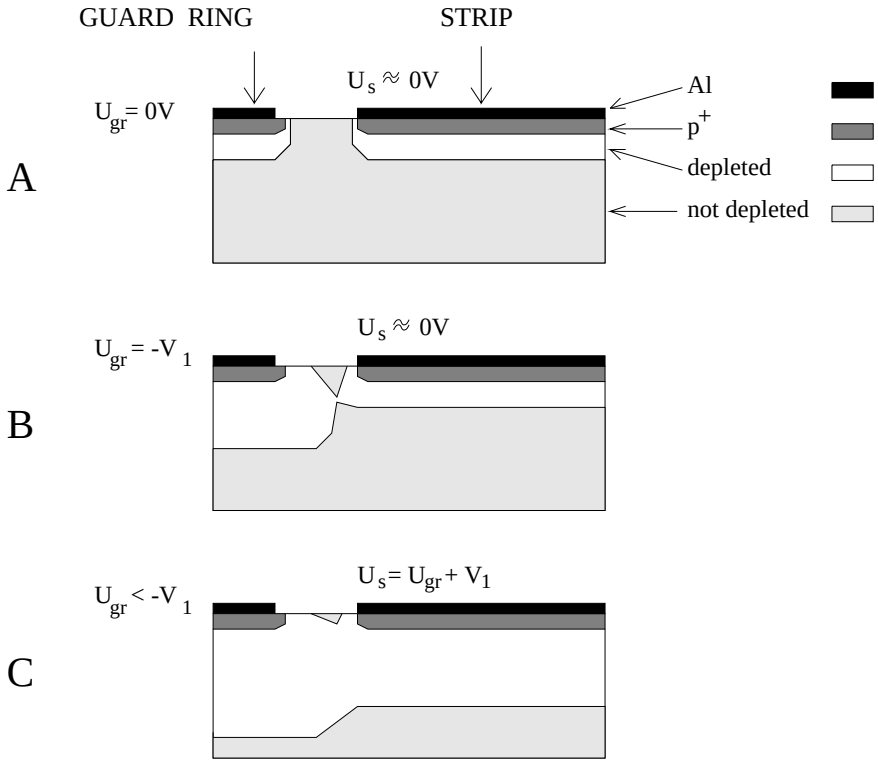

Figure 3.9: Illustration of the punch-through mechanism used to bias the single strips on the junction side. U_{gr} indicates the voltage applied to the guard ring and U_s the potential level of the individual strips.

When no voltage is applied (situation A in the figure) both the guard ring and the single strip are surrounded by a shallow depletion zone caused by the diffusion of the charge carriers. With increasing negative voltage, the depletion zone around the reverse biased guard ring grows. This continues until the two depletion regions touch each other, as shown in situation B. A further increase of the bias voltage will remove positive charges (holes) from the floating strips. This hole transport is a punch-through current. This stops as soon as it has charged up the floating strip high enough to change the potential in the bulk, in such a way that a barrier for the holes is created. While holes are drained from the floating strips to the guard ring, the detector leakage current carries additional holes to the junction side. In steady conditions the punch-through current and the leakage current are equal and the voltage difference (of a few Volts) between guard ring and strips remains almost constant, therefore allowing depletion around the floating strips, as shown in C.

The punch-through acts then as a dynamical resistor whose characteristics are defined by its geometry, in particular the distance of the strips from the guard ring. The equivalent resistance between strips and guard ring is about R = 60-100 $M\Omega/I_{leak}[nA]$. This means something of the order of 200 MΩ for a typical 0.5 nA strip leakage current. The effective interstrip resistance on the junction side is then between 10 and 100 GΩ.

It is important to guarantee that the potential drop between the guard ring and all the strips is constant across the whole detector to avoid field distortions.

3.3.3 Design and bias scheme of the ohmic side

Figure 3.10 shows a cross section and a top view of the ohmic side. The metallized n^+ strips are 12 μm wide and have a pitch of 50 μm. Between every two adjacent n^+ strips, there are 12 μm wide p^+ strips. These are left floating and, when the detector is completely depleted, they interrupt the surface electron accumulation layer and separate the n^+ strips. Each n^+ strip has a bonding pad for connection to preamplifiers. Consequently also in the ohmic side the readout pitch can be any multiple of 50 μm.

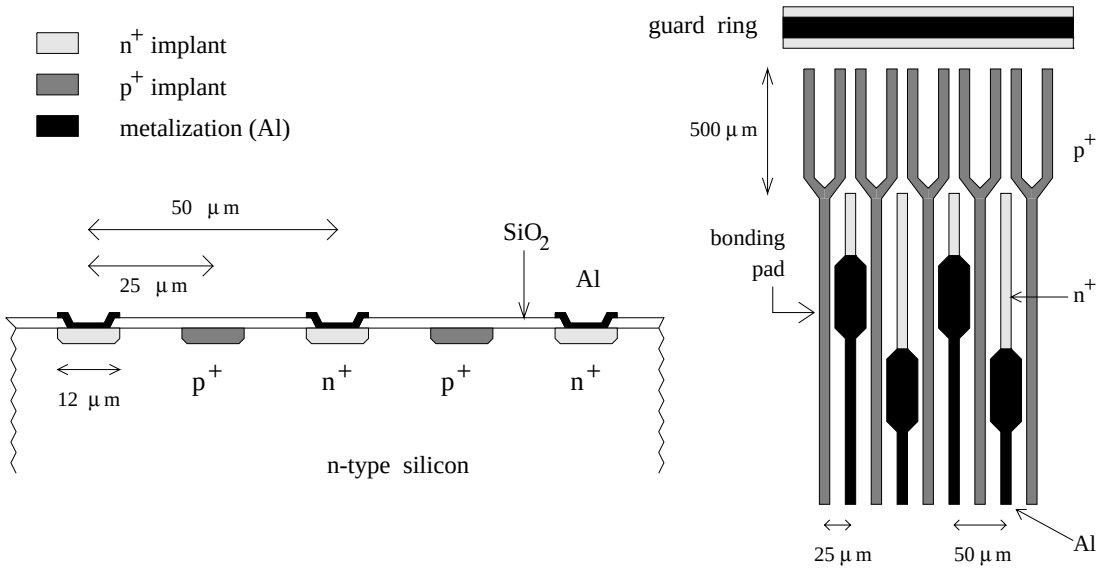

Figure 3.10: Cross section (left) and top view (right) of the ohmic side of the CSEM double sided detectors.

The biasing of the n^+ strips is done via a common n^+ guard ring which surrounds the whole active area. However the principle is totally different with respect to the junction side. Use is made of the electron accumulation layer itself [6].
As shown in picture 3.10 on the right, the p^+ implant is shaped in such a way to form a channel between the end of the n^+ strips and the guard ring. This electronic channel defines an ohmic resistor. The value of the resistor is determined by the channel geometry (its width and its length) and is generally tuned to be equal to a few MΩ when the detector is fully depleted.
The bias voltage is then applied only to the guard ring and is brought to the single strips via the resistors. The channel structure is repeated at both ends of every strip in order to improve the overall homogeneity of the field. The same structure determines also the interstrip resistance, which turns out to be of the order of several GΩ.

3.4 AC coupling

The implementation of the biasing schemes described above allows an AC connection of the strips to the charge amplifiers. In contrast to the detectors described in the previous chapter, the coupling capacitors are not integrated on the counter itself. A hybrid solution was chosen and external capacitor chips were processed on an independent quartz substrate.

The integration of large capacitors on the detectors is certainly a very compact and elegant solution. But, to perform reliably, a more complex and delicate fabrication process must be used. A high quality insulation oxide must be grown on a large area. It must be also very thin (100-200 nm) to provide a sufficiently high coupling capacitance. And the amount of active pinholes must be minimized.

This choice optimizes the detector behaviour and facilitates its assembly. But the higher complexity of the technology brings a decrease of the detector production yield and consequently a rise of the costs.

On the other hand, the use of separate coupling capacitors can prove cost-effective. The yield problems have to be faced independently for detectors and capacitors. The limitations arising from the coupling oxide are transferred to the much smaller and relatively less expensive chip.

Of course, using separate capacitors doubles the number of needed bonds. In our case this was not a critical problem because of the limited size of the project (we had a total of about 16000 channels from double sided detectors), but this can be inconvenient for devices of larger scale.

The capacitor chips were also produced by CSEM [9, 10]. Each chip (13 mm long, 6.425 mm wide and 0.52 mm thick) contains 128 capacitors with effective 50 μm pitch. Every single channel is connected on one end to one strip of the detector and on the other to the input of the charge amplifiers. The capacitors are made with a double polysilicon layer, interleaved with a dielectric, as shown in figure 3.11 on the left.

The measured capacitance is approximately 200 pF; the stray capacitance of single channels is about 0.3 pF (this value is so small thanks to the use of quartz as substrate). The parallel insulation resistance is larger than 100 GΩ and the breakdown voltage is about 8-12 V.

In order to protect the capacitors from accidental high-voltage transients, they are equipped with protective Zener diodes against capacitor breakdown. This is illustrated in figure 3.11 on the right. The leakage current of the polysilicon diodes is sufficiently low and does not appreciably contribute to the noise. The diodes provide also a good protection against electrostatic discharges during the later parts of their fabrication process (chip dicing and handling), thus allowing a higher yield.

We got 6 wafers from a batch of capacitor chips produced by CSEM in 1994. Each wafer contains 68 chips. All chips were tested individually at CSEM and only those with 100% good capacitors were used. For our batch the yield was lower than usual: we had only 150 chips with no defects out of 408 (a yield of 37% versus the usual 50%).

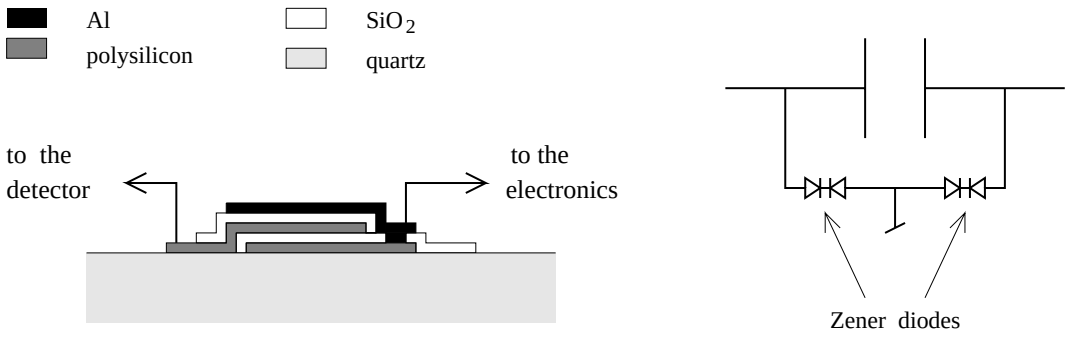

Figure 3.11: Schematic cross section (left) of a capacitor channel in the external chip on quartz substrate.

3.5 Measurement of the detector quality

As in the case of the single sided microstrip counters, systematic and detailed static electric measurements have been performed on the double sided detectors.

In this case the tests were even more crucial for the selection of the counters later used for the construction of LASD. In fact, in a contract such as we had with CSEM, the producer and the customer share the risk: no specifications are fixed, the producer delivers one full batch of detectors without any preliminary test, at a fixed price, and the customer has to perform fully the selection. There is no guarantee on the production yield but the price per detector can be significantly lower than in the other type of contract. In addition the agreement was rather safe in our case, as the detector design was based on a well proven technology.

We received 24 full wafers, not yet cut. On the base of first basic tests (behaviour of the leakage current and value of the depletion voltage), the 10 best counters were chosen. On those all other measurements were performed in a very detailed way in order to select the 7 highest quality detectors. These were brought back to the producer for cutting. Afterwards their leakage current was measured once again (to be sure that the cutting procedure did not affect the detector quality) and finally the counters were ready for mounting on the ceramic boards. The measurements performed and the obtained results will be described in the following sections.

The handling of double sided detectors is even more delicate than for the single sided, since there are structures on both sides of the silicon layer and mechanical damage must be avoided. We used a special jig to fix the counter during the measurements. The full wafer was placed on a circular teflon structure on a metal support. The contacts to the side under measurement were realized as in the case of the single sided detectors, at the probe station. The biasing line on the other side of the counter was reached by a single needle also fixed to the support. Biasing the detector using the proper connections is an essential condition to perform correct and sensible measurements.

3.5.1 The leakage current

The total leakage current of all 24 detectors was measured and used as a criterion to select the best wafers. The IV curve was recorded in order to study the leakage current behaviour. A typical curve is shown in figure 3.12. The measurement was performed applying an increasing positive voltage to the n-side bias line and collecting the current generated in the active area from the inner guard ring on the p-side kept at ground potential.

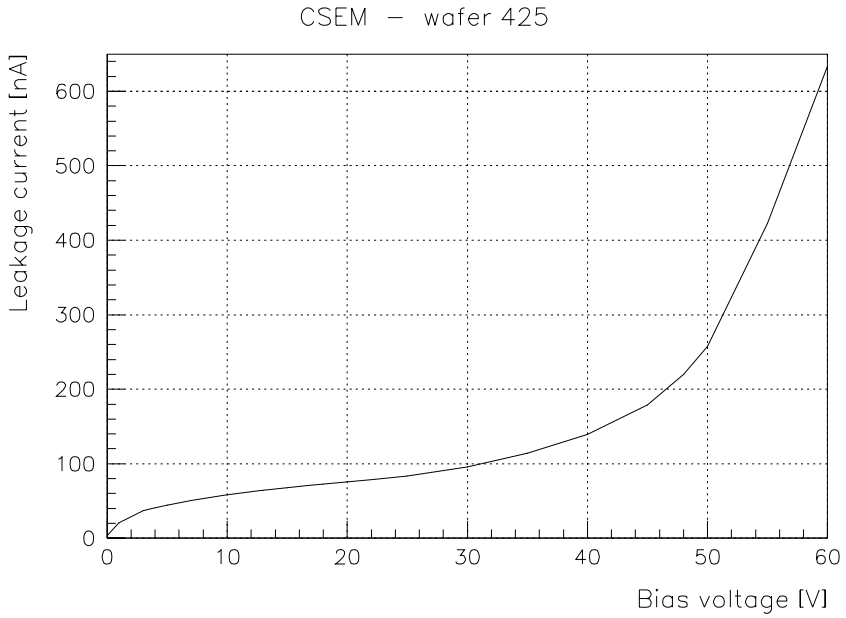

Figure 3.12: IV curve: dependence on the applied bias voltage of the current collected by the inner guard ring on the junction side.

The current level at depletion voltage (about 20 V for this detector, as shown in the next section) is very low. The increase of current which happens above depletion voltage is generally due to surface contributions from the back side of the counter.

The distribution of the current measured at 50 V for 21 detectors is shown in figure 3.13. The remaining 3 counters had an extremely high leakage current at low voltage and were immediately excluded from further tests. The mean current level for all 21 counters was 2.8 μA, corresponding to approximately 81 nA/cm^2, 2.7 nA/strip on the p-side and 2.2 nA/strip on the n-side (only readout strips are considered). These values already indicated good control of the production process and good quality detectors.
For further tests we selected the 10 detectors with lower current, below 1 μA. For these 10 counters the average value of the current was 0.5 μA, corresponding to approximately 15 nA/cm^2, 0.5 nA/strip on the p-side and 0.4 nA/strip on the n-side.
The stability in time of the current flowing in the junction was checked for a few counters over several hours (detectors showing instabilities or a large increase of current would have been rejected). Normally the behaviour was very stable, sometimes reaching constant levels after an initial drift to lower values.

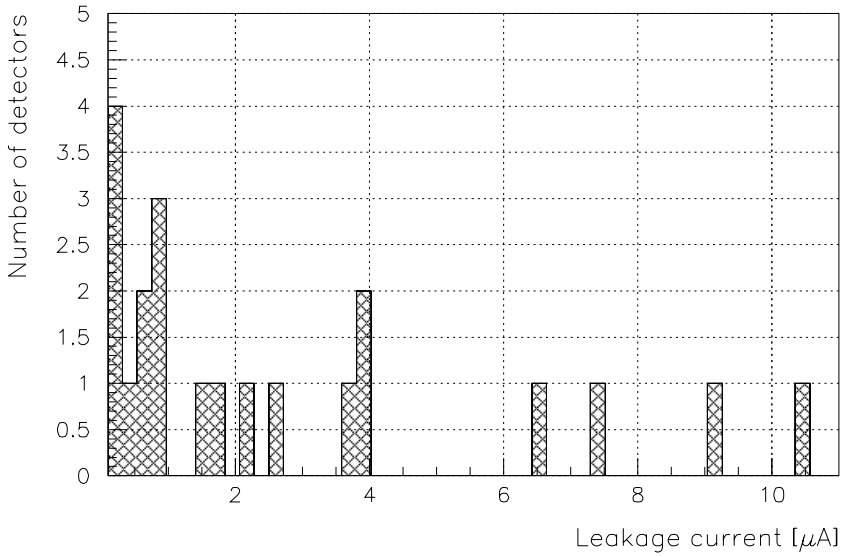

Figure 3.13: Distribution of the leakage current from the active area measured at 50 V for the 21 working detectors.

3.5.2 Depletion voltage

For all wafers the CV curve was recorded in order to determine the depletion voltage of the detectors and estimate the silicon resistivity.
Having the whole wafer available, we could measure the CV curve both on the full detector and on simple diodes included in the test structures. In particular we used a round diode with guard ring, with 0.1 cm^2 area. A relatively large surface diode approximates the shape of a parallel plate capacitor much better than the microstrip detector, especially in the case of double sided. Consequently the measurement of the bulk capacitance shows a more regular dependence on the applied bias voltage.
Figure 3.14 shows the behaviour of C (on top) and $1/C^2$ (on bottom) for the full microstrip counter (on the left) and for the diode (on the right). The diode curves allow a very precise determination of the depletion voltage of the wafer under study (approximately 22 V in this case). For all 21 measured detectors the value of depletion voltage was between 15 and 45 V. This result shows that also in this case silicon wafers with very high resistivity (6-20 kΩ·cm) were used.

With this measurement we confirmed the correct operation of the 10 detectors showing lower leakage currents. Consequently these were chosen for all the following detailed tests to select the 7 detectors needed for installation.

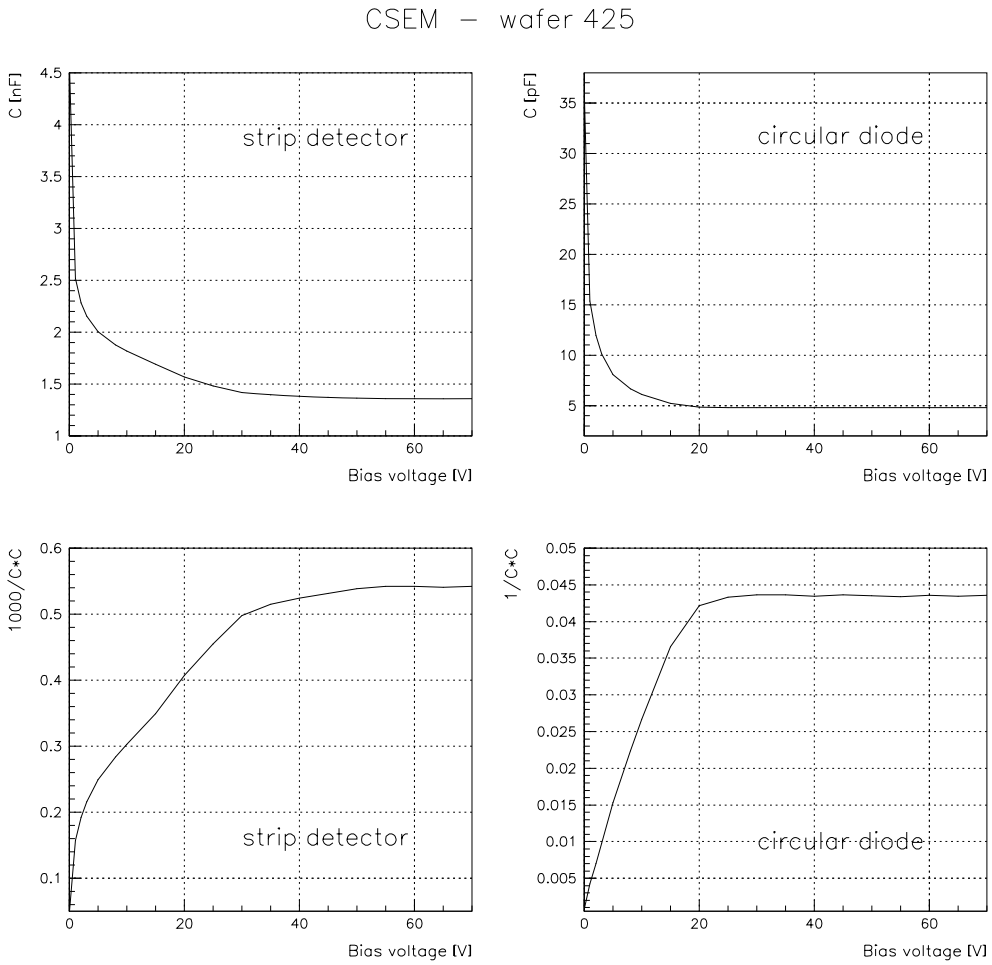

Figure 3.14: CV curve: dependence of C (top) and $1/C^2$ (bottom) on the applied voltage for the full microstrip detector (left) and for the circular diode included in the test structures on the same wafer (right).

3.5.3 Potential drop at the p^+ strips

As described in paragraph 3.3.2, the strips on the junction side are biased via a punch-through mechanism. This brings the individual strips to a potential level slightly higher than the one at the bias line, depending on the geometry of the channel.

In order to check if the mechanism was properly working and if the potential level at the strip was uniform throughout the whole counter (to guarantee uniformity of the field in the silicon bulk), the potential drop has been measured on few strips for the 10 selected detectors.

To perform this measurement, an increasing positive voltage was applied to the n-side of the counter, the inner guard ring of the p-side was kept at ground and the potential level of single strips was recorded with the HP Semiconductor Parameter Analyzer.

An example of the measured curve is shown in figure 3.15 for one strip of the detector on wafer 425.

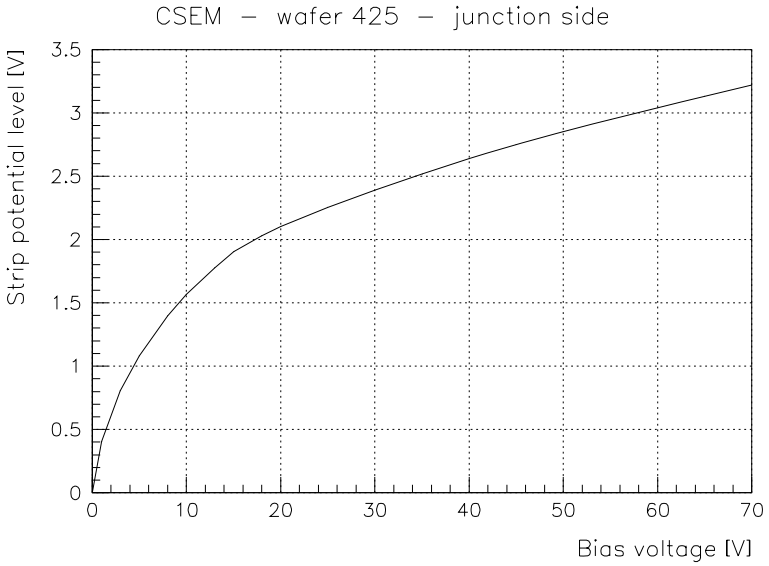

Figure 3.15: Dependence of the potential level measured at one individual strip on the junction side on the applied bias voltage, as an effect of the punch-through biasing mechanism.

The potential difference between the inner guard ring and the individual strips was measured to be between 2.5 and 4 V for the 10 detectors tested. The value was always uniform within each counter. Systematic variations from one edge to the opposite one never exceeded a few percent.

3.5.4 Interstrip resistance on the p-side

The resistance between adjacent strips on the junction side was measured in the same way as for the single sided detectors. From the dependence of the induced current on a variable voltage difference applied between one strip and its two neighbours, we estimated the interstrip resistance to be higher than several tens of GΩ.
Also in this case few groups of strips were measured by random sampling in different regions of the counters to check the uniformity of the resistance value. The result was satisfactory showing a resistance value constant at the percent level.

3.5.5 Interstrip capacitance on the p-side

The interstrip capacitance measurement was also performed as described in the previous chapter. For 50 μm readout pitch, the measured value was 8.5 pF, corresponding to 1.3 pF/cm relative to the strip length.
This result is in good agreement with the one obtained in the case of the single sided detectors for the same readout pitch. The higher value corresponds to the slightly larger width of the strips in the double sided counters.

3.5.6 Bias resistance on the n-side

The strips of the ohmic side are biased via an electronic channel as described in section 3.3.3. The value of the effective resistance can be measured similarly as for the polysilicon resistors of the single sided detectors.
In addition, this measurement provides an important tool to check the separation mechanism on the n-side when the dependence of the resistance value on the bias voltage is studied. For low values of the reverse bias applied across the junction, the depleted region extends from the junction side towards the ohmic side but does not reach it. Consequently the electron accumulation layer placed under the Si-SiO_2 interface is still present connecting the n^+ strips to each other and to the guard ring. In that condition the resistance measured between the guard ring and a single strip (and also between adjacent strips, as we will see in the next section) is only a few kΩ. When the reverse bias reaches a value high enough to fully deplete the junction, the p^+ stops interrupt the electron layer and the resistor values increase to the operational value.

An example of the dependence of the bias resistance value on the voltage applied across the junction is shown in figure 3.16. At a given voltage a disturbance ΔV (±250 mV) is applied to one strip with respect to the guard ring and the resulting current is measured. From the slope of this IV curve the evaluation of the bias resistance can be obtained. The measurement is repeated at increasing reverse voltage.

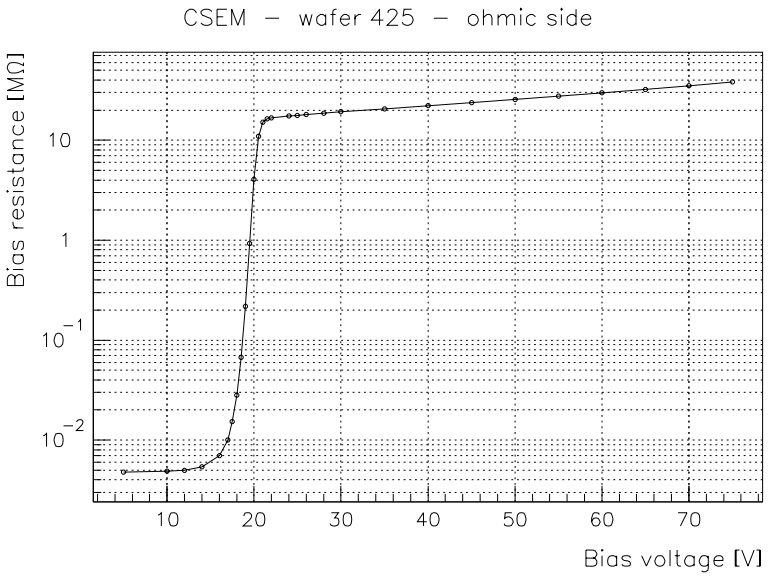

Figure 3.16: Dependence of the n-side bias resistor value on the applied bias voltage. The sharp increase around 20 V indicates the point at which the full separation on the ohmic side is effectively reached.

From this measurement and the one described in the following section we obtain the best evaluation of the recommended operational voltage of the double sided detectors. The average value of bias resistance was measured to be between 15 and 30 MΩ for all tested detectors.

3.5.7 Interstrip resistance on the n-side

The dependence of the interstrip resistance on the applied bias voltage reflects the effect described in the previous section. This is probably the most relevant measurement to verify the working conditions of the ohmic side and to decide if the detector can be used for precise position determinations.

Figure 3.17 shows the dependence of the resistance on the reverse bias. A voltage difference varying between -250 mV and +250 mV is applied between one n^+ strip and its two neighbours. The induced current is recorded and the resistor value calculated. The measurement was repeated at different bias voltages. One can see the sharp rise of the resistance from few kΩ to several tens of GΩ when full separation is reached.

This behaviour was equally reproduced in the other counters. Normally defects (strips not well separated) were limited to less than 1% of the lines. Only for one of the 10 chosen detectors we found a larger region with lower resistance values. This counter was discarded from the selection.

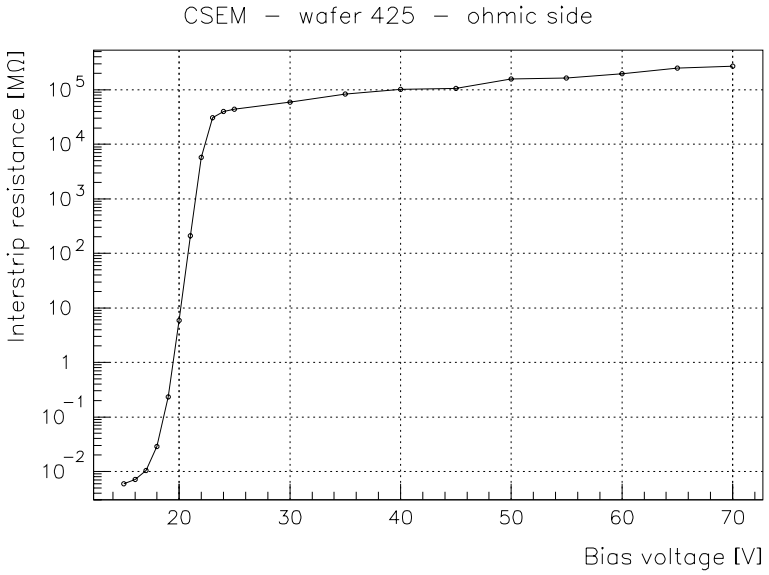

Figure 3.17: Dependence of the n-side interstrip resistance on the applied bias voltage. As in the previous figure, the sharp increase around 20 V indicates the point at which the full separation on the ohmic side is effectively reached.

3.5.8 Interstrip capacitance on the n-side

The value of the interstrip capacitance on the ohmic side is also depending on the bias voltage and reaches a constant minimum only when full separation is realized. For lower voltages the electron layer which is still present reduces the effective distance of diffusion lines and significantly increases the capacitance value. The total capacitance was estimated to be approximately 13.7 pF, corresponding to 2.6 pF/cm at 50 μm readout pitch.

Summary

The measurements performed allowed the selection of the 9 best detectors and the study of their operation. Seven of them were then cut and mounted with the readout electronics, for use in SELEX. Six were later installed at Fermilab and one is kept as spare.
We can estimate an overall production yield of approximately 70%, in agreement with the results reported by the ALEPH group on a larger number of counters produced in several years.

3.6 Mounting procedure

In order to connect the two sides of the microstrip detectors to the readout electronics, we decided to make use of two independent ceramic boards instead of a more complex double sided hybrid.
The 600 μm thick Al_2O_3 boards carry the capacitor chips, the SVX readout chips, individual voltage regulators for the SVXs, surface mounted components and all communication lines between the readout chips and the external electronics boards. Capton cables are used for the connection to the main boards.
Each detector is equipped with one *p-side board* carrying 8 chips to read out the 1024 p^+ strips on the junction side and one *n-side board* with 10 chips for the 1280 n^+ strips on the ohmic side. The readout chips are located on two orthogonal edges of the detectors.

The mounting procedure was particularly delicate. A top view of the boards, the detector and the intermediate ceramic spacers is shown in figure 3.18. The detector lies between the two ceramic boards and the whole is fixed by the additional spacers. The greatest care had to be taken in order to develop a safe mounting procedure without risk to break the thin silicon layer.

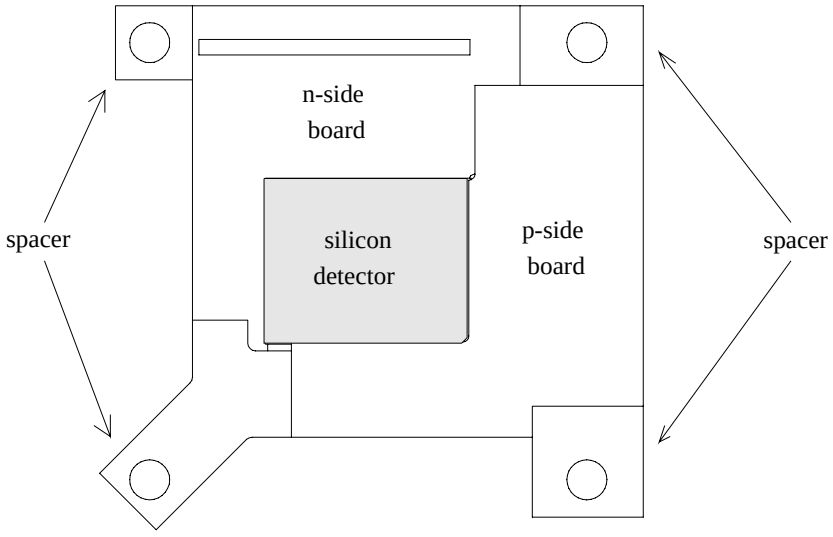

Figure 3.18: Top view of the two ceramic boards, the silicon detector and the spacers used to mount the double sided counters [13].

First we checked the flatness of all ceramic boards. This is unfortunately not optimal as the process for the printed circuit involves high temperature steps and the deposited thick film, while cooling, tend to bend the ceramics. The effect was reduced by also depositing a few layers on the back side of the boards.
The detectors were cut 1 mm larger on all four sides with respect to the normal scribe line, in order to guarantee a bigger surface for gluing the silicon to the ceramics. This additional dead area around the sensitive region of the counter does not represent a serious problem for the geometry of fixed target experiments. Longer bonds are required between the pads on the capacitor chips and the pads of the microstrips. This was the reason for a relatively high number of bonding failures, which nevertheless affected less than 1% of the lines.
The silicon detectors are (300±20) μm thick. In order to limit the stress applied directly on the silicon, the gap between two boards was fixed to about 630 μm by the ceramic spacers. The remaining distance was filled with glue. The spacers precisely glued to the boards are the ones which finally keep the whole structure fixed.

We made use of a special structure with a high precision 3D moving table together with metal jigs designed for the purpose. For every detector we proceeded as follows.
The n-side board, already equipped with three spacers, was placed on a metal support and held by vacuum. The silicon detector was fixed on a chuck covered with teflon, mounted on the movable part of the structure. Then it was moved close to the board, precisely aligned with respect to the board edge and the capacitors chips with the help of a microscope, and glued to the ceramics. The n-side board and the detector, held by vacuum, were left for one hour in an oven to make the glue harden, and then fixed again to the main structure. At this point the p-side board was placed on the movable chuck and precisely aligned with respect to the detector using the microscope. Finally the second board and the last spacer were glued to the silicon and the whole device was placed in the oven.

The extensive care taken to develop this procedure and test it with dummy glass layers, to design and produce the high precision mechanical tools allowed us to safely mount all seven detectors without any damage or accident.

3.7 The readout electronics

The silicon counters are biased applying a positive voltage to the n^+ strips and the ground level to the p^+ strips, via the respective guard ring. The readout lines are then connected to the coupling capacitors located on the external chips. These capacitors can withstand only very small voltage differences. Therefore we were forced to keep the readout electronics of the two sides at different potential levels, floating with respect to each other.
This circumstance has a crucial importance for the operation of our detectors, particularly with respect to the use of sparsification. Having the two electronics floating and at the same time coupled via the silicon detector makes the system extremely sensitive to any external noise source. Furthermore, if standard power supplies are used, the potential levels of the two sides are not stable enough for an optimal operation in sparse mode. In fact, any potential variation induces an effective shift of the threshold levels and this causes a serious degradation of the performance and a drop of efficiency.

The problem could be cured if the detectors were read out completely, without zero suppression. Collecting the pedestal value of all channels for all events provides the possibility to compute offline common mode shifts, correct for them, and extract the hit information without any degradation. But as already explained before, this readout mode is not practical in a fixed target experiment. Consequently we had to find a way to improve the biasing system and to protect the device from external noise.

The study of the problem required several steps before an acceptable solution was reached. Proper shielding and grounding of the device containing one detector with its readout electronics, together with a 0.5 mF capacitor placed in parallel with the silicon detector between the two electronics boards already brought the noise to an acceptable level. During tests performed in the lab and at test beam facilities the noise level was approximately 5-8 ADC counts. However such a noise level still limits the position resolution of the counters and lowers their detection efficiency.
Efforts were then made to improve the power supply system. Initially the bias for the electronics was provided by low noise standard power supplies connected to the normal net. All efforts to shield every connection, to filter possible noise from the net itself and to use higher quality supplies did not substantially change the situation.
The real solution consisted of replacing the power supplies of the n-side electronics with batteries, as shown in figure 3.19. Batteries are the cleanest power source and allowed us to remove the connection to the net on one side of the device.

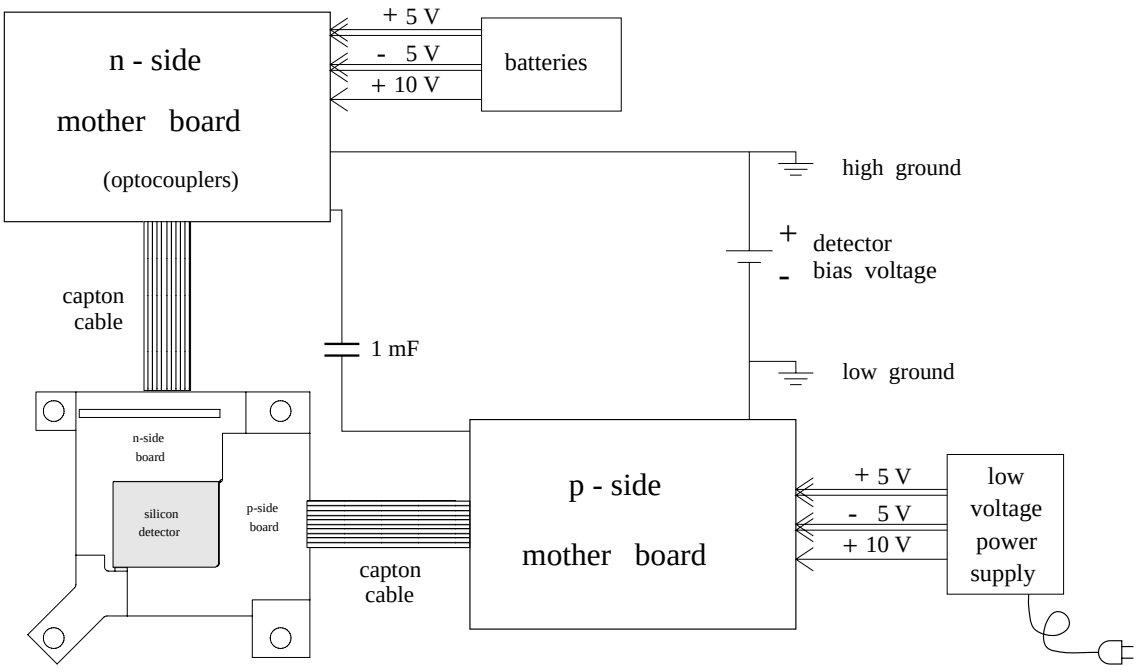

Figure 3.19: Schematic view of the power connections for the double sided readout electronics.

Due to the relatively high current necessary to operate the readout electronics (about 1 A), batteries have to be regularly recharged. Every board can be connected to two independent battery sets by a switching device and the batteries can be reloaded in turn.
With the implementation of this supply system the noise level was reduced to approximately 2-4 ADC counts on both sides of the detectors. Generally the noise on the n-side is slightly higher than on the p-side due to the larger value of the load capacitance.

Figure 3.20 shows the pedestal level (top) and the noise profile (bottom) on the p-side (left) and on the n-side (right) of a double sided detector measured in the lab. In this case the Al_2O_3 boards were connected to external electronics mother boards equivalent to the ones used in WA89.
The slight noise increase visible on the n-side at high channel numbers was simply due to inadequate shielding used in the lab. The effect was not seen at the test beam facilities.

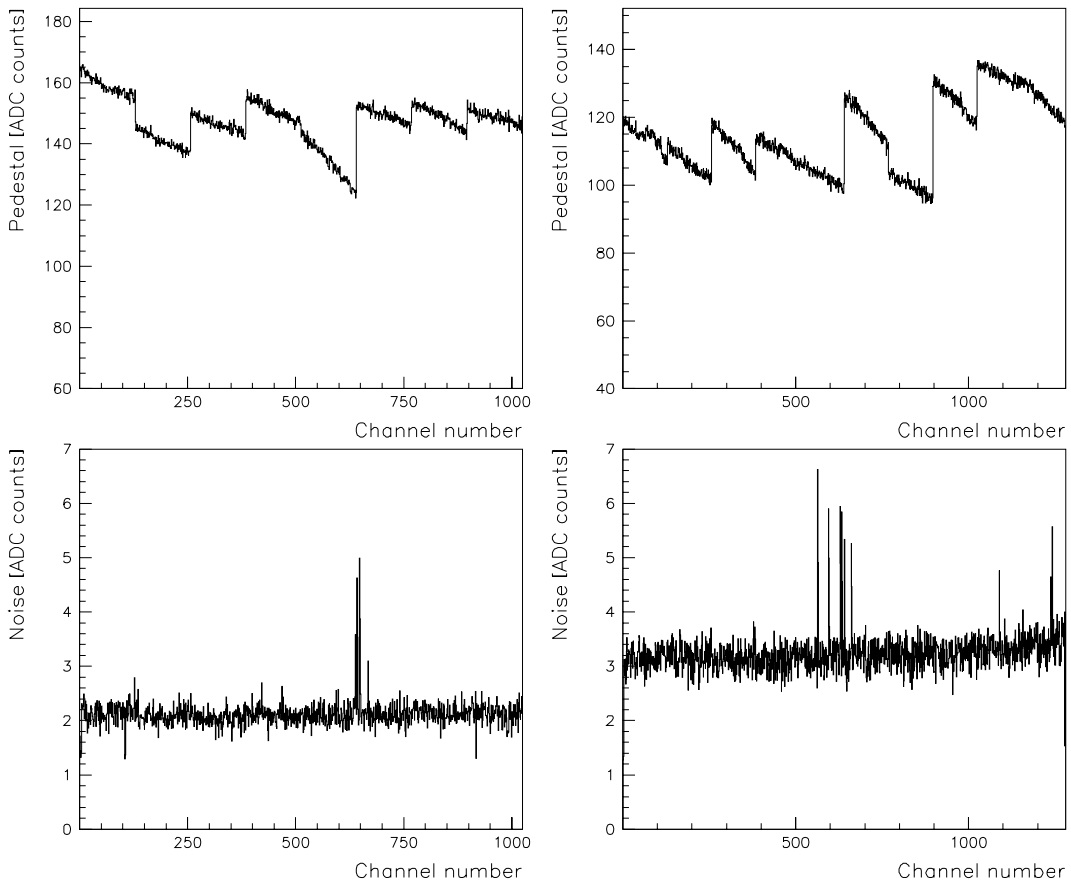

Figure 3.20: Pedestal level (top) and noise profile (bottom) on the p-side (left) and on the n-side (right) of a double sided detector tested in the lab with WA89-type electronics.

The main electronics boards had to be adapted for the readout of the double sided counters. In particular for the n-side, optocouplers were needed in order to decouple all voltage levels, digital and analog data, and all control signals from the high potential level. These

devices introduce about 25-30 nsec delay in the data transfer. This delay does not pose a problem in the synchronisation of the readout.
Two different kinds of electronics boards were developed. The first type was a modification of the design used in WA89 in order to be able to readout the new detectors in the setup at CERN. A second type was developed to make our detectors compatible with the SELEX readout system at Fermilab. This will be briefly illustrated in the last section of this chapter.
Both systems could be used and tested during all the studies performed at CERN, in the lab and at the test beams.

It should be stressed that this was the first example of double sided detectors operated in sparse mode to be integrated in a high energy physics experiment. No similar device was developed and operated in particle beams before.

3.8 Test beam results

The described detectors were tested using high energy particle beams at CERN on three occasions, one in October, 1994, one in May, 1995, and the last one in November-December, 1995. High energy electrons and pions from the SPS (in the first two cases) and from the PS (in the last case) were used.
The main aim was to verify the behaviour of the double sided detectors in an experimental area, check their stability, evaluate their efficiencies and position resolution, check the charge partition on the ohmic side and the charge correlation between the two faces.
A schematic view of the test beam setup is shown in figure 3.21.

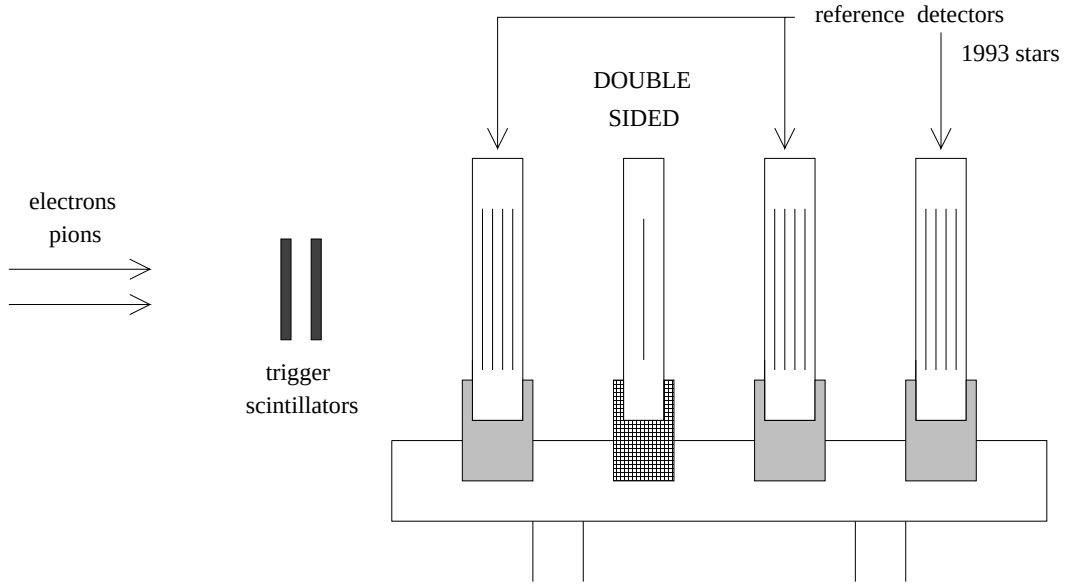

Figure 3.21: Schematic view of the test beam setup, with the 1993 WA89 stars used as reference detectors and the double sided counter under study.

The trigger was given by the coincidence between two plastic scintillators placed in front of all detectors.
Beam tracks were reconstructed by a telescope formed by the three stars installed in WA89 in 1993. As described in the previous chapter, they consist of 12 microstrip planes with 25 μm readout pitch. They were fixed and aligned on a precision bench.
They measure three points for each of the four projections y, z, and $\pm 45^o$. With this information space tracks were reconstructed with high precision using very strict criteria. For example, in order to study the behaviour of the double sided detector, we could restrict ourselves to tracks having a hit in all 12 reference planes. Normally 6 planes were required.
The double sided detector was placed between the first and the second star, and fixed and aligned on the bench. The p^+ strips were measuring the vertical coordinate of traversing particles, while the n^+ strips measured the horizontal one.
In total three different double sided have been tested in the beam. Because of the uniform behaviour they showed, consistent with the lab tests, we did not install in the area the other four detectors.

During the test beam periods we extensively studied the overall behaviour of the double sided counters. We could monitor the leakage current of the detectors over long operation periods, the stability of the calibration of the readout electronics and we could make systematic tests to reduce the noise on the detectors and to improve their shielding.
In winter, 1995, the double sided counters were fully read out with the SELEX type electronics (described in the following section) while in the previous tests the standard WA89 readout chain was used.

The collected data were first used during the test beam period itself to verify the correct operation of the whole setup and the quality of the applied calibration. Later on they were used for an accurate study of the detector performance and for the determination of the most important parameters such as efficiencies and resolution.
The best data have been collected during the last test beam, when the noise of the detectors had been minimized by the use of batteries for the n-side electronics. A detailed analysis of those data is being performed and will be thoroughly described in [14]. I report here only some preliminary results. More details will be given in the reference mentioned above.

Pedestal levels and noise profiles were regularly monitored and stored. They provide the first check of the stability of operation of the detectors. Even though the use of batteries significantly reduced the noise, we could still see occasional jumps of the pedestal level. This effect was further reduced by proper shielding of the detector box and of cables, but not completely eliminated. This can be a source of inefficiency, but less than 1%.
Using a random trigger from a gate generator we stored events which are not correlated to the beam particles and consequently are supposed to contain only noise hits. The detectors were calibrated so that individual strips should show noise hits in only 0.1% of the cases. Strips firing in more than 5% of the cases were not considered to be reliable and were always suppressed.

Tracks reconstructed by the telescope were used to predict the impact point on the double sided detector under study. With this information we could estimate its detection efficiency

during the whole test beam period.
The measured efficiency strongly depended on the noise level of the detector. During the first test beam in 1994, with a noise of about 6-8 ADC counts, we reached efficiencies of only 92-94%. In the last tests the situation was optimized and we obtained much higher efficiencies. One example is shown in table 3.1 where the results from one run taken in autumn, 1995 are shown. In this case space tracks were reconstructed using hits in the y and z reference planes and were used to calculate efficiencies of the other single sided detectors (s and t projections) and of the double sided.

Detector number	Detector type	Projection	Efficiency
17	single sided	s	99.62±0.09
18	single sided	t	99.55±0.10
25	single sided	s	99.95±0.03
26	single sided	t	99.77±0.07
29	single sided	s	99.98±0.02
30	single sided	t	99.53±0.10
5	double sided: p-side	z	97.91±0.22
6	double sided: n-side	y	98.44±0.19

Table 3.1: Efficiencies of the single sided detectors measuring the s and t coordinate and of the double sided counter installed at the test beam in autumn 1995.

The numbers listed in the table show once again the excellent quality of our single sided counters and the extremely good results finally obtained with the double sided. One has to remember that the advantages offered by the double sided counters correspond to a much more complex device to operate. Especially in our case, reading out the detectors in sparse mode, reaching a comparable performance of single sided and double sided is indeed a success.

The cluster size distribution is very similar on the p- and the n-side of the detectors, indicating the correct operation of the separation mechanism for the ohmic side. If strip separation were not fully achieved, the interstrip resistance would still be lower than needed and the charge would spread over several strips: The fact that the cluster size is comparable on the two sides of the counters indicates good ohmic separation.

All tests were repeated using a pattern with one integration window (see paragraph 2.4.1). The noise profile and the efficiencies measured are completely compatible with the results shown above for two integration readout.

The detailed description of the program used to perform the analysis of the test beam data and more extensive results will be available in reference [14].

3.9 The application: SELEX at Fermilab

As already mentioned earlier in this chapter, the described detectors were prepared for the SELEX experiment at Fermilab. SELEX (Segmented Large-X Baryon Spectrometer) or E781 is a fixed target experiment with a high intensity hadron beam at the Fermi National Accelerator Laboratory [15].
The experiment uses a well-identified beam of pions, protons and hyperons to collect a large sample of charmed hadrons, especially baryons, to study their production and decay properties. The first beam particles were seen in E781 in June, 1996. The data taking period will extend for at least 14 months in 1996 and 1997.
The beam has a mean energy of about 650 GeV and the channel is able to provide both a negative and a positive particle beam of approximately $2 \cdot 10^6$ ptc/sec.
The experiment incorporates a "topological" charm trigger based on the reconstruction of high momentum tracks from the downstream spectrometer extrapolated into the silicon vertex detector. The software trigger looks for events with a miss-distance between the reconstructed beam track and at least one of the high momentum tracks.
SELEX aims at collecting 10^6 reconstructed charm events, half of which of charmed baryons.

The main physics goals of E781 can be summarized as follows:

- Study of the weak decay characteristics of charmed baryons, with high statistics;
- Study of the strong interaction production characteristics of charmed hadrons, comparing $\pi^{\pm}$, p and Σ^- beams;
- Study of the electromagnetic form factors of unstable hadrons, by means of hadron-electron scattering;
- Use of the Primakoff effect to study hadron polarizability and other hadron structure phenomena, including a search for hybrid meson states of the form $(q\overline{q}g)$;
- Study of double charm production and search for doubly-charmed baryon and exotic baryon production.

E781 is a forward spectrometer with large acceptance and three magnetic stages. The experimental layout is shown in figure 3.22.
The most relevant components of the spectrometer include:

- Very high precision silicon beam and vertex detectors. The latter has 30 μrad angular resolution for 100 GeV/c tracks;
- Excellent momentum resolution for high momentum, small angle tracks (of the order of 0.5% for 500 GeV/c tracks);
- Large acceptance first stage spectrometer for measuring associated charm particle decay tracks and de-excitation pions from excited charm hadrons;

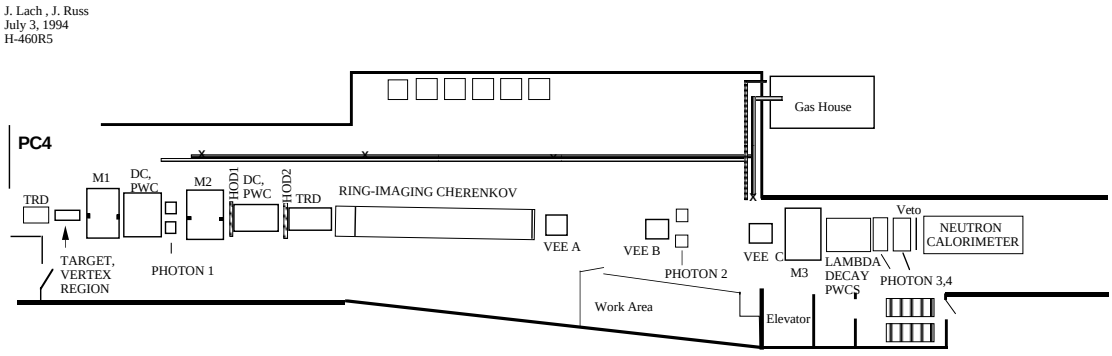

Figure 3.22: E781 layout.

- Moderate acceptance second stage spectrometer with electron identification and Ring Imaging Cherenkov tagging of all transmitted particles;
- Forward Λ decay spectrometer to reconstruct decay products of Ξ and Ω decays;
- 3-stage lead glass photon coverage of the entire forward hemisphere.

SELEX differs from the CERN hyperon beam experiment WA89 (described in the next chapter) by having a more flexible, higher energy and higher intensity beam, a broader range of momentum coverage, a faster data acquisition system and an improved spectrometer system. Having three stages of spectrometer magnets rather than one allows a good momentum resolution even at high energies.

3.9.1 The Large Angle Silicon Detector

The detector subsystem provided by our group is called LASD (Large Angle Silicon Detector). It consists of silicon microstrip counters located downstream of the vertex area. Their purpose is to cover the beam region of the downstream wire- and drift-chambers to improve track resolution and separation in this area and to allow a precise momentum measurement.

Our group is particularly interested in the study of hadron-electron elastic scattering processes in order to determine hadron charge radii. We expect to measure with 1% accuracy the electromagnetic charge radius of $\pi^{\pm}, p$ and Σ^{-}. Due to flux limitations, the measurement for $K^{\pm}, \Sigma^{+}$ or Ξ^{-} will be limited to 10% precision [16].

For this study it is essential to measure the momenta and the scattering angles of the hadron and of the electron with very high precision. High resolution detectors placed downstream the vertex area, in proximity of the magnets, substantially improve the quality of the tracking and the momentum determination of the spectrometer.

In particular our microstrip detectors are placed at the downstream end-plate of the first magnet (M1 in figure 3.22), and at both end-plates of the second magnet (M2). They are grouped in three identical structures and their position is aligned around the axis of the negative beam.
Each of the three groups consists of two single sided and two double sided detectors. The latter ones determine two points for the vertical and the horizontal coordinate while the former ones measure one point for each of the two projections at $+45^o$ and -45^o. All detectors have 50 μm readout pitch. The system includes a total of 21504 readout channels.
The single sided counters used in LASD are the Hamamatsu detectors described in the previous chapter. Six of the detectors with 50 μm readout pitch installed in 1994 in WA89 have been dismounted and adapted for use in SELEX in 1995 (since no further run of WA89 was foreseen).
The double sided detectors have been described in detail in this chapter.
The motivations for the choice of double sided counters were the reduction of material in the beam and the introduction of this comparatively new technology in fixed target experiments.

In the following sections I will schematically describe the readout of the silicon detectors in SELEX and the structure of the LASD setup. Some considerations about the radiation damage induced on the silicon counters will conclude the discussion.

The readout electronics

All silicon microstrip detectors in SELEX are equipped with the SVX readout chips. The basic components of the silicon readout system are shown in figure 3.23.

The microstrip detector boards are connected by means of capton cables to external electronics mother boards called Driver Cards. They are located as close as possible to the silicon counters.
The driver cards for LASD have a different design from those used for the other microstrip detectors in SELEX. This was imposed by the use of double sided detectors. At the same time we could keep the pin assignment on the micro-connectors for the capton cables identical to the one in the WA89 setup. Consequently the detector boards are compatible with both readout systems and can be easily moved from one to the other.

The SRS (SVX Readout Sequencer) is an upgraded version of the SRS module described in the previous chapter. It downloads the pattern from the local computer system to the SVX chips and handles the system initialization and the system control of the whole readout procedure. One single SRS controls all silicon planes in SELEX.

Data collected from the SVX chips are sent via the driver card to the FSDA (Fastbus SVX Data Accumulator) [17]. One FSDA channel is required for two silicon detector subplanes and two channels are packed in a single width Fastbus module. LASD uses in total 5 FSDAs.

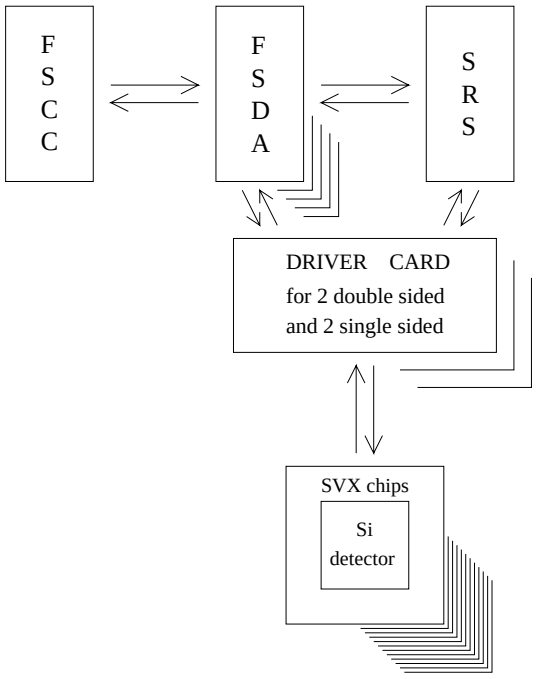

Figure 3.23: Components of the silicon detector readout system.

The FSDA module is able to perform several functions online. The main ones are listed below:

- digitize the analog pulse height of the hit strips;
- store the pedestal level for all individual channels. An offspill pedestal taking procedure must be regularly performed and pedestal levels must be loaded in the FSDA memory;
- map each address and subtract the corresponding pedestal;
- perform further sparsification of noise hits by checking if the signal after pedestal subtraction is higher than a lower level threshold (for example one or two counts);
- store the address of bad channels to be always excluded from the readout;
- merge the odd and even streams of mapped hits for detectors read out from two opposite edges, as in the case of the 20 μm readout pitch counters in the vertex area;
- store all event data with a header and a word count;
- buffer multi event fragments from all FSDA modules to build all SVX data for each event, and send them to the E781 DAQ system.

The complex functions listed above are required to reduce the amount of data to transfer to the central farm and to limit the computation necessary for data preparation.

The time needed for the readout of one hit (including the channel address and the digitized analog signal) is approximately 0.6 μsec. The data words are stored in two byte format with 12 bits of strip address and 4 bits of pulse height.
Data are then transferred to the FSCC (Fastbus Smart Crate Controller) which collects data from all detector subsystems and sends them via an optical link to the central computer.
The electronic trigger deadtime is required to be less than 30 μsec per average trigger and the readout of all event data from all modules must be completed in an average of less than 100 μsec, to guarantee a 70% livetime at 10 kHz trigger rate.

LASD setup

The LASD microstrip detectors are divided in three identical structures fixed respectively at the downstream end-plate of the first magnet, the entrance and the exit end-plate of the second magnet. The open window of the end-plates has an area of 610x534 mm^2 in the first case and 610x280 mm^2 for the second magnet. It is clearly extremely important to reduce the amount of material around our detectors in the open gap area.
Therefore a special mechanical mounting had to be designed in order to position the detectors precisely, fix them in a very stable way and at the same time limit the amount of scattering material.
The structure used to mount the detectors is shown in figure 3.24. The main frame was realized with a 6 mm thick honeycomb layer (corresponding to less than 1% of a radiation length) reinforced at the edges by Stesalit profiles. Each frame carries one single sided and one double sided detector and there are two frames per package.

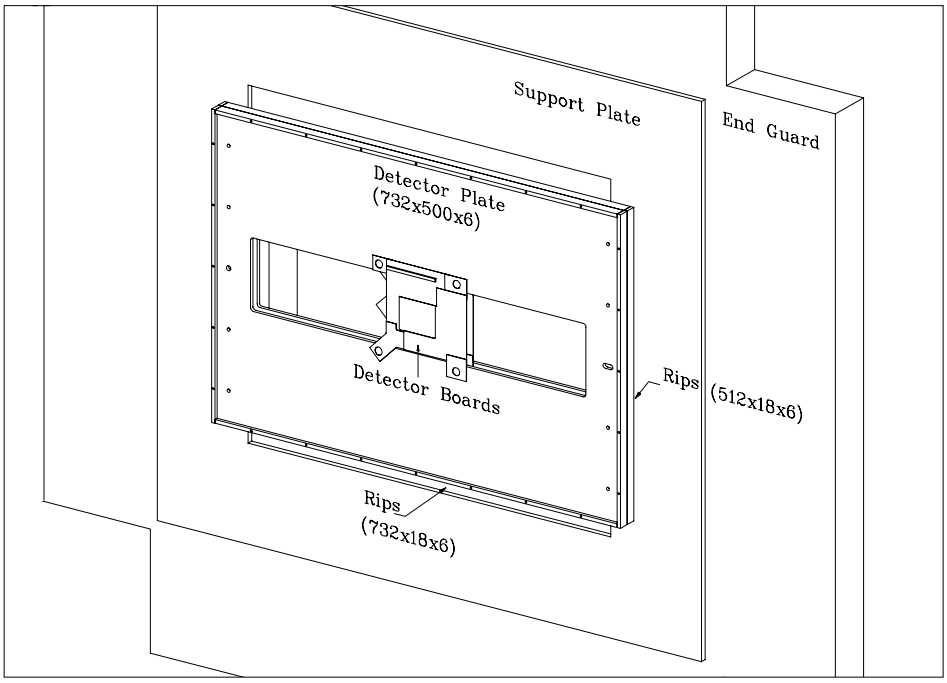

Figure 3.24: Support structure to fix the silicon detectors to the magnet end-plate (here called End Guard) [13].

The package is attached to the magnet end-plate by means of massive clamps fixed at the four corners of the end-plate. They allow the movement of the frames in the vertical plane in order to align the detectors with respect to reference points marked on the end-plate.
The ceramic boards carrying the silicon detectors were aligned to the honeycomb structure using a computer controlled Olivetti measuring machine at CERN [18]. The alignment is done with an optical system by means of a microscope. The measurement error is of the order of 3 μm in the two coordinates on the frame plane.
The photograph below shows one fully mounted double sided detector while it is aligned to the honeycomb frame, with the microscope of the Olivetti machine.

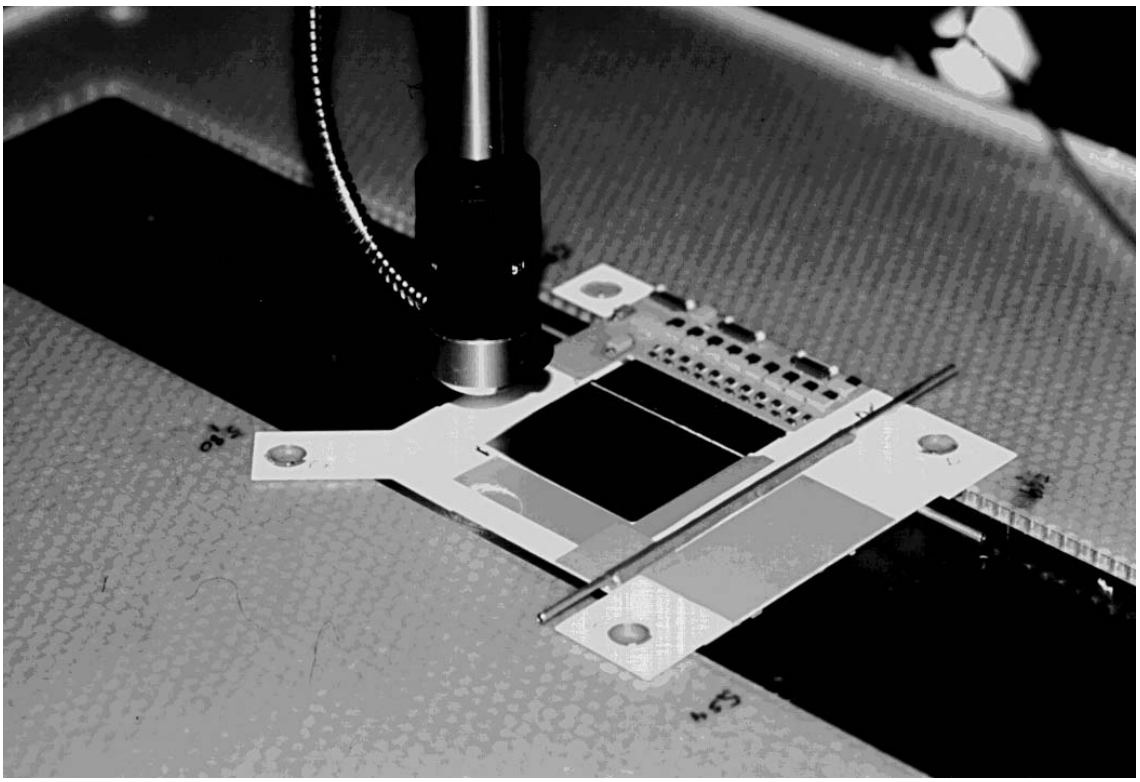

Figure 3.25: Photograph of a double sided detector mounted on the honeycomb frame. An optical system was used for the alignment. The microstrip detector and the ceramic boards are visible: The small aluminum tube is used for the cooling.

Each package with four detectors is covered by two aluminum foils with the double function of shielding and defining a closed volume which is constantly flushed with nitrogen.

The detectors lie just outside the volume of the magnet and the end-plates. This region is not completely free from magnetic field lines. In addition the magnets are ramped up and down for every spill (10 sec to ramp up, 20 sec full field during spill, 5 sec to ramp down

and other 25 sec until the next cycle). This must be taken into account for the electronics located on the driver cards (fixed directly to the end-plates). Some modifications had to be introduced so that the electronics would not be influenced by the magnet ramping. Another problem could arise from the fact that the end-plates are pulled towards the magnet while ramping. Measurements done at Fermilab showed that the displacement is negligible at the end-plate outer corners, where our structure is fixed.

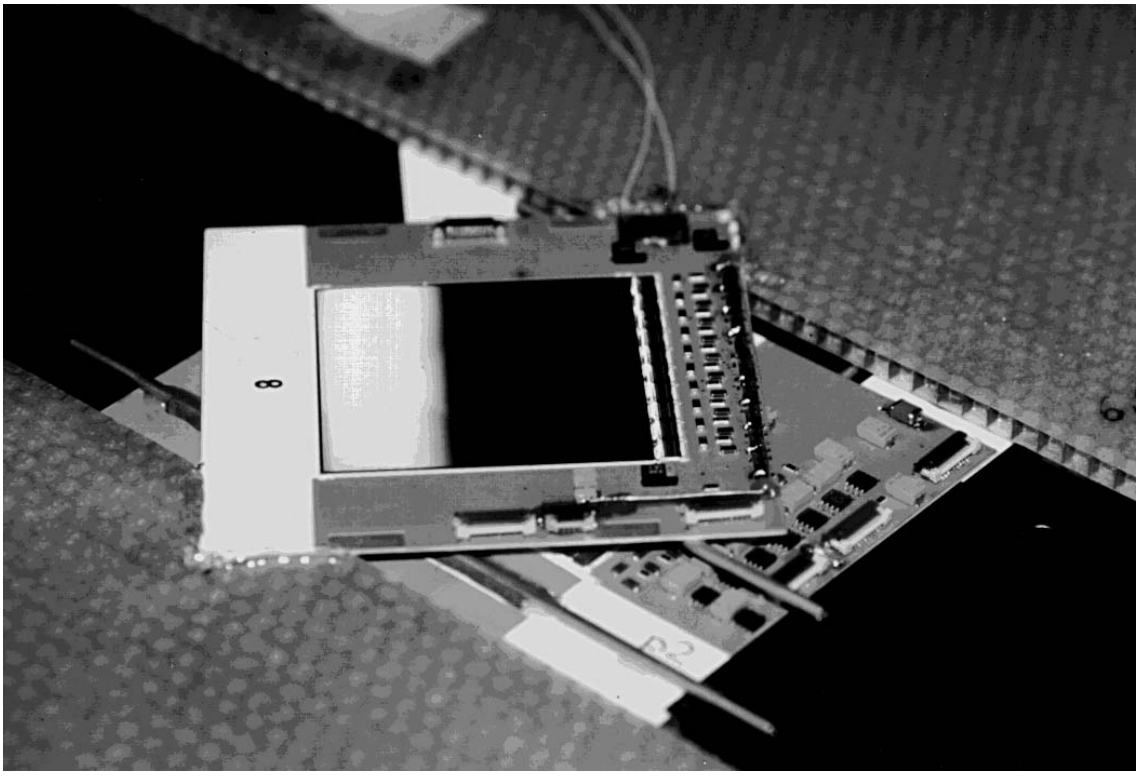

Figure 3.26: Photograph of a single sided detector mounted on the honeycomb frame , on the opposite side of the double sided counter (visible below).

During the data taking period, the access to the whole experimental area is restricted for safety reasons. In addition the distance between the end-plates and the adjacent detectors is limited to few tens of centimeters. Access to the microstrip counters is extremely difficult, therefore it is very important to position the mounting structures very precisely and guarantee the most stable working conditions of the detectors.
In particular monitoring and remote control of the system parameters are required. This includes the measurement of the detector leakage currents and their stability; the monitor of the applied voltages and of the temperature of the ceramic boards; the possibility to set and control from remote all bias voltages.
The voltages for the microstrip detectors and the driver cards for the junction sides are provided by a CAEN Multichannel Power Supply System, Model SY 527 [19]. This

device can store the values of the applied voltages and the measured detector currents and transfer them to the central computer system via a CAMAC interface.
A PT100 temperature sensor was glued on each detector board. The sensors are read out by dedicated CAMAC modules and the values are stored in the Fermilab Epicure database [20].
All the information is therefore available to monitor the stability of operation of the microstrip detectors.

In order to guarantee an even better stability of the silicon counters a cooling system has been implemented. It was developed on the base of the cooling system used in the vertex area of WA89 using an underpressure leakless water system. It consists of a 150 W fridge as heat exchanger, a water reservoir, a circulating pump, a vacuum pump and water tubes connecting the three packages of detectors at the three end-plates. Aluminum tubes with a 2 mm inner diameter were placed on the back side of each readout board in correspondence of the SVX chips and glued with heat conductive aluminum-epoxy glue.
The cooling system allows the temperature of the detectors to be kept during operation between 20 and 25^{o}C.

Radiation damage

An important point concerns the problem of radiation damage of the silicon detectors due to the high beam rate. It is rather difficult to give a realistic estimate of the induced effects if the final beam parameters are not known in detail. Depending on the beam spot at the target, the beam divergence, and the particle momentum distribution the beam size at our detectors varies. Based on very preliminary assumptions, the particle flux and the deposited dose can be estimated. The hyperon beam should have an intensity of about $2{\cdot}10^6$ ptc/sec incident on the experimental target, distributed over an area of about 6x11 mm^2. With a preliminary estimate of its divergence in the vertical and the horizontal projection, together with the sweeping effect of the magnets, we can expect a beam spot size of about 20x18 mm^2 at the exit of the first magnet, 32x24 mm^2 at the entrance of the second magnet, and 40x30 mm^2 at the exit of the second magnet.
Assuming $2{\cdot}10^6$ ptc/sec for 14 months of beam at full efficiency (to have an upper limit of the particle flux), a total of $2{\cdot}10^{13}$ particles cross the silicon detectors.
At the location of the first package of LASD, if the beam is spread over an area of 3.6 cm^2, the detectors will receive a particle flux of approximately $5.5{\cdot}10^{12}$ ptc/cm^2 and a total dose of about 75 krad. For the last group of detectors the flux over the 12 cm^2 area should be $1.7{\cdot}10^{12}$ ptc/cm^2 and the dose of 22 krad.
At this radiation level, no serious damage should be induced on the counters. Tests performed by the ALEPH group indicate that no relevant degradation of the detector performance should be seen for doses below 100 krad [21]. The major effects we expect are an increase of the leakage current and a possible variation of the value of the biasing resistors on the n-side.
All numbers mentioned in this last section are rough estimates. They are only meant to give an order of magnitude of the radiation level and the importance of the problem. The precise estimate of damage effects will be possible once the final beam parameters are

accurately measured.
For a general discussion of radiation damage induced on single sided and double sided silicon detectors see, for example, references [22] and [23]. We do not expect any significant radiation damage of the readout electronics because they are not directly hit by the beam particles.

Bibliography

[1] S.M. Sze, “Physics of semiconductor devices”, Wiley, New York, 1981

[2] B.S. Avset et al, “A new microstrip detector with double-sided readout”, IEEE Trans. on Nucl. Sci., Vol. 37, No. 3, June 1990, 1153-1161

[3] G. Bagliesi et al., “A double sided readout silicon strip detector: a new device for vertex detection in high energy experiments”, INFN PI/AE 1986/10

[4] P. Holl et al., “The ALEPH minivertex detector”, Nucl. Instr. and Meth. A257 (1987) 587-590

[5] G. Batignani et al., “Test results on double sided readout silicon strip detectors”, IEEE Trans. on Nucl. Sci., Vol. 36, No. 1, February 1989, 40-45

[6] P. Holl et al., “A double-sided silicon strip detector with capacitive readout and a new method of integrated bias coupling”, IEEE Trans. on Nucl. Sci., Vol. 36, No. 1, February 1989, 251-255

[7] G. Batignani et al., “Development of double side readout silicon strip detectors”, Nucl. Instr. and Meth. A273 (1988) 677-681

[8] G. Batignani et al., “Double-sided readout silicon strip detectors for the ALEPH minivertex”, Nucl. Instr. and Meth. A277 (1989) 147-153

[9] H. Becker et al., “New developments in double sided silicon strip detectors”, IEEE Trans. on Nucl. Sci., Vol. 37, No. 2, April 1990, 101-106

[10] G. Batignani et al., “Beauty physics and double-sided Si microstrip detectors”, INFN PI/AE 1990/13

[11] G. Batignani et al., “Development and performance of double sided silicon strip detectors”, Nucl. Instr. and Meth. A310 (1991) 160-164

[12] G. Batignani et al., “Recent results and running experience of the new ALEPH vertex detector”, IEEE Trans. on Nucl. Sci., Vol. 39, No. 4, 1992, 701-706

[13] Gala Konorova, March 1995

[14] J. Simon, diploma thesis, in preparation, Universität Heidelberg, 1996

[15] R. Edelstein et al., “A proposal to construct SELEX - Segmented Large-X Baryon Spectrometer”, Fermilab, November 1987

[16] K. Königsmann et al., “Electromagnetic radii of hyperons using SELEX”, H-note 574, Internal Note, Fermilab, August 1992

[17] P. Neoustroev and V. Stepanov, “Fastbus SVX Data Accumulator (FSDA)”, Technical Reference, Fermilab, October 1994

[18] C. Boudineau, CERN

[19] CAEN, Model SY 527, Universal Multichannel Power Supply System, Reference Manual, 1995

[20] E. Dambik et al., “The Epicure control system”, Fermilab Conf-93/288

[21] ALEPH Collaboration, “Proposal for a new vertex detector for ALEPH”, CERN/LEPC 93-8 and LEPC/PI Add.1, May 1993
R. Johnson and R. Rennels, “Radiation damage measurements on ALEPH double-sided silicon strip test structures”, ALEPH 94-099, MINIV 94-004, June 1994

[22] RD20 Collaboration, “Radiation tolerance of single-sided silicon microstrips”, Nucl. Instr. and Meth. A339 (1994) 511-523

[23] RD20 Collaboration, “Radiation damage studies on single-sided and double-sided silicon microstrip detectors”, Nucl. Instr. and Meth. A348 (1994) 449-453

Chapter 4

The hyperon beam experiment WA89

WA89 is a fixed target experiment at the CERN Super Proton Synchrotron (SPS) with a secondary hyperon beam to study hadrons with charm and strangeness content [1]. Its predecessor experiment at CERN, WA62, collected data in 1980 with a hyperon beam of 135 GeV/c. The aim was to continue the physics program of WA62 with an improved apparatus and with a beam of higher energy to improve yields and higher intensity to enlarge statistics.
WA89 had three physics beam times, in 1991, 1993, and 1994, and a total of approximately 550 million triggers were recorded.
Previous experiments which contributed results in the same field are ACCMOR (with proton, kaon and pion beams at CERN), E400 and BIS2 (at Fermilab and Serpukhov respectively, with a neutron beam) and ARGUS (at the e^+e^- collider at DESY). Present competing experiments are E687 and E791 (with a photon and a pion beam respectively, at Fermilab) and CLEO (at the e^+e^- collider in Cornell). In summer, 1996, the new hyperon beam experiment SELEX (E781, mentioned in the previous chapter) will start taking data at Fermilab.
In this chapter I will review the physics goals of WA89 and describe its experimental setup.

4.1 Physics goals

The main physics topics addressed by WA89 are listed below.

Study of charmed and charmed-strange baryons.
The knowledge of baryons with charm and charm-strangeness content is still rather limited. While the Λ_c^+ is relatively well measured, the charm-strange baryons Ξ_c^0, Ξ_c^+ and Ω_c^0 still need considerably more statistics and more precise measurements. The search for the excited states $\Xi_c^{0\prime}$ and $\Xi_c^{+\prime}$ (where the two light quarks have spin parallel) and for states with spin=3/2 (Ξ_c^*, Ω_c^*) is of great interest.
The ground state baryons mainly studied by WA89 are listed in table 4.1 with some of their more relevant characteristics. The indicated decay channels are given as examples of topologies studied in WA89.

Particle	Quark content	Mass [MeV/c^2]	Lifetime [psec]	Decay channels	Ref.
Λ_c^+	(cud)	2285.1 ± 0.6	$0.200^{+0.011}_{-0.010}$	$\Lambda\pi^+\pi^+\pi^-$ $pK^-\pi^+$ $\Sigma^+\pi^+\pi^-$	[3, 4]
Ξ_c^0	(csd)	2470.3 ± 1.8	$0.098^{+0.023}_{-0.015}$	$\Xi^-\pi^+$ $\Xi^-\pi^+\pi^+\pi^-$ $\Sigma^-K^-\pi^+\pi^+$	[5]
Ξ_c^+	(csu)	2465.1 ± 1.6	$0.35^{+0.07}_{-0.04}$	$\Lambda K^-\pi^+\pi^+$ $\Xi^-\pi^+\pi^+$ $\Sigma^+K^-\pi^+$	[6]
Ω_c^0	(css)	2710 ± 5	0.065±0.02	$\Omega^-\pi^-\pi^+\pi^+$ $\Xi^-K^0\pi^+$ $\Sigma^+K^-K^-\pi^+$	[7, 8]

Table 4.1: Charmed and charmed-strange baryons and their relevant properties [2]. For each particle only a few of the more probable (known) decay channels are indicated as examples of topologies studied in WA89.

In particular for these particles we want to:
- determine masses and lifetimes
- determine production cross sections and study their dependence on the transverse momentum p_t, on the Feynman variable x_F and on the mass number A of the target nucleon
- study decay channels and determine relative branching ratios.

Study of hyperon properties such as

- their production cross sections
- Ξ and Ω resonances [9, 10]
- hyperon polarization [11, 12]
- hyperon charge radii, by looking at the hyperon-electron elastic scattering

Search for exotic multiquark states like

- the diquarkonium U(3100) ($sq\overline{q}\overline{q}$) [13] first reported by the WA62 collaboration
- the pentaquark state P ($\overline{c}s3q$ or $\overline{s}s3q$) [14]
- the double strange dibaryon H (uuddss) [15]

4.2 The setup

Figure 4.1 shows the WA89 experimental setup as it was during the 1993 data taking period. The only relevant changes done in 1994 concern the vertex area, as it will be described in a following section.
The apparatus was designed as a large acceptance forward spectrometer centered around the superconducting Omega magnet. The hyperon beam comes in from the left side, along the direction defined as x (according to the Omega reference system, where z is pointing upwards).

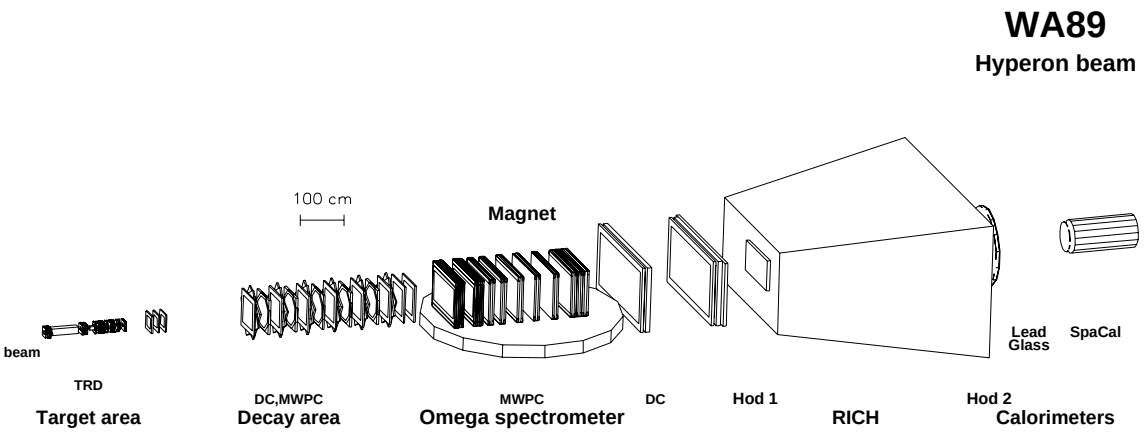

Figure 4.1: WA89 experimental setup in 1993.

The setup consists of:

- a **beam region** with a transition radiation detector (TRD) used to distinguish pions from hyperons and silicon microstrip detectors to reconstruct the beam track;
- the **vertex region** which includes the interaction target, trigger scintillators, and the vertex detector. High resolution silicon microstrip counters are used to reconstruct the production point and the decay point of short lived particles;
- the **decay area** follows. In WA89 it is essential to have good acceptance for hyperons and kaons emerging from the decays of charmed baryons. Therefore the target is placed approximately 15 m upstream of the magnet center, providing a 10 m long field-free decay region. Λ, Ξ^-, Ω^-, and K^0_S decays can be determined with high precision by measuring their momentum in the spectrometer and their trajectories by reconstructing straight tracks. The decay area is equipped with drift chambers (called Lambda chambers) and MultiWire Proportional Chambers (MWPC called Octogons);
- the momenta of charged particles are measured by the **Omega spectrometer**. Inside the magnet volume and immediately behind it, MWPCs and drift chambers allow the reconstruction of tracks;

- a **Ring-Imaging CHerenkov detector** (RICH) serves for the identification of charged pions, kaons and protons;
- right before and after the RICH two scintillator walls are mounted and used as **hodoscopes** for the trigger;
- a lead glass **electromagnetic calorimeter** measures the energy of photons emitted in radiative decays, identifies π^0s and electrons, and enables studies of final states involving Σ^0s;
- a **SPAghetti hadronic CALorimeter** (SPACAL) is used to measure the energy of neutrons.

The tracking detectors cover about ± 50 mrad with respect to the beam axis.
The acceptance of the spectrometer corresponds approximately to the range $0.3 \leq x_F \leq 1$.
All single parts will be described in more detail in the following sections.

4.3 The hyperon beam

The physics program of WA89 mostly addresses hadrons (baryons particularly) with strangeness content. For the production of these states in a fixed target experiment (where the acceptance is largest in the forward direction) it seemed advantageous to use a hyperon beam. The presence of a strange quark already in the projectile is expected to enhance the production of hadrons with strangeness in the forward direction (high x_F). This is called the *leading particle effect*. Furthermore, the presence of three quarks (instead of a quark and an antiquark) in the projectile should enhance baryon production.
Hyperons can be obtained with a primary beam of protons reacting with a target. In this case the production of strange particles is suppressed with respect to that of non-strange particles by a factor $1 / \lambda^n$, where λ depends on x_F (of the order of 20 for x_F=0.5) and n is the number of units of strangeness [16]. As a consequence the production rate of Ξ^- (s=2) and Ω^- (s=3) is suppressed with respect to Σ^- (s=1) which is the main hyperon constituent of our beam.
Together with the hyperons, also pions are created by the proton beam. The expected number of pions produced with momentum p per incoming proton and per target nucleus is

$$N_\pi = \sigma_{inv} \cdot p^2 \cdot \frac{\Delta p}{p} \cdot \Delta\Omega \qquad (4.1)$$

where σ_{inv} is the invariant pion cross section. It is a function of x_F which, at high energies, can be well approximated by $x_F = p / p_0$ where p_0 is the proton beam momentum.
Figure 4.2 shows the production rate per spill of pions and hyperons as a function of x_F.
In WA89 an average beam spill contains about $1.8 \cdot 10^5 \Sigma^-$ and $4.5 \cdot 10^5 \pi^-$. Ξ^-s and Ω^-s in the beam are about 1.2% and less than 0.1% relatively to Σ^-s. The amount of K^-s and $\overline{p}$s are below 1% and 0.1%, respectively. The average x_F of our beam is about 0.75.

In November, 1989, a new beamline (called Y1) was brought into operation for the hyperon beam [17]. A beam of 4×10^{10} protons per spill (2.58 sec) with a momentum of 450 GeV/c

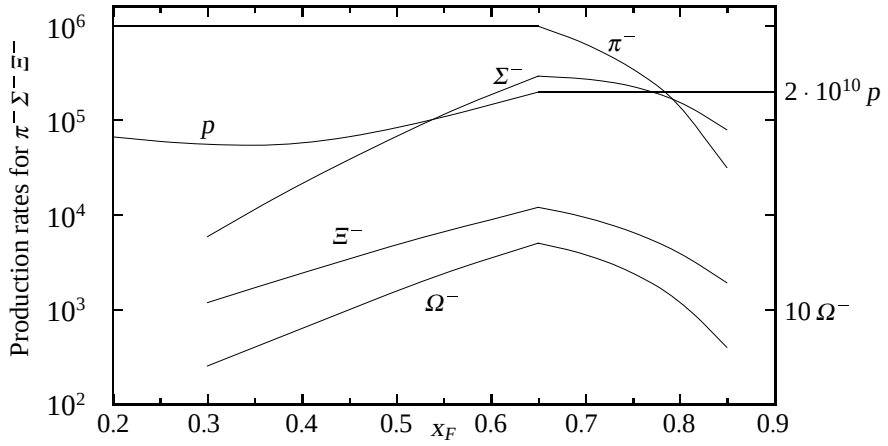

Figure 4.2: Production rate of the beam particles as a function of x_F and necessary proton rate. The y axis on the left gives the particle rates for pions, Σ^- and Ξ^-, the one on the right for Ω^- and protons. The pion curve shows a plateau because the total beam flux is limited to 10^6 ptc/sec.

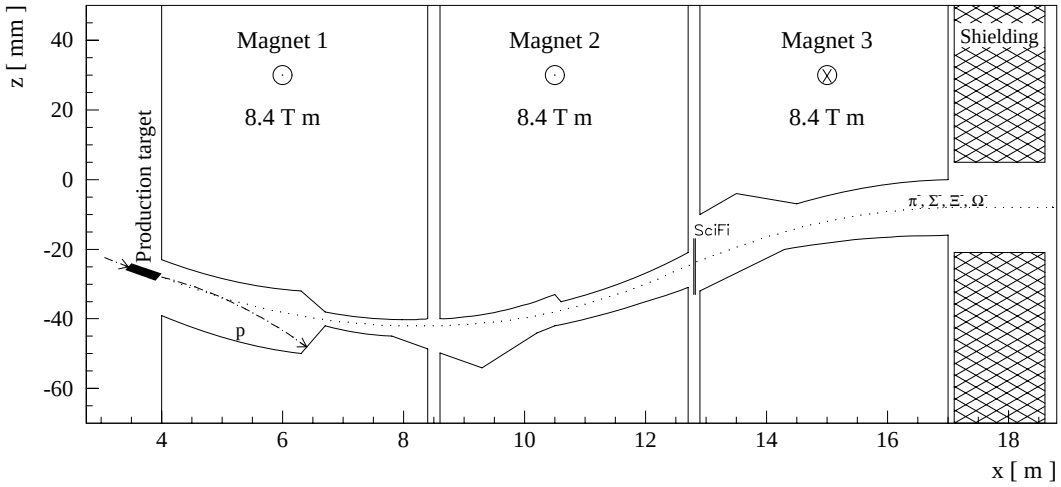

Figure 4.3: The magnetic channel for the hyperon beam.

is extracted from the CERN Super Proton Synchrotron (SPS) every 14.4 sec and brought to the West Area. The proton beam is deflected downwards by a bending magnet and hits a cylindrical beryllium rod with 2 mm diameter and 40 cm length along the beam direction. This target is followed by a magnetic beam channel that selects negative particles within a given momentum range. The channel is shown in figure 4.3.

The choice of negative particles has been made in order to have a lower background, since the non-interacting protons of the primary beam have the opposite sign.

Three bending magnets, with an integrated field strength of 8.4 Tm each, deflect the charged particles in the vertical plane. The space between the poles is filled with tungsten blocks that define the actual beam channel. The tungsten (dense material with short interaction length) absorbs both the positive particles and the negative ones lying outside the desired momentum range. Some pockets inserted in the channel walls interrupt straight lines

leading to the exit window, along which neutral particles could reach the experimental target.
Because of the short lifetime of the Σ^-, the beamline has been made as short as possible ($\approx$ 13 m from the hyperon production target to the end of the magnetic channel, and $\approx$ 16 m to the experimental target). The resulting beam has an average momentum of 340 GeV/c and a momentum spread of about 7%. The size of the beam spot at the experimental target is 3.6 cm horizontally and 1.5 cm vertically, with a dispersion of 0.6 mrad in the horizontal plane and 1.0 mrad in the vertical plane.
The hyperon production target can be moved in the vertical direction in order to select various beam momenta and correspondingly vary the beam rate and, in particular, the Σ^- / π^- ratio.

The beam hodoscope

The beam momentum is measured by a SCIntillating FIber (SCIFI) hodoscope placed in front of the last bending magnet and the beam microstrip detectors. It measures the particle position in the bending plane (z direction) with approximately 250 μm accuracy.
The scintillating fibers have a rectangular cross section (1x0.5 mm^2). Three fibers in a row are put together to form one channel and this is connected via a light guide to one pixel of a 64-channel photomultiplier. There are two hodoscopes of 64 fibers each put in series.
The efficiency of the hodoscope is about 90% and the resolution of the beam momentum is approximately 1%.

The TRD

Since the WA89 beam contains π^- and Σ^- particles in a ratio of about 3:1 a fast rejection of beam pions is necessary to strongly reduce the trigger rate. A Transition Radiation Detector (TRD) is used to perform particle identification and provides the information to the trigger.
Transition Radiation (TR) is produced when a charged particle crosses the interface between two media with different dielectric properties and consequently different refractive indices. The intensity of the TR has a linear dependence with the γ=E/mc^2 factor of the moving particle. Consequently, this effect can be used to discriminate between charged particles with similar momentum but different mass. In case of WA89, for a beam momentum of 330 GeV/c, the Σ^- has $\gamma \approx 276$ while the lighter π^- has $\gamma \approx 2358$.
For $\gamma \approx 10^3$ the detectable TR photons have energies in the range of 2-20 keV. Most of the emission takes place within a forward cone of half angle $1/\gamma$, i.e. essentially along the line of flight of the particle (for highly relativistic particles). Owing to this angular distribution, the X-rays emitted from a radiator cannot be separated from the ionization charge created by the particle crossing the detector. This ionization charge constitutes a background for the measurement. In order to keep it small as compared to the TR signal, MWPCs filled with a heavy gas like xenon are commonly used. The thin layers of high Z materials can be thick enough to allow sufficient absorption of the X-rays and thin enough to limit the ionization signal. The probability of emission of a keV photon is $\approx 10^{-2}$. Therefore a

typical TRD is made by a periodic structure of many interfaces such as in a series of foils and air gaps or in a fiber material.

In WA89, the TRD was installed between the end of the hyperon channel and the experimental target. It consists of 10 radiator/chamber sets with a total length of 85 cm (this must be kept short to reduce the loss of Σs through decay).
Each set consisted of a 68 mm thick radiator and two MWPCs to detect the X-rays. The radiator was an inhomogeneous material consisting of fibers with a thickness of 5-25 μm is used, acting as a multiboundary system. Each MWPC has two consecutive detection volumes each 4 mm thick, filled with a gas mixture of 90% xenon and 10% methane.
In order to obtain good energy resolution ($\sigma \approx$8%) and a lower amplifier load, a wire spacing of 2 mm was chosen and the output signal of the amplifiers of three adjacent wires is added before passing a high/low discrimination system. The chambers are operated at very low gain (A≈500) to reduce space charge effects.
Using low noise charge amplifiers the total charge deposited in each chamber is measured. The resulting signals are compared with two thresholds (set by DACs) for each plane separately: a low level threshold is used for noise rejection and timing purposes; an upper level threshold selects the pion signals and is optimized for $\Sigma - \pi$ discrimination.
The pion signature consists of at least three single MWPCs with at least one discriminator fired. The online flag for pion rejection used for triggering is available about 910 nsec after the passage of the beam particle. A pion rejection of 95±2% was obtained with a Σ detection efficiency of 82±1%.
Using an offline likelihood method, an overall π rejection rate of ≈99% for a Σ detection efficiency of more than 77% was obtained.
A more general introduction to TRDs and details on the performance of the WA89 TRD can be found in references [10] and [18].

The target

The experimental target was segmented along the direction of the beam and consisted of four layers of 5x5 cm^2 area. The first one was a 4 mm thick slice of copper, followed by three layers of carbon, each 2.2 mm thick. The latter ones were made of pressed diamond powder, with a density of 3.25 g/cm^3. The target slabs were spaced by 2 cm and were placed in a closed box flushed with helium gas to reduce secondary interactions in air.
The 4 mm of copper correspond to 28% X_0 (where X_0 indicates a radiation length) and 2.66% λ_I (where λ_I represents the nuclear interaction length). Each slice of carbon is equivalent to 1.67% X_0 and 0.83% λ_I. The whole target corresponds to about 5.1% of a nuclear interaction length: this guarantees a good interaction rate without having too many secondary interactions of the produced hadrons inside the target itself.
The choice of different materials for the target was done in order to measure the dependence of production cross sections on the nuclear mass number A of the target material.

4.4 Tracking detectors

For the 1993 run period, major efforts were devoted to improving the tracking detectors following the target. The aim was a more efficient track reconstruction and track linking between the Omega spectrometer, the decay region, and the vertex detector. After the 1991 run period it was found that the low efficiency of the existing detectors (in the vertex and in the decay area) led to a number of poorly measured or fake tracks, resulting in incorrectly reconstructed secondary vertices. This strongly deteriorated the capability to measure the lifetime of short lived particles. Therefore new detectors were introduced in the vertex region (new microstrip planes with SVX readout) and in the decay area (Octogon chambers).

4.4.1 Silicon microstrip detectors

Two sets of silicon microstrip planes were placed just upstream and downstream of the experimental target. The former ones were used to reconstruct the trajectory of the beam particle. The latter ones formed the vertex detector and were used to measure the decay particle tracks with the best possible precision. The high spatial resolution was needed in order to determine precisely the production point (called primary or main vertex) and the decay point (secondary vertex) of charm particles. Only this condition allows to measure correctly their lifetime.
As already mentioned in chapter 2, the layout of the vertex area was different during the 1993 and the 1994 run periods. The two different layouts are shown in figure 4.4 and figure 4.5 respectively.

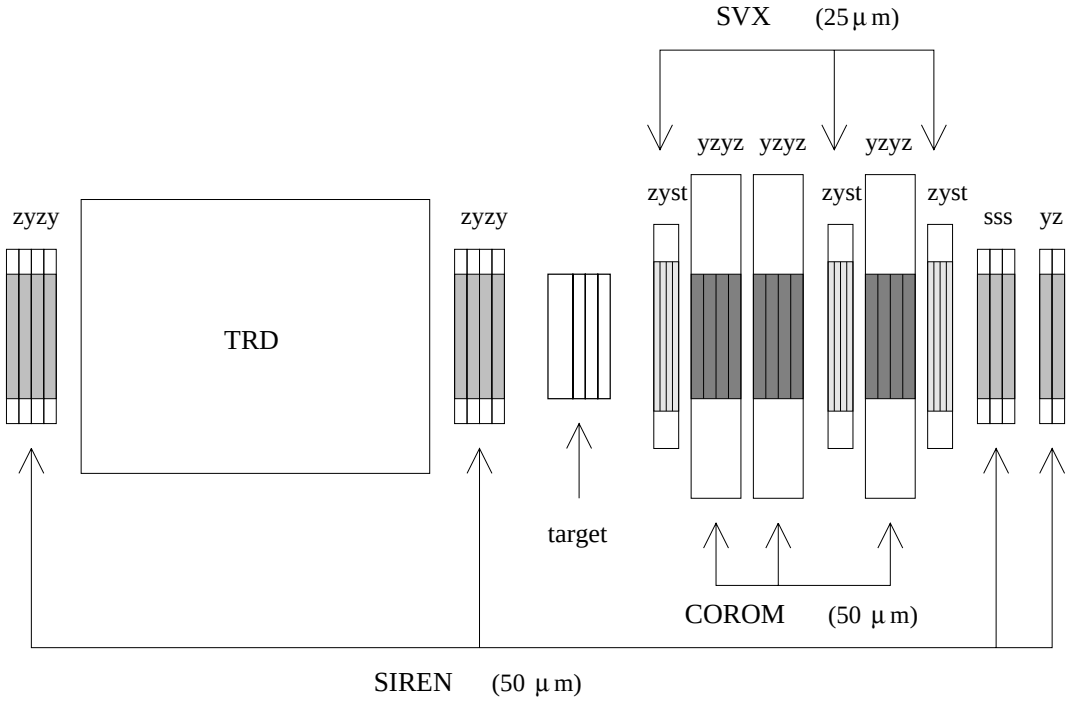

Figure 4.4: Vertex area layout in 1993.

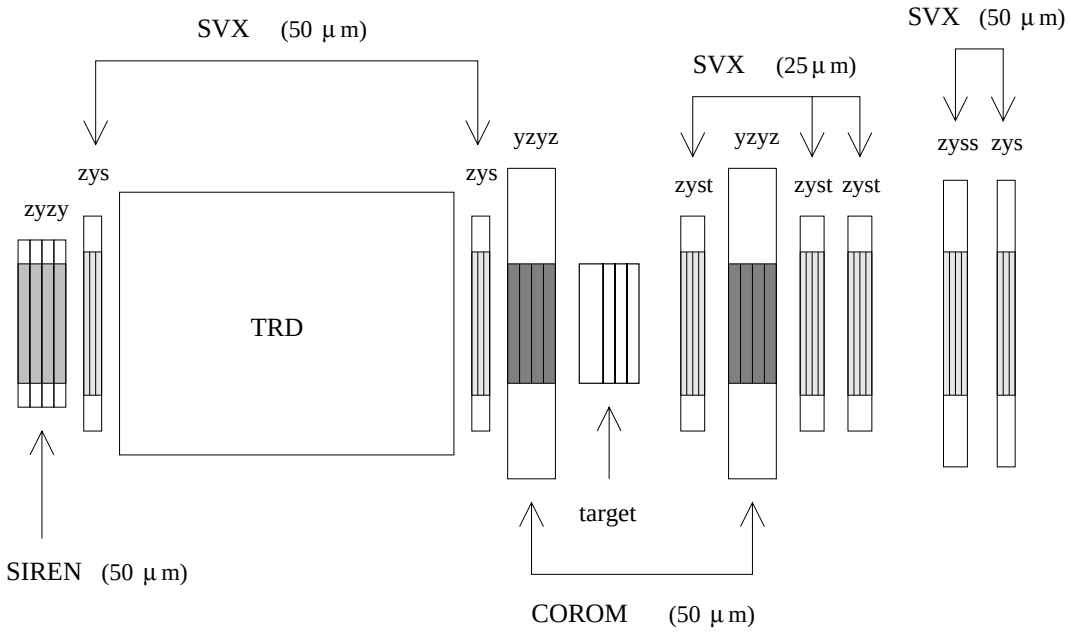

Figure 4.5: Vertex area layout in 1994.

Upstream of the target in 1993 (1994) there were 8 (14) microstrip planes, 4 (6) measuring the y coordinate and 4 (6) measuring the z coordinate. In 1994 there were additionally 2 planes measuring the s projection. All detectors had 50 μm readout pitch and 300 μm thickness. Part of them were placed upstream of the TRD in order to increase the lever arm in the track fitting and reduce the error.
The vertex detector, downstream of the target, consists of total 29 (23) planes. In particular there were 10 (7) y planes, 10 (7) z planes, 6 (6) s planes and 3 (3) t planes (where s and t represents the directions at $+45^o$ and -45^o with respect to the z axis). Having four projections allows the reconstruction of tracks in three dimensions.
The microstrip planes used in WA89 are equipped with different readout electronics, as indicated in the two figures. The system of silicon detectors equipped with SVX readout chips has been described in detail in chapter 2 and its performance has been discussed there. In the following I will briefly describe the other two readout standards used, indicated as SIREN and COROM readout.

SIREN readout

Silicon detectors equipped with the SIREN readout were already assembled in the early 80s [19] and developed for use in WA82 at the Omega facility. This experiment studied charmed particles produced in hadronic interactions. There the detectors were used for a fast on-line trigger based on the measurement of the impact parameter of tracks relative to the primary vertex [20]. The microstrip counters used in WA89 have 5x5 cm^2 active area, 1000 strips per plane at 50 μm pitch and 300 μm thickness.
The detectors were mounted on ceramic plates, which acted as a detector support and

fanout. Capton foils provided the connection of the single channels to external boxes with the preamplifiers.

These were MSD2 [21] and MSP1 [22] hybrid amplifiers. They have a noise per channel of approximately 1000 electrons, 50 nsec shaping time and a current gain of about 200.

The signals from the preamplifiers were transferred in a fully parallel way to FASTRO cards, where they were amplified and discriminated. Strips with a signal above a threshold (which is common to 256 channels) are detected and their addresses are encoded in 16 bit words. These signals are then read out by CAMAC SIREN modules. The readout is purely digital, consequently the spatial resolution is of the order of 50 μm/$\sqrt{12}$ = 14.4 μm.

During the 1993 run period, the average efficiency of these detectors was very poor (between 75% and 80%).

COROM readout

The COROM detectors had been developed for the WA92 experiment, to find secondary vertices for beauty identification [23]. They were used in a fast trigger to select events where at least two tracks have impact parameter to the main vertex higher than a preset value.

The microstrip counters have 5x5 cm^2 active area, 2048 strips per plane at 25 μm pitch and 300 μm thickness. The planes were arranged in quadruplets measuring the vertical and the horizontal projections.

Every detector was equipped with 16 Front End (FE) boards, each of them processing the signals coming from 128 strips. The data were processed by two CMOS chips, one for the analog part (ICAR) and one for the digital part (FEROS). ICAR has 16 channels (containing a low noise preamplifier and a shaper with 150-300 nsec peaking time) with a multiplexer, and provides the analog information. There are eight ICAR chips on each FE board.

The output of each ICAR fed an external comparator with a programmable threshold. The output of the comparators was then given to the FEROS chip. This encoded the coordinates of the hit strips in 10 bits and calculated the multiplicity within the group of 128 strips.

Via an interface board placed close to the detectors, the FE boards were connected to the readout system through a Fastbus board called COROM (COordinate and multiplicity ReadOut Module). Each COROM module was able to handle two silicon planes, distributing timing signals, programming and controlling the threshold values, reading out multiplicities and the coordinates of hit strips. The COROM module can also perform cluster search among the hit coordinates and compare the multiplicity data with a programmable window for trigger purposes.

The multiplicity information was available in COROM 2.5 μsec after an interaction, while 2.6 μsec the first coordinate was available, followed by the others each 100 nsec.

Using only the digital information, the spatial resolution was of the order of 25 μm/$\sqrt{12}$ = 7.2 μm. The average efficiency of COROM detectors during the 1993 run was approximately 85-90%.

4.4.2 The decay area

After the vertex region, the decay area extended for about 10 m to allow hyperons and K_S^0 particles to decay before they entered the magnetic spectrometer. Several gas chambers were used to reconstruct their tracks.

Lambda chambers

In the decay region, there were six sets of drift chambers called Lambda chambers [8], having an active area of 80x80 cm^2. Each set consisted of three double planes, one pair with the wires oriented in the y direction and the others turned by $+60^o$ and -60^o, to allow reconstruction in space.
In every double plane the two 10 mm thick drift regions were separated by a free space of other 10 mm. The two planes were shifted with respect to each other by half the distance between two neighbouring counting wires in order to solve left-right ambiguities if the hit density is not too high.
The distance between a potential and a sense wire was 2.5 cm and the maximum drift time was 500 nsec. The chambers had a space resolution of about 350 μm. Their efficiency was strongly dependent on the beam rate and was lower in the central area of the chambers due to the high beam particle flux. In average it was approximately 88%.
In order to improve the bridging between the decay region and the spectrometer, other two drift planes were placed at the entrance of the Omega magnet. The wires were oriented in the z direction.

Octogon chambers

In order to increase the efficiency in the central area mentioned above, in 1993 some newly built MWPCs were added. They were called Octogon chambers and had 1 mm wire spacing and 4 mm gap. The width of their frames corresponded to those of the Lambda chambers, but only the central region was active on an area of 128 mm diameter.
Five sets were interleaved with the Lambda chambers. Each set consisted of four planes measuring y, z, $+45^o$ and -45^o projections. Their average efficiency was of approximately 98%.

M1 chambers

In order to improve the track bridging between the vertex area and the decay region, three sets of MWPC were placed about half a meter behind the silicon detectors. Each set consisted of four MWPC with 1 mm wire spacing and total 256 wires per plane. They were indicated as M1 chambers and they measured y, z, $+10.14^o$, and -10.14^o projections.

4.4.3 The Omega spectrometer

The momentum of charged particles was measured using the magnetic spectrometer consisting of the Omega magnet and its complement of MWPCs and drift chambers [24]. Omega is a superconducting magnet with a 1.3 m wide entrance window, 1.4 m distance between the poles and 4 m diameter, thus offering large acceptance. It provides a mean field of 1.8 T in the negative z direction, for an integrated field of about 7.4 Tm. Inside the magnetic field the tracking is performed by several MWPCs. Their setup for the 1993 and the 1994 runs is described below.
Immediately inside the entrance of the magnet there are the first 20 planes (called B chambers), with an active area of 152x93 cm^2, 2 mm wire spacing and 760 wires per plane. The planes are arranged in groups of two and they measure three different projections in the following sequence: u (+10.14^o with respect to the field direction), y, v (-10.14^o) and again y.
Between the B chambers and the next set of planes there are 36 cm free. Afterwards there is a second set of 25 planes (A chambers). They also have 2 mm wire spacing and total 760 wires, but cover a larger active area, equal to 150x120 cm^2. These are arranged in eight groups of three planes each, covering the y, u, and v direction. In the 7th group there is an additional plane with the wires perpendicular to the magnetic field (z plane).
In order to increase the lever arm for the momentum measurement for higher energy particles and allow a precise extrapolation of the tracks to the RICH, other chambers were placed at the exit of the magnet. There were two sets of drift chambers (called DC1 and DC2) at a distance of 2 m from each other. Each frame consisted of two staggered y planes, one u, and one v plane with an active area of 320x160 cm^2 and 4 mm wire spacing. Their spatial resolution was 220 μm in y and 1200 μm in z. In every set there were two additional MWPCs (respectively MY1-MY2 in the DC1 and MY3-MY4 in the DC2 frame). The information given by the four MY y planes is also used for the trigger in combination with the hodoscopes.
The momentum resolution of the Omega spectrometer is $\Delta p / p^2 \approx 10^{-4}(\mathrm{GeV}/c)^{-1}$ for tracks reaching DC2 (corresponding to 3.6% for particles with 360 GeV/c maximum momentum in WA89) and $\Delta p / p^2 \approx 10^{-3}(\mathrm{GeV}/c)^{-1}$ for tracks not entering the drift chambers. The efficiency is on average 95% for the MWPCs and 98% for the drift chambers.

4.5 Detectors for particle identification

4.5.1 The RICH

To study charmed-strange baryons and search for exotic states such as the U and the H dibaryon, $\pi / K / p$ ($\overline{p}$) identification of decay particles is necessary for momenta up to and beyond 100 GeV/c. In particular, it is very important to be able to identify kaons, protons and antiprotons in a background of at least ten times as many pions.
For this purpose a Ring Imaging CHerenkov (RICH) detector [25] was placed behind the Omega spectrometer. It was used to measure the velocity of traversing particles. This information, combined with the momentum measurement done with the spectrometer,

allows the identification of particles in the acceptance of the detector.
When a charged particle moves in a medium with higher velocity than the speed of light in that medium, it emits Cherenkov radiation. This situation corresponds to the condition $\beta = v / c > 1 / n$, where v is the velocity of the particle and n is the refractive index of the medium. With respect to the particle trajectory the Cherenkov radiation is emitted at an angle θ given by

$$\cos\theta = \frac{1}{\beta n}. \tag{4.2}$$

In a RICH detector a radiator volume (where the charged particles produce the Cherenkov light) is followed by a spherical mirror. This reflects the emitted photons back to the focal sphere of the mirror, where the photons arrive and form a ring-shaped image. For small angles the radius of the ring at the focal sphere is

$$\mathrm{r} = L \cdot tan\theta \approx L \cdot \theta \tag{4.3}$$

where L is the focal length of the mirror. Consequently the accurate measurement of the ring radius allows the determination of the particle velocity.

A RICH detector was already installed at the Omega facility and had been used by the experiments WA69 (photoproduction) and WA82 (hadroproduction) between 1984 and 1988. In 1989 a major upgrade of the detector took place, including the replacement of the central part of the mirror array, the introduction of new UV-detecting drift chambers and a new gas system. Since then the RICH was used by WA89 during all its data taking periods. A schematic drawing representing the RICH structure is shown in figure 4.6.

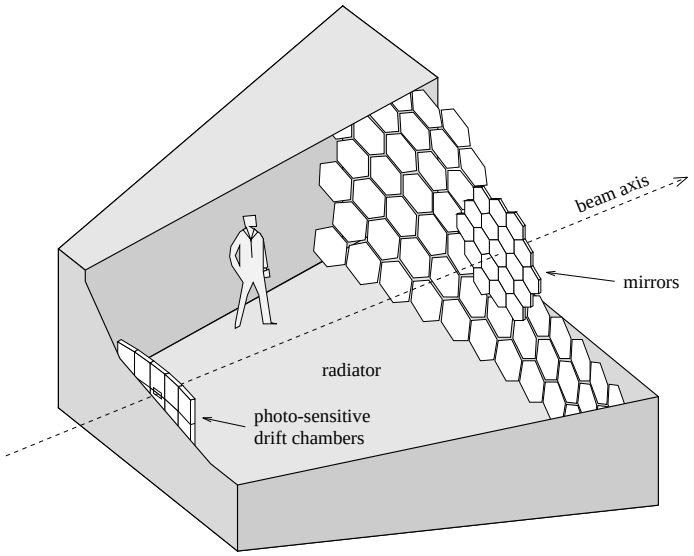

Figure 4.6: The RICH detector in WA89.

The radiator vessel is 5 m long, has a volume of about 120 m^3 and is filled with nitrogen at atmospheric pressure (n=1.0003). The detectable photons lie in the wavelength range

160-220 nm. At the downstream end of the detector a mosaic of 93 hexagonal mirrors approximate the shape of an overall spherical mirror with 10 m radius of curvature and 5 m radius focal sphere. The array consisted of 19 mirrors of 44 cm diameter placed in the center, surrounded by 74 mirrors of 70 cm diameter, for a total area of 7x4 m^2.
The Cherenkov photons produced in the radiator are reflected and focused on the focal sphere of the mirror. The photon detectors are positioned to form a cylindrical surface such that the focal sphere is in average 10 mm behind their entrance window.

There were five UV-sensitive drift chambers covering an active surface of 1.6x0.75 m^2, in total. They measured the two coordinates of the photon conversion points in their plane: the horizontal coordinate by the counting wire address, the vertical one by the drift time. The geometrical acceptance allows detection of all tracks emerging from the spectrometer with momentum p>12 GeV/c.
The chambers are 6 cm deep and have a 3 mm thick quartz window towards the radiator volume to allow the UV photons to enter. Ethane was chosen as counting gas because of its low diffusion coefficients and good counting properties of single photoelectrons. The ethane is saturated with Tetrakis(dimethylamino)ethylene (TMAE), which has a very low ionization energy (5.3 eV) and consequently very efficiently absorbs UV photons. In the wavelength interval 160 nm < λ < 220 nm, TMAE has an average quantum efficiency of about 0.3. In order to have short absorption length to limit parallax errors, the whole system is kept at a temperature of 30^{o}C at which the TMAE absorption length is approximately 11 mm. This in turn necessitates heating the RICH and the gas supply system to above 40^{o}C to avoid any danger of TMAE condensation.
Each chamber has two symmetrical parts separated by a common central high voltage electrode, kept at -40 kV. UV photons traversing the quartz window create photoelectrons in the sensitive chamber volume. These are guided by a homogeneous drift field of 1 kV/cm towards the counting modules at the upper and lower end of the chamber (the corresponding drift velocity in ethane is 5.3 cm/μsec). Homogeneity of the drift field is ensured by potential strips on the window and on the side and back walls of the drift volume (connected to the central electrode by a resistor chain). The maximum drift path is 41 cm.
The chambers have two detachable counting modules, each having 128 counting wires with 2.54 mm pitch, 15 μm radius and 60 mm sensitive length. For the definition of the individual counting cells and for suppression of photon cross-talk, separator plates made of Al_2O_3, with dimension of 60x18 mm^2 and a thickness of 0.25 mm, are inserted between the counting wires, forming a venetian blind structure. The plates carry conductive strips for field shaping, to focus the photoelectrons onto the counting wires.
Because of the high number of charged particles traversing the chambers before reaching the radiator, the counting action of the chambers has to be gated in order to suppress field distortion and photoelectron losses from space charge in the drift region. This is achieved by setting the potential of the uppermost strips of the venetian blinds such that they inhibit transfer of photoelectrons to the counting wires. After a trigger, the chambers are “opened” for 8 μsec, corresponding to the maximum drift time.

The signals from the wires were amplified by current sensitive preamplifiers and fed into discriminator modules. Thresholds were set to detect single electrons and for groups of

eight neighbouring wires to identify signals from charged particle tracks. The discriminator signals were then sent to multihit TDCs.

The space resolution for single photoelectrons is affected by chromatic dispersion, mirror alignment, parallax errors, transverse and longitudinal diffusion in ethane. The resolution achieved under experimental conditions is determined by measuring the distance of every hit to the ring centers predicted from tracks observed in the drift chambers in front of the RICH and results to be σ_γ=2.8 mm. The corresponding angular resolution is 0.58 mrad.

The error on the radius measurement can be expressed as

$$\sigma_{radius} = \frac{\sigma_\gamma}{\sqrt{N_{det}}} \tag{4.4}$$

where N_{det} is the number of detected photons per ring. It is therefore essential to detect as many photons as possible. From offline calibration of the 1993 beamtime, the mean number of photoelectrons per ring, averaged over all chambers and all runs, was determined to be 15.5. Taking into account the relation

$$N_{det} = N_0 L \sin^2\theta \tag{4.5}$$

the value N_0=55 cm^{-1} for the effective quality factor of the WA89 RICH was obtained.

The difference in ring radii for two particles of masses m_1 and m_2, having the same momentum p is given by

$$r \cdot \Delta r \approx L^2 \left(\frac{m_1^2 - m_2^2}{2p^2} \right) c^2. \tag{4.6}$$

The condition $\beta \cdot n > 1$, or equivalently $\gamma > 41$, for nitrogen, translates into a lower momentum threshold for radiation emission and consequently for particle identification, depending on the particle mass. The thresholds for the different particles are: $p_\pi > 6$ GeV/c, $p_K > 20$ GeV/c and $p_p > 40$ GeV/c.

For a known momentum (measured by the spectrometer), the position and radius of the ring for the different mass hypotheses (e, π, K and p) can be predicted from track parameters and mirror geometry.

A maximum likelihood approach is used for particle identification (more details can be found in reference [26]). For each mass hypotheses a probability density function of the two space coordinates to observe a signal or background hit is evaluated for every hit. A likelihood function is calculated for each hypotheses by multiplying the function values computed for all individual detected hits.

To discriminate different mass hypotheses, a cut on the ratio of the likelihoods is applied. For the analysis of experimental data, simultaneous cuts for different likelihoods ratios (depending sometimes on the momentum) are used.

The algorithm, tested on a sample of $\Lambda \rightarrow p\pi$ decays, gives a separation of protons and pions with 90% efficiency and a rejection by a factor of 10 or more at a momentum of 150 GeV/c. Kaons and pions can be separated up to about 90 GeV/c and kaons and protons up to about 150 GeV/c. By providing this information, the RICH played a key role in the whole data analysis of WA89. References [25, 26, 27] present a detailed description of the RICH detector and a deeper discussion of the obtained results.

4.5.2 The electromagnetic calorimeter

A lead glass electromagnetic calorimeter for photon detection was placed downstream of the RICH. One aim is to study possible radiative decays of charmed baryons and hyperon resonances. It is also used to search for decay channels of charmed and exotic states containing a Σ^0 or a π^0 through their decays $\Sigma^0 \to \Lambda^0\gamma$ and $\pi^0 \to \gamma\gamma$ (for example $\Xi_c^0 \to \Lambda K^- \pi^+ \pi^0$, $\Xi_c^0 \to \Sigma^0 K^- \pi^+$, etc.).
Lead glass blocks were arranged in a circular array of 1 m radius around the direction of the beam (at its center two modules have been left out to provide a beam hole). This size corresponds to an estimated acceptance of 70% for photons coming from charmed baryon decays at x_F = 0.3 and of 60% for both photons from π^0 decays at the same x_F.
There were a total of 642 blocks, made of lead glass of type SF57 which has a very high lead content and consequently a very short radiation length (1.546 cm) compared to other glasses. The face size of a single module was 7.5x7.5 cm^2, corresponding to $(1.44 \cdot R_M)^2$, where R_M is the Molière radius. The blocks were 36 cm long, corresponding to 23 radiation lengths (more than 97% of an electromagnetic shower of energy up to 100 GeV is released in such a layer of lead glass).
The Cherenkov light produced in the lead glass by electromagnetic showers was collected by a photomultiplier covering about 41% of the surface of the block. The photomultipliers were especially designed to provide a high linearity over a wide range.
Their anode signals were transferred via 120 m long coaxial cables to FASTBUS ADC modules, the distance provided the delay necessary for triggering, then sparsified and finally sent to the central event builder.
A xenon flash lamp was used for a constant monitoring of the pulse height provided by each channel. The light pulses were delivered by optical fibres to the backplane of each module covering the Cherenkov light spectrum in the lead glass. For the offline analysis the calibration factors of all modules are corrected according to the monitor measurements.
After an initial calibration done at a test beam in 1991 with an electron beam, the calorimeter was recalibrated for every run by comparing the reconstructed π^0 mass with the reference one. The mean mass resolution is σ = 4.2 MeV, while the energy resolution is

$$\frac{\sigma(E)}{E} = \frac{0.056}{\sqrt{E[GeV]}} + 0.02 \qquad (4.7)$$

and the average spatial resolution is σ(x) = 0.6 cm.
Since the calorimeter was located far from the experimental target (28.4 m), the invariant mass resolution of secondary states containing photons or π^0s is more sensitive to the energy resolution than to the position resolution.
A more detailed description of the calorimeter and its performance can be found in references [12] and [28].

4.5.3 The hadronic calorimeter

The most downstream detector was the SPAghetti hadronic CALorimeter (SPACAL). It is used to detect neutral hadrons and consequently it allows the reconstruction of final states with neutron content [29]. Determining the energy and impact point of neutrons,

the decays $\Sigma^+ \to n\pi^+$ (BR=48.3%) and $\Sigma^- \to n\pi^-$ (BR=99.8%) are reconstructed. This allows the study of Σ decay channels of charmed baryons.

The hadronic calorimeter is of the "spaghetti" type [30] with 176855 scintillating fibers embedded in lead plates, used as passive absorber. The fibers, made of SCSN-38 polystyrene, are 1 mm in diameter and 2.2 m long. They are mounted along the beam direction and grouped in 155 hexagonal modules (with 43 mm side length and 1141 scintillating fibers each). SPACAL has a total weight of 20 tons.

Particles traversing the calorimeter produce scintillation signals which are then collected by photomultipliers at the rear end of the modules (one photomultiplier per module). Their output signals are then stored in an ADC. A flash lamp system is used to monitor the stability of the readout chain from the photomultiplier on.

In addition a SCIntillating TILe hodoscope (SCITIL) was mounted just in front of the calorimeter in order to identify the charge of traversing particles [31] and reject the charged particles. The single tiles (matching exactly the hexagonal structure of the SPACAL modules) have wavelength-shifting fibers embedded in the scintillator. These serve the double purpose of primary light collection and subsequent light transmission to high gain photomultipliers located outside the active hodoscope area. The global efficiency of the hodoscope was ≥98%.

The total detector area facing the beam was 1 m in diameter and the active area is 0.75 m in diameter. The volume ratio of lead to the fibers was 4:1. This should give a compensating calorimeter (namely the ratio of the electromagnetic response to the hadronic response should be close to 1). This ratio was measured to be e/h=1.15.

The calorimeter length corresponded to 266 radiation lengths and 9.5 nuclear interaction lengths (=21 cm in the fiber/lead combination). Consequently all the energy of electromagnetic showers and 99% of the energy of hadronic showers is contained in the calorimeter up to an energy of several hundred GeV.

High energy neutrons were detected by looking for hadronic showers with a minimum energy of 40 GeV and a reconstructed shower barycenter that could not be linked to a track found in the spectrometer. To determine the direction of the neutron, one further needs the coordinates of the Σ decay vertex from tracking information.

The calorimeter is calibrated module by module before every data taking period using electrons and pions at test beam facilities. The energy and space resolution for hadronic showers there determined are

$$\frac{\sigma(E)}{E} = \frac{0.31}{\sqrt{E}} + 0.026 \qquad \text{and} \qquad \sigma_{yz} = \frac{31.4}{\sqrt{E}} + 2.4\text{mm} \tag{4.8}$$

and for electromagnetic showers

$$\frac{\sigma(E)}{E} = \frac{0.124}{\sqrt{E}} + 0.012 \qquad \text{and} \qquad \sigma_{yz} = \frac{17.1}{\sqrt{E}}\text{mm} \tag{4.9}$$

An introduction to spaghetti calorimeters and a more detailed presentation of SPACAL and its performance in WA89 can be found in references [29], [30], [31] and [32].

4.6 The trigger and data collection

In order to limit the amount of data stored on tape, a system of detectors and electronics modules selects the useful events. It is necessary to exclude the cases where no interaction took place, to identify the incoming particle as a Σ^- and select events having a topology interesting for the different channels studied by WA89.
The detectors used for the trigger were four scintillators placed in the target region, two hodoscopes (H1 and H2) and two proportional chambers (MY) located behind the Omega spectrometer.
The first two trigger scintillators were placed upstream of the experimental target, the first one (B1) in front of the TRD, and the second (B2) behind the TRD. Two other scintillators (B3 and B4) were placed after the target, behind the twelfth plane of silicon microstrips and act as interaction counters. Therefore, the first part of the vertex detectors can be treated as a target in the analysis.
The first hodoscope was placed in front of the RICH and consists of 64 scintillators of 18x100 cm^2 area. These are staggered so that they overlap by one third of their surface and cover a total area of 200x100 cm^2. The second hodoscope, placed behind the RICH, had 110 cm long counters, narrower in the central part (18 cm) and wider in the outer part (27 cm). They were arranged in a way similar to H1 and cover a total area of 300x110 cm^2.
The information provided to the trigger logic concerns the passing of particles, their multiplicity and the hit correlation between the hodoscopes and the proportional chambers. The decision to read out an event proceeds in several steps.

Definition of the beam. From the coincidence of the B1 and B2 scintillators a rate of 640000 particles per spill was obtained. Four scintillators placed at the exit of the beam channel set a veto on particles belonging to the beam halo. An upper threshold on the signal provided by B2 allows rejection of interactions which took place in the TRD. These four signals reduce the rate to 500000 per spill.
Very fast gate. The beam definition and the multiplicity signal provided by the B3 and B4 scintillators define a *Very Fast Gate*. If the multiplicity is bigger or equal two, a signal available 150 nsec after the crossing of the target is used to start some of the detectors (COROM, SVX, Lambda chambers). The rate is reduced to 13000 per spill.
Fast gate. The multiplicity information provided by H1 says if the tracks belonging to the current event lay in the acceptance of the spectrometer. If the multiplicity is higher than three, a *Fast Gate* was generated. This signal is available after 320 nsec to start the readout of all proportional chambers. (Rate of 9000 per spill).
Momentum criterion. In the channels studied in WA89, at least one baryon carrying a large fraction of the momentum in the forward direction is expected. With the position information provided by the second hodoscope behind the RICH it is possible to determine the charge of the high momentum particles. Events are selected when there was either one positive track with more than 55 GeV/c and one negative track with more than 35 GeV/c, or two positive tracks with more than 55 GeV/c each.
Matrix reduction. Low momentum particles emerging from secondary interactions in the spectrometer can give the same signature in H2 as high momentum tracks. To reject these

particles one can correlate the information of the two hodoscopes and the proportional chambers. This was done with the help of a *trigger matrix* with programmable memory modules from MBNIM standard [33]. The momentum and matrix criteria together provide the *Slow Gate* which reduces the rate to 4200 events per spill.
TRD information. As last condition the information from the TRD on the beam particle identification is used. This information is available after 910 nsec and triggers the readout of the RICH and the calorimeters.

Each *gate* has a complementary *clear* which stops the readout of the already triggered detectors and clears their readout electronics in case of rejection at the next trigger level.
In particular in 1994 a dedicated trigger for neutrons was introduced. A minimum energy deposit in SPACAL gives a *fast gate* as alternative to the normal interaction trigger. After comparison of the cluster information of SPACAL and SCITIL, charged hadrons are rejected by issuing a *very slow clear*.
On an accepted trigger signal a fast readout was performed within 500 μsec for the whole experiment. After every full readout, there is a *reset signal* which re-inizializes all readout electronics.

Data from the single spectrometer components were read out by CAMAC, FASTBUS and VME modules and then transferred to CHI (CERN Host Interface) FASTBUS modules. From there they are transferred to a central CHI connected to six DECstations which wrote the data to tape on Exabyte drives with a capacity of 2 Gbytes per cassette.

Bibliography

[1] A. Forino et al., "Proposal for a new hyperon beam experiment at the CERN SPS using the Omega facility", CERN/SPSC/87-43, SPSC/P233, August 1987
WA89 Collaboration, "Hyperon beam physics at Omega", CERN/SPSLC 92-39, SPSLC M-499, July 1992

[2] The Particle Data Group, "Review of particle properties", Phys. Rev. D3 (1994)

[3] A.N. Aleev et al., "The Λ_c^+ production by 40-70 GeV neutrons on carbon", Z. Phys. C23 (1984) 333-338
S. Barlag et al., "Measurement of the lifetime of the charmed baryon Λ_c^+", Phys. Lett. B184 (1987) 283-296
J.C. Anjos et al., "Measurement of the Λ_c^+ lifetime", Phys. Rev. Lett. 60 (1988) 1379-1385

[4] S. Brons, "Studium der Produktion von Charm-Mesonen und Charm-Baryonen aus Sigma$^-$-Kern-Wechselwirkungen" Dissertation, Universität Heidelberg, 1994

[5] P. Avery et al., "Observation of the charmed strange baryon Ξ_c^0", Phys. Rev. Lett. 62 (1989) 863-865
S. Barlag et al., "First measurement of the lifetime of the charmed strange baryon Ξ_c^0", Phys. Lett. B236 (1990) 495-500
P.L. Frabetti et al., "Measurement of the lifetime of the Ξ_c^0", Phys. Rev. Lett. 70 (1993) 2058-2061
F. Dropmann, "Der Nachweis von Zerfällen der charmed strange Baryonen Ξ_c^+ und Ξ_c^0 im Hyperonstrahlexperiment WA89", Dissertation, Universität Heidelberg, 1994

[6] S.F. Biagi et al., "Observation of a narrow state at 2.46 GeV/c^2 - a candidate for the charmed strange baryon A$^+$", Phys. Lett. B122 (1983) 455-460
S.F. Biagi et al., "Measurement of the lifetime of the charmed strange baryon A$^+$", Phys. Lett. B150 (1985) 230-241 S. Barlag et al., "Measurement of the mass and lifetime of the charmed strange baryon Ξ_c^+", Phys. Lett. B233 (1989) 522-529
P.L. Frabetti et al., "Measurement of the mass and lifetime of the Ξ_c^+", Phys. Rev. Lett. 70 (1993) 1381-1384
CLEO Collaboration, "Observation of the Ξ_c^+ charmed baryon decays to $\Sigma^+K^-\pi^+$, $\Sigma^+\overline{K}^{*0}$ and $\Lambda K^-\pi^+\pi^+$", Phys. Lett. B365 (1996) 431-436

[7] S.F. Biagi et al., "Properties of the charmed strange baryon A$^+$ and evidence for the charmed doubly strange baryon T0 at 2.74 GeV/c^2", Z. Phys. C28 (1985) 175-210
E687 Collaboration, "First measurement of the lifetime of the Ω_c^0", Phys. Lett. B357 (1995) 678-684
WA89 Collaboration, "Measurement of the Ω_c^0 lifetime", Phys. Lett. B358 (1995) 151-161
Z. Ren, "Hadronic weak decays of the charmed doubly-strange baryon Ω_c^0", Dissertation, Universität Heidelberg, 1995

[8] L. Schmitt, "Untersuchung der Lebensdauer des Baryons Ω_c^0 mit Charm und doppelter Strangeness im Hyperonenstrahlexperiment WA89", Dissertation, Universität Heidelberg, 1995

[9] S.F. Biagi et al., "First observation of Ω^* resonances", Z. Phys. C31 (1986) 33-45
S.F. Biagi et al., "Ξ^* resonances in Ξ^--Be interactions. 1. Diffractive production in the ΛK^- and $\Xi^-\pi^+\pi^-$ channels", Z. Phys. C34 (1987) 15-40

S.F. Biagi et al., "Ξ^* resonances in Ξ^--Be interactions. 2. Properties of Ξ(1820) and Ξ(1960) in the $\Lambda\overline{K}^0$ and $\Sigma^0\overline{K}^0$ channels", Z. Phys. C34 (1987) 175-199

[10] A. Trombini, "Inclusive production of Ξ^* resonances in Σ^-C and Σ^-Cu interactions at 330 GeV/c", Dissertation, Universität Heidelberg, 1992

[11] M.I. Adamovich et al., "Measurement of the polarization of $\Lambda^0, \overline{\Lambda}^0, \Sigma^+$ and Ξ^- produced in a Σ^- beam of 330 GeV/c", Z. Phys. A350 (1995) 379-386

[12] H. Rudolph, "Aufbau eines elektromagnetischen Kalorimeters und Messung der Polarisation inklusiv produzierter Λ^0 und Σ^+", Dissertation, Inst. für Kernphysik, Univ. Mainz, 1992

[13] M. Bourquin et al., "Evidence for narrow states decaying into ($\Lambda\overline{p}$ + pions) at 3.1 GeV/c^2 with charges +1, 0 and -1", Phys. Lett. B172 (1986) 113-118
H.-W. Siebert, "Evidence for the U(3100) and related states", Nucl. Phys. B (Proc. Suppl.) 21 (1991) 183-186
K. Martens, "Die Suche nach dem Zerfall U$^+$(3100) in Lambda, Antiproton und zwei positive Pionen in dem Hyperonenstrahlexperiment WA89", Dissertation, Universität Heidelberg, 1994
U. Müller, "Betrieb eines ringabbildenden Tscherenkowdetektors und Suche nach der exotischen U(3100)-Resonanz", Dissertation, Universität Mainz, 1994

[14] H.J. Lipkin, "New possibilities for exotic hadrons - anticharmed strange baryons", Phys. Lett. B195 (1987) 484-488
F. Charignon, "Étude de la production du Λ_c^+ et recherche du pentaquark dans les données de l'expérience WA89 du CERN", Grenoble, 1995

[15] R.L. Jaffe, "Perhaps a stable dihyperon", Phys. Rev. Lett. 38 (1977) 195-204
M. Godbersen, "Untersuchung von Di-Lambda Produktion in Sigma - Nukleon Wechselwirkungen", Dissertation, Universität Heidelberg, 1991
E. Alberson, Search for the H dibaryon in Σ^- - nucleon interactions", Dissertation, Universität Heidelberg, 1993

[16] H.W. Atherton et al., "Precise measurements of particle production by 400GeV/c protons on beryllium targets", CERN 80-07, August 1980
T.R. Cardello et al., "Charged-hyperon production by 400GeV protons", Phys. Rev. D32 (1985) 1-10

[17] P. Grafström, "A study of a high-energy Σ^- beam for the Omega spectrometer in the West Area", CERN/SPSC 88-4, January 1988
P. Grafström, "A Σ^- beam for the Omega spectrometer in the West Hall at CERN", CERN/SL/90-104 EA, September 1990

[18] S. Paul, "Particle identification using transition radiation detectors", CERN/PPE 91-199, November 1991
W. Brückner et al., "The transition radiation detector in the hyperon beam experiment WA89 at CERN", MPI H-V14-1995, May 1995, to be published in Nucl. Instr. and Meth. A

[19] E. H. M. Heijne et al, "Development of hardware around a silicon microstrip detector", Nucl. Instr. and Meth. 226 (1984) 63-67

[20] M. Adamovich et al, "A microstrip vertex detector for studying charm hadroproduction", Nucl. Instr. and Meth. A309 (1991) 401-410

[21] P. Jarron and M. Goyot, "A fast current sensitive preamplifier (MSD2) for the silicon microstrip detector", Nucl. Instr. and Meth. 226 (1984) 156-162

[22] J.P Avondo et al., "Low noise front-end electronics for microstrip position sensors and vertex detectors for experiments at TeV energies", Nucl. Instr. and Meth. A241 (1985) 107-114

[23] A. Beer et al., "A highly integrated trigger and readout system for a silicon micro-strip detector installed at the CERN OMEGA spectrometer", CERN/ECP 91-27, December 1991

[24] W. Beusch, "Omega Prime", CERN/SPSC/77-70 (1977)

[25] W. Beusch et al., "The RICH counter in the CERN hyperon beam experiment", Nucl. Instr. and Meth. A323 (1992) 373-379
H.-W. Siebert at al., "The Omega-RICH", Nucl. Instr. and Meth. A343 (1994) 60-67
U. Müller et al., "The recent performance of the Omega RICH detector in experiment WA89 at CERN", Nucl. Instr. and Meth. A371 (1996) 27-32

[26] U. Müller et al., "Particle identification with the RICH detector in experiment WA89 at CERN", Nucl. Instr. and Meth. A343 (1994) 279-283

[27] J. Engelfried, "Einsatz eines ringabbildenden Cherenkovzählers zur Suche nach dem exotischen Zustand U(3100)", Dissertation, Universität Heidelberg, 1992
U. Müller, "Betrieb eines ringabbildenden Tscherenkowdetektors und Suche nach der exotischen U(3100)-Resonanz", Dissertation, Universität Mainz, 1994

[28] W. Brückner et al., "The electromagnetic calorimeter in the hyperon beam experiment at CERN", Nucl. Instr. and Meth. A313 (1992) 345-356

[29] A. Simon, "Results from an integrated electromagnetic and hadronic Pb-scintillating fiber calorimeter" and "Detecting and triggering on neutrons using the SPACAL Pb-scintillating fiber calorimeter", Internal Notes, 1990-1991

[30] D. Acosta et al., "Electron-pion discrimination with a scintillating fiber calorimeter" Nucl. Instr. and Meth. A302 (1991) 36-46
D. Acosta et al., "Localizing particles showering in a spaghetti calorimeter", Nucl. Instr. and Meth. A305 (1991) 55-70
D. Acosta et al., "Electron, pion and multiparticle detection with a lead/scintillating-fiber calorimeter", Nucl. Instr. and Meth. A308 (1991) 481-508

[31] M. Beck et al., "A scintillating tile hodoscope with WLS fibre readout", Nucl. Instr. and Meth. A355 (1995) 351-358

[32] C.V. Scheel, "The spaghetti calorimeter", PhD thesis, Amsterdam University, NIKHEF, 1994

[33] W. Beusch et al., "A fast on-line trigger for events with multiple high transverse momuntum tracks", Nucl. Instr. and Meth. A249 (1986) 391-398

Chapter 5

Charm reconstruction and analysis methods

Raw data collected in WA89 during the 1993 beam period were treated for charm analysis in several steps.
They were first of all processed in a standard procedure called *data production* in order to perform the basic event reconstruction. This procedure consists of two main steps. First tracks are reconstructed and the momentum is determined for particles crossing the Omega spectrometer.
The second step takes care of particle reconstruction and identification. Two-prong V0 decays of Λs and K^0s, and Ξ and Ω hyperon decays are reconstructed. Additional packages for subdetectors like the TRD, the RICH, the lead glass calorimeter and SPACAL, are also used. They provide information about the beam particle identity, the RICH identification for decay daughters, and finally photon, π^0, and neutron detection.

The search for charmed hadrons was then performed using a dedicated package called *xip2*. The strategies used for the candidate search, the primary vertex reconstruction and event selection will be described in the central part of this chapter. The method used for the determination of charm hadron lifetimes is presented in the last section.

5.1 Track reconstruction

The track reconstruction is done with TRIDENT [1], a software package developed for the CERN Omega spectrometer, modified and adapted to the WA89 setup. The program reconstructs single tracks and for particles traversing the magnetic field region the momentum is calculated.
First, track segments are reconstructed separately for the various tracking detectors. In particular, this is done sequentially for the lever-arm and the proportional chambers of the Omega spectrometer, the Octogon and Lambda chambers, and finally for the silicon microstrips.
The procedure to find the track segments is different for the various subdetectors. For the chambers inside Omega and behind it, space points are found by combining the hit information from different projections of each multi-chamber package. These space points

are then used to fit a curved track from which the particle momentum and charge sign are determined.

For the chambers in the decay region, individual projections are first reconstructed and then combined to form space tracks.

The same procedure is followed in the microstrips. The y, z, and s projections are first fitted separately. Then the program tries to merge them to form space tracks. If one z, one y, and one s projection are found to fit a space track, this is unambiguously determined and hits found in the t planes are attached to further improve the track fit. If only two of the three projections are found, the program requires hits in the t planes and uses them to resolve ambiguities (no projection can be reconstructed from three t planes, but the hits still provide very useful information).

A significant improvement of track reconstruction in the vertex region was obtained with the addition of the SVX detectors in 1993. Their high detection efficiency and the four projections measured by them allow a higher yield of space tracks being formed from projections.

A cross section of the target area with tracks reconstructed in the microstrip detectors is shown in figure 5.1. On the left side the beam track is visible, detected by the beam silicon counters. The four interaction targets are then followed by the microstrip vertex detectors.

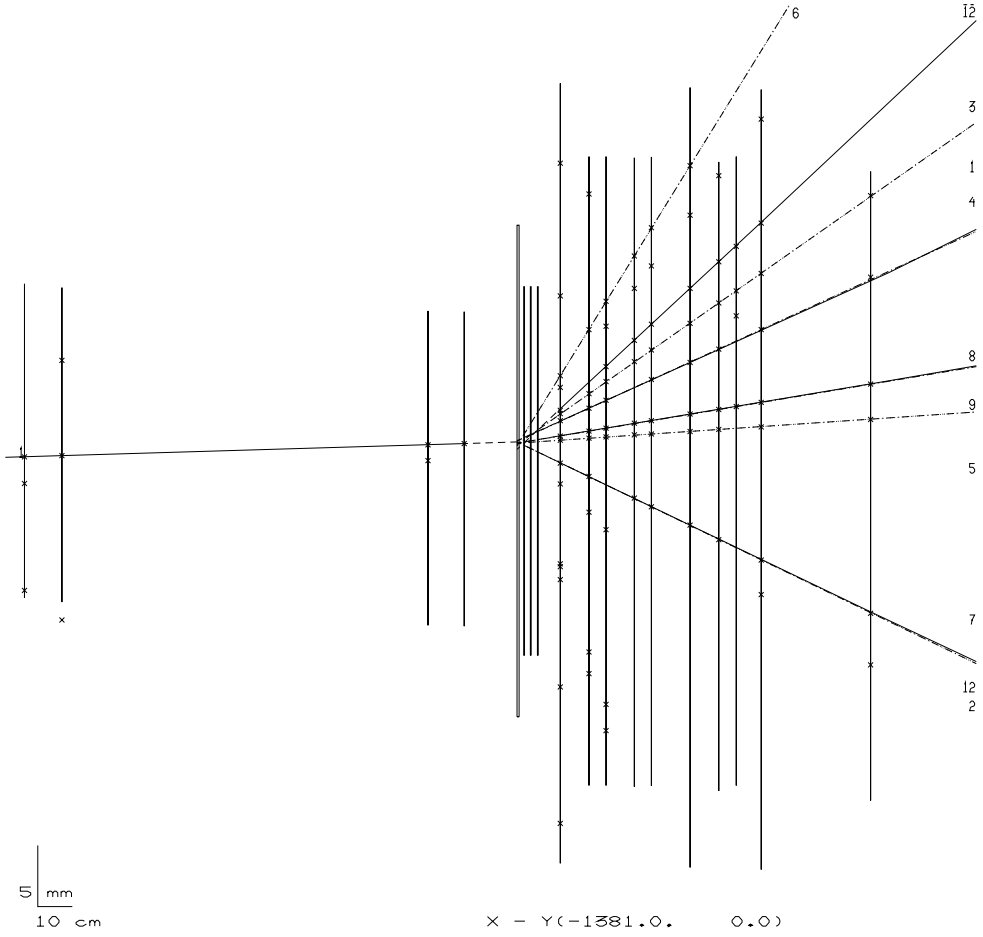

Figure 5.1: Tracks reconstructed in the WA89 microstrip vertex detector.

In the second step, the single segments are bridged to each other to form full tracks. The bridging procedure starts from the downstream part of the apparatus, where tracks are better separated from each other, and proceeds backwards to the vertex region.

Once a microstrip space segment has been bridged to a track from the downstream chambers, the measured momentum is used to perform a correlated fit of the microstrip segment to properly take into account the effect of multiple scattering. In addition the result of the pattern recognition is revised, unused hits or unused projections can be recuperated and hits with a significant deviation from the track can be rejected.

Figure 5.2 shows one event reconstructed by TRIDENT with all tracking detectors. On the left the beam and the vertex microstrip detectors are shown, followed by the M1, the Lambda and the Octogon chambers. The rectangular box indicates the Omega magnet with the spectrometer chambers, followed by the lever-arm chambers.

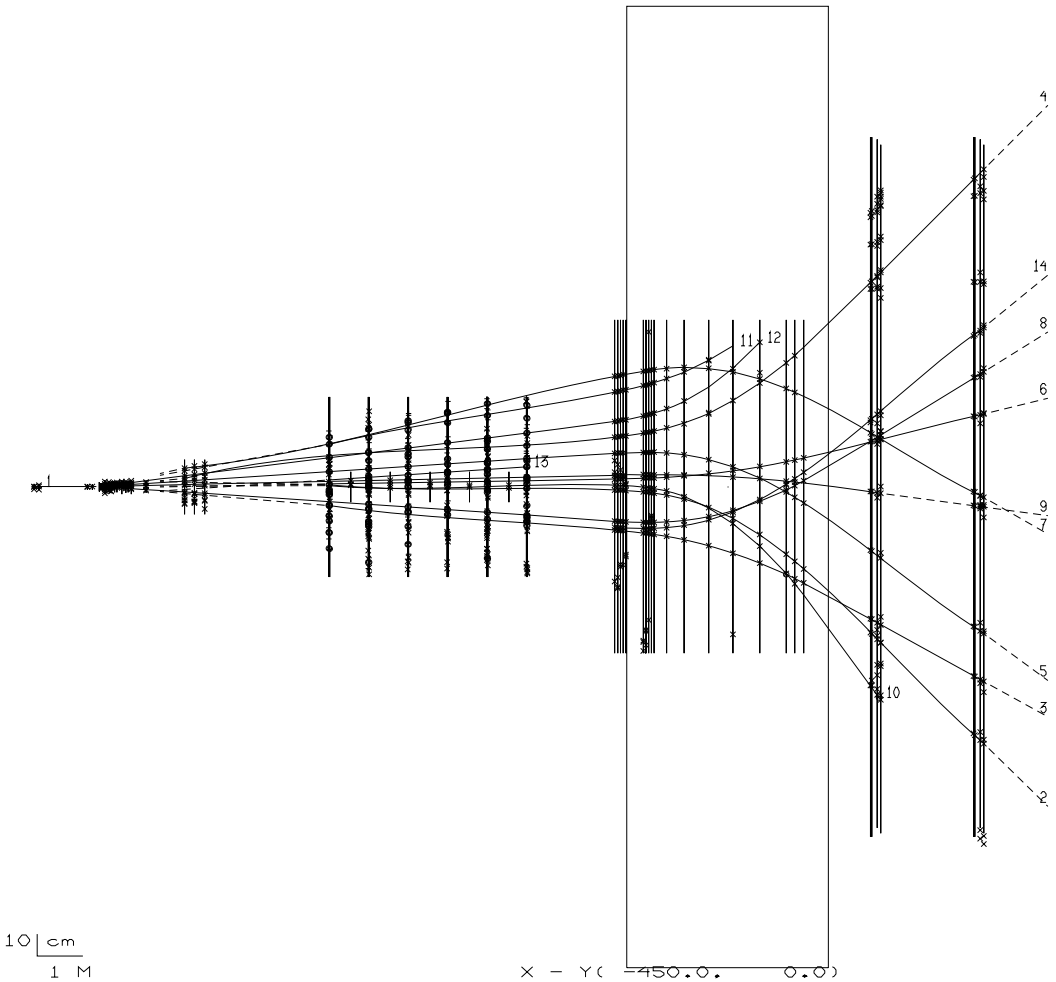

Figure 5.2: WA89 event reconstructed by TRIDENT using all tracking detectors: the microstrip planes on the left, followed by the M1, Lambda and Octogon chambers; the Omega spectrometer (in the box) and the lever-arm chambers behind Omega (the last planes on the right).

The track bridging and reconstruction efficiencies are estimated using minimum bias Monte Carlo events. The following numbers refer to all particles with momentum higher than 2 GeV/c. For lower momenta efficiencies drop sharply due to acceptance limitations and stronger multiple scattering effects.
The tracking efficiency in the Omega chambers, in the decay region and in the microstrip detectors is equal to 93.9%, 82.5% and 97.3% respectively. The bridging efficiency is about 93% and the overall reconstruction efficiency for the momentum range indicated is approximately 86%.

5.2 Particle reconstruction

The reconstruction of special types of particles such as V0s, Ξs and Ωs, and the analysis of data provided by detectors not used for the tracking are done within the frame of the PHYNIX package.
The program has a main part called SKELETON which can be used for selecting and writing data, and can call a set of different packages:

- *TRD* for offline TRD data analysis;
- *RICH* for the RICH data analysis;
- *V0* for the reconstruction of Λ^0, K^0_S, Ξ^-, Ω^- and their antiparticles;
- *LG* for the lead glass data analysis;
- *SPACAL* for the analysis of the hadronic calorimeter data;
- optional packages for the individual user's specific data analysis.

The program is very flexible and controlled via a file listing desired options.
In the standard procedure for the WA89 data production the *V0*, the *RICH* and the *LG* packages are always implemented. During the processing, several streams are saved. Apart from the one containing all events, there are other streams based on the selection of reconstructed particles, like V0s, proton-kaon combinations, etc. The output is normally written in DST (Data Summary Tape) format.
For the analysis presented in the following chapter, the information provided by the *V0* package and the particle identification based on the RICH data analysis were extensively used.

5.2.1 Two-prong V0 decays of Λ and K^0

The *V0* package provides an identification of Λ^0, $\overline{\Lambda}^0$, and K^0_S particles based on the kinematic reconstruction of their decay into one positive and one negative particle. The cascade decays of Ξ^-, $\overline{\Xi}^+$, Ω^- and $\overline{\Omega}^+$ are searched for, using the identified V0 particles.

The *V0* package consists of three main parts: first two-prong vertices of tracks with opposite charge are reconstructed; then the invariant mass is calculated and the V0s are

selected according to mass, geometry and quality criteria; finally the search for Ξs and Ωs is performed.

The reconstructed decay channels, the corresponding branching ratios and the world average values of the lifetimes are listed in table 5.1.

Reconstructed decay channel	Branching ratio (%)	Lifetime (x10^{-10} sec)
$\Lambda^0 \to p\pi^-$ $\overline{\Lambda}^0 \to \overline{p}\pi^+$	63.9 ± 0.5	2.632 ± 0.020
$K_S^0 \to \pi^+\pi^-$	68.61 ± 0.28	0.8926 ± 0.0012
$\Xi^- \to \Lambda^0\pi^-$ $\overline{\Xi}^+ \to \overline{\Lambda}^0\pi^+$	99.887 ± 0.035	1.639 ± 0.015
$\Omega^- \to \Lambda^0 K^-$ $\overline{\Omega}^+ \to \overline{\Lambda}^0 K^+$	67.8 ± 0.7	0.822 ± 0.012

Table 5.1: V0, Ξ and Ω decay channels reconstructed in the *V0* package, with the corresponding branching ratios and lifetimes (data are taken from reference [2]).

Two-prong vertices are reconstructed considering track pairs with opposite charge starting in the same detector region (microstrips, Lambda chambers or Omega spectrometer). Their closest distance of approach (CDA) and vertex position are calculated and are used to select candidates. A vertex is accepted if the CDA is below a certain limit (50 μm if the tracks start in the microstrips, 5 mm in the Lambda chambers and 3 cm in Omega) and if the vertex is clearly separated from the preliminary reconstructed position of the main interaction point (the separation must be more than 2 cm for two-prong vertices in the microstrips and more than 12 cm in the Lambda chambers).

The invariant mass for each accepted two-prong vertex is calculated for the mass hypotheses of the Λ, $\overline{\Lambda}$ and K_S^0 decay channels listed in the above table. Candidates are selected as V0s if the difference between the reconstructed and the reference mass is less than $\pm$ 25 MeV/c^2. Decays with reconstructed mass in the intervals [-75,-25] MeV/c^2 and [+25,+75] MeV/c^2 are marked as sideband events for background studies. The error of the reconstructed mass for a given particle is estimated as a function of its momentum, and the location of the first measured points of the decay tracks, using empirical correlations.

The kinematic identification is, however, not unambiguous over the whole phase space and one vertex can be associated with more than one V0 particle. This occurs for some particular angles between the two daughter particles. The consequence is an ambiguity between Λ^0s and K^0s which, for 1993 data, affects about 1.7% of all recorded events.

The mass distributions for K_S^0 and Λ particles reconstructed by the *V0* package using part of 1993 data are shown in figure 5.3.

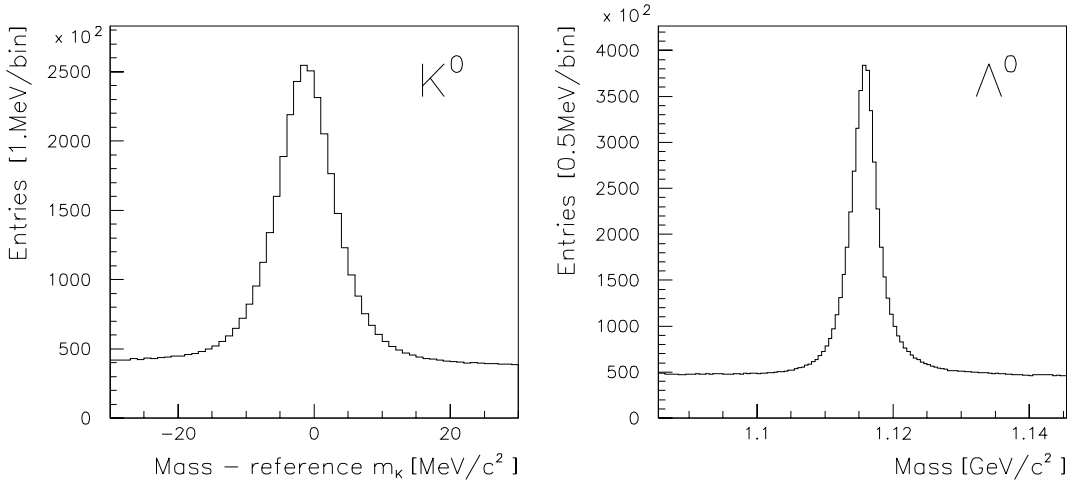

Figure 5.3: Sample of K^0s and Λ^0s reconstructed by the *V*0 package using 1993 data.

5.2.2 Ξ and Ω reconstruction

The third step of the *V0* package is dedicated to the search for the cascade decays of Ξs and Ωs given in table 5.1. The extrapolated track of Λs and $\overline{\Lambda}$s found in the decay region and inside the Omega spectrometer are combined with the remaining charged tracks starting in the Lambda chambers.
If the CDA of the Λ and the charged track is smaller than 3 cm, the invariant mass is calculated considering the various decay hypotheses. Candidates are accepted if the difference between the reconstructed and the reference mass is in the range of ± 25 MeV/c^2. Other entries in the $\pm$ 75 MeV/c^2 mass window are used for background studies.

Since Ξ^-s and Ω^-s are charged particles, they leave a track in the vertex detector before they decay. Consequently, to improve the purity of the Ξ and Ω sample, the attempt is made to bridge the candidates to unused tracks reconstructed in the microstrip detectors. The background is much lower for the matched hyperons.
It is also possible to assign the measured momentum to the microstrip track and refit it taking into account multiple scattering effects.

A further selection is done with the following criteria:

- good quality of the bridging to the microstrip track;
- check whether the decay Λ shares any track with a K^0_S and flag ambiguous cases;
- the quality of the reconstructed Λ is checked: its mass should lie in a window of $\pm 2.5\ \sigma$.

Figure 5.4 shows the mass plots for the reconstructed Ξ^-s from part of the 1993 data. On the left all Ξ^- decays are shown, while on the right only the candidates successfully bridged to microstrip tracks and for which $\Lambda - K^0_S$ ambiguous cases have been rejected are plotted.

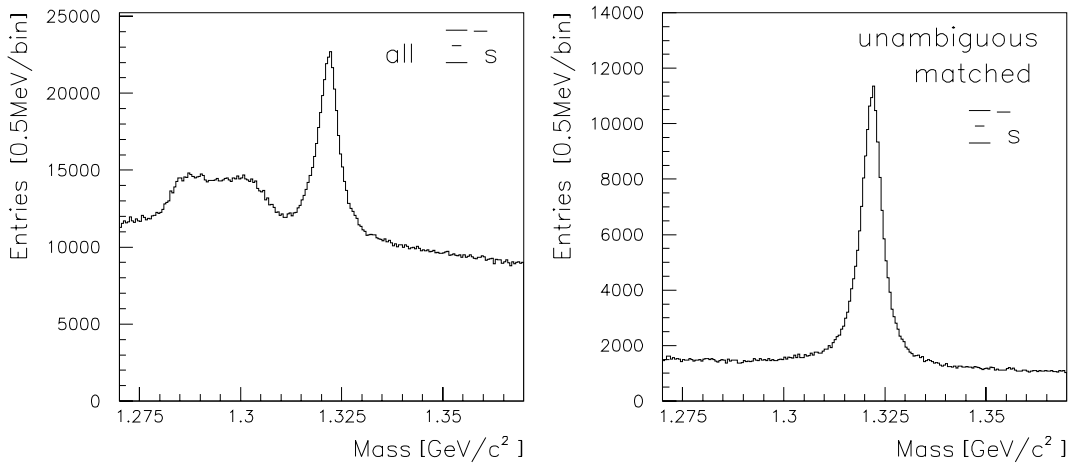

Figure 5.4: Sample of Ξ^-s reconstructed by the $V0$ package using approximately half of 1993 data. On the left all found Ξ^-s are shown: the shoulder on the left side of the peak is due to ambiguities between Λs and K^0s. The plot on the right shows only the cascades which are bridged to microstrip tracks and for which the ambiguous cases have been rejected.

5.2.3 RICH particle identification

Figure 5.5 shows one event reconstructed in the RICH detector. The five drift chambers are indicated by the rectangular boxes. The figure shows the hits recorded in the RICH chambers, the track impact points extrapolated from the Omega spectrometer (indicated by crosses) and the predicted rings for the pion mass hypothesis. The charge and momentum of the extrapolated tracks are shown on the bottom.

For each charged track falling within the geometrical acceptance of the RICH detector, the RICH package assigns a likelihood for it to be a proton, a K^-, a π^- or an electron or the corresponding antiparticles. Tracks are extrapolated from the spectrometer to predict ring centers and the radii of the different mass hypotheses. After hit reconstruction in the RICH chambers and some noise reduction, a maximum likelihood method is applied.
It is assumed that the measured coordinates of each Cherenkov photon are described by a probability density function (p.d.f.) which depends on the particle hypothesis. So for each possible hypothesis j we assume a p.d.f. $f_j(\vec{x}^{(i)})$ to observe photon i at its measured position $\vec{x}^{(i)}$.
If m photons are observed, the joint probability to find all m photons at their measured positions is given by:

$$\prod_{i=1}^{m} f_j(\vec{x}^{(i)}) d\vec{x} \tag{5.1}$$

Furthermore the Cherenkov photons are distributed over a ring of radius R_j for the hypothesis j. As the spatial resolution is finite, a Gaussian distribution $r^{(i)}$ is assumed for the photon radii.

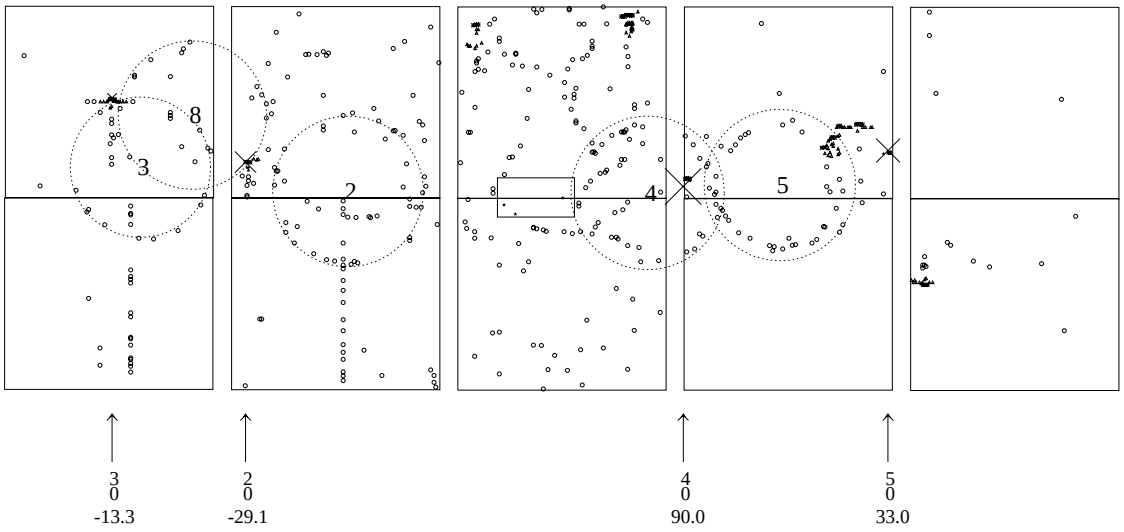

Figure 5.5: Event reconstructed in the RICH detector. The track impact points extrapolated from Omega are indicated by crosses and the predicted rings for the pion mass hypothesis are drawn. The numbers in the last row give the particle charge and momentum.

Assuming a certain distribution B of background hits, constant over a surface A and not depending on the hypothesis j, and integrating the signal and noise distributions over A, the analytical expression for the p.d.f. $f_j(\vec{x}^{(i)})$ is obtained. Next, we take into account the probability of observing exactly m photons, which should follow a Poissonian distribution

$$\frac{e^{-p_j} p_j^m}{m!} \tag{5.2}$$

where p_j is the sum of the expected number of signal and background photons in the surface A.

The likelihood function for hypothesis j is

$$L_j = \frac{e^{-p_j} p_j^m}{m!} \prod_{i=1}^{m} f_j(\vec{x}^{(i)}) \tag{5.3}$$

For all particles traversing the RICH the value of the likelihood function is calculated for each hypothesis: L_e, L_π, L_K and L_p respectively for the electron, pion, kaon, and proton hypothesis. If a particle is below threshold (γ<41) it is supposed to produce no Cherenkov light and only noise hits should be detected. In this case the background likelihood $L_0 = \frac{e^{-b} b^m}{m!} B^m$ is evaluated and considered.
The RICH acceptance also drops rather fast for particles with momentum lower than about 12 GeV/c^2, giving a low efficiency for particles with a momentum below this limit.

The RICH information is stored in PHYNIX common blocks and can be later used in the event analysis. The content of the information depends on the particle momentum p and

can be summarized as shown in table 5.2. A particle is considered out of acceptance if less than half a ring is seen within the chambers.

RICH word stored	1	2	3	4	5
$p \geq 45$ GeV/c	L_0	L_e	L_π	L_K	L_p
25 GeV/c$\leq p <$45 GeV/c	-1	L_e	L_π	L_K	L_0
$p <$25 GeV/c	-2	L_e	L_π	L_0	L_0
out of acceptance	-100	-100	-100	-100	-100

Table 5.2: RICH information stored in PHYNIX, depending on the particle momentum, for the different mass hypotheses.

Generally during the analysis, for the particles under study we calculate the ratio

$$R_j = \frac{L_j}{max(L_i, i = p, K, \pi, e, noise; i \neq j)} \tag{5.4}$$

The mass hypothesis for which R_j is maximum is the most likely. Such information can be used to positively identify particles (asking for the relative ratio to be bigger than all other hypotheses) or to identify them negatively (rejecting the cases where other mass hypotheses are more probable than a certain limit).

An example of the use of RICH cuts is shown in figure 5.6. The invariant mass of K^+K^- two prong vertices is calculated to reconstruct ϕ decays. In the first plot on the left it is only required that the kaons are in the RICH acceptance. In the middle plot only the negative kaon is positively identified while in the last plot both kaons are positively identified.

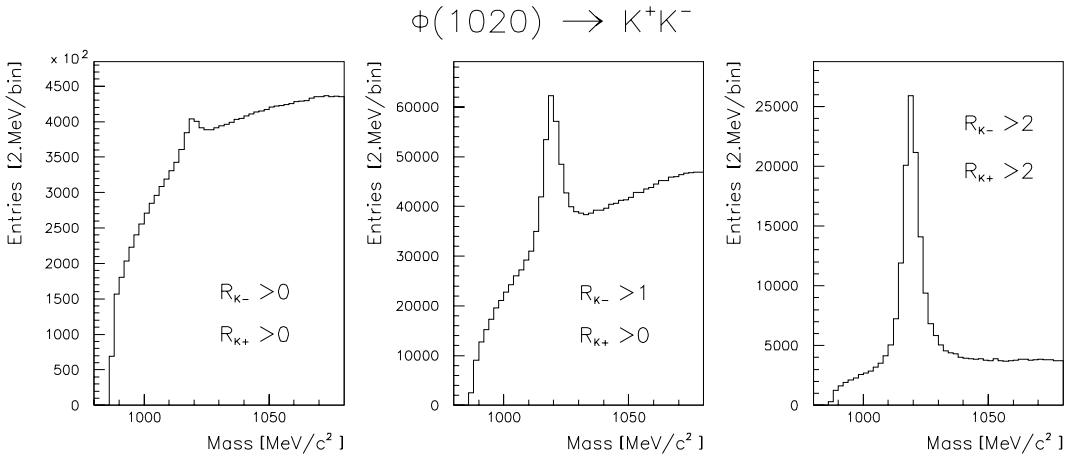

Figure 5.6: Reconstruction of the $\phi(1020) \rightarrow K^+K^-$ decay applying RICH cuts for the two charged daughters.

5.3 Charm reconstruction with *xip2*

The search for charmed hadrons was performed using the *xip2* code, based on a "candidate driven approach". This approach consists of forming candidates for the defined decay channel using space tracks provided by the basic reconstruction packages. The combinations found are selected on the base of mass, geometry, and quality criteria and, for the accepted candidates, the remaining tracks are used to search for a well defined primary vertex. If this is also found, all relations between primary and secondary vertices are determined and events are selected according to quality criteria. On the selected events a more precise cut optimization procedure is performed interactively to isolate the signal from background events.
In the following I will describe these steps in more detail. In particular, more studies have been made of the main vertex in order to optimize the track selection and the vertex reconstruction.

5.3.1 Charm candidate selection

The chosen decay channel is defined describing the daughter particles, their identity and their charge. For all particles reconstructed in the apparatus arrays are filled with the track parameters and the momentum information provided by PHYNIX common blocks.
Among all recorded space tracks which could be used as daughters of the searched hadron, "good" tracks are selected according to the following criteria:

- space and projection tracks for which the covariance matrix is not invertible are rejected, as they cannot be used for any vertex reconstruction;
- tracks identified as daughters of V0s, Ξs and Ωs (and their antiparticles) are excluded as well as microstrip space or projection tracks which have been bridged to hyperons;
- charged tracks must have their first measured point in the microstrip planes; if they start in more downstream detectors, they will not be used to form candidates;
- V0s, Ξs and Ωs are accepted only if their reconstructed mass lies in a certain window around the reference mass;
- V0s sharing one or two tracks are rejected;
- hyperons bridged to two microstrip projections rather than to a space track may also be rejected.

With the selected good tracks, all combinations are tried in order to form candidates. Combinations where a track is used more than once are rejected. For each used track the available RICH information is checked and a bit mask is set accordingly. This is then compared with a mask of imposed cuts. If the required conditions are not satisfied, the combination is dropped. The default configuration of conditions corresponds to no effective cut. The user can impose various requirements, both for positive and for negative identification of one or more particles.

For all found candidates, the invariant mass is calculated and compared with the reference mass of the searched particle. If the difference is below a predefined limit (generally 200-300 MeV/c^2 to allow for sideband studies), the combination is accepted and the secondary vertex is fitted.

The user can set several cuts concerning the secondary vertex in FFREAD cards and they are applied here to further select interesting candidates. The cuts normally used are listed below:

- the maximum distance between every pair of tracks in the candidate must be smaller than an upper limit (usually chosen between 300 μm and 1 mm);
- bad fits are rejected;
- the quality of the vertex (expressed as probability or χ^2) is checked and, if it is above the set limit, the combination is excluded. Normally the upper limit is set to 10-30 for the vertex χ^2 divided by the numbers of degrees of freedom.

For all candidates passing these cuts the code proceeds looking for a corresponding main vertex.
For the secondary vertex of the candidates finally selected, the following quantities are stored for the later analysis:

- the vertex position in the x coordinate and the relative error *secxe*;
- the vertex quality, *secqual* which can be expressed as probability or by the corresponding χ^2;
- the closest distance of approach of individual daughter tracks to the reconstructed vertex (*seccda*);
- the maximum distance between pairs of tracks in the candidate (*secdmax*).

Figure 5.7 shows the distributions of the quantities mentioned above for a sample of candidates for the $\Xi_c^+ \to \Xi^-\pi^+\pi^+$ decay before applying any selection. This channel is a good representative example: it has a three-prong secondary vertex including a cascade hyperon. For this reason it has been chosen to show the following plots.
The top left plot shows the distribution of the error on the secondary vertex position for the different targets: the copper layer, the group of three slices of diamond, and the first microstrip planes. The errors are higher for copper than for diamond due to stronger effects from multiple scattering. The top right plot shows the secondary vertex quality expressed as χ^2. The bottom left histogram shows the distribution of the closest distance of approach of candidate tracks to the reconstructed secondary vertex. The mean value is approximately 31 μm.
On the bottom right the distribution of the maximum distance between pairs of tracks in the candidate is plotted. The mean value is about 42 μm.

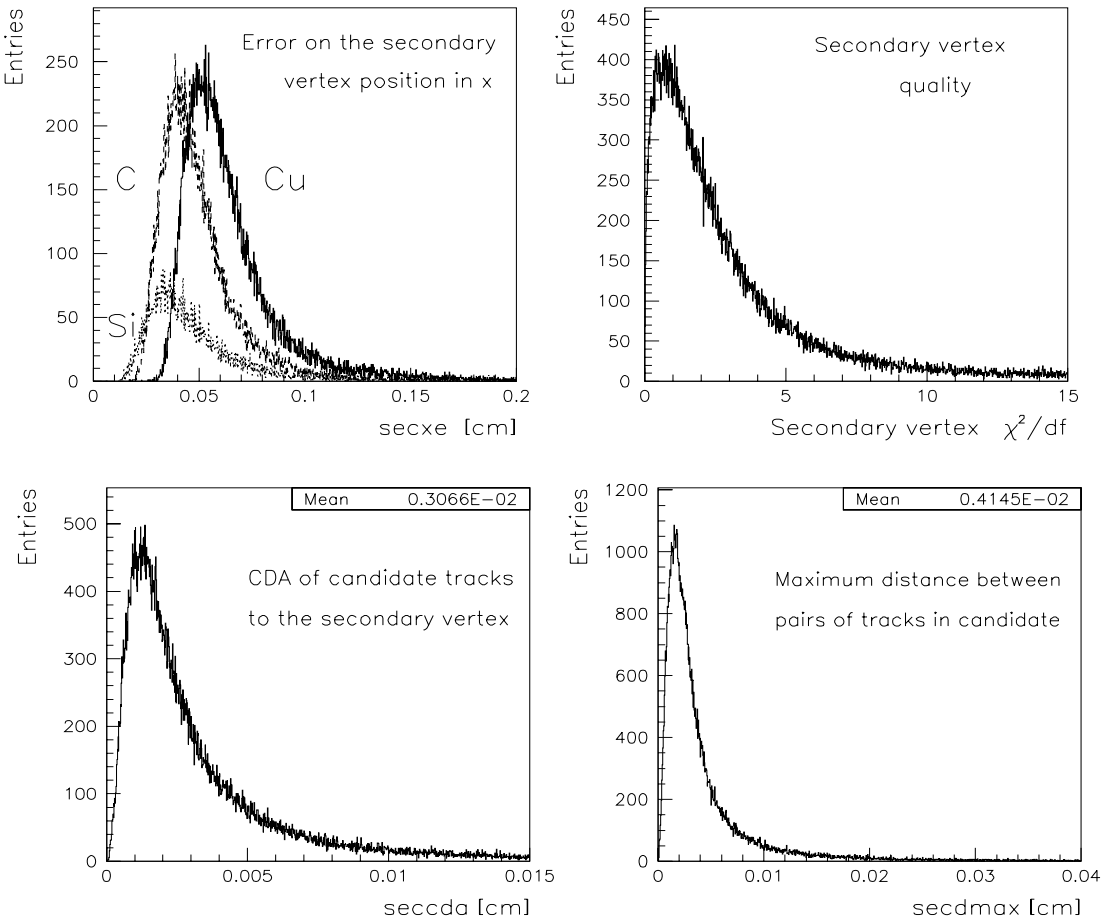

Figure 5.7: Distribution of the secondary vertex parameters for a three charged prong decay. See the text for further comments.

5.3.2 Main vertex reconstruction

For each candidate found, the code tries to reconstruct a main or primary vertex which satisfies quality criteria.

First of all, tracks which can be used to form the main vertex are collected. The user can choose to use only space tracks or include also projections; to keep or to exclude microstrip segments which are not bridged to tracks in the spectrometer and consequently have no momentum measured; to include the beam track or not.

All channels studied here always include the beam and non-momentum tracks (to which a 5 GeV/c momentum was assigned), but the y and z projections not matched to space tracks were rejected.

Among the chosen tracks a selection is performed following the same criteria listed for the charm candidate search. In addition the tracks used for the corresponding candidate are flagged and excluded, microstrip tracks bridged to cascades can be recuperated and used, and finally the hit pattern in the microstrip detectors is checked for all considered tracks. The user can require the first measured point of each track not to be too far downstream (in number of silicon planes) with respect to the secondary vertex. This check is done to exclude tracks starting clearly downstream of the candidate decay vertex.

A further filter on microstrip space tracks is performed to exclude probable beam tracks (from pile-up or interacting more downstream); tracks with bad quality of the matching of the two projections; tracks with a suspicious (for example, very discontinuous) hit pattern.

The procedure to form the main vertex with the selected tracks is as follows:

- The intersection of every pair of tracks is calculated. With this information the intersection volume defined by all considered tracks is estimated and compared with a *box* value imposed by the user as maximum volume for the main vertex. Track pairs are then excluded one by one and the volume is estimated for every configuration. The procedure continues until the vertex volume is smaller than the preset *box*;

- With the surviving tracks (if there are at least three) a vertex is fitted and the relative probability is evaluated. This is compared with the user's requirement on the vertex quality (*mvx_prej*). If the cut is not satisfied, a multi step track rejection mechanism starts;

- If the ratio of the χ^2 of the worst track to the χ^2 of the second worst track is higher than a *mvx_1rej* cut imposed by the user the worst track is rejected. This step is intended to immediately exclude tracks with evident very low quality;

- Among the remaining *n* tracks, each is excluded in turn and the vertex probability is calculated. The best combination of *(n-1)* tracks is selected and for that one the probability is again compared with the *mvx_prej* cut;

- If the quality cut is satisfied, the vertex is accepted. Otherwise the rejection mechanism on the *(n-1)* track combination starts again from the point described two steps before. The procedure continues until a good vertex is found or stops when less than three tracks are left. If no vertex is found, the candidate is rejected.

For the found main vertices, the following parameters are calculated and stored for later analysis:

- the vertex position in the longitudinal coordinate *x* and the relative error (*mainxe*);

- the main vertex quality *mainqual* expressed as χ^2 or as probability;

- the closest distance of approach of individual tracks to the reconstructed main vertex (*maincda*);

- the number of degrees of freedom of the vertex *maindf*, depending on the number of tracks included in the fitted vertex, and their type (space tracks, beam if it is used, projections, other non-momentum tracks).

The distribution of the reconstructed *x* position of main vertices for minimum bias events is shown in figure 5.8. Besides the main copper and diamond targets, the first 12 microstrip planes of the vertex detector are also considered as interaction target.

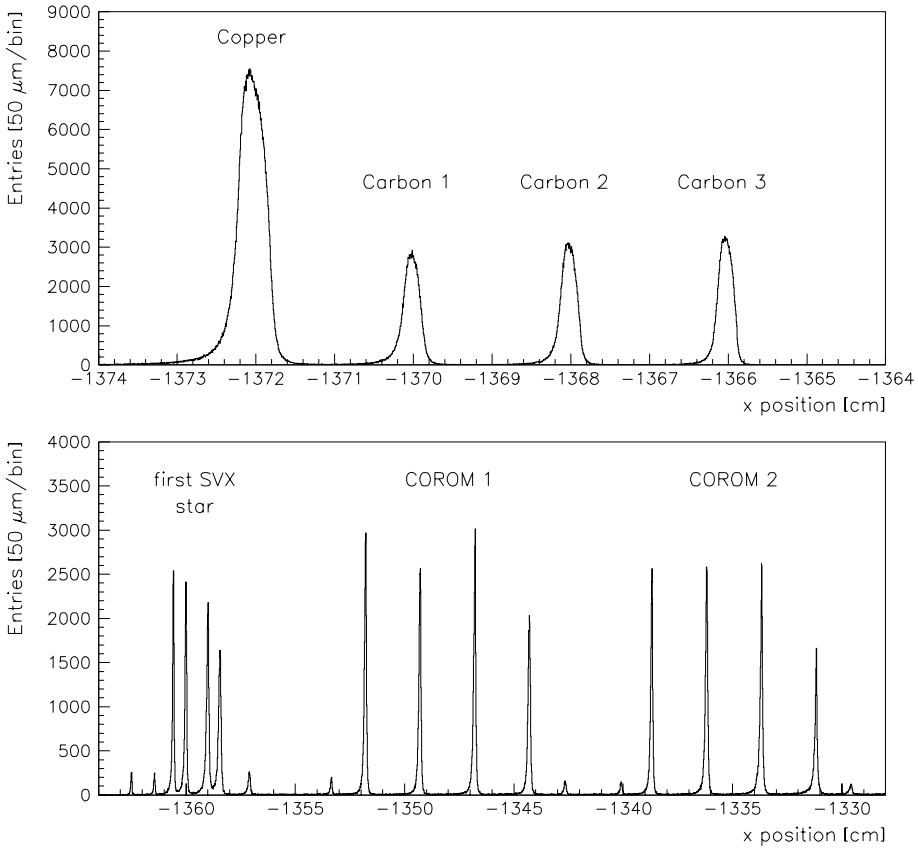

Figure 5.8: Distribution of the reconstructed x position of main vertices in copper and diamond and in the first 12 planes of silicon microstrips.

Figure 5.9 shows the calculated error on the main vertex position in x for the different targets. The better resolution in the case of the diamond and silicon targets is evident.

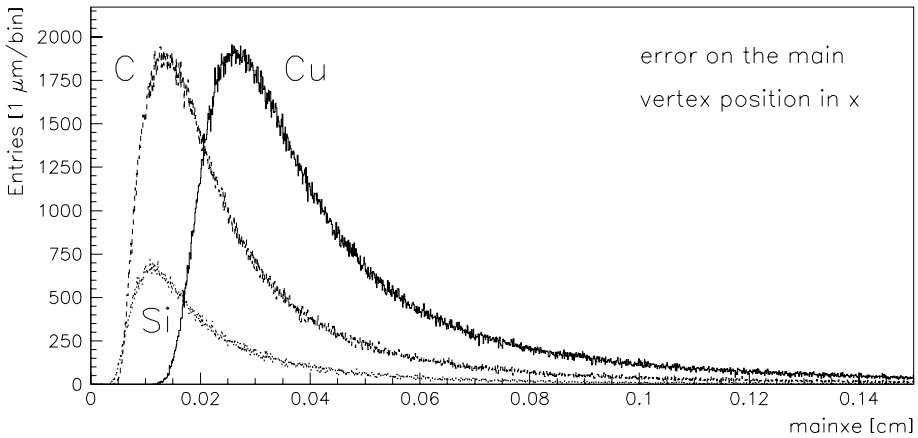

Figure 5.9: Distribution of the calculated error on the x position of main vertices found in the copper, diamond and silicon targets respectively.

The dependence of the main vertex quality on the applied cuts (*box*, *mvx_1rej* and *mvx_prej*) has been studied in order to optimize the primary vertex selection.
Figure 5.10 shows the main vertex probability distribution depending on different applied cuts. The starting configuration (first histogram on top on the left and central histogram in the second and third row) corresponds to the requirements:

$$box \leq 1 \text{ cm}^3 \text{ ; } mvx\_1rej = 10 \text{ ; } mvx\_prej \geq 1\%$$

The other histograms show the behaviour of the calculated probability for different cuts. Only one cut is varied in each case and its new value is indicated in the figure.

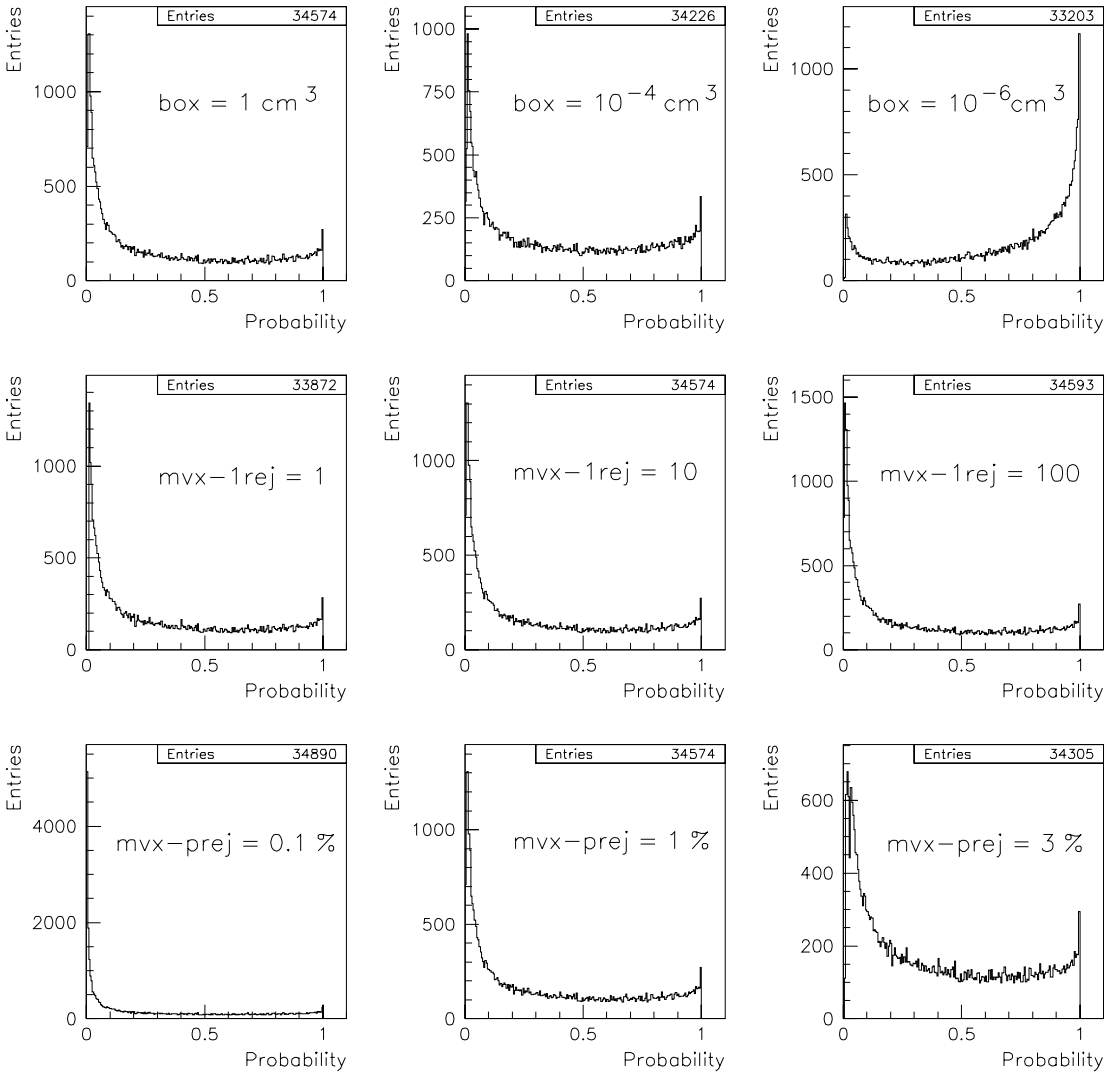

Figure 5.10: Distribution of the main vertex probability for different sets of cuts (see the text for further explanations).

If all (and only) good vertices are correctly reconstructed, the probability has a flat distribution between 0 and 1. In reality also fake vertices are found and they populate the region at low values of probability giving the visible rise towards 0. In other cases too

many tracks can be rejected and vertices are reconstructed with very few tracks. These vertices can have higher probability and cause a rise of the probability distribution at 1.
An example of the latter case is given in the top right plot in figure 5.10. If the main vertex volume is requested to be smaller than 10^{-6} cm^3, too many tracks are rejected. The resulting distribution is artificially distorted towards values with higher probability. For box values between 10^{-4} and 1 cm^3 the probability distribution shows a normal behaviour and this range will be considered for the volume cut.
No clear dependence of the probability distribution on the variation of the *mvx_prej* cut is visible from the plots in the second row, indicating that this cut is not crucial for the selection of primary vertices. For the variation of the cut on the main vertex probability (last row) the distributions are rather similar. However for a cut at low values like 0.1%, the rise towards 0 becomes very prominent. Consequently higher probability cuts will be always used.

The distribution of the main vertex quality expressed as χ^2 depending on different applied cuts is shown in figure 5.11.

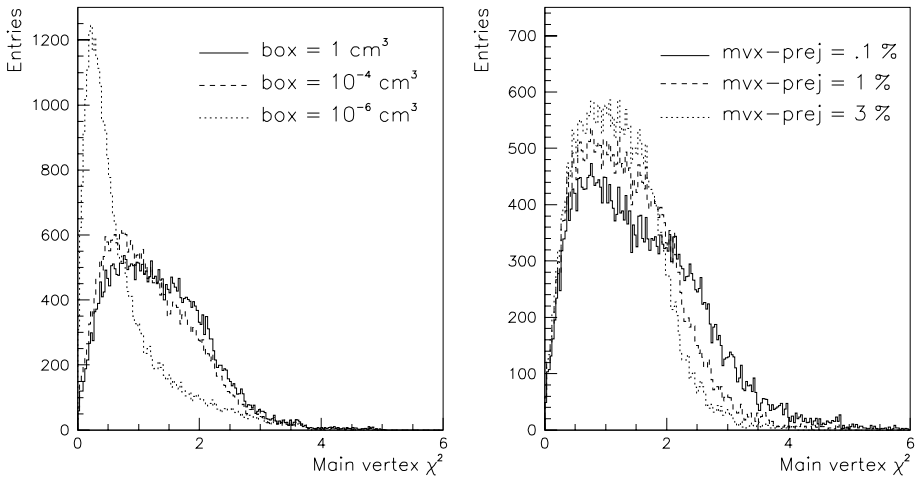

Figure 5.11: Distribution of the main vertex quality expressed as χ^2 for different sets of cuts.

The composition of the reconstructed main vertices depending on the different sets of cuts is summarized in table 5.3. In particular, the mean number of tracks, of space tracks, of microstrip non-momentum tracks, and the percentage of cases where the beam track is included are listed.
The main vertex composition confirms the observations given above. A too small vertex box causes the loss of many useful tracks. The request of a too high vertex probability also causes the loss of useful tracks, but to a lesser degree.

The study of these distributions guided the choice of the cuts used for the search of charm candidates. The volume of the main was normally requested to be lower than 1 cm^3; the *mvx_prej* parameter was set to 10, in order to slightly increase the speed of the routine; the probability cut was chosen between 0.5 and 2%.

box	mvx_1rej	mvx_prej	all tracks	space tracks	other tracks	with beam
1 cm^3	10	1%	5.73	3.73	2.08	82.7%
10^{-4} cm^3	10	1%	5.30	3.54	1.95	78.8%
10^{-6} cm^3	10	1%	3.79	2.82	1.52	50.1%
1 cm^3	1	1%	5.71	3.72	2.07	81.8%
1 cm^3	100	1%	5.74	3.73	2.08	82.7%
1 cm^3	10	0.1%	5.77	3.54	2.11	82.8%
1 cm^3	10	3%	5.66	3.72	2.00	81.9%

Table 5.3: Average track composition of main vertices for different sets of applied cuts. In particular the mean number of all tracks, of space tracks and of non-momentum tracks is listed and, in the last column, the percentage of cases in which is beam track is included.

5.3.3 Separation and impact parameters

The possibility to reconstruct the production and the decay point of short living particles as well identified and separated vertices is very important in the search for charmed hadrons and it is an essential condition in order to measure their lifetime.

Topological cuts on the separation between vertices and on the impact parameter of the candidate and of its individual daughters with respect to the primary vertex are a useful tool to reject background events.

After the determination of the main and the secondary vertex of a given candidate, the separation in space and in the longitudinal direction and their errors are calculated.

For each vertex the errors in the three coordinates define an ellipsoid (normally the error in the longitudinal direction is sensibly larger than in the transversal plane). The error on the separation in space is calculated as illustrated in figure 5.12. The main and the secondary vertex are connected by a segment (d_s). Its intersections with the two error ellipsoids determine the values σ_1 and σ_2. These are combined to give the total error $\sigma = \sqrt{\sigma_1^2 + \sigma_2^2}$.

In the following step impact parameters are evaluated and stored.

The total impact parameter is given by the distance of the extrapolated track of the candidate from the main vertex, shown as b_{cand} in figure 5.13. Because the charm candidate should emerge from the primary interaction point, its extrapolated track should point to it. Therefore the total impact parameter is requested to be small.

The impact parameter of each individual daughter track to the main vertex is also calculated. The decay products should not all point to the main vertex. Requesting that one or more of them have a large impact parameter, helps to reject candidates built from tracks emerging directly from the primary interaction point. *xip*2 stores the information about the minimum and the maximum values of the individual impact parameters and the corresponding errors. These variables can be used to optimize the candidate selection.

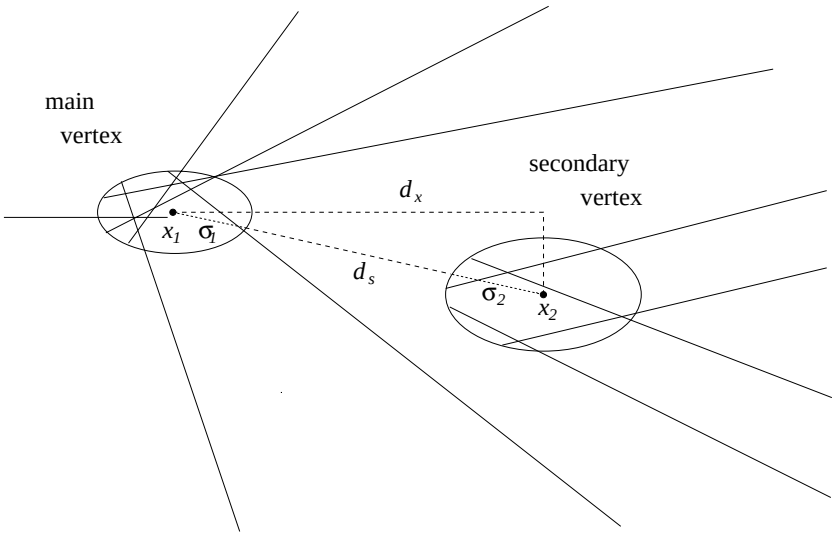

Figure 5.12: Determination of the error on the separation in space between the secondary and the primary vertex ($\sigma = \sqrt{\sigma_1^2 + \sigma_2^2}$). d_x is the separation in the longitudinal direction and d_s the separation in space. The error ellipsoids are schematically indicated.

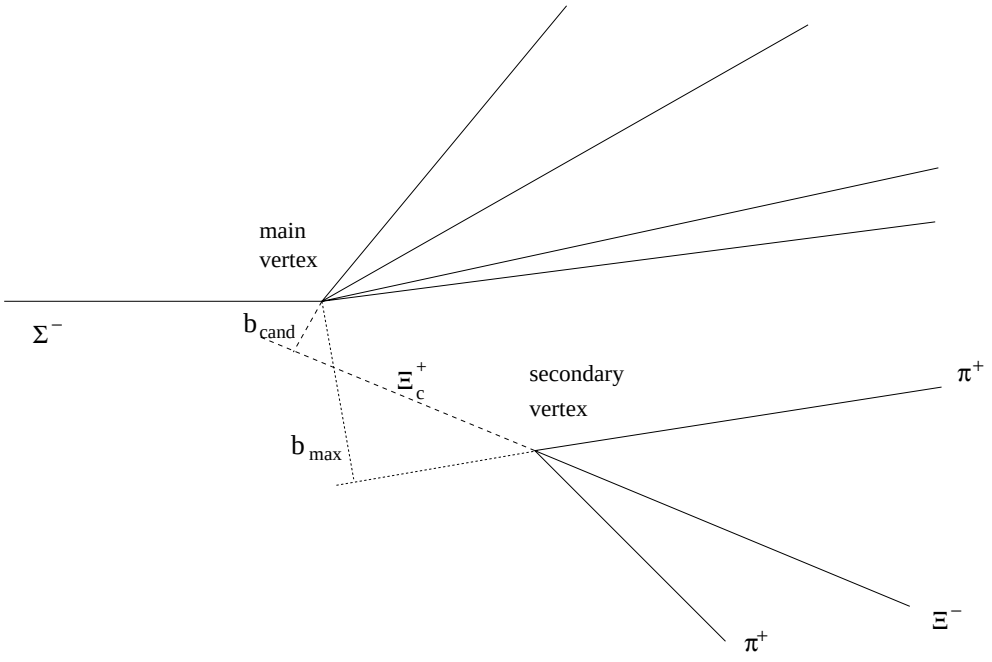

Figure 5.13: Definition of the impact parameter of the candidate (b_{cand}) and of the maximum impact (b_{max}) of individual daughter tracks with respect to the main vertex.

5.4 Lifetime measurement method

In order to determine the decay time of a particle, the measurable quantities to be considered are the length of its decay path and its momentum, from which its decay time is calculated on an event by event basis. The relativistic decay time is expressed as:

$$t = \frac{d_s}{\gamma\, v} = \frac{d_s}{\gamma\, \beta\, c} \tag{5.5}$$

where d_s is the length of the decay path in space, γ is the Lorentz factor, and v is the particle velocity in the laboratory system.
The decay time distribution is described by a probability density function following the exponential decay law:

$$f_\tau(t) = \frac{1}{\tau} \cdot e^{-t/\tau} \tag{5.6}$$

where τ is the mean lifetime of the particle. The distribution is normalized to give a unitary probability when integrated in the time range $[0,+\infty]$.
The mean lifetime τ is connected to the particle decay width Γ by the relation: $\tau = \frac{\hbar}{\Gamma}$.
The value of the mean lifetime τ can be estimated if several decays of the particle under study are detected and the distribution of the decay time is fitted.

5.4.1 The maximum likelihood method

In this approach, the mean lifetime is determined using an *unbinned maximum likelihood method*. To each individual event selected in a decay channel, we assign a likelihood determined on the base of the decay distribution described above. For a sample of n measured events, the likelihood function is defined as the product of the individual probability densities:

$$L(\tau) = \prod_{i=1}^{n} f_\tau(t_i) \tag{5.7}$$

Maximizing $L(\tau)$ gives the best estimate for the value τ of the mean lifetime.
In order to simplify the calculation from the mathematical point of view, the negative logarithmic likelihood function is minimized:

$$\ell(\tau) \;=\; -\log L \;=\; -\sum_{i=1}^{n} \log f_\tau(t_i) \tag{5.8}$$

Before applying the described method to real data, several experimental considerations must be taken into account: they are described in the following paragraphs.

The experimental resolution

The limited resolution of the experimental apparatus induces errors on all measured quantities, including the decay path length and the particle momentum. The detector

resolution induces a smearing of the decay time distribution from the purely exponential behaviour to the curve indicated in figure 5.14.

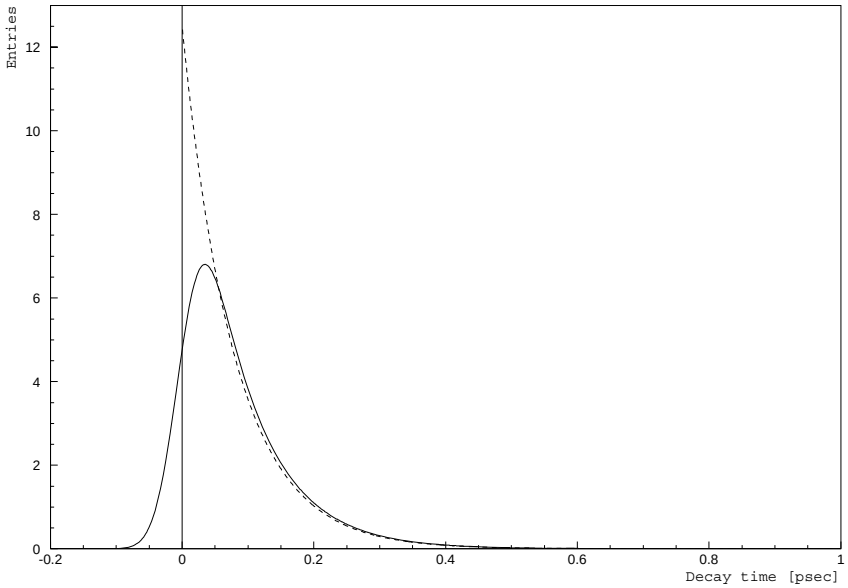

Figure 5.14: The theoretical exponential behaviour of the lifetime distribution (dashed curve) and the measured distribution smeared by the effect of a Gaussian resolution function (full line).

The effect induced by the spatial and momentum resolution of the apparatus is taken into account by convoluting the exponential distribution with a resolution function, determined experimentally. The decay distribution is now given by:

$$f_{\tau,res}(t) = \frac{1}{\tau} \int_0^\infty e^{-\frac{\theta}{\tau}} g_{res}(t-\theta) d\theta \qquad (5.9)$$

The lifetime resolution function for our apparatus has been determined using a sample of minimum bias background events. The decay time distribution for the selected events is shown in figure 5.15.
The obtained distribution is best described by the sum of two Gaussians with the following parameters:

	Width [fsec]	Mean [fsec]	Relative weight
First Gaussian	32.7 ± 0.7	-1.8 ± 0.5	0.842
Second Gaussian	87.3 ± 3.4	0.9 ± 2.2	0.158

Our resolution function is determined by a dominant component of 33 fsec and a second component of 87 fsec, corresponding to an average value of about 40 fsec. This good resolution is due to the high spatial precision provided by the microstrip vertex detector.
The measured parameters were fixed and used for the lifetime measurements presented in the following chapter.

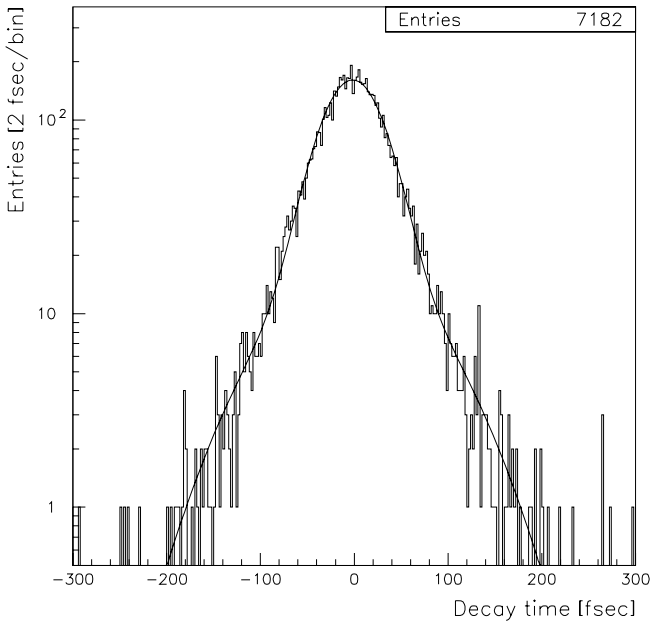

Figure 5.15: Distribution of the decay time for a sample of minimum bias events.

Bias induced by selection criteria

The cuts applied in order to select the signal events can induce a distortion on the decay time distribution. In particular, topological cuts on the vertex separation, the various impact parameters, and the maximum decay path, impose a lower and an upper limit to the measurable lifetime. The value of these limits has to be determined event by event and the appropriate correction applied.
The estimate of the quantities t_{min} and t_{max} depends on the applied cuts. Examples of topological selection criteria and the corresponding minimum decay time cut are illustrated below.
Vertex separation cut: A cut on the vertex separation (in the longitudinal direction or in space) is directly a minimum decay time cut, depending on the particle momentum. If the separation is requested to be larger than $n_1 \cdot \sigma$, the corresponding minimum lifetime cut is:

$$t_{min}^{sep} = \frac{n_1 \cdot \sigma_d}{\gamma\ \beta\ c} \tag{5.10}$$

where σ_d is the value of one standard deviation.
Cut on the separation from the target edge: The separation from the target edge is treated in a similar way. If it is required to be larger than $n_2 \cdot \sigma$, the minimum measurable decay time is:

$$t_{min}^{sep\_tar} = \frac{n_2 \cdot \sigma_t + x_{mt}}{\gamma\ \beta\ c} \tag{5.11}$$

where σ_t is the value of one sigma, and x_{mt} is the distance of the main vertex from the target edge.

Impact parameter of daughter tracks: The influence of a cut on the impact parameter of the daughter tracks with respect to the main vertex is illustrated in figure 5.16 on the left, for the case of a maximum impact parameter cut. The situation is equivalent when the cut is on the minimum or the average daughter impact parameter. If the condition requested for the impact parameter is to be larger than $n_3 \cdot \sigma$, using a simple proportionality law, the cut on the decay time is given by:

$$t_{min}^{dau\_imp} = \frac{n_3 \cdot \sigma_b}{b_{meas}} \cdot \frac{d_{meas}}{\gamma\, \beta\, c} \tag{5.12}$$

where σ_b is the value of one sigma, b_{meas} is the measured impact parameter, and d_{meas} is the measured decay path.

Closest distance of approach of primary tracks to the secondary vertex: The requirement that tracks emerging from the primary vertex are further than a certain limit from the reconstructed secondary vertex also induces a minimum cut on the measurable lifetime, as illustrated in figure 5.16 on the right. If the CDA is required to be larger than $n_4 \cdot \sigma$, the cut on the decay time is given by:

$$t_{min}^{CDA\_main} = \frac{n_4 \cdot \sigma_{CDA}}{CDA_{meas}} \cdot \frac{d_{meas}}{\gamma\, \beta\, c} \tag{5.13}$$

where σ_{CDA} is the value of one sigma, CDA_{meas} is the measured closest distance of approach, and d_{meas} is the measured decay path.

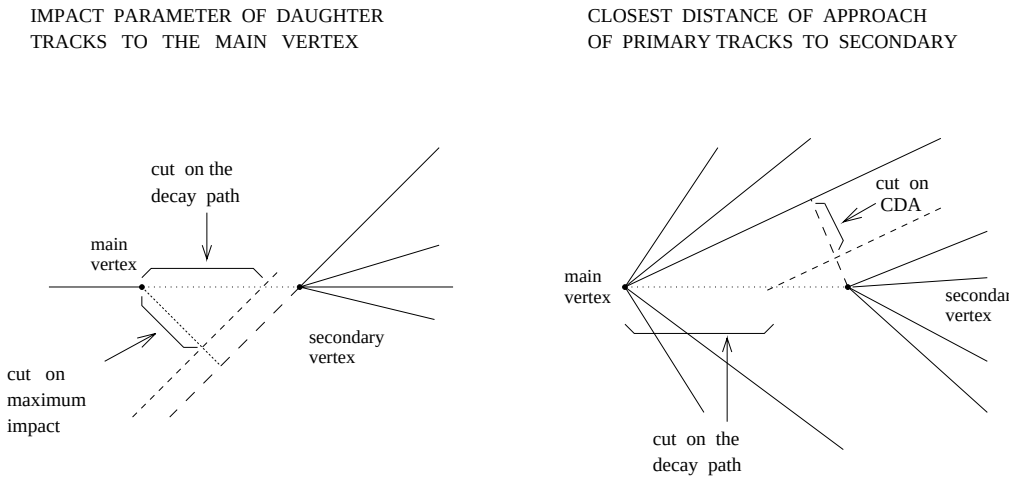

Figure 5.16: Schematic representation of the influence of topological cuts on the minimum measurable lifetime.

For the topological cuts listed above, the corresponding time cut has to be calculated event by event and the effective minimum lifetime cut is given by the maximum of the determined t_{min} values:

$$t_{min} = max(t_{min}^{sep}, t_{min}^{sep\_tar}, t_{min}^{dau\_imp}, t_{min}^{CDA\_main}, \ldots) \tag{5.14}$$

including only the cuts applied for the sample under study.

The effective maximum lifetime cut is estimated in a similar way. If the decay path length is requested to be lower than d_{max} (for example to exclude secondary vertices reconstructed in the downstream targets), the maximum lifetime cut is:

$$t_{max} = \frac{d_{max}}{\gamma\,\beta\,c} \tag{5.15}$$

Once t_{min} and t_{max} are determined, in the unbinned likelihood method the correction is done renormalizing the decay distribution function in the following way:

$$f_{\tau,res}(t) = \frac{\frac{1}{\tau}\int_0^\infty e^{-\frac{\theta}{\tau}} g_{res}(t,\theta)d\theta}{\int_{t_{min}}^{t_{max}} dT \frac{1}{\tau}\int_0^\infty e^{-\frac{\theta}{\tau}} g_{res}(T,\theta)d\theta} \tag{5.16}$$

The possible distortion of the decay time distribution induced by other cuts (like momentum or track quality cuts, RICH identification requirements, etc.) is checked using Monte Carlo generated events and comparing the distribution before and after applying the cuts. If the efficiency is not uniform over a certain time range, a correction function must be calculated and eventually included in the lifetime fitting routine.
No distortions have been seen in the decay channels analysed for this work, consequently there was no need for other corrections than the ones for the topological cuts.

Background lifetime

Besides true events, the invariant mass plot of charm candidates also contains background events. Part of them are due to a topological background, i.e., events not containing any charm but having a geometrical track combination resembling the charm decay topology. The decay time distribution of this type of background is symmetric around zero and should be described by the resolution function introduced before.
In addition to this, there may also be a combinatorial background, partly due to reconstructed charm decays where one or more of the real daughter tracks have been replaced by other tracks. In order to be able to describe this component of the background, an exponential contribution must sometimes be added to the two Gaussians mentioned before. However, the amount of combinatorial background and its decay time distribution depend on the decay channel considered and the applied cuts. Consequently, the necessity of the additional exponential has to be checked in every single case.

5.4.2 The *taufit* fitting routine

The method described so far has been used to develop a lifetime fitting routine called *taufit* [3]. The routine applies the maximum likelihood method explained above, using the decay time distribution function given in formula (5.16) and the discussed options to describe the background. The signal and background distributions are weighted by the mass distribution, described by a Gaussian for the signal peak and a polynomial for the background entries.
The total decay time distribution is therefore given by:

$$f_{\tau,B,res} = \eta f^S_\eta(m) f^S_{\tau,res}(t) + (1-\eta) f^B_\eta(m) f^B_{B,res}(t) \tag{5.17}$$

where $\eta = \frac{S}{S+B}$, S being the number of true charm events and B the background events in the whole considered mass window; $f_\eta^S(m)$ is the Gaussian distribution of the signal component of the mass plot and $f_\eta^B(m)$ is the polynomial distribution for the background; $f_{\tau,res}^S(t)$ is the decay time distribution of equation (5.16) from which the signal mean lifetime can be determined; and $f_{B,res}^B(t)$ is the decay time distribution for the background entries. The expression of the latter one depends on the necessity to introduce an additional exponential or not.

The *taufit* routine offers the possibility of performing the fit in several ways:

1. All variables can be fitted at the same time: the parameters of the lifetime resolution function, the mass distribution, the signal (and background) lifetime from the exponential distribution;

2. The user can fit the resolution function separately, fix it for the following steps and then fit mass and lifetime together;

3. Otherwise, after the separate determination of the resolution function, the mass and the lifetimes can be fitted independently.

For the lifetime measurements presented in the next chapter, the resolution function was determined separately and kept fixed for all other fitting steps. This was done in order to reduce the amount of events that the fitting routine has to treat. It was also checked that the resolution function measured from different data samples for the various decay channels analysed was basically the same and the negligible differences did not influence the result on the signal lifetime.
At this point, the approach described in 2) is preferable as all correlations are considered correctly. But this mode does not converge in all cases, especially when the background level is very high and too many parameters have to be fitted simultaneously. The approach used will be indicated in each case.

Bibliography

[1] J.C. Lassalle et al., “TRIDENT: a track and vertex identification program for the CERN Omega particle detector system”, Nucl. Instr. and Meth. 176 (1980) 371-379

[2] The Particle Data Group, “Review of particle properties”, Phys. Rev. D3 (1994)

[3] L. Schmitt, WA89 Internal Note, August 1996

Chapter 6

Analysis of charmed hadron decays

The high spatial resolution of the microstrip detectors in the WA89 vertex region and the measurement of different projections allow the reconstruction of space tracks with high precision. This, in turn, allows the determination with good resolution of the decay point of short living charmed hadrons (with lifetimes ranging between 5×10^{-14} and 10^{-12} sec) by the reconstruction and the identification of their daughter tracks. The production point of charmed hadrons can also be determined with similar precision.
The reconstruction of separate primary and secondary vertices provides a powerful tool to reduce the significant level of combinatorial background present in data samples for the search of charmed particles.
Additional use of the information provided by the different detectors in the experimental apparatus allows further rejection of background events and isolation of the charm signals. In particular, the high resolution information given by the vertex detector allows clear separation cuts and relatively strong topological selection criteria. The information on particle identity provided by the RICH detector can also improve the purity of the candidate sample.
Knowing the production and the decay point, it is possible to estimate the flight distance of the particles under study, measure their decay time on an event by event basis, and evaluate their lifetime.
In this chapter I will present the results obtained in the search for the charmed mesons $\overline{D}^0$ and D^- and for the charmed strange baryon Ξ_c^+. The procedure followed to obtain the charm signals, the selection cuts applied, the estimated lifetime and the dependence of the signal and its lifetime on the variation of the selection criteria used will be presented [1].

Correction of particle momenta

From the reconstruction of Λ and K_S^0 decays in WA89 a shift of the reconstructed mass with respect to the reference mass was observed. This shift is ascribed to distortions of the Omega magnetic field and misalignments, which induce a systematic track shift of about 255 μrad on all bending angles. This, in turn, induces shifts of the reconstructed particle momenta, which have the opposite sign for positively and negatively charged particles.

[1] For this analysis, 1993 data produced with TRIDENT version 18.6 and PHYNIX version 18 were used

A momentum correction was determined empirically using Λ^0, K^0, and Ω^- candidates and further checked with a systematic study of $D^0, \overline{D}^0, D^+$, and D^- mass distributions [1]. The correction is expressed by the following formula:

$$\vec{p} \Rightarrow \vec{p} \cdot (1.006 + 10^{-4} \cdot charge \cdot |\vec{p}|) \tag{6.1}$$

where $\vec{p}$ is the momentum vector of each daughter particle. The invariant mass is then calculated taking into account the scaled momenta. This correction has been applied to all decay channels presented in this chapter.
The uncertainty on the factor 1.006 induces a systematic error on the mass measurement. For values of the factor varying between 1.005 and 1.007 the corrected masses used to determine the empirical formula are still compatible with the corresponding reference masses. Consequently the systematic uncertainty on the mass will be estimated from the difference between the corrected mass value calculated in the two extreme cases.

6.1 Charmed mesons

The first part of the analysis presented in this chapter concerns the reconstruction and lifetime measurement of the anti-charmed mesons $\overline{D}^0$ and D^- using the decay channels

$$\overline{D}^0 \to K^+\pi^- \qquad \text{(BR=4.01±0.14 \%)}$$
$$D^- \to K^+\pi^-\pi^- \qquad \text{(BR=9.1±0.6 \%)}$$

For this purpose a filter was performed with the *xip*2 code on the whole sample of 1993 data, consisting of approximately 140 millions events. For the requested topologies, the filter selected events according to mass, geometry, and quality criteria reducing the data sample by a factor of about 25. For the individual channels, events were further processed and selected to produce the final data sample on which the interactive search for the signal and the study of cuts were performed. A summary of the cuts applied in the two data processing steps are listed in table 6.1.

Filter criteria	$\overline{D}^0 \to K^+\pi^-$	$D^- \to K^+\pi^-\pi^-$
Mass window for candidates	± 200 MeV/c^2	± 200 MeV/c^2
Decay vertex quality (χ^2 per degree of freedom)	≤ 20	≤ 15
Distance between tracks in candidate	≤ 1 mm	≤ 1 mm
Main vertex volume	≤ 1 cm^3	≤ 1 cm^3
Main vertex probability	≥ 0.5%	≥ 0.5%
Interaction targets	Cu + C	Cu + C
Vertex separation in space	≥ 3σ	≥ 5σ
Global impact parameter	≤ 300 μm	≤ 300 μm
Kaon RICH identification	$R_K \geq 0$	$R_K \geq 0$

Table 6.1: Criteria used to select the data sample for the search of charmed mesons.

6.1.1 The $\overline{D}^0 \to K^+\pi^-$ decay channel

Figure 6.1 shows the mass distribution of all candidates selected by the cuts listed above for the decay channel $\overline{D}^0 \to K^+\pi^-$. The reference mass ($1864.6 \pm 0.5$ MeV/c^2) is indicated.

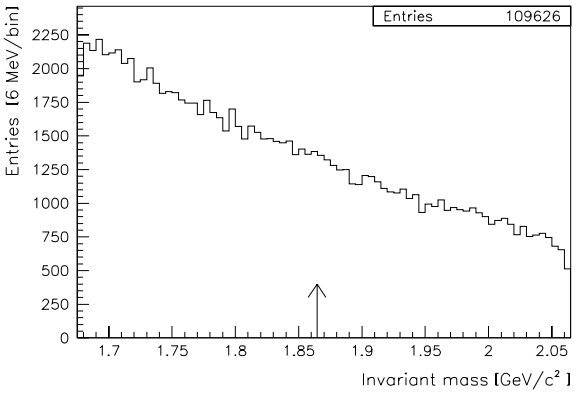

Figure 6.1: Mass distribution of all candidates for the $\overline{D}^0 \to K^+\pi^-$ decay channel. The arrow indicates the reference mass.

The mass spectrum of the selected $\overline{D}^0$ signal is shown in figure 6.2. The fitted parameters are indicated below.

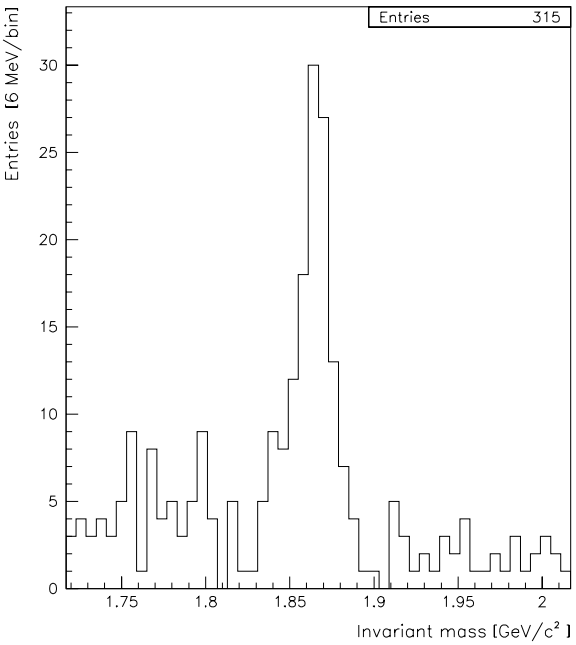

Figure 6.2: Mass distribution of the selected events for the $\overline{D}^0 \to K^+\pi^-$ decay channel.

Mass	:	1864.4 ± 1.3 (stat.) ± 1.5 (syst.) MeV/c^2
Width (1σ)	:	$9.35^{+1.25}_{-1.12}$ (stat.) MeV/c^2
Signal S	:	96.9 ± 9.2
Background B	:	17
Significance Σ	:	9.1

The significance was calculated as

$$\Sigma = \frac{S}{\Delta S} \approx \frac{S}{\sqrt{S+B}} \tag{6.2}$$

where S and B indicate the number of signal and background events respectively, in a mass window of ± 20 MeV/c^2 around the peak mass.

The cuts applied on the sample shown in figure 6.1 to obtain the $\overline{D}^0$ signal are listed in table 6.2.

Cut description	Cut value
Main vertex quality (χ^2 per degree of freedom)	≤ 3.5
Secondary vertex quality (χ^2)	≤ 5
Error on the secondary vertex position in x	≤ 700 μm
Vertex separation in the x coordinate	$\geq 4\sigma$
Secondary vertex separation from the target edge	≥ 0
Global impact parameter	$\leq 2.5\sigma$
Average impact parameter of individual candidate tracks wrt the main vertex	$\geq 5\sigma$
Kaon RICH identification	$R_K > 1$
Pion momentum	≥ 10 GeV/c

Table 6.2: Cuts applied to select the $\overline{D}^0$ signal.

The relatively long lifetime of the $\overline{D}^0$ ($\tau_{\overline{D}^0} = 0.415 \pm 0.004$ psec [2]) allows the placement of a 4σ cut on the separation in the longitudinal direction. The value of σ is determined in this case by the squared sum of the errors on the main and the secondary vertex positions in x, and its mean value is about 600 μm for the selected events.
Furthermore, the secondary vertex is required to lie outside of the interaction targets. This cut rejects vertices reconstructed with tracks emerging from secondary interactions taking place in the targets themselves and is very efficient in reducing background.
In the laboratory system, the angle between daughter tracks in a two body decay is rather large. The decay tracks do not point back directly to the primary vertex and, if extrapolated upstream, they have a significant distance from the vertex itself. Consequently it is possible to apply a strong cut (5 σ in this case) on the average impact parameter of the two decay tracks with respect to the main vertex.
In this decay channel, with two well measured tracks of charged particles, the candidate total impact parameter is determined with high precision and we can require it to be below 2.5 σ. The mean value of the impact parameter for the selected events is approximately 20 μm.
The positive RICH identification of the kaon is essential to produce such a clean signal. If the kaon is out of the RICH acceptance or below threshold, the background level is very high and extremely difficult to reduce because of the large number of pions.

The selected signal is almost equally shared between the copper and the carbon targets, which correspond to 2.66% and 2.49% of an interaction length respectively. Figure 6.3 shows on the left the events having the main vertex reconstructed in copper and on the right those with the main vertex located in one of the three diamond slices.

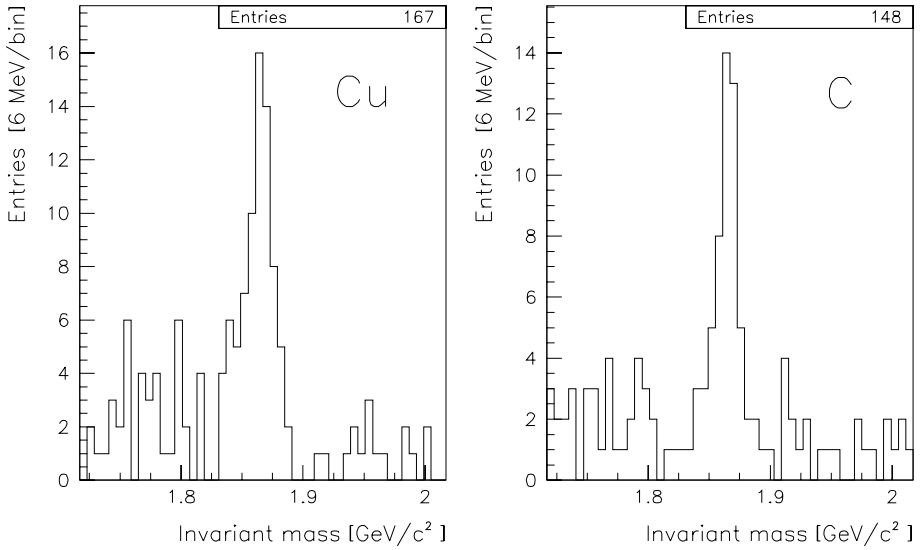

Figure 6.3: Distribution of $\overline{D}^0$ candidates for which the main vertex was reconstructed in the copper target (on the left) and in the diamond target (on the right).

For the events in the $\overline{D}^0$ signal band, the main vertices were reconstructed with a mean number of 6.6 tracks, of which an average of 4.2 are space tracks with measured momentum and 2.4 are microstrip non-momentum space tracks. The beam track was included in 82% of the cases. The mean error on the primary vertex position in x is approximately 400 μm. The closest distance of approach of tracks in the secondary and in the main vertex is 15 and 80 μm respectively. The reconstructed momentum of the candidates is between 40 and 220 GeV/c and the mean flight path is of the order of 1.5-2 mm. The kaon and pion tracks show very high quality: they have an average of 9 hits recorded in the first 12 microstrip planes and their χ^2 is lower than 3.

Figures 6.4 and 6.5 show the dependence of the mass distribution on the variation of the most relevant cuts. In figure 6.4 the cuts varied are: the error on the x position of the secondary vertex (*secxe*); the total impact parameter of the charm candidate (*imp-par*); the average value of the impact parameters of the two individual tracks with respect to the main vertex (*av-imp*); the RICH likelihood ratio R_K for the kaon. In this case only one cut is varied at the time, while all others are kept fixed to the value indicated in the table 6.2. In figure 6.5 the dependence on the separation cuts is shown, in particular on *xseps*, the separation in the longitudinal direction expressed in σ; *xseptargs*, the separation of the secondary vertex from the target edge, also in σ; and on a lifetime cut. In this case the separation cuts had been removed from the selection function and only one of the three listed above is applied in turn.

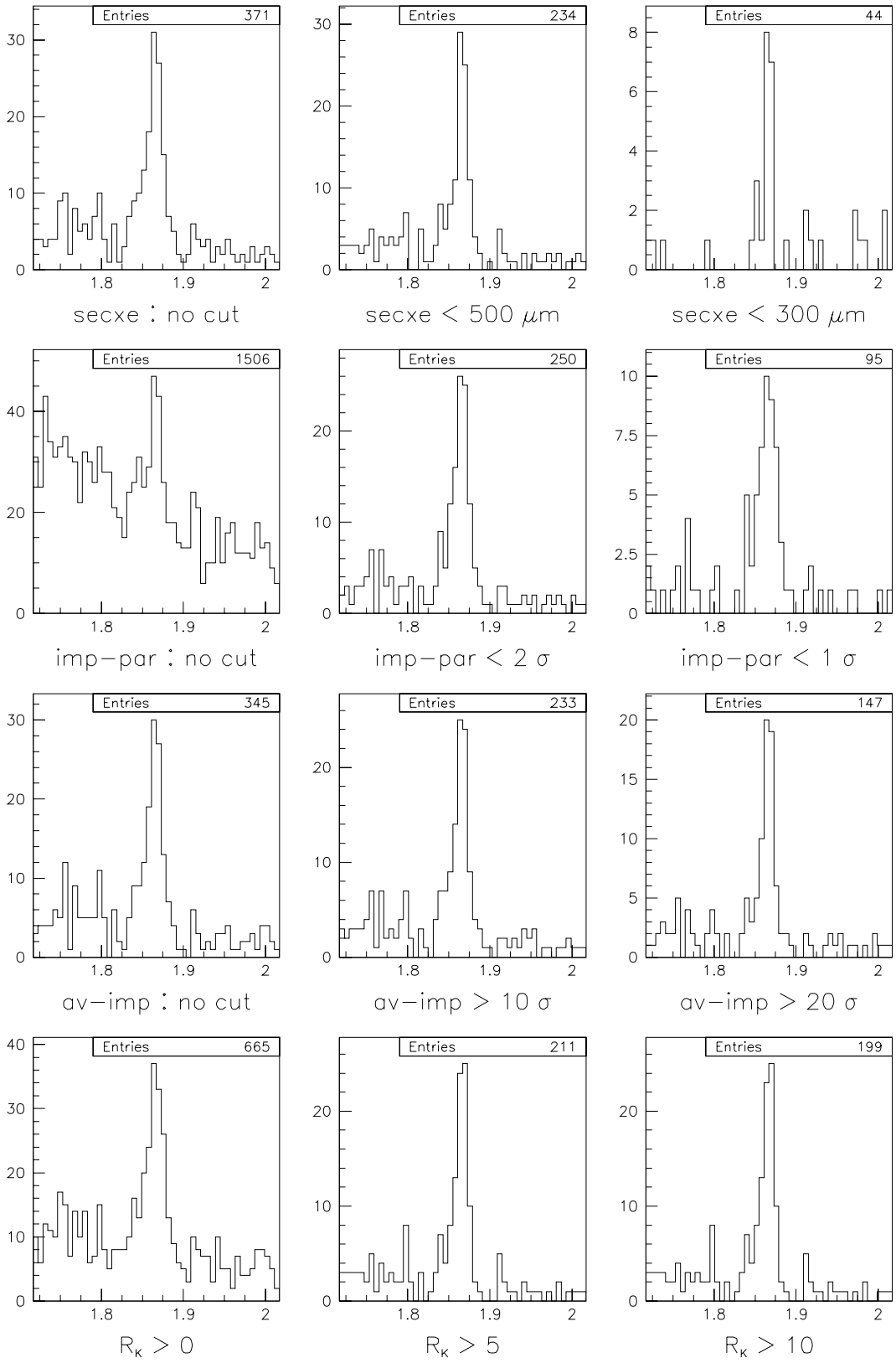

Figure 6.4: Dependence of the $\overline{D}^0$ mass spectrum on the variation of some of the most relevant cuts (see the text for further explanations regarding the single cuts).

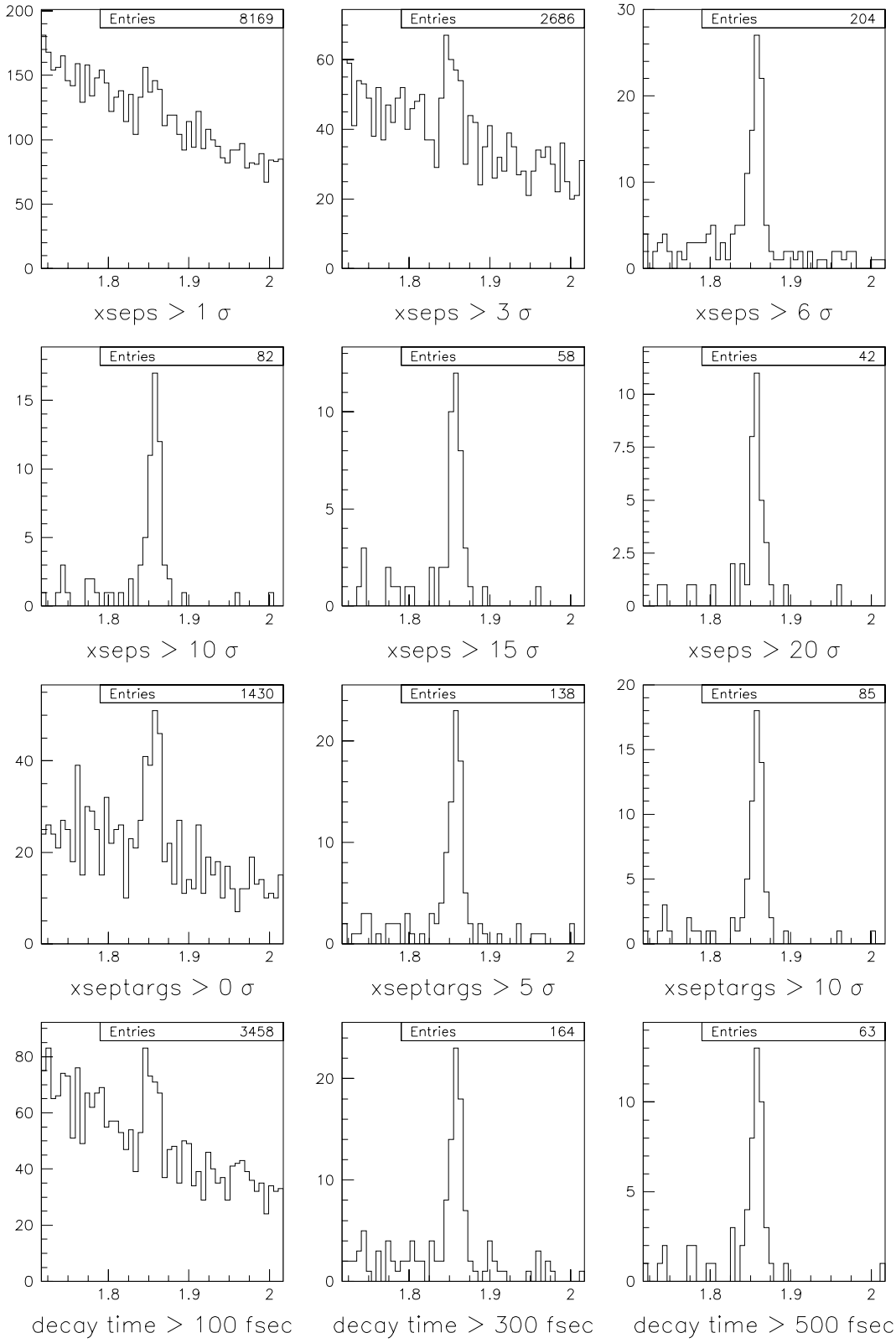

Figure 6.5: Dependence of the $\overline{D}^0$ mass spectrum on the variation of separation cuts (see the text for further explanations).

6.1.2 $\overline{D}^0$ lifetime measurement

The $\overline{D}^0$ lifetime was measured with the candidates selected for the mass spectrum shown in figure 6.2. The fitting routine presented in the previous chapter was used.

Because of the very low background level and consequent high purity of the data sample, it was possible to fit at the same time the signal and background lifetime distributions weighted by the mass distribution. In the present case it was necessary to fit an exponential distribution to describe the background lifetime in addition to the Gaussians of the resolution function. A possible reason for this can be summarized as follows: Very strong separation cuts isolate very few background events with such long decay times that they can no longer be described by the two Gaussians indicated before. The additional exponential takes into account this effect induced by very high separations. The same effect was observed with Monte Carlo generated events when the component of combinatorial background was considered.

In the described conditions the signal and the background lifetimes were measured to be

$$\tau_{\overline{D}^0} = 0.433^{+0.054}_{-0.046} \quad \text{(stat.)} \quad \text{psec}$$

$$\tau_{bkg} = 0.078^{+0.007}_{-0.006} \quad \text{(stat.)} \quad \text{psec}$$

The value of the statistical error is rather high due to the limited statistics available: using approximately 100 events, an error of about 10% is expected.

The obtained result is in good agreement with the reference value of the $\overline{D}^0$ lifetime given by the Particle Data Group [2]:

$$\tau^{ref}_{\overline{D}^0} = 0.415 \pm 0.004 \quad \text{psec}$$

Figure 6.6 shows the distribution of the logarithmic likelihood and the correlation plots for some of the variables fitted for the lifetime determination. In the top row the logarithmic likelihood function for the signal lifetime (on the left) and for the exponential component of the background lifetime (on the right) are shown. The intersection of the dashed horizontal line with the likelihood distributions indicates the value of the measurement errors (1 σ).

The bottom plots show the correlation between the signal lifetime and the reconstructed mass (on the left) and between the signal and background lifetime (on the right). This last plot shows the absence on any correlation between the signal and background fitted lifetime values, a good indication that the introduction of the additional exponential for the background does not distort the signal lifetime measurement.

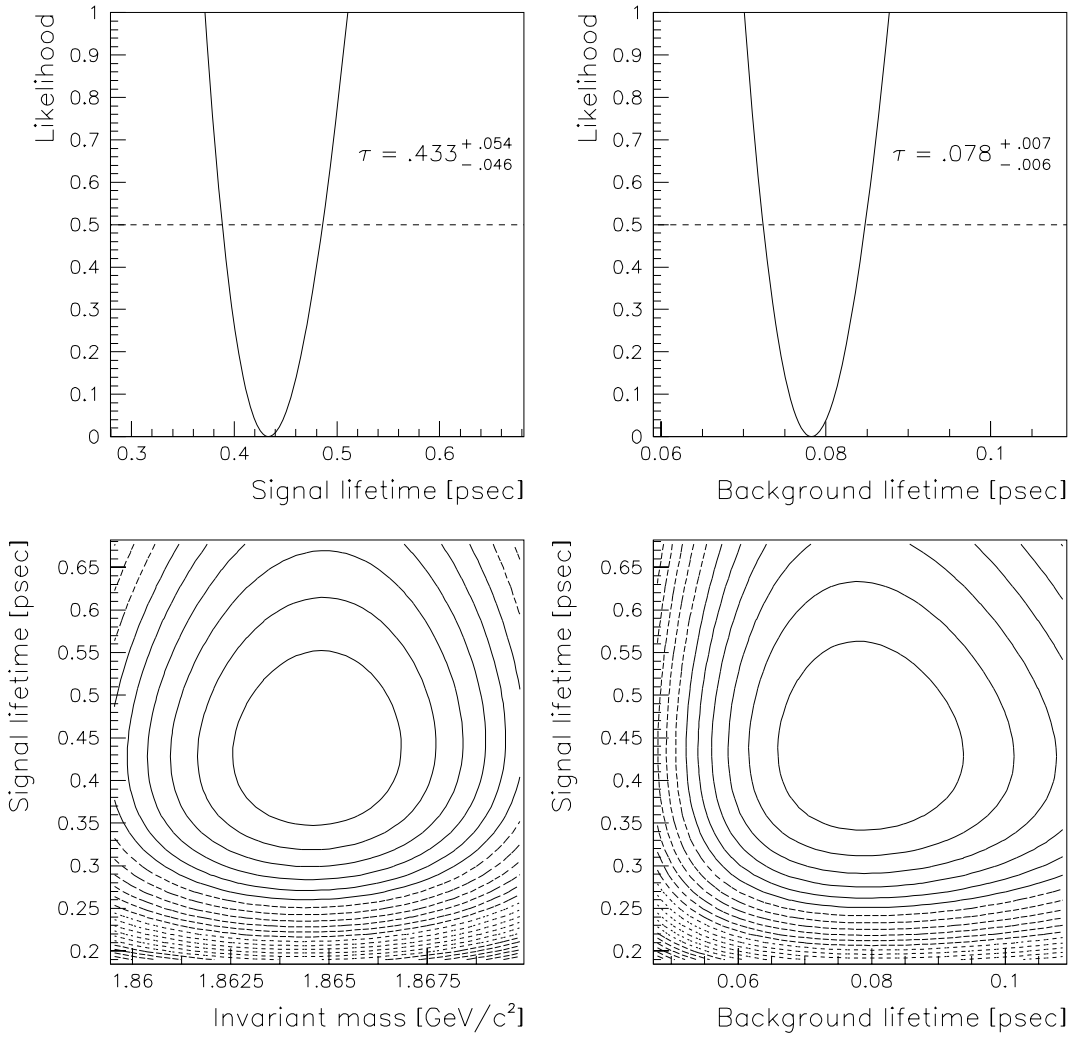

Figure 6.6: Distribution of the logarithmic likelihood function for the signal and background lifetime for the sample of $\overline{D}^0$s (on top) and correlation plots for the signal lifetime, the mass and the background lifetime (on bottom).

The topological cuts which were taken into account to calculate the effective minimum lifetime cut on an event by event basis are listed below:

- the cut on the separation in the longitudinal direction (*xseps*);
- the cut on the separation from the target edge (*xseptargs*);
- the cut on the average impact parameter of the two daughter tracks to the main vertex (*av-imp*).

In order to check possible systematic effects on the lifetime evaluation induced by the topological cuts, the measurement was repeated varying the cuts listed above and the behaviour was studied. The dependence of the measured signal and background lifetime on the variation of the three mentioned cuts is shown in figures 6.7, 6.8 and 6.9 for *xseps*, *xseptargs* and *av-imp* respectively. The reference lifetime value is shown for comparison.

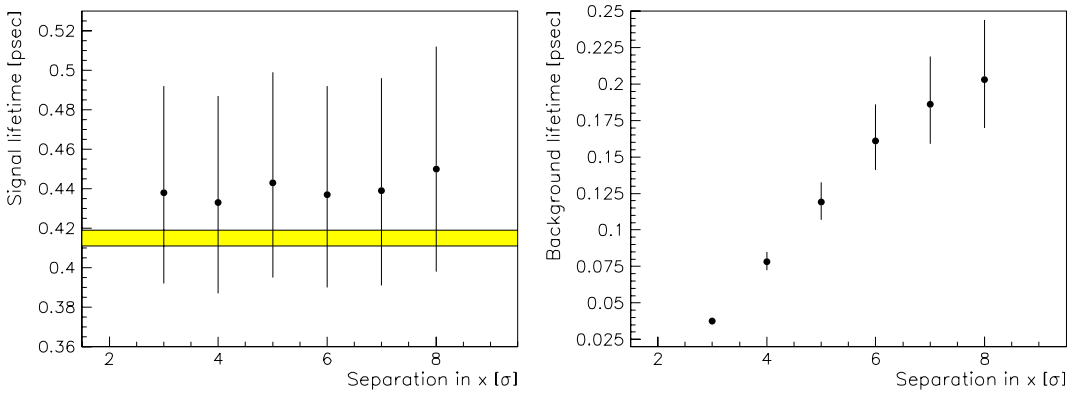

Figure 6.7: Dependence of the measured signal and background lifetime for the $\overline{D}^0$ sample on the separation cut in the longitudinal coordinate. The grey band in the left plot indicates the reference lifetime value.

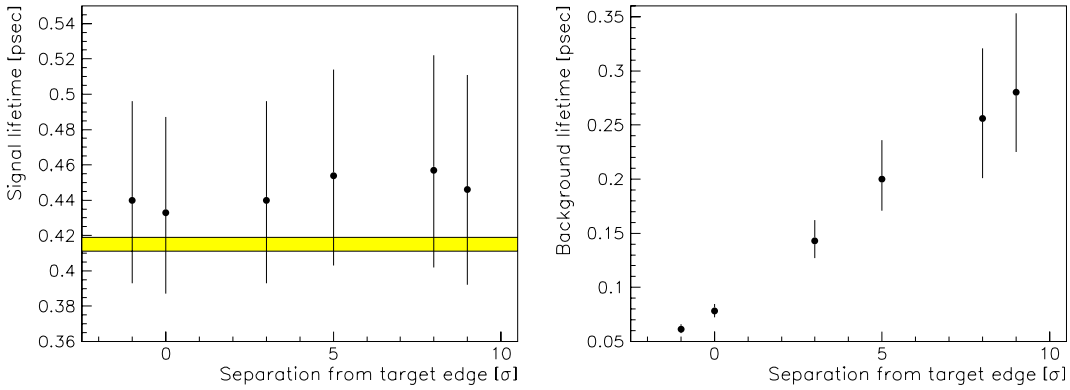

Figure 6.8: Dependence of the measured signal and background lifetime for the $\overline{D}^0$ sample on the separation cut from the target edge. The grey band in the left plot indicates the reference lifetime value.

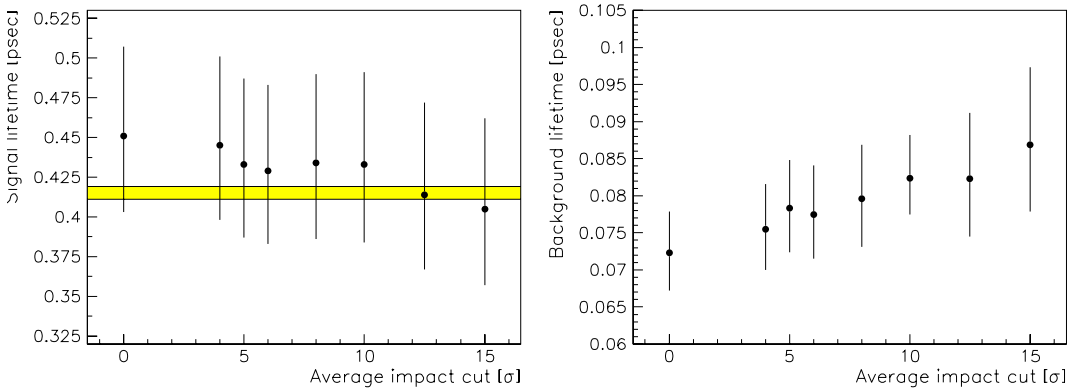

Figure 6.9: Dependence of the measured signal and background lifetime for the $\overline{D}^0$ sample on the cut on the average impact parameter of the two daughter tracks to the main vertex. The grey band in the left plot indicates the reference lifetime value.

The measured lifetime shows no strong systematic dependence on the variation of the topological cuts, particularly in figures 6.7 and 6.8 where the separation in the longitudinal direction and the separation from the target edge are varied. A moderate dependence is visible in figure 6.9, but still small compared to the large statistical error. Nevertheless the attempt was made to give an estimate of the systematic error on the measured lifetime. The procedure used to determine the limits between which the cut values are varied in order to estimate the variation of the lifetime results is described below.

The fitting routine used considers all events belonging to a defined mass band (normally of $\pm$ 150 MeV/c^2) around the mass peak. Once the mass spectrum has been fitted with the polynomial describing the background and the Gaussian for the signal, the area defined by the two distributions is calculated. The area of the polynomial gives the total number of background events present in the considered sample (B_{tot}), while the area of the Gaussian gives the number of signal events (S). The ratio S / (S + B_{tot}) was calculated for the reference situation used for the lifetime measurement, corresponding to the cuts indicated in table 6.2.
For each of the three topological cuts the lower and higher cut values were determined as those giving a S / (S + B_{tot}) ratio lower than the reference situation by 30% and higher by 30% respectively. The lifetime was then estimated for the events selected by the low, reference, and high cut values. With the three measured points, the lifetime variation induced by the individual cuts was calculated. Since the ratio S / (S + B_{tot}) depends on the width of the considered mass window, this was varied from $\pm$ 100 MeV/c^2 to $\pm$ 200 MeV/c^2 and the fit was repeated. The corresponding lifetime variation was also taken into account as contribution to the systematic error.

The cut values selected with the criterion explained above and the four contributions to the systematic error due to the three topological cuts and the considered mass window are summarized in table 6.3.

Cut	low cut value	reference cut value	high cut value	lifetime variation
xseps	$\geq 3\ \sigma$	$\geq 4\ \sigma$	$\geq 5\ \sigma$	0.005 psec
xseptargs	$\geq$ -1 σ	$\geq 0\ \sigma$	$\geq 3\ \sigma$	0.0035 psec
av-imp	$\geq 0\ \sigma$	$\geq 5\ \sigma$	$\geq 15\ \sigma$	0.023 psec
mass window	$\pm$ 100 MeV/c^2	$\pm$ 150 MeV/c^2	$\pm$ 200 MeV/c^2	0.002 psec

Table 6.3: Estimate of the contributions to the systematic error on the measured $\overline{D}^0$ lifetime value.

The four contributions are then summed in quadrature and the systematic error is calculated to be approximately 0.024 psec.
In conclusion, the lifetime measurement on the selected sample of $\overline{D}^0$ events shown in figure 6.2 gives the following result:

$$\tau_{\overline{D}^0} = 0.433^{+0.054}_{-0.046}\ \text{(stat.)} \pm 0.024\ \text{(syst.)} \quad \text{psec}$$

6.1.3 The $D^- \to K^+\pi^-\pi^-$ decay channel

Figure 6.1 shows the mass distribution of all candidates selected by the cuts listed in table 6.1 for the decay channel $D^- \to K^+\pi^-\pi^-$. The reference mass (1869.4 ± 0.4 MeV/c^2) is indicated.

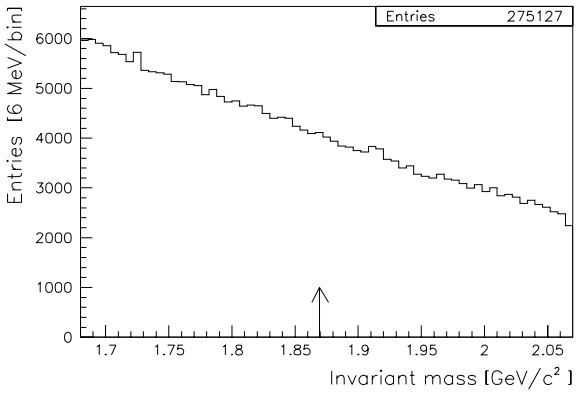

Figure 6.10: Mass distribution of all candidates for the $D^- \to K^+\pi^-\pi^-$ decay channel. The arrow indicates the reference mass.

The selected D^- candidates are shown in figure 6.11. These events were used to determine the mass parameters listed below.

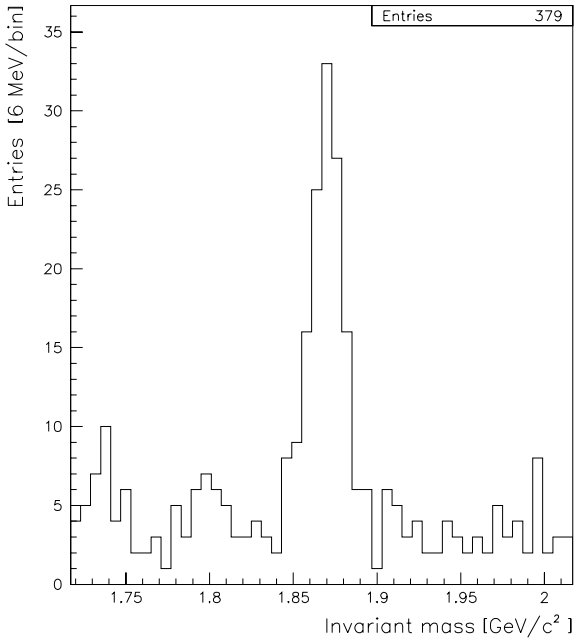

Figure 6.11: Mass distribution of the selected events for the $D^- \to K^+\pi^-\pi^-$ decay channel.

Mass	:	1869.5 ± 1.2 (stat.) ± 1.5 (syst.) MeV/c^2
Width (1σ)	:	$9.32^{+1.09}_{-1.00}$ (stat.) MeV/c^2
Signal S	:	107.9 ± 10.6
Background B	:	20
Significance Σ	:	9.5

As was shown for the $\overline{D}^0$ candidates, the signal is almost equally distributed between the copper and the carbon targets.

The selection criteria used to obtain the D^- signal are listed in table 6.4.

Cut description	Cut value
Main vertex quality (χ^2 per degree of freedom)	≤ 3.5
Secondary vertex quality (χ^2 per degree of freedom)	≤ 5
Error on the secondary vertex position in x	≤ 700 μm
Vertex separation in the x coordinate	$\geq 6\sigma$
Secondary vertex separation from the target edge	≥ 0
Secondary vertices reconstructed in the following targets	excluded
Global impact parameter	$\leq 3\sigma$
Minimum impact of the daughter tracks to the main vertex	$\geq 2\sigma$
Kaon RICH identification	$R_K \geq 1$
Pion momentum	≥ 15 GeV/c

Table 6.4: Cuts applied to select the D^- signal.

Most cuts are similar to those used to select the $\overline{D}^0$ signal; only significant differences will be pointed out here.

The D^- has a longer lifetime ($\tau_{D^-} = 1.057 \pm 0.015$ psec [2]) than the $\overline{D}^0$, so a stronger separation cut in the longitudinal direction (6 σ) is applied.

Secondary vertices are requested to lie outside of the interaction target in which the corresponding main vertex has been reconstructed. In addition, all cases where the decay vertex is found in one of the downstream targets are rejected in order to exclude secondary interactions. In contrast, because of the “long” lifetime the mean decay path of the candidates found is larger than 1.7 cm. Consequently, several vertices are expected in the region around the downstream targets (the average distance between the copper and carbon layers is 2 cm). For the determination of the mass parameters, all vertices lying inside the downstream targets have been excluded. A different approach was followed for the lifetime measurement and will be discussed in the next section.

The minimum impact parameter of the individual daughter tracks to the main vertex was required to be larger than 2 σ. This cut rejects events where the candidate tracks are pointing directly to the main vertex.

The mean number of tracks used for the main vertices of the selected D^- candidates was 5.8. In average 3.8 space tracks and 2.1 microstrip non-momentum tracks were used; the beam track was included in 79% of the cases.

The mean error on the primary vertex position in x is approximately 410 μm. The closest distance of approach of tracks to the reconstructed secondary and main vertex is 25 and 85 μm respectively. The kaon and pion tracks have a χ^2 lower than 3. The candidate momentum ranges between 50 and 250 GeV/c.

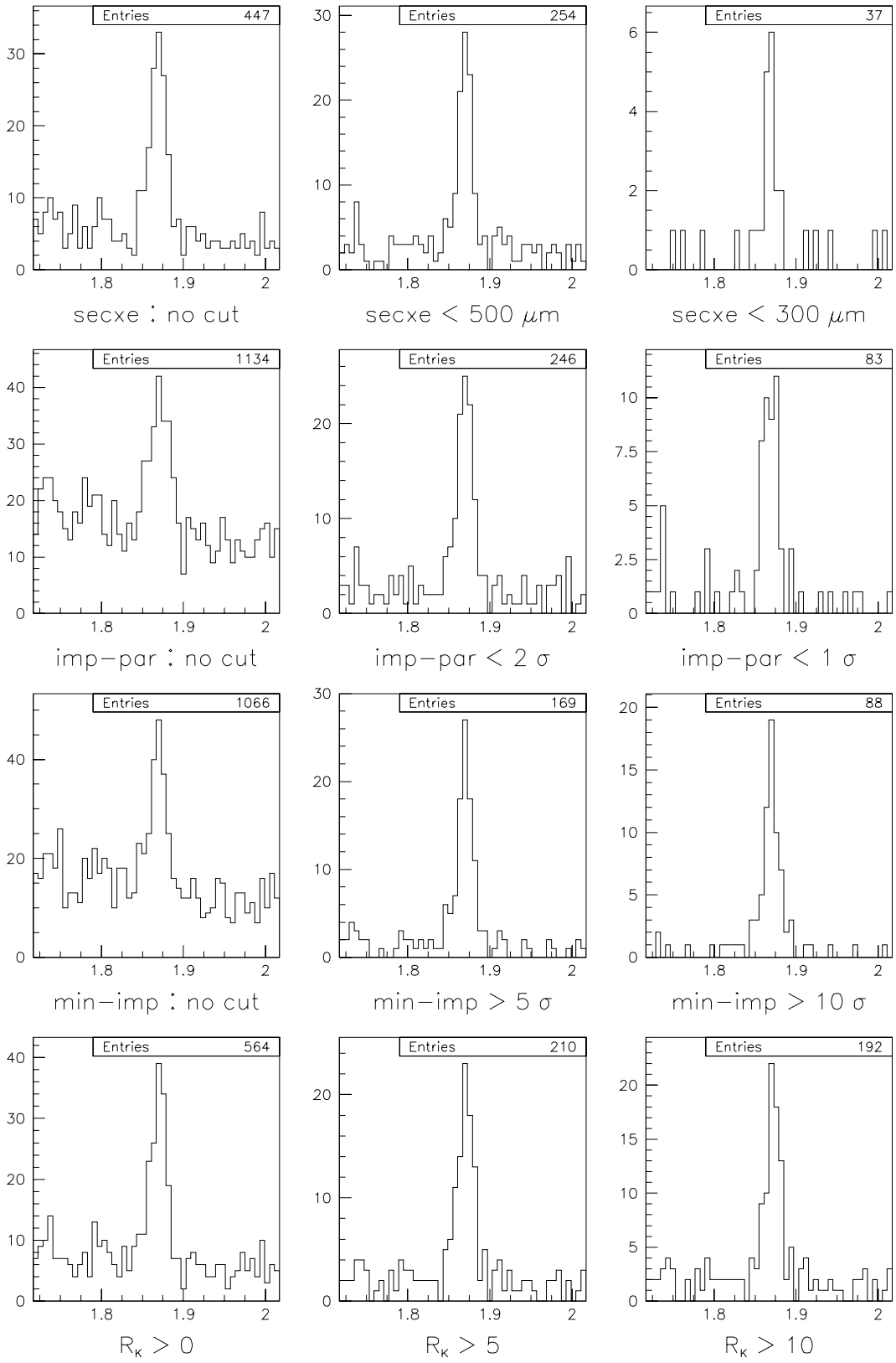

Figure 6.12: Dependence of the D^- mass spectrum on the variation of some of the most relevant cuts (see the text for further explanations regarding the single cuts).

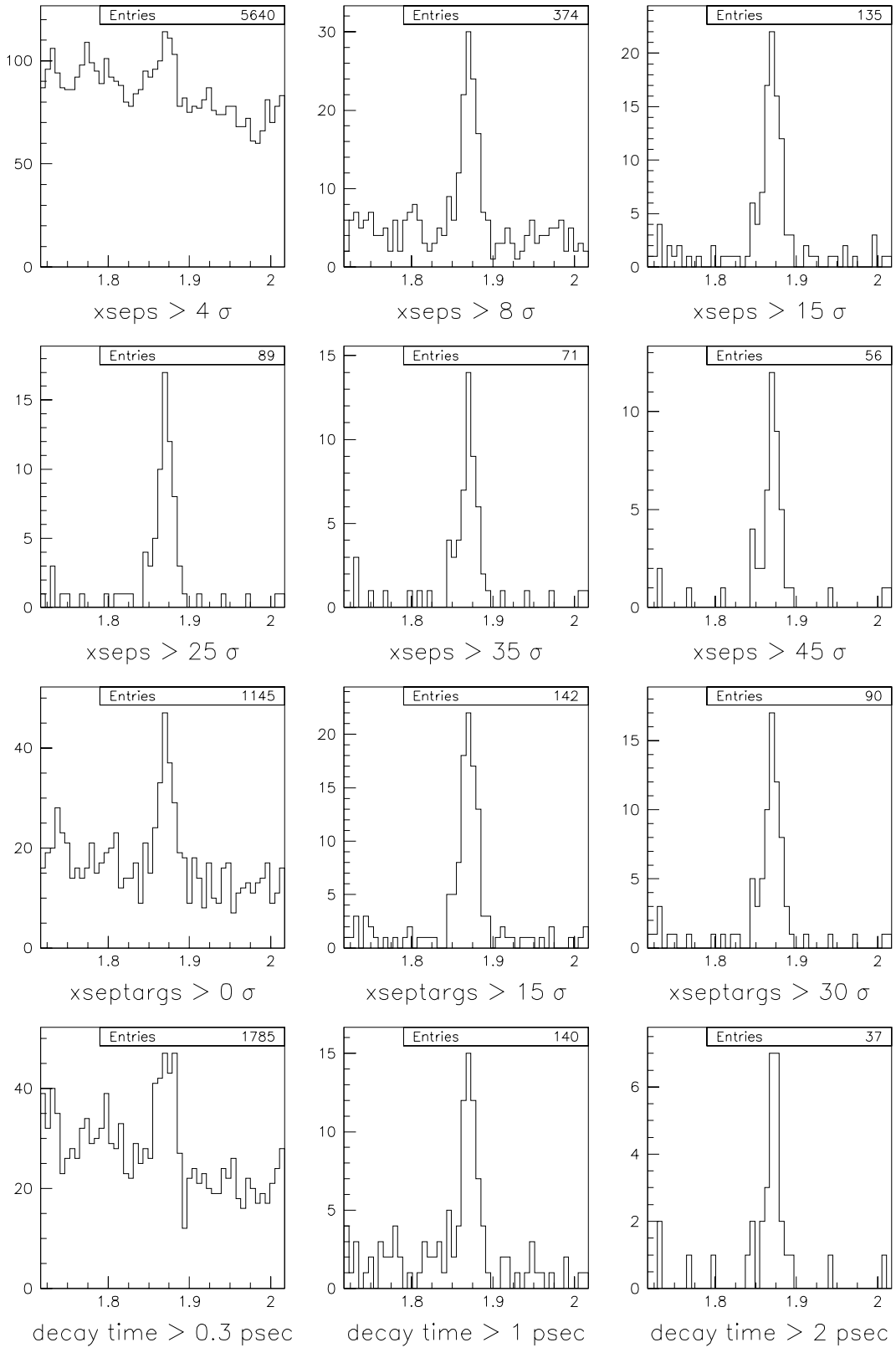

Figure 6.13: Dependence of the D^- mass spectrum on the variation of separation cuts (see the text for further explanations).

Figures 6.12 and 6.13 show the dependence of the mass spectrum on the variation of the most significant cuts. The cuts varied, shown in figure 6.12, are the following ones: the error on the secondary vertex position (*secxe*); the candidate impact parameter (*imp-par*); the minimum impact parameter of individual tracks to the main vertex (*min-imp*); the RICH likelihood ratio R_K for the positively charged kaon. Only one cut is varied at a time keeping all others fixed to the values given in table 6.4.

The dependence on various separation cuts is shown in figure 6.13. *xseps* indicates the separation in the longitudinal direction in σ; *xseptargs* represents the secondary vertex separation from the edge of the target where the corresponding main vertex lies; and in the last row the variation of the lifetime cut is illustrated.

In this case only one at a time of these three separation cuts is applied.

6.1.4 D^- lifetime measurement

As mentioned in the previous section, the long lifetime of the D^- mesons implies the presence of several decay vertices lying within the targets downstream of the primary vertex. These candidates can be easily confused with simple secondary interactions of a particle emerging from the main vertex. For the mass plot the easiest and safest way to avoid these cases was to reject *all* secondary vertices reconstructed inside any target.

On the other hand, this solution strongly distorts the decay time distribution used for the lifetime measurement. Consequently a different approach was followed to select the events for the lifetime evaluation.

The secondary vertices reconstructed inside downstream targets were again considered. In order to exclude the suspected secondary interactions, stronger cuts were applied in addition to the selection criteria listed in table 6.4. A very efficient rejection was obtained requesting the following two conditions:

- smaller error on the reconstructed x position of the secondary vertex; the cut was reduced from 700 to 600 μm;
- the distance from the decay vertex of tracks which were not used either for the secondary or for the primary vertex (*cdaomn*) must be larger than 100 μm.

The new set of cuts slightly reduced the sample of events but removed the danger of including fake events in the lifetime fit. The mass spectrum of the selected candidates is shown in figure 6.14. The fitted number of signal and background events and the relative significance are indicated below.

Signal S	:	96.1 ± 9.2
Background B	:	10
Significance Σ	:	9.3

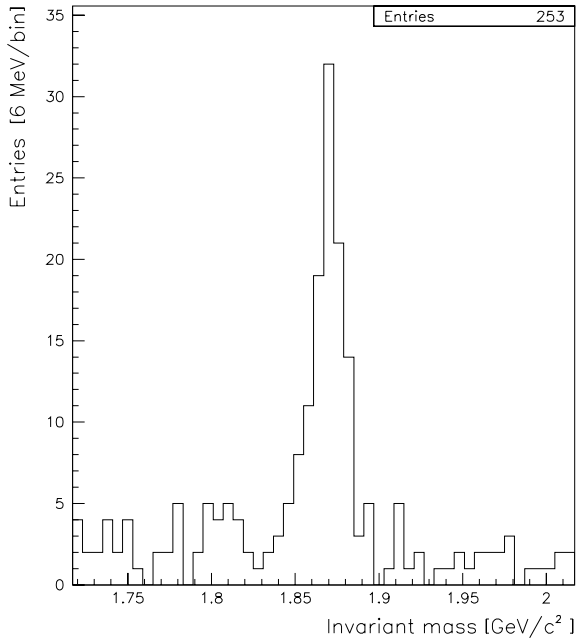

Figure 6.14: Mass distribution of the events selected for the D^- lifetime measurement

The fitting routine described in the previous chapter was used. Also in this case an additional exponential distribution was used to take into account background events at very large separations.

With the selected events the signal and the background lifetimes were measured with the following result:

$$\tau_{D^-} = 0.991^{+0.113}_{-0.098} \text{ (stat.) psec}$$

$$\tau_{bkg} = 0.334^{+0.037}_{-0.033} \text{ (stat.) psec}$$

The obtained result is again in good agreement with the reference value of the D^- lifetime given by the Particle Data Group [2]:

$$\tau^{ref}_{D^-} = 1.057 \pm 0.015 \text{ psec}$$

The top part of figure 6.15 shows the distribution of the logarithmic likelihood function for the fitted signal lifetime (left) and for the exponential component of the background lifetime (right). The bottom plots show the correlation between the signal lifetime and the reconstructed mass (left) and between the signal and background lifetime (right). The last plot shows that there is no correlation between the fitted lifetime values of signal and background, as for the $\overline{D}^0$.

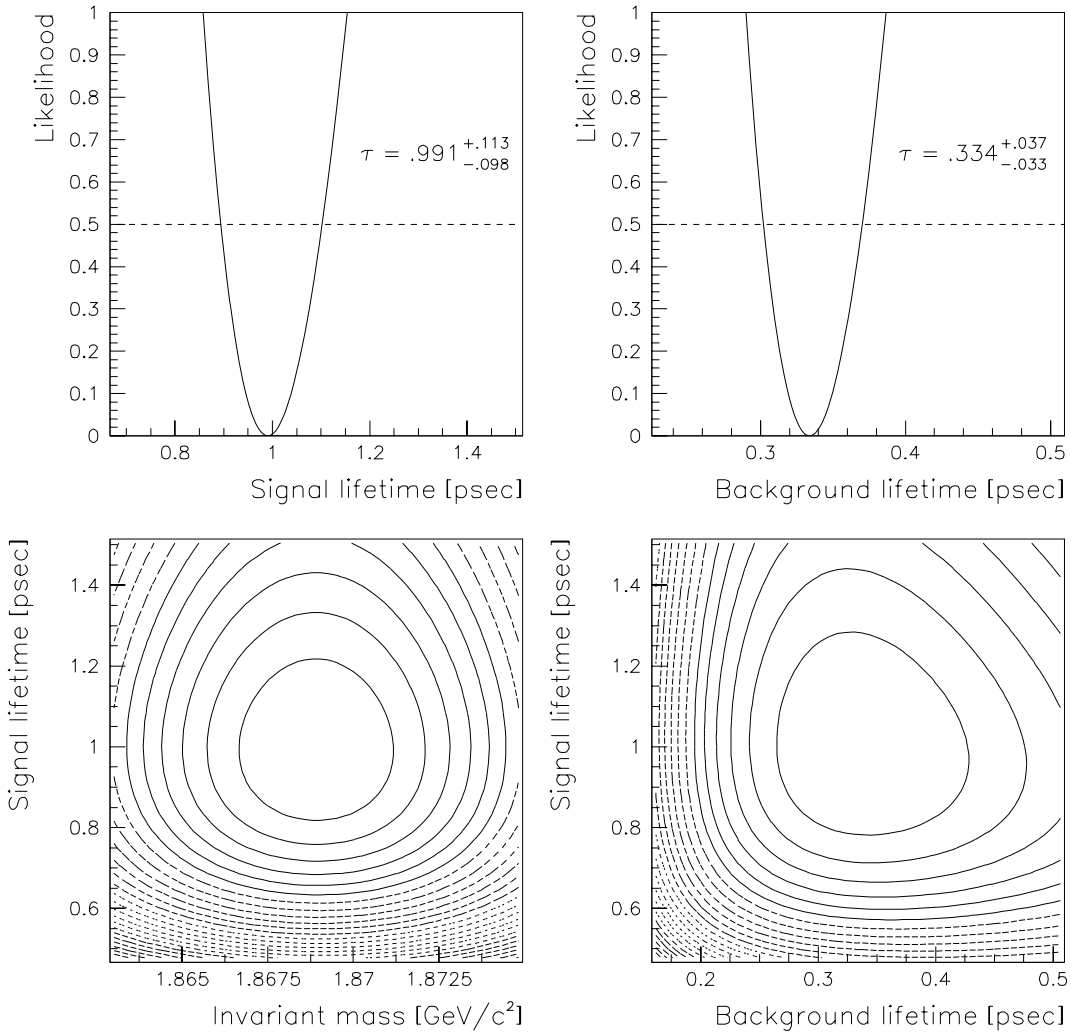

Figure 6.15: Distribution of the logarithmic likelihood function for the signal and background lifetime (on top) and correlation plots for the signal lifetime, the mass and the background lifetime (on bottom) for the sample of D^- candidates.

Also in this case the effective minimum lifetime cut for each event was calculated taking into account the following topological cuts:

- the cut on the separation in the longitudinal direction (*xseps*);
- the cut on the separation from the target edge (*xseptargs*);
- the cut on the minimum impact parameter of the individual daughter tracks with respect to the main vertex (*min-imp*).

The dependence of the measured signal and background lifetimes on the variation of these cuts is shown in figures 6.16, 6.17, and 6.18 for *xseps*, *xseptargs*, and *min-imp* respectively. The reference lifetime value is shown for comparison. No significant dependence on the *cdaomn* cut was observed.

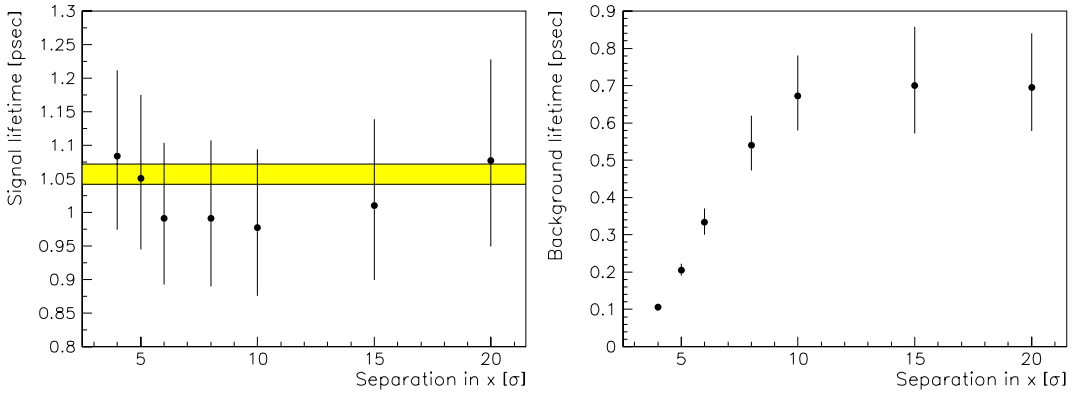

Figure 6.16: Dependence of the measured signal and background lifetime for the D^- sample on the separation cut in the longitudinal coordinate. The grey band in the left plot indicates the reference lifetime value.

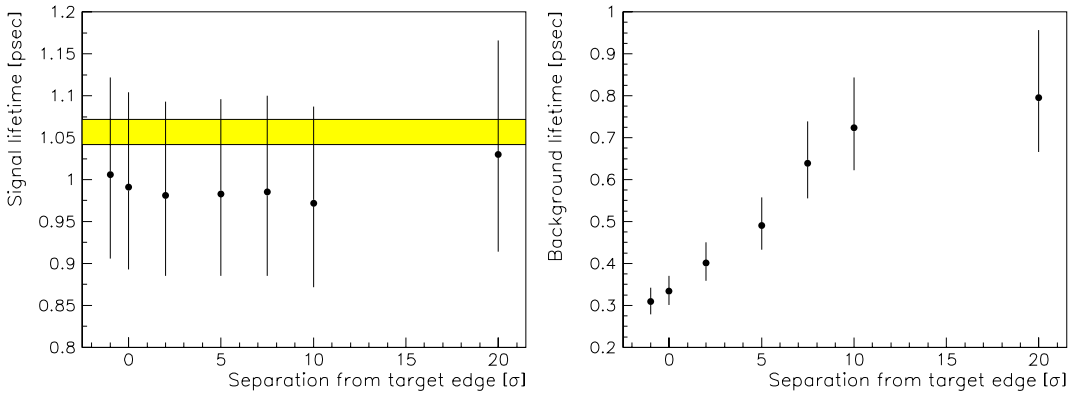

Figure 6.17: Dependence of the measured signal and background lifetime for the D^- sample on the separation cut from the target edge. The grey band in the left plot indicates the reference lifetime value.

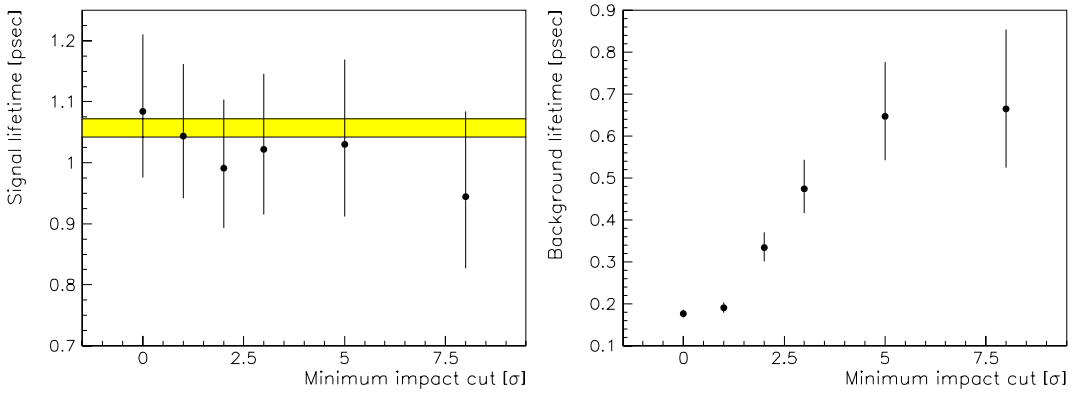

Figure 6.18: Dependence of the measured signal and background lifetime for the D^- sample on the cut on the minimum impact parameter of the daughter tracks to the main vertex. The grey band in the left plot indicates the reference lifetime value.

The systematic error on the D^- signal lifetime was estimated with the same method used for the $\overline{D}^0$.
The limits between which the cut values were varied, the single contributions to the systematic error due to the three topological cuts, and the mass window are listed in table 6.5.

Cut	low cut value	reference cut value	high cut value	lifetime variation
xseps	$\geq 5\ \sigma$	$\geq 6\ \sigma$	$\geq 10\ \sigma$	0.037 psec
xseptargs	$\geq -6\ \sigma$	$\geq 0\ \sigma$	$\geq 7.5\ \sigma$	0.026 psec
min-imp	$\geq 1\ \sigma$	$\geq 2\ \sigma$	$\geq 5\ \sigma$	0.026 psec
mass window	$\pm$ 100 MeV/c^2	$\pm$ 150 MeV/c^2	$\pm$ 200 MeV/c^2	0.014 psec

Table 6.5: Estimate of the contributions to the systematic error on the measured D^- lifetime value.

The four contributions are then summed in quadrature and the systematic error is calculated to be approximately 0.054 psec.
In conclusion, the lifetime measurement on the selected sample of D^- events shown in figure 6.14 gives the following result:

$$\tau_{D^-} = 0.991^{+0.113}_{-0.098}\ (\text{stat.}) \pm 0.054\ (\text{syst.}) \quad \text{psec}$$

6.2 The charmed strange baryon Ξ_c^+

The analysis presented so far was mostly intended as a preparatory work for the more important and more challenging search for the charmed strange baryon Ξ_c^+ and the measurement of its lifetime. The Ξ_c^+ baryon, with quark content (usc), has been seen by several experiments but the available statistics is still very limited.
The reference mass value determined by the Particle Data Group [2] is

$$m_{\Xi_c^+}^{ref} = 2465.1 \pm 1.6 \quad \mathrm{MeV/c^2}$$

based on the most significant measurements made through 1994, which are listed in the following table. Recent publications confirm the reference value.

Experiment	Beam	Decay channels	Entries	Mass [MeV/c^2]	Ref.
WA62	Σ^-	$\Lambda^0 K^- \pi^+ \pi^+$	82	2460 ± 25	[3]
E400	n	$\Lambda^0 K^- \pi^+ \pi^+$	56	$2459 \pm 5 \pm 30$	[4]
ACCMOR	π^-, K^-	$\Xi^- \pi^+ \pi^+$ $\Sigma^+ K^- \pi^+$	6	$2466.5 \pm 2.7 \pm 1.2$	[5]
ARGUS	e^+e^-	$\Xi^- \pi^+ \pi^+$	30	$2465.1 \pm 3.6 \pm 1.9$	[6]
CLEO	e^+e^-	$\Xi^- \pi^+ \pi^+$	23	$2467 \pm 3 \pm 4$	[7]
E687	γ	$\Xi^- \pi^+ \pi^+$	30	$2464.4 \pm 2.0 \pm 1.4$	[8]

Other decay channels seen by CLEO and E687 are $\Omega^- K^+ \pi^+$, $\Xi^0 \pi^+$, $\Xi^0 \pi^+ \pi^0$ and $\Xi^0 \pi^- \pi^+ \pi^+$.

The Ξ_c^+ is the charmed baryon expected to have the longest lifetime, as illustrated in chapter 1. But the determination of a precise value of the lifetime is extremely difficult because of the limited available statistics.
The reference value reported by the Particle Data Group [2] is

$$\tau_{\Xi_c^+}^{ref} = 0.35^{+0.07}_{-0.04} \quad \mathrm{psec}$$

and it is based on the measurements listed in the following table.

Experiment	Decay channels	Entries	Measured lifetime [psec]	Ref.
WA62	$\Lambda^0 K^- \pi^+ \pi^+$	53	$0.48^{+0.21\ +0.20}_{-0.15-0.10}$	[9]
E400	$\Lambda^0 K^- \pi^+ \pi^+$	102	$0.40^{+0.18}_{-0.12} \pm 0.10$	[4]
ACCMOR	$\Xi^- \pi^+ \pi^+$, $\Sigma^+ K^- \pi^+$	6	$0.20^{+0.11}_{-0.06}$	[5]
E687	$\Xi^- \pi^+ \pi^+$	30	$0.41^{+0.11}_{-0.08} \pm 0.02$	[8]

The analysis presented in this work was dedicated to the search for Ξ_c^+ candidates in the decay channels

$$\Xi_c^+ \to \Lambda^0 K^- \pi^+ \pi^+$$
$$\Xi_c^+ \to \Xi^- \pi^+ \pi^+$$

and to the measurement of the Ξ_c^+ lifetime. The results of the analysis are presented in the following sections.

6.2.1 The $\Xi_c^+ \to \Lambda^0 K^- \pi^+ \pi^+$ decay channel

For the search of the decay channel $\Xi_c^+ \to \Lambda^0 K^- \pi^+ \pi^+$ a dedicated data sample selected by PHYNIX was used. The sample consisted of approximately 5.6 million events containing:

- a Λ^0, with a reconstructed mass within ±10 MeV/c^2 from the reference mass;
- a negatively charged kaon satisfying RICH cuts depending on the particle momentum p_K. In particular the following conditions were required:

if	p_K < 20 GeV/c	$L_K/L_\pi > 3$
if	20 GeV/c < p_K < 30 GeV/c	$L_K/L_\pi > 2$ and $L_K/L_p > 0.5$
if	p_K > 30 GeV/c	$R_K > 3$

- a positive track measured in the microstrip detectors with closest distance of approach to the kaon track not larger than 100 μm.

Using the *xip*2 code a further filter was performed in order to isolate candidates for the $\Lambda^0 K^- \pi^+ \pi^+$ channel. The criteria applied are listed in table 6.6.

Filter criteria	$\Xi_c^+ \to \Lambda^0 K^- \pi^+ \pi^+$
Mass window for candidates	± 200 MeV/c^2
Secondary vertex quality (χ^2 per degree of freedom)	≤ 15
Distance between tracks in candidate	≤ 500 μm
Main vertex volume	≤ 1 cm^3
Main vertex probability	≥ 2%
Vertex separation in space	≥ 0
Global impact parameter	≤ 150 μm
Kaon RICH identification	$R_\pi \le .33$; $R_K \ge 0$

Table 6.6: Criteria used to select the data sample for the search of $\Xi_c^+ \to \Lambda^0 K^- \pi^+ \pi^+$ candidates.

The total sample of candidates obtained with the selection described above is shown in figure 6.19.

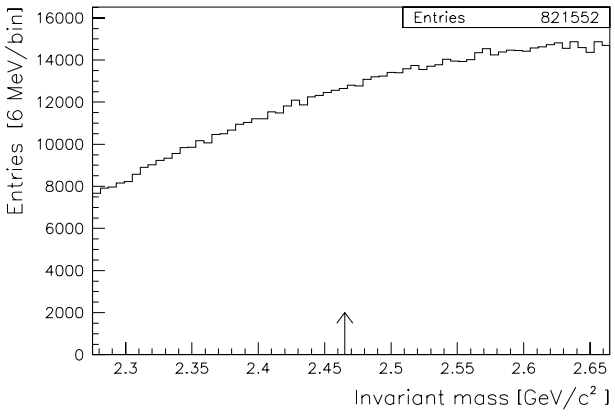

Figure 6.19: Mass distribution of all candidates for the $\Xi_c^+ \to \Lambda^0 K^- \pi^+ \pi^+$ decay channel. The arrow indicates the reference mass.

For this decay channel the candidate parameters are affected by larger uncertainties because of the presence of a Λ among the daughter particles. The hyperon carries most of the candidate momentum, but the decay vertex can be fitted only with the other three charged daughters and therefore it has a large error. Moreover the momentum vector of the Λ has larger errors compared with reconstructed charged tracks because in most cases its daughters are only reconstructed in the decay area: this significantly contributes to the uncertainty of the candidate momentum vector. These effects are clearly reproduced by Monte Carlo generated events.
The mass spectrum of the selected Ξ_c^+ signal is shown in figure 6.20. The fitted parameters are indicated below.

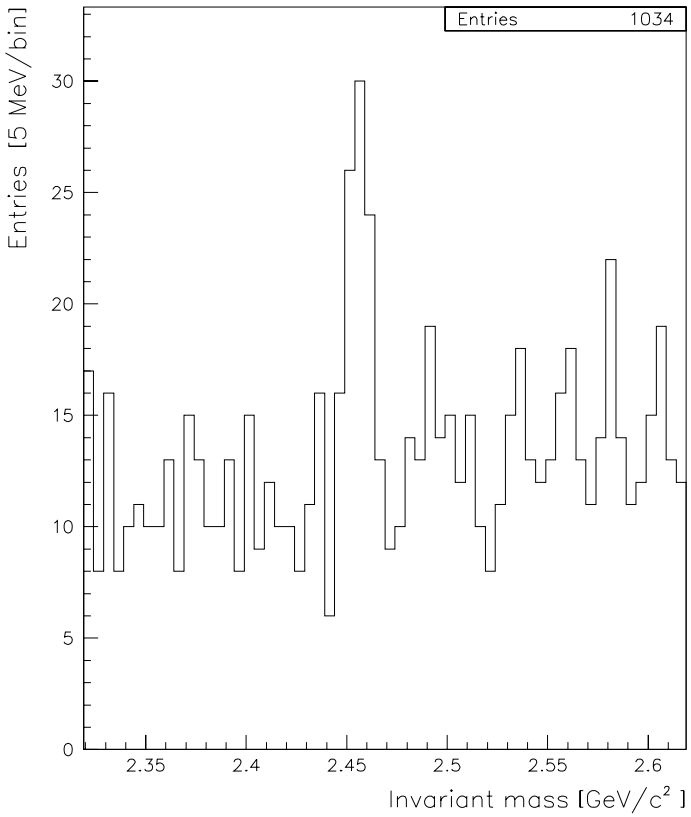

Figure 6.20: Mass distribution of the selected events in the $\Xi_c^+ \to \Lambda^0 K^- \pi^+ \pi^+$ decay channel.

Mass	:	2457.5 ± 1.4 (stat.) ± 6 (syst.) MeV/c^2
Width (1σ)	:	$5.0^{+1.0}_{-0.9}$ (stat.) MeV/c^2
Signal S	:	44.0 ± 9.9
Background B	:	38
Significance Σ	:	4.9

In this case a large systematic error has been assigned, in order to take into account possible mass shifts induced by the uncertainty on the Λ momentum vector. The difference of the measured invariant mass of the Ξ_c^+ candidates from the reference value is at the level

of about 3 σ (considering only the statistical error). A first attempt to apply a constraint fit which forces the extrapolated Λ track in the decay vertex, shifts the candidate mass towards higher values. However further and deeper investigations have to be done in this direction and a more precise study will allow to reduce the systematic error.

The cuts applied on the initial sample to obtain the shown Ξ_c^+ signal are listed in table 6.7. The situation is evidently different from the case of charmed mesons. The background level is very high and more cuts are needed in order to extract the signal. In addition to several topological cuts, quality criteria are used to select Λ particles; momentum cuts are applied to the Λ, the kaon, and the higher momentum pion; only clearly identified kaons are considered.

Cut description	Cut value
Main vertex quality (χ^2 per degree of freedom)	≤ 2.5
CDA of primary tracks to the reconstructed vertex	≤ 400 μm
Secondary vertex quality (χ^2 per degree of freedom)	≤ 1
Vertex separation in space	$\geq 3\sigma$
Global impact parameter	$\leq 6\sigma$
Average impact parameter of the daughter tracks to the main vertex	$\geq 1\ \sigma$
CDA of primary tracks to the secondary vertex	$\geq 1.5\ \sigma$
Kaon RICH identification	$R_K \geq 3$; $R_p \leq 0.015$
Kaon momentum	≥ 25 GeV/c
Momentum of the higher energy pion	≥ 5 GeV/c
CDA of Λ daughters	≤ 4 mm
Separation between Λ and secondary vertex	≥ 5 cm
Λ momentum	≥ 50 GeV/c
Proton (Λ daughter) RICH identification	$R_p \geq 0$; $R_\pi \leq 0.6$

Table 6.7: Cuts applied to select the Ξ_c^+ signal in the $\Lambda^0 K^- \pi^+ \pi^+$ decay channel.

Besides stronger requirements on the main and the secondary vertex quality, more topological cuts have been used. The average impact parameter of the charged daughter tracks is requested to be larger than 1 σ. Furthermore, the closest distance of approach of tracks emerging from the main vertex with respect to the decay vertex is checked. In order to reject events in which primary tracks lie too close to the secondary vertex, their CDA must be larger than 1.5 σ (the mean value of 1 σ is approximately 30 μm). This is an extremely efficient criterion to reject background events, as shown in figure 6.21. The cut on the global impact parameter is not as strong as in the case of the charmed mesons because of the presence of the extrapolated and not measured Λ track among the daughters.
The conditions which must be satisfied by the Λ candidates are the following: the closest distance of approach of the two daughter tracks must be smaller than 4 mm; the reconstructed Λ decay vertex must lie downstream of the secondary vertex; the momentum must

be larger than 50 GeV/c; the daughter proton must have been in the RICH acceptance and $\Lambda - K_S^0$ ambiguities are excluded by rejecting identified pions.
Clearly identified kaons are selected with the RICH cut $R_K \geq 3$ and anti-protons are excluded. The mean value of the momentum of the selected kaons is approximately 52 GeV/c.

Among the cuts listed in table 6.7, the ones which are more significant for the selection of the signal are: the secondary vertex quality (*secqual* indicates the vertex χ^2 divided by the number of degrees of freedom); the closest distance of approach of tracks emerging from the main vertex to the decay vertex (*cdamtmin*); the average impact parameter of daughter tracks to the primary vertex (*av-imp*) and the RICH identification of the kaon.
The behaviour of the mass spectrum on the variation of these cuts is shown in figure 6.21. The signal shows a good behaviour on the variation of the more significant cuts, compatible with the high level of background.

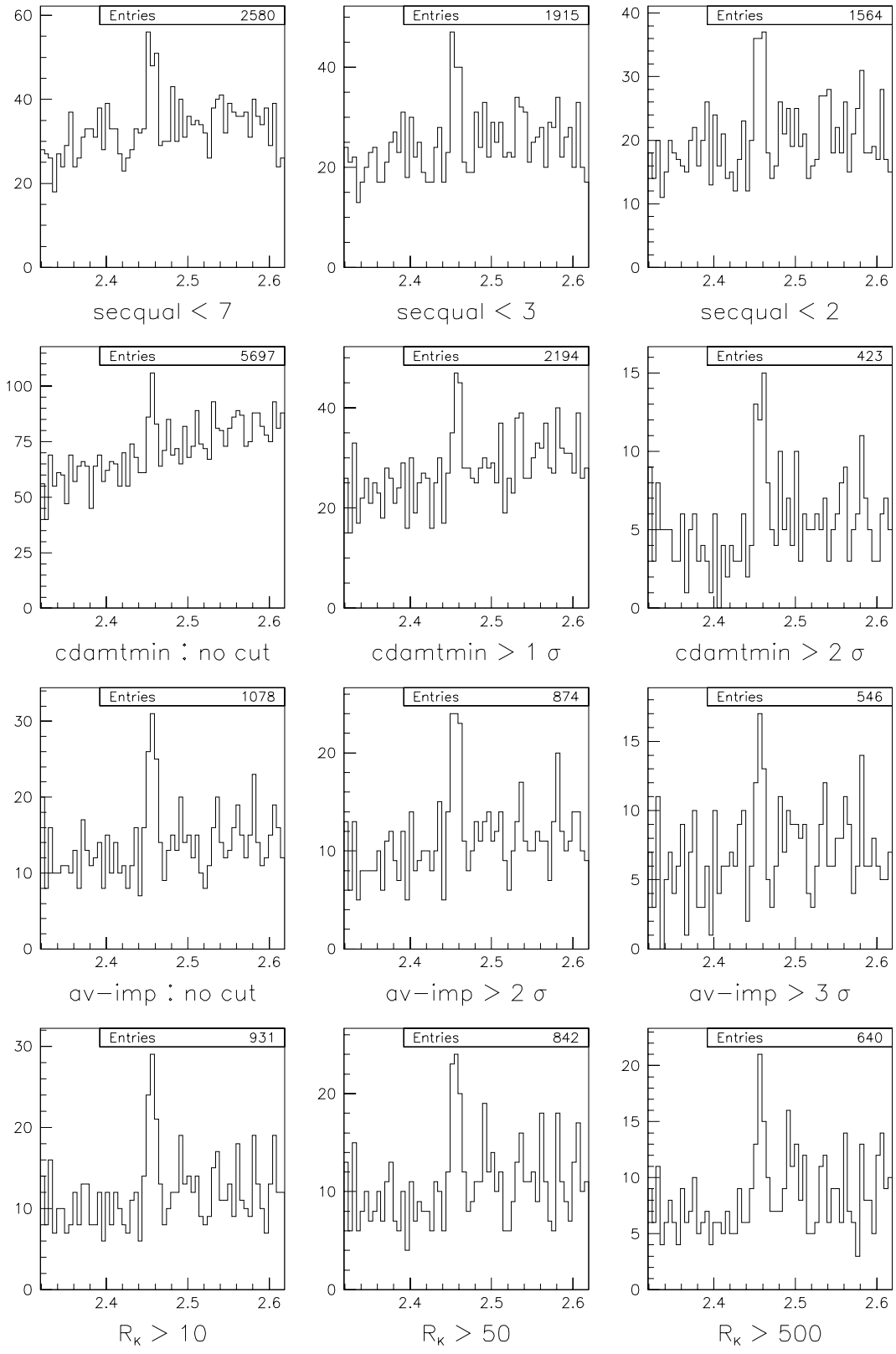

Figure 6.21: Dependence of the Ξ_c^+ mass spectrum on the variation of the most significant cuts (see the text for further explanations regarding the single cuts).

The separation between the primary and the secondary vertex is requested to be larger than 3 σ in space. It should be stressed that the mean errors are much larger in this sample than for the charmed mesons. As already mentioned, the secondary vertex position and its error are calculated using only the charged tracks (the kaon and the two pions). Since the largest part of the candidate momentum is carried by the Λ, the three charged daughters have relatively low momenta. This is true in particular for the pions of the sample here discussed since the RICH identification selects kaons with momentum higher than 20 GeV/c. For this reason the error on the decay vertex position in the longitudinal coordinate turns out to be large, with a mean value of 1 mm in the selected sample, comparable to the 900 μm error estimated with Monte Carlo generated events. The mean value of this error was approximately 500 μm for the mesons.

For the selected candidates the mean error on the main vertex position is approximately 600 μm, and this value is also slightly larger than the average 400 μm measured for the charmed mesons.

A feature of the selected sample of candidates is that the region of large separations is populated by a very limited number of events. This can be partly explained with the low available statistics.

The behaviour of the mass spectrum on the variation of the separation cut is shown in figure 6.22.

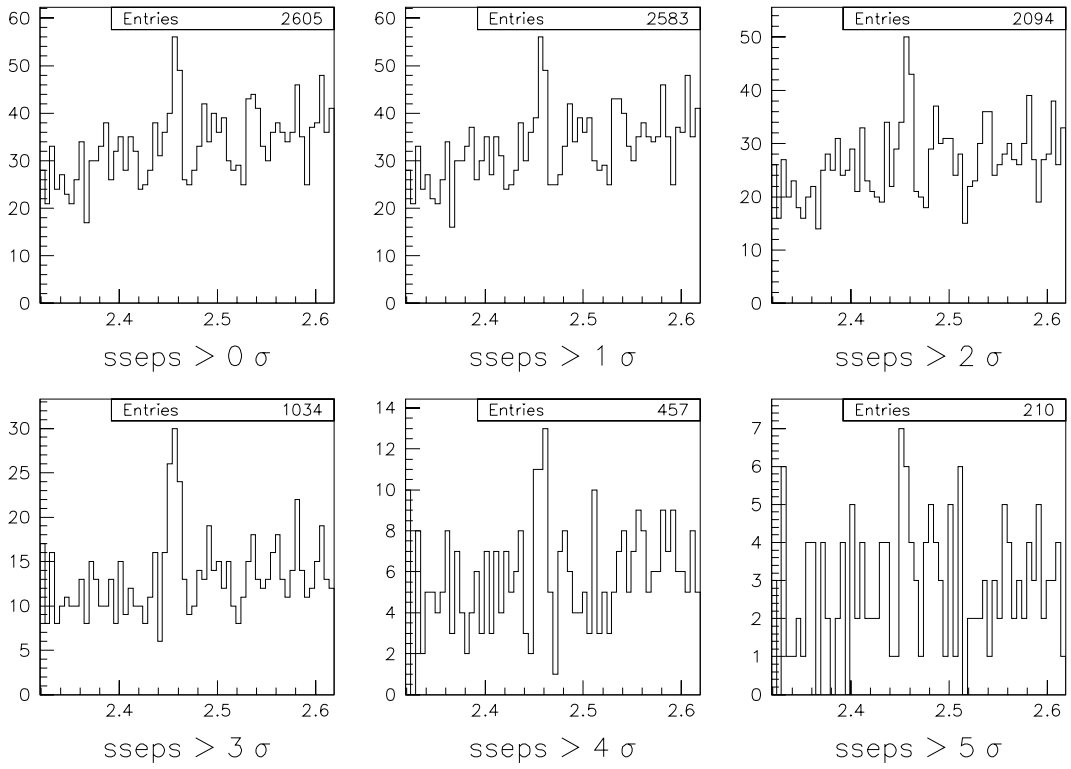

Figure 6.22: Dependence of the Ξ_c^+ mass spectrum on the variation of the separation cut.

6.2.2 Ξ_c^+ lifetime measurement

The candidates selected as described above in the $\Xi_c^+ \to \Lambda^0 K^- \pi^+ \pi^+$ decay channel were used for the lifetime measurement.
Owing to the very high level of background, it was not possible to fit simultaneously the mass distribution and the signal and background lifetime distributions. Moreover the fit of an additional exponential for the background decay time distribution gives a background lifetime value compatible with 0.
Thus the background lifetime was described by the two standard Gaussians and the signal lifetime was fitted with an exponential distribution. The lifetime value obtained is:

$$\tau_{\Xi_c^+} \quad = \quad 0.35^{+0.12}_{-0.08} \quad \text{(stat.)} \quad \text{psec}$$

The large errors are due to the limited statistics and the uncertainty on the length of the decay path originating from the errors on the primary and the secondary vertices, which are larger in this sample than for the charmed mesons discussed in the previous section.
The logarithmic likelihood function obtained from the fit of the signal lifetime is shown in figure 6.23.

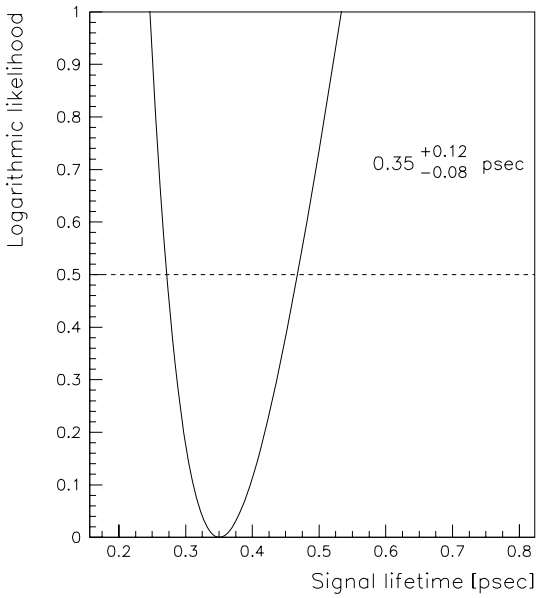

Figure 6.23: Distribution of the logarithmic likelihood function for the signal lifetime measured from the $\Xi_c^+ \to \Lambda^0 K^- \pi^+ \pi^+$ decay channel.

The topological selection criteria taken into account to calculate the minimum lifetime cut on an event by event basis are the following:

- the cut on separation in space (*sseps*);
- the cut on the closest distance of approach of primary tracks to the decay vertex (*cdamtmin*);
- the cut on the average impact parameter of the daughter tracks to the main vertex (*av-imp*).

Systematic errors on the measured lifetime induced by these cuts were studied. The following figures show the dependence of the lifetime value on the variation of the three cuts mentioned above and on other cuts which are relevant to the lifetime determination: the total impact parameter, the Λ momentum, and (less critical) the RICH identification of the kaon.

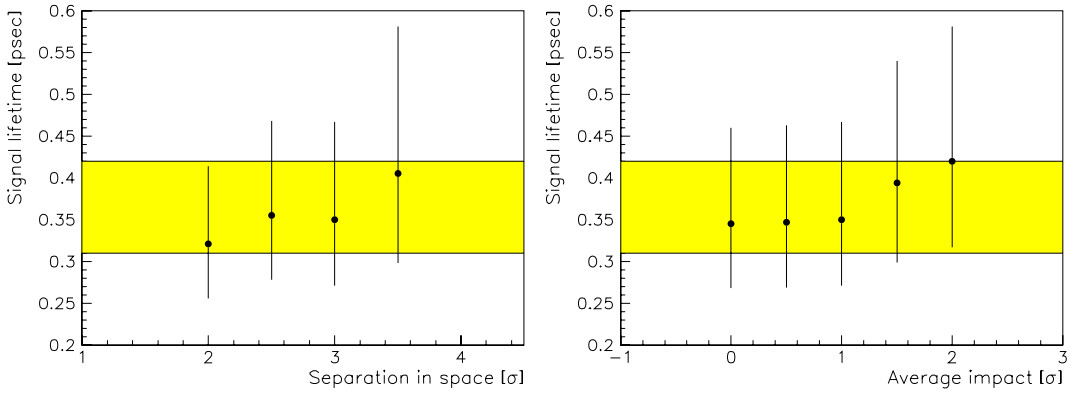

Figure 6.24: Dependence of the measured signal lifetime for the $\Xi_c^+ \to \Lambda^0 K^- \pi^+ \pi^+$ sample on the cut on the separation in space (on the left) and on the average impact parameter of the daughter tracks to the main vertex (on the right). The grey band indicates the reference lifetime value.

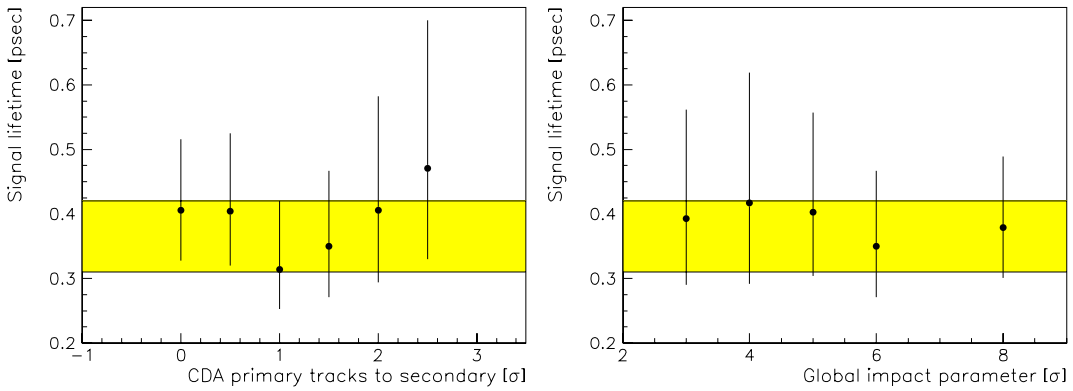

Figure 6.25: Dependence of the measured signal lifetime for the $\Xi_c^+ \to \Lambda^0 K^- \pi^+ \pi^+$ sample on the cut on the closest distance of approach of tracks in the primary vertex to the secondary vertex (on the left) and on the candidate impact parameter (on the right). The grey band indicates the reference lifetime value.

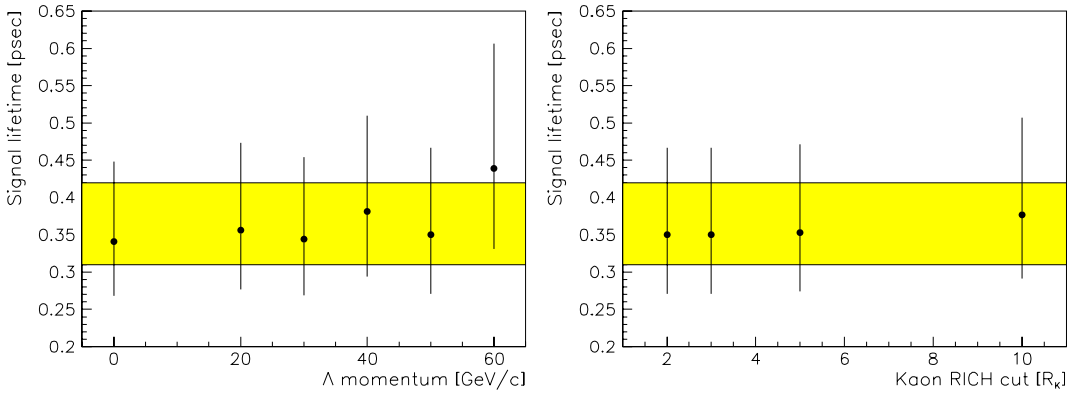

Figure 6.26: Dependence of the measured signal lifetime for the $\Xi_c^+ \to \Lambda^0 K^- \pi^+ \pi^+$ sample on the cut on the Λ momentum (on the left) and on the kaon RICH identification (on the right). The grey band indicates the reference lifetime value.

No strong systematic dependence of the lifetime value on the cut on the global impact parameter, the Λ momentum, or the RICH identification of the kaon are visible.
The other three topological cuts described above were taken into account to estimate the systematic error on the Ξ_c^+ lifetime, following the same method used for the mesons.
The limits between which the cut values were varied, the single contributions to the systematic error due to the three topological cuts and the considered mass window are listed in table 6.8.

Cut	low cut value	reference cut value	high cut value	lifetime variation
sseps	$\geq 2\ \sigma$	$\geq 3\ \sigma$	$\geq 3.5\ \sigma$	0.042 psec
cdamtmin	$\geq 1\ \sigma$	$\geq 1.5\ \sigma$	$\geq 2\ \sigma$	0.046 psec
av-imp	$\geq 0\ \sigma$	$\geq 1\ \sigma$	$\geq 2\ \sigma$	0.038 psec
mass window	$\pm$ 100 MeV/c^2	$\pm$ 150 MeV/c^2	$\pm$ 200 MeV/c^2	0.008 psec

Table 6.8: Estimate of the contributions to the systematic error on the measured Ξ_c^+ lifetime value.

The four contributions are then summed in quadrature and the systematic error is calculated to be approximately 0.073 psec.
In conclusion, the lifetime measurement on the selected sample of Ξ_c^+ events in the $\Lambda^0 K^- \pi^+ \pi^+$ decay channel gives the following result:

$$\tau_{\Xi_c^+} = 0.35^{+0.12}_{-0.08}\ \text{(stat.)} \pm 0.07\ \text{(syst.)} \quad \text{psec}$$

6.2.3 The $\Xi_c^+ \to \Xi^- \pi^+ \pi^+$ decay channel

The second investigated decay channel is $\Xi_c^+ \to \Xi^- \pi^+ \pi^+$. The data used for the candidate search were the sample of about 500000 matched Ξ^- candidates selected by the $V0$ package. The invariant mass plot containing all selected candidates is shown in figure 6.27.

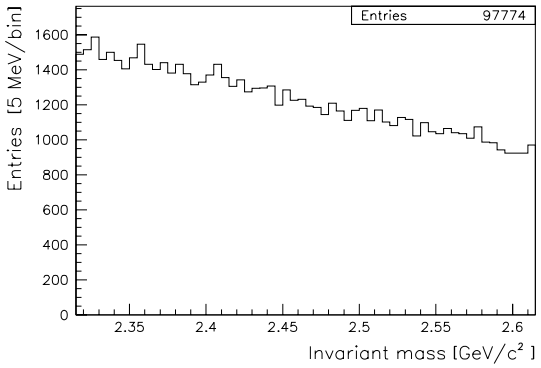

Figure 6.27: Mass distribution of all candidates selected for the $\Xi_c^+ \to \Xi^- \pi^+ \pi^+$ decay channel.

The signal found in this channel is shown in figure 6.28. The fitted parameters are indicated below.

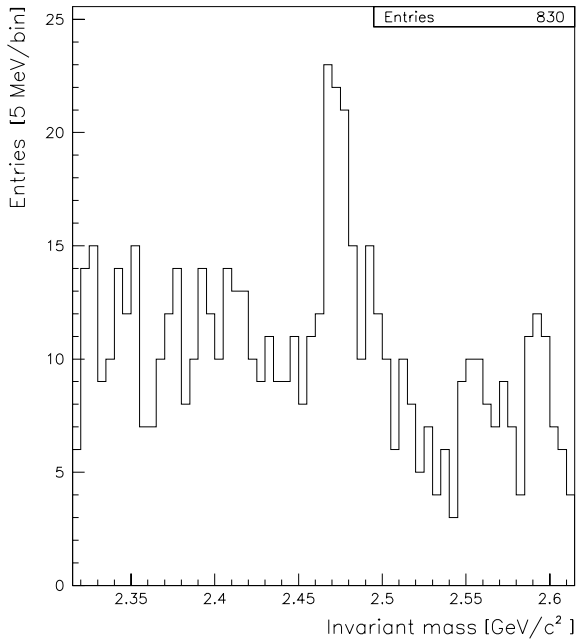

Figure 6.28: Mass distribution of the selected events in the $\Xi_c^+ \to \Xi^- \pi^+ \pi^+$ decay channel.

Mass	:	2468.4 ± 1.6 (stat.) ± 1.8 (syst.) MeV/c^2
Width (1σ)	:	$4.5^{+1.7}_{-1.0}$ (stat.) MeV/c^2
Signal S	:	37.4 ± 7.9
Background B	:	44
Significance Σ	:	4.1

Cut description	Cut value
Main vertex quality (χ^2 per degree of freedom)	≤ 3
Error on the main vertex position in x	≤ 500 μm
Maximum χ^2 of a main vertex refitted including one of candidate daughter track	≥ 1.5
Secondary vertex quality (χ^2 per degree of freedom)	≤ 2
Error on the secondary vertex position in x	≤ 900 μm
Minimum χ^2 of a secondary vertex refitted including one unused track	≥ 0.3
Vertex separation in space (both signs!)	$\geq 3.6\sigma$
Global impact parameter	$\leq 5\sigma$
Maximum impact parameter of individual candidate tracks wrt the main vertex	$\geq 1.5\ \sigma$
RICH identification of the higher momentum pion	$R_K \leq 3$; $R_p \leq 3$
RICH identification of the lower momentum pion	$R_K \leq 1$
Separation between Ξ^- and secondary vertex	≥ 80 cm
Ξ^- momentum	≥ 35 GeV/c
Quality of the Ξ^- bridging ("scaled" χ^2, see text)	≤ 70

Table 6.9: Cuts applied to select the Ξ_c^+ signal in the $\Xi^-\pi^+\pi^+$ decay channel.

The cuts applied to obtain the shown Ξ_c^+ signal are listed in table 6.9. The selection of the signal in the $\Xi^-\pi^+\pi^+$ decay channel required a large number of cuts in order to reduce the background to the level shown in figure 6.28.

Besides the standard cuts on the quality and the error in the x position of the main and the secondary vertices, two new cuts were introduced for this channel. In order to exclude candidates where all daughter tracks seem to belong to the primary vertex, the code takes one daughter track at the time and fits the main vertex again including that track. For each candidate the worst case is taken (corresponding to the daughter track which is farthest from the main vertex) and the new vertex is required to have a χ^2 larger than 1.5.

In a similar way, tracks which have not been used either for the main or for the secondary vertex, are attached to the decay vertex and a new fit is performed. In all cases, the new vertex with best quality (the one including the unused track lying closest to the decay vertex) is considered and its χ^2 is required to be larger than 0.3. This cut rejects candidates having other unused tracks apparently belonging to the decay vertex, indicating a decay with a higher number of prongs or a secondary interaction. The pions are negatively identified, excluding kaons and protons clearly identified by the RICH.

A higher purity sample of Ξ^-s is obtained selecting hyperons with momentum higher than 35 GeV/c, and with the decay vertex well downstream of the secondary vertex, and requiring a good quality of the bridging. This quality is expressed with a χ^2 distribution scaled to a range between 0 and 255.

A significant number of candidates for the $\Xi^-\pi^+\pi^+$ decay channel could be selected only

by allowing for both positive and negative separations between the main and the secondary vertices. The possibility of reconstruction of the primary vertex downstream of the decay point is due to the limited resolution and efficiency of the tracking detectors, and to the apparatus acceptance: If several tracks emerging from the main vertex are not detected or they are reconstructed with very large errors, the fitted vertex position can be significantly displaced with respect to the real production point.
In the three previous decay channels there was also a significant number of candidates showing negative vertex separation. The better statistics of those channels allowed rejection of those entries. In this case, accepting only positive vertex separations reduces the sample by a factor of about two, and the remaining signal (shown in figure 6.29) is no longer significant enough for a lifetime measurement. Consequently, in this analysis, the decay channel $\Xi^-\pi^+\pi^+$ could not be used for the lifetime study of the Ξ_c^+ baryon.

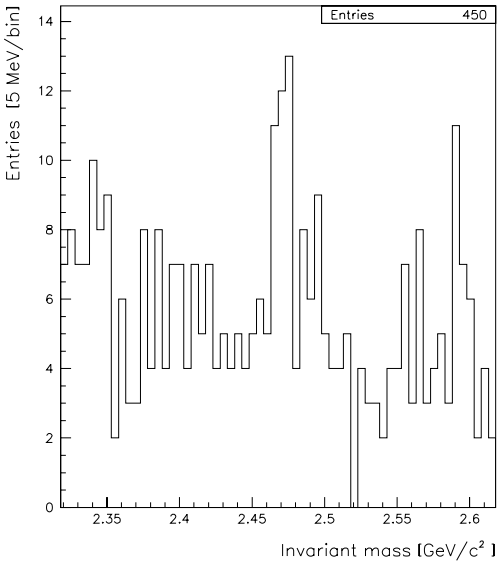

Figure 6.29: $\Xi_c^+ \to \Xi^-\pi^+\pi^+$ mass spectrum: positive separation only.

Signal S	:	15.4 ± 5.8
Background B	:	18
Significance Σ	:	2.7

The dependence of the mass distribution on the variation of the most relevant cuts is shown in figures 6.30 and 6.31. In figure 6.30 the cuts varied are: the error on the x position of the main vertex (*mainxe*); the maximum χ^2 of main vertices refitted including a daughter track of the candidate (*clctmx*); the error on the x position of the secondary vertex (*secxe*); the minimum χ^2 of secondary vertices refitted including an unused track (*clotcn*).
In figure 6.31 the cuts varied are: the global impact parameter of the charm candidate (*imp-par*); the maximum impact parameter of the individual daughter tracks with respect to the main vertex (*max-imp*); the quality of the Ξ^- bridging (*ibrsig*); the vertex separation in space (*sseps*). One cut at a time is varied, while all others are kept fixed to the value indicated in the table 6.9.

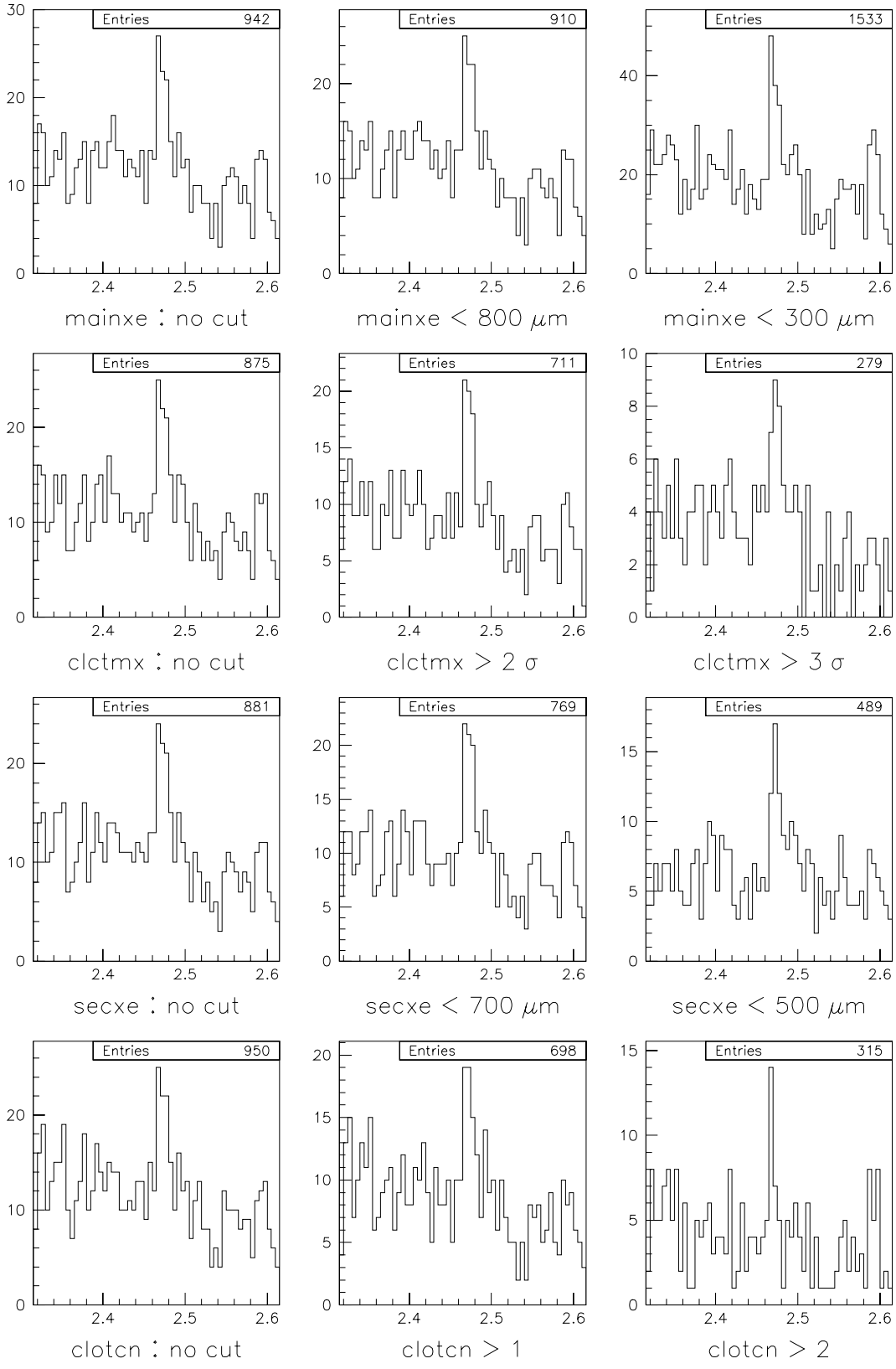

Figure 6.30: Dependence of the $\Xi_c^+ \to \Xi^- \pi^+ \pi^+$ mass spectrum on the variation of some of the most relevant cuts (see the text for further explanations regarding the single cuts).

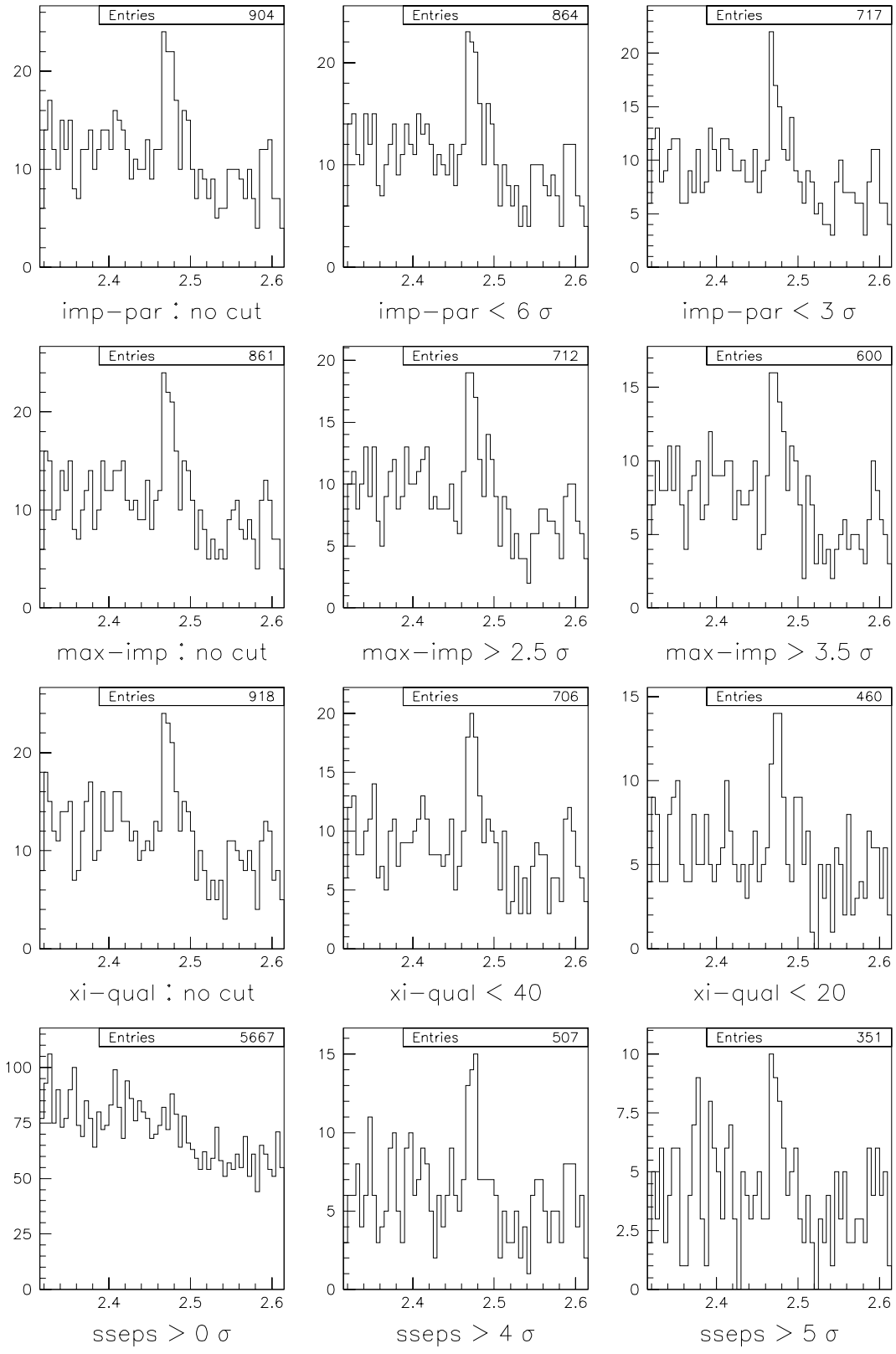

Figure 6.31: Dependence of the $\Xi_c^+ \to \Xi^- \pi^+ \pi^+$ mass spectrum on the variation of some of the most relevant cuts (see the text for further explanations regarding the single cuts).

Bibliography

[1] E. Chudakov, WA89 Internal Note, July 1996

[2] The Particle Data Group, “Review of particle properties”, Phys. Rev. D3 (1994)

[3] S.F. Biagi et al., “Observation of a narrow state at 2.46 GeV/c^2 - a candidate for the charmed strange baryon A^+”, Phys. Lett. 122B (1983) 455-460

[4] P. Coteus et al., “Production of the charmed strange baryon Ξ_c^+ by neutrons”, Phys. Rev. Lett. 59 (1987) 1530-1533

[5] S. Barlag et al., “Measurement of the mass and lifetime of the charmed strange baryon Ξ_c^+”, Phys. Lett. B233 (1989) 522-529

[6] H. Albrecht et al., “Measurement of $\Xi(c)$ production in e^+e^- annihilation at 10.5 GeV center-of-mass energy”, Phys. Lett. B247 (1990) 121-126

[7] M.S. Alam et al., “Measurement of the isospin mass splitting Ξ_c^+-Ξ_c^0”, Phys. Lett. B226 (1989) 401-406

[8] P.L. Frabetti et al., “Measurement of the mass and lifetime of the Ξ_c^+”, Phys. Rev. Lett. 70 (1993) 1381-1384

[9] S.F. Biagi et al., “Measurement of the lifetime of the charmed strange baryon A^+”, Phys. Lett. B150 (1985) 230-241

Chapter 7

Discussion of results

The analysis work presented in this thesis was devoted to the search for the anti-charmed mesons $\overline{D}^0$ and D^- in the decay channels:

$$\overline{D}^0 \to K^+\pi^- \qquad D^- \to K^+\pi^-\pi^-$$

and the charmed strange baryon Ξ_c^+ in the decay channels:

$$\Xi_c^+ \to \Lambda^0 K^-\pi^+\pi^+ \qquad \Xi_c^+ \to \Xi^-\pi^+\pi^+$$

produced by a Σ^- beam of 340 GeV/c at the fixed target experiment WA89 at CERN.
Candidates were selected using topological criteria and particle identification based on the information provided by the RICH detector. The high spatial resolution of the silicon microstrip detectors placed in the vertex region and the measurement of four projections allow the reconstruction of space tracks with high precision. This is an essential condition in order to be able to reconstruct separate production and decay vertices of charmed hadrons and thus isolate charm candidates from a very large background.
The mass of the charmed hadrons mentioned above was determined with the candidates found. Moreover, the selected mesons and the Ξ_c^+ candidates in the $\Lambda^0 K^-\pi^+\pi^+$ decay channel were used to estimate the respective lifetime values. The obtained results will be discussed below.

7.1 Measurements of masses of charmed hadrons

With the candidates selected for the decay channels listed above, the mass of the $\overline{D}^0$, D^- and Ξ_c^+ charmed hadrons was estimated. The obtained mass values are listed in table 7.1 and are compared with the respective world average values from reference [1]. For all measurements presented here, both the statistical and the systematic errors are quoted, with the statistical one first. The procedure followed to determine the systematic errors is described in the previous chapter.

The meson candidates are reconstructed using tracks of long-living charged particles (kaons and pions) which are detected in the microstrip counters, traverse the decay region and the Omega spectrometer, and, at least for the kaons, enter the RICH detector.

Decay channel	Number of candidates	Signal significance	Reconstructed mass [MeV/c^2]	Reference mass [MeV/c^2] [1]
$\overline{D}^0 \to K^+\pi^-$	96.9 ± 9.2	9.1	$1864.4 \pm 1.3 \pm 1.5$	1864.6 ± 0.5
$D^- \to K^+\pi^-\pi^-$	107.9 ± 10.6	9.5	$1869.5 \pm 1.2 \pm 1.5$	1869.4 ± 0.4
$\Xi_c^+ \to \Lambda^0 K^-\pi^+\pi^+$	44.0 ± 9.9	4.9	$2457.5 \pm 1.4 \pm 6$	
$\Xi_c^+ \to \Xi^-\pi^+\pi^+$	37.4 ± 7.9	4.1	$2468.4 \pm 1.6 \pm 1.8$	2465.1 ± 1.6

Table 7.1: Mass of the charmed hadron candidates found, compared with the world average values.

The momentum and the track parameters of the daughter particles are determined with high precision. In order to take into account magnetic field distortions and chamber misalignments, momenta have been corrected with the empirical formula described at the beginning of chapter 6. The agreement between the reconstructed invariant mass and the reference values is excellent.

The situation is different for the Ξ_c^+ candidates in the $\Lambda^0 K^-\pi^+\pi^+$ decay channel. The Λ^0 carries most of the candidate momentum, but its momentum vector is affected by large errors: It is determined using the information on the momentum of the pion and the proton, which, in most of the cases, are detected only in the decay region, downstream of the vertex area. Consequently, the resolution on the track parameters and the measured momentum vector is lower than for particles detected in the microstrip counters. These larger errors cause a more significant uncertainty on the momentum vector of the mother Λ particle. This is a possible reason for the difference of the measured invariant mass of the Ξ_c^+ candidates in the $\Lambda^0 K^-\pi^+\pi^+$ decay channel from the reference value: The disagreement is at the level of about 3 σ.
The possibility of a significant mass shift induced by the Λ candidates is at the moment neither confirmed nor disproved by other significant signals of charmed baryons with a Λ among the daughter particles seen in WA89 1993 data. Further and deeper investigations have to be done in this direction.

Λ candidates are used to reconstruct Ξ^- decays, but the problem is no longer present for the Ξ^-s since their track is measured in the microstrip detectors: Using the microstrip track segment for the bridging, a strong constraint is added in the determination of the track parameters and the momentum vector. The mass determined with the candidates selected in the $\Xi^-\pi^+\pi^+$ decay channel is compatible with the reference mass within one standard deviation.

7.2 Measurements of lifetimes of charmed hadrons

A maximum likelihood method has been used to measure the mean lifetime of the selected charmed hadrons. The fitting routine and the method to correct for topological cuts were thoroughly tested on the meson samples and then applied to the Ξ_c^+ candidates found in the $\Lambda^0 K^-\pi^+\pi^+$ decay channel. For the events selected in the $\Xi^-\pi^+\pi^+$ decay channel, the request of positive vertex separation in order to allow the lifetime measurement, reduced

significantly the signal. The remaining events (showing a significance lower than 3) were not used to measure the mean lifetime.
The decay time resolution function, which contains the information about the spatial and momentum resolution of the apparatus, was determined with minimum bias events. It is best described by the sum of two Gaussian distributions with a width of 33 and 87 fsec, respectively, and a relative weight of 84:16. This corresponds to an average resolution of approximately 40 fsec, a very good value to be ascribed to the high resolution of our microstrip vertex detector. The determined resolution function is convoluted with the decay time exponential distribution as explained in chapter 5.

The results obtained for the $\overline{D}^0$ and D^- candidates, compared with the reference values from reference [1], are listed in table 7.2.

Decay channel	Number of candidates	Signal significance	Estimated lifetime [psec]	Reference value [psec] [1]
$\overline{D}^0 \to K^+\pi^-$	96.9 ± 9.2	9.1	$0.433^{+0.054}_{-0.046} \pm 0.024$	0.415 ± 0.004
$D^- \to K^+\pi^-\pi^-$	96.1 ± 9.2	9.3	$0.991^{+0.113}_{-0.098} \pm 0.054$	1.057 ± 0.015

Table 7.2: Estimated lifetime for the selected anti-charmed mesons candidates, compared with the world average values.

The large errors on the lifetime values are due to the limited available statistics: with about 100 events a 10% error is expected. The procedure to determine the systematic errors induced by topological selection criteria is described in chapter 6. Studies on Monte Carlo generated events indicate the absence of other systematic effects.
The measured lifetimes are in very good agreement with the world average values.
The study of the better known charmed mesons was intended as a preparatory work for the treatment of the Ξ_c^+ signal, making a detailed study of the procedure to correct for selection criteria and of the unbinned maximum likelihood fitting method.

7.2.1 The lifetime of the Ξ_c^+ charmed strange baryon

The method was then applied to estimate the mean lifetime of the Ξ_c^+ candidates selected in the $\Lambda^0 K^-\pi^+\pi^+$ decay channel. The situation is different from the case of the selected mesons, because of a much higher level of background. The fit was made in two steps, for the mass distribution first and then for the signal lifetime, while the two distributions could be fitted simultaneously for the meson samples. The difference between the fit done in one or in two steps was tested on the mesons, using samples with different signal to noise ratios and the obtained results from the two fit modes were completely compatible.
The mean lifetime value measured from the sample of selected Ξ_c^+ candidates is:

$$\tau_{\Xi_c^+} = 0.35^{+0.12}_{-0.08}\ (\text{stat.}) \pm 0.07\ (\text{syst.}) \quad \text{psec}$$

The large errors are due to the limited statistics and to the effect induced by a high level of background events.

The other four existing measurements of the Ξ_c^+ lifetime are listed in table 7.3.

Experiment	Decay channels	Entries	Measured lifetime [psec]
WA62	$\Lambda^0 K^- \pi^+ \pi^+$	53	$0.48^{+0.21\ +0.20}_{-0.15-0.10}$
E400	$\Lambda^0 K^- \pi^+ \pi^+$	102	$0.40^{+0.18}_{-0.12} \pm 0.10$
ACCMOR	$\Xi^- \pi^+ \pi^+$, $\Sigma^+ K^- \pi^+$	6	$0.20^{+0.11}_{-0.06}$
E687	$\Xi^- \pi^+ \pi^+$	30	$0.41^{+0.11}_{-0.08} \pm 0.02$

Table 7.3: Previous measurements of the Ξ_c^+ lifetime reported by the PDG group [1].

With these measurements, the world average value is estimated to be:

$$\tau^{ref}_{\Xi_c^+} = 0.353^{+0.070}_{-0.045} \quad \text{psec}$$

Figure 7.1 shows the comparison between the previous measurements, the world average value, the lifetime value measured in this work and the new average calculated including this result. The asymmetric statistical and systematic errors of each measurement have been summed in quadrature.

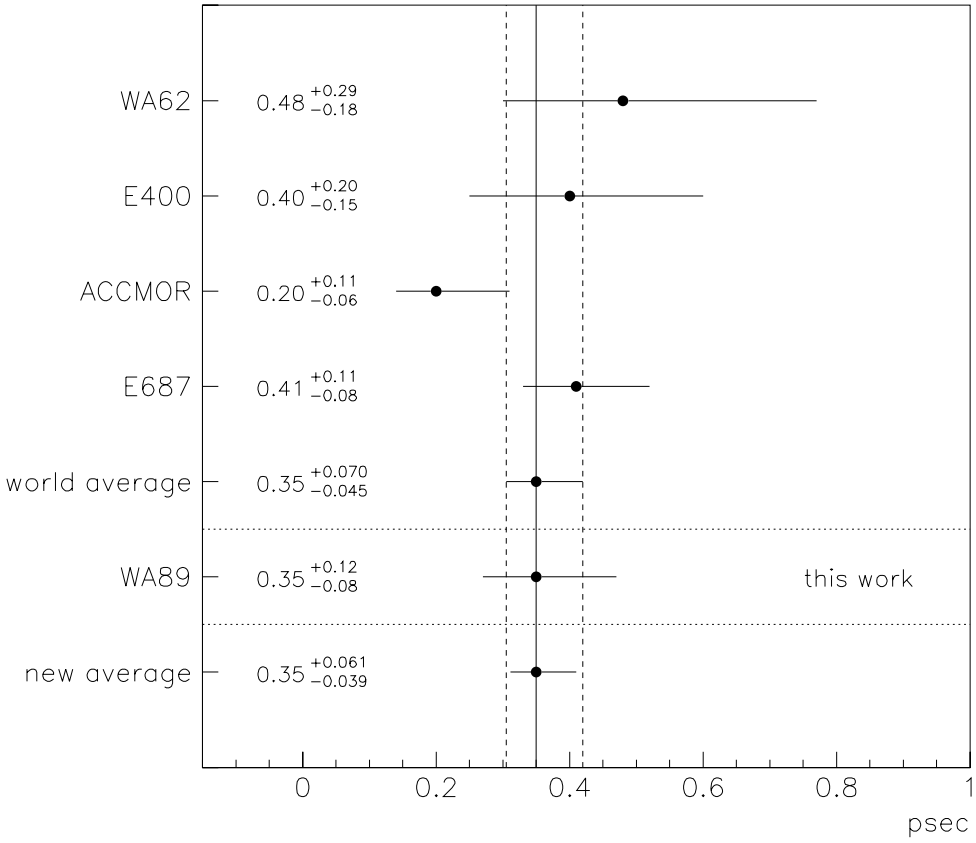

Figure 7.1: Comparison between previous measurements, the current world average value, the result of this analysis and the new average calculated including this result for the Ξ_c^+ mean lifetime.

The new average was calculated with the five measured lifetime values following the indications given by the Particle Data Group ([1], p. 1180). Each considered measurement x_i has asymmetric errors δx_i^+ and δx_i^-. In making the average, for each measurement the error δx_i used for the fit was determined in the following way:

$$\delta x_i\,(\overline{x}, x_i, \delta x_i^+, \delta x_i^-) = \begin{cases} \delta x_i^+ & \text{if } \overline{x} > x_i + \delta x_i^+ \\ \frac{\delta x_i^+ - \delta x_i^-}{\delta x_i^+ + \delta x_i^-}(\overline{x} - x_i + \delta x_i^-) + \delta x_i^- & \text{if } x_i - \delta x_i^- \le \overline{x} \le x_i + \delta x_i^+ \\ \delta x_i^- & \text{if } \overline{x} < x_i - \delta x_i^- \end{cases} \tag{7.1}$$

The average is calculated as:

$$\overline{x} = \frac{\sum_i w_i x_i}{\sum_i w_i} \qquad \text{where} \qquad w_i = 1 / (\delta x_i)^2 \tag{7.2}$$

As the error δx_i depends on the average $\overline{x}$, several iterations have to be done to converge to a stable result. The new asymmetric errors are calculated as:

$$(\delta\overline{x})^{\pm} = (\sum_i w_i^{\pm})^{-1/2} \qquad \text{where} \qquad w_i^{\pm} = 1 / (\delta x_i^{\pm})^2 \tag{7.3}$$

The new average obtained including the lifetime value measured in this work is:

$$\tau_{\Xi_c^+}^{new} = 0.354^{+0.061}_{-0.039} \text{ psec}$$

The world average value is confirmed and its errors are reduced by approximately 13%.

The determined value of the Ξ_c^+ lifetime favors Guberina's prediction for the hierarchy of the lifetimes of charmed baryons mentioned in chapter 1:

$$\tau(\Omega_c^0) \simeq \tau(\Xi_c^0) < \tau(\Lambda_c^+) < \tau(\Xi_c^+)$$

Using the world average value of $0.200^{+0.011}_{-0.010}$ psec for the Λ_c^+ lifetime and the new average lifetime of the Ξ_c^+ given above, the ratio

$$\frac{\tau(\Xi_c^+)}{\tau(\Lambda_c^+)} = 1.77^{+0.45}_{-0.37}$$

is obtained. Compared with the various predictions (1.0 for Voloshin and Shifman's model including soft gluon effects; 1.6 for Guberina's non-relativistic quark model; 1.3 for Blok and Shifman's model which considers higher order operators), the result seems to favor the plain non-relativistic quark model from Guberina et al.
The significant difference between the lifetimes of the four charmed baryons which decay weakly suggests that the W-exchange and light quark interference effects are large compared to the c-quark spectator decay.
Only the selection of larger samples of charmed baryons for the study of their lifetimes will allow measurements with smaller errors and will give more precise indications about the relative strength of the various contributions to the decay amplitude.

Bibliography

[1] The Particle Data Group, "Review of particle properties", Phys. Rev. D3 (1994)

Summary

WA89 is a fixed target experiment with a 340 GeV/c hyperon beam at the SPS at CERN. One of the main topics of its physics program is the study of the properties of charmed baryons. For the measurement of their lifetimes, silicon microstrip detectors are an essential tool to measure with the required resolution the production and the decay point of short living particles.
Large area, 25 μm pitch detectors were tested, equipped with readout electronics performing zero suppression, and operated in WA89 during two data taking periods. The silicon counters showed excellent quality, confirmed by the very good performance of the vertex detector in WA89. A resolution of about 5 μm in the transversal plane, and 400 μm in the longitudinal direction were obtained.
The spatial information provided by the microstrip detectors allows the reconstruction of primary and secondary vertices with high precision. With an analysis program based on a candidate driven approach, the anti-charmed mesons $\overline{D}^0$ and D^- and the charmed strange baryon Ξ_c^+ have been reconstructed in the following decay channels:

$$\begin{aligned} \overline{D}^0 &\rightarrow \quad K^+\pi^- \\ D^- &\rightarrow \quad K^+\pi^-\pi^- \\ \Xi_c^+ &\rightarrow \quad \Lambda^0 K^-\pi^+\pi^+ \\ \Xi_c^+ &\rightarrow \quad \Xi^-\pi^+\pi^+ \end{aligned}$$

The selected candidates were used to measure the mean lifetimes. An unbinned maximum likelihood method was applied and the following results were obtained:

$$\begin{aligned} \tau_{\overline{D}^0} &= \quad 0.433^{+0.054}_{-0.046}\ (\text{stat.}) \pm 0.024\ (\text{syst.}) \quad \text{psec} \\ \tau_{D^-} &= \quad 0.991^{+0.113}_{-0.098}\ (\text{stat.}) \pm 0.054\ (\text{syst.}) \quad \text{psec} \end{aligned}$$

$$\tau_{\Xi_c^+} = \quad 0.35^{+0.12}_{-0.08}\ (\text{stat.}) \pm 0.07\ (\text{syst.}) \quad \text{psec}$$

The lifetime values measured for the mesons are in good agreement with the reference values, proving the validity of the method used.
The existing measurements of the Ξ_c^+ lifetime are very few and all are affected by large errors due to the limited statistics available. The result presented in this work confirms the world average value and reduces its errors by approximately 13%. It agrees, within the errors, with theoretical predictions.
Only higher statistics measurements with smaller errors will allow a better understanding of the interplay of weak and strong interactions in the decay of heavy flavors and the relative weight of the processes involved.

A significant improvement in tracking and pattern recognition for the reconstruction of charmed hadron decays can be achieved with the use of double sided microstrip detectors. The development and the test of a system with double sided counters and zero suppression readout has been presented. The device is now installed at the “next generation” hyperon beam experiment SELEX at Fermilab, downstream of the vertex area. The success of the project supports the possibility of including double sided detectors close to the vertex area to limit the amount of scattering material and improve pattern recognition.

List of Figures

List of Tables

Personal contributions

I joined the WA89 Collaboration in September, 1993, and took part in the data taking period in 1994.
Large part of my work was devoted to the silicon microstrip detectors, both the single sided installed in the vertex area of WA89 and the double sided developed for the SELEX experiment. For all detectors described in the thesis, I performed the electrical tests at the probe station, the selection of the counters for installation and I took part in the mounting and assembly of the whole devices. Particularly for LASD, I supported the choice of double sided detectors, participated to the design of the device, and tested all components for the assembly of the system. I took part to all test beams which took place between 1994 and the end of 1995, preparing and monitoring the detectors, participating to the data taking and the on-line analysis of the data. I also participated to the first phase of installation at Fermilab.
On the analysis side, I have used the *xip*2 code developed by other members of the collaboration. Using this code, I have performed systematic studies on the procedure to reconstruct primary vertices. The code was then used to filter the data as described in the thesis and finally select the candidates presented.

The WA89 Collaboration

Univ. Bristol: V. J. Smith, D.M. Newbold.
CERN: P. Grafström, W. Klempt
Univ. Genoa / INFN: D. Barberis, L. Rossi.
ISN Grenoble / IN2P3: C. Bérat, M. Buénerd, F. Charignon, J. Chauvin, A. Fournier, Ph. Martin, M. Rey-Campagnolle, R. Touillon, E. Vesin.
Max-Planck-Institut für Kernphysik, Heidelberg: E. Albertson, M. Beck, K.-H. Brenzinger, S. Brons, W. Brückner, Ch. Busch, Ch. Büscher, U. Dersch, F. Dropmann, S. G. Gerassimow, M. Godbersen, Th. Haller, M. Heidrich, N. Keller, K. Königsmann, I. Konorow, S. Masciocchi, R. Michaels, H. Neeb, S. Paul, B. Povh, Zh. Ren, L. Schmitt, A. Trombini, K. Vorwalter, R. Werding, E. Wittmann.
Univ. Heidelberg: M. Boss, F. Faller, S. Kluth, K. Martens, H. Rieseberg, H.-W. Siebert, A. Simon, O. Thilmann, E. A. Tschudakow, G. Wälder.
Univ. Mainz, Inst. für Kernphysik: U. Müller, G. Rosner, H. Rudolph, B. Volkemer, Th. Walcher.
Lebedew Phys. Inst., Moskow: M. I. Adamowitsch, Ju. A. Alexandrow, M. W. Sawertjajew.
Ch. Newsom (Univ. Iowa), Ch. Scheel (NIKHEF Amsterdam).

Acknowledgements

I would like to thank Prof. Bogdan Povh for accepting me in his group and giving me the opportunity to participate to both experiments, WA89 at CERN and SELEX at Fermilab. I have greatly enjoyed the possibility to get in touch with two research centers and learn different methods, habits, and styles of work. The period spent at the MPI in Heidelberg gave me the chance of starting my way in the German “world”: I have certainly learnt a lot in the variety of experiences I was offered in the last three years.
I would like to thank Prof. Kay Königsmann, who supervised with great energy my first steps in the new group, and always followed my work.
I would like to thank Prof. Franz Eisele for accepting to be the Gutachter of this thesis.
All my gratitude goes to Dr. Stephan Paul, spokesman of WA89 but especially a good friend. I thank him for his patience, his being always ready to listen, to help, to suggest, to encourage, and especially for his smile, and the strength and the optimism he is able to communicate. I have greatly enjoyed spending these years in his group and he certainly taught me a lot on the human side as well as on the physics one!
I would like to thank Igor Konorov, who had to stand the infinite number of my questions about readout electronics and so many other things. He was a constant teacher for me, not only for the technical work, but also for the transparent way of facing and solving troubles, and, above everything, for his incredible patience, which, on the contrary, I sometimes lack.
I am really feeling grateful to the whole WA89 collaboration for these years spent together, working, fighting for the best, rushing to satisfy deadlines, but also learning, knowing each other and making part of our way together. I would like to thank:
Roland Werding for the friendly introduction he gave me to WA89, SVXs and test beams, but also for his bright thinking and energetic acting.
Mathias Beck and Thomas Haller for the cheerful company and the patience for so many things in which I have not joined them.
Eugene Chudakov for the fruitful discussions and the valuable example as a good physicist.
Burkhard Volkemer for the numerous discussions and especially for the good culinary expertise.
Frank Dropmann who first developed the code I used for the analysis.
Jürgen Zimmer for the excellent technical support which made our microstrip devices well standing, aligned and perfectly built; and for the beautiful pictures of the detectors he took for me.
Ogmundur Runolfsson for the patience and the great skill in bonding all our detectors.
Dirk Meier for the happy times spent together for SELEX.
Malte, Margret and Svenja Godbersen, Vince Smith, Matthias Heidrich, and Sergej Gerassimov for their friendship.
The SELEX group from the MPI, for the cheerful company, the share of work they could take away from me, the help in many little things and the fruitful discussions.
The group in Heidelberg, for the time we spent there together.
The group in Grenoble and the one from Russia for the nice occasions we had together.

The SELEX Collaboration who friendly accepted me, and especially Jim Russ, Jürgen Engelfried and Peter Cooper.
Claudia Schröder for the great help to organize things in Heidelberg.
I would like to thank all the people who read my thesis and helped me really a lot to improve it with corrections, suggestions and good ideas: Prof. Ron Ransome for the great work of proof reading almost everything! and patiently correcting my poor English; Dr. Lars Schmitt, who really read every single line and listened to all my questions and worries. His help in doing the work, writing, discussing and correcting is really invaluable; Dr. Stephan Paul, who found the time to read and correct many chapters; Prof. Hans Siebert, Dr. Matthias Heidrich and Dr. Uli Müller who corrected some parts.
I would like to thank Marcelle Rey-Campagnolle in a special way, for the care and the affection she had for me: I am really grateful and happy to have met this sweet and strong woman.
I would like to thank Mr. Yamamoto and Mr. Mayer from Hamamatsu Photonics for the fruitful discussions, the beautiful photos and the always very interesting meetings; Prof. Bosisio from INFN Pisa and Mr. Perret from CSEM for their great help concerning the double sided detectors.

I would like to thank my lovely friends Gabriella, Silvio, Stefano, Martin and Britta for their support, their patience for my always being busy or far away: Your affection always supports me and cheers me up in every situation or place where I am.
Besonders herzlich danke ich meinem lieben Lars, für die ständige Unterstützung und für die Hilfe, die so wichtig war, um diese Arbeit zu vollenden. Aber, vor allem waren seine Liebe, seine Zärtlichkeit und die unendliche Fröhlichkeit die Quelle der Energie und der Freude und werden es immer sein.
Und, natürlich auf Deutsch, danke ich meinen guten Freunden Alexander und Dominique (désolée, pas encore en français!).
Ed infine vorrei ringraziare la mia famiglia ed in modo davvero speciale i miei genitori: mi avete dato la libertà di seguire gli studi che tanto amo e l'opportunità di imparare, viaggiare, conoscere e crescere, stando purtroppo lontana da voi. Vi ringrazio per il vostro grande amore, per la vostra pazienza e per il continuo supporto che mi avete dato, in mille modi. E, al di la' della fisica che continuerò ad imparare, spero soprattutto di saper realizzare nella mia vita i valori in cui crediamo, la serietà, l'onestà, la generosità e la tenerezza che voi mi avete insegnato.